

In situ Measurements of Chemical Compositions during TIG-Welding by Laser-Induced Breakdown Spectroscopy

Dissertation

zur Erlangung des akademischen Grades

Doktoringenieur

(Dr.-Ing.)

von M. Sc. Ugur Alp Taparli

geboren am 05.03.1987 in Kadiköy, Türkei

genehmigt durch die Fakultät für Maschinenbau
der Otto-von-Guericke-Universität Magdeburg

Gutachter:

Prof. Dr.-Ing. habil. Thomas Kannengießer

Prof. Dr.-Ing. Jonas Hensel

Promotionskolloquium am 08.01.2024

Abstract

In this work, the use of Laser-induced Breakdown Spectroscopy (LIBS) for hot crack detection during welding by in-situ measurement of the chemical composition in the molten pool was investigated. The aim was to explore welding process control using LIBS to avoid metallurgically induced welding defects.

Welding metallurgy is a complex field where the final microstructure, and thus the mechanical properties of welds, can be influenced by various metallurgical aspects. These can lead to changes in the local chemical composition of the molten pool and consequently, to changes in solidification conditions. This determines the overall weldability of the material and hence the end quality of the product. The final microstructure and thus the mechanical properties of the solidified weld are determined by parameters such as the partition coefficients of the main alloying elements in the melt, temperature gradients in the molten pool, and local solidification conditions.

Hot cracks that may occur during the solidification process are the most common welding defects. To avoid hot cracks, in-situ measurement of the chemical composition of the molten pool during the welding process can be utilized if it allows for a change in local solidification conditions through the variation of welding parameters. An appropriate method for in-situ monitoring of the molten pool composition is LIBS. Short laser pulses are used to generate a plasma on the surface of the melt. A spectrometer then analyzes the emitted radiation to determine the element-specific composition. The advantages of LIBS are simultaneous multi-element detection, non-contact measurement from a safe distance, and rapid analysis. This makes LIBS a promising method for measuring or monitoring chemical element concentrations in metal melts with high spatial and temporal resolution.

Overall, this work emphasizes the importance of hot crack detection during welding and thus the potential of in-situ monitoring methods for improving the quality of welds. By online measurement of element contents, changes in the molten weld pool composition can be detected and countermeasures initiated before welding defects occur. This reduces rework and associated costs and times, leading to improved efficiency and profitability in the metal and manufacturing industry.

This work investigated the use of LIBS for monitoring the welding process of stainless steel grades with tungsten inert gas welding (TIG welding). The study showed that the spatial resolution of LIBS measurement can be achieved with approximately 200 μm and at least 1 mm away from the weld pool. The study also found that the flow rate of the shielding gas Ar during welding has no influence on the detected LIBS signal. However, the most important result is that LIBS can be used to measure chemical elements during welding and that changes in chemical composition can be measured with high temporal and spatial resolution. The investigation focused on understanding the hot crack behavior of high-alloyed stainless steels, with particular emphasis on the chemical composition of the weld metal. To deepen the

understanding, a model was developed based on the online available chemical composition of the main alloying elements to calculate the partition coefficient of solid and liquid phases in the mushy zone. In addition, an offline inspection of the fully welded joints was performed to enable a comparison of the chemical composition distribution between the liquid and solid states. Austenitic solidification is the main reason for the hot crack behavior of the investigated stainless steels, with the austenite-promoting element nickel having approximately up to 4wt% higher values than the measured reference values of the selected stainless steels.

Zusammenfassung

In dieser Arbeit wurde der Einsatz der Laser-induzierten Breakdown-Spektroskopie (LIBS) zur Heißriss-Detektion während des Schweißens mittels *in situ* Messung der chemischen Zusammensetzung im Schmelzbad untersucht. Das Ziel war, eine Schweißprozesskontrolle mittels LIBS zur Vermeidung von metallurgisch bedingten Schweißfehlern zu eruieren.

Die Schweißmetallurgie ist ein komplexes Feld, in dem die endgültige Mikrostruktur, und damit die mechanischen Eigenschaften der Schweißnähte, durch verschiedene metallurgische Aspekte beeinflusst werden können. Diese können zu Änderungen der lokalen chemischen Zusammensetzung des Schmelzbades und daraus resultierend, zu Änderungen der Erstarrungsbedingungen führen. Dies bestimmt die Schweißbarkeit des Materials insgesamt und damit auch die Qualität des Produkts. Die endgültige Mikrostruktur und damit die mechanischen Eigenschaften der erstarrten Schweißnaht, werden von Parametern wie den Partitionskoeffizienten der Hauptlegierungselemente in der Schmelze, Temperaturgradienten im Schmelzbad und den lokalen Erstarrungsbedingungen bestimmt.

Heißrisse, die während des Erstarrungsprozesses auftreten können, sind die am häufigsten auftretenden Schweißfehler. Zur Vermeidung von Heißrissen kann prinzipiell die *in situ*-Messung der chemischen Zusammensetzung des Schmelzbads während des Schweißprozesses genutzt werden, wenn dadurch eine Änderung der lokalen Erstarrungsbedingungen über die Variation der Schweißparameter möglich ist. Eine geeignete Messmethode zur *in situ*-Überwachung der Schmelzbadzusammensetzung ist LIBS. Dazu werden kurze Laserpulse verwendet, um ein Plasma auf der Oberfläche der Schmelze zu erzeugen. Ein Spektrometer analysiert dann die emittierte Strahlung zur Bestimmung der elementspezifischen Zusammensetzung. Die Vorteile von LIBS sind die simultane Mehrfachelementerkennung, die berührungslose Messung aus sicherer Entfernung und die Schnelligkeit der Analyse. Dies macht LIBS zu einer vielversprechenden Methode für die Messung bzw. Überwachung chemischer Elementkonzentrationen in Metallschmelzen mit hoher Orts- und Zeitauflösung.

Insgesamt hebt diese Arbeit die Bedeutung der Heißrissdetektion während des Schweißens und damit das Potenzial von *in situ*-Überwachungsmethoden für die Qualitätsverbesserung von Schweißungen hervor. Durch die online-Messung der Elementgehalte können somit Änderungen der Schmelzbadzusammensetzung detektiert werden und vor dem Auftreten von Schweißfehlern Gegenmaßnahmen eingeleitet werden. Dadurch werden Nacharbeiten reduziert und damit verbundene Kosten und Zeiten minimiert, was zu einer verbesserten Effizienz und Rentabilität in der Metall- und Fertigungsindustrie führt.

Diese Arbeit untersuchte die Verwendung von LIBS zur Überwachung des Schweißprozesses von Edelstahlsorten mit Wolfram-Inertgas-Schweißen (WIG-Schweißen). Die Studie zeigte, dass die räumliche Auflösung der LIBS-Messung mit ca. 200 μm und mindestens 1 mm von dem Schweißbad entfernt realisiert werden kann. Die Studie stellte auch fest, dass der

Durchfluss des Schutzgases Ar beim Schweißen keinen Einfluss auf das detektierte LIBS-Signal hat. Das wichtigste Ergebnis ist aber, dass LIBS für die Messung chemischer Elemente beim Schweißen zu verwenden ist und dass Änderungen in der chemischen Zusammensetzung mit hoher Zeit- und Ortsauflösung gemessen werden können. Die Untersuchung konzentrierte sich darauf, das Heißrissverhalten von hochlegierten Edelstählen zu verstehen, wobei insbesondere die chemische Zusammensetzung des Schweißguts untersucht wurde. Um das Verständnis zu vertiefen, wurde ein Modell entwickelt, das auf der online verfügbaren chemischen Zusammensetzung der Hauptlegierungselemente basiert, um den Partitionskoeffizienten der festen und flüssigen Phasen in der Mushy-Zone zu berechnen. Darüber hinaus wurde eine Offline-Inspektion der fertig geschweißten Nähte durchgeführt, um einen Vergleich der chemischen Zusammensetzungsverteilung zwischen dem flüssigen und festen Zustand zu ermöglichen. Die austenitische Erstarrung ist der Hauptgrund für das Heißrissverhalten der untersuchten Edelstähle, wobei das austenitfördernde Element Nickel, ca. bis 4wt% höhere Werte aufweist als die gemessene Referenzwerte der ausgewählten Edelstähle.

Contents

1.	Introduction.....	11
2.	Literature review	13
2.1.	Genesis and development of steel.....	13
2.1.1.	Status quo of the global production and consumption.....	14
2.1.2.	Alloy steel	15
2.2.	Transport phenomena in materials.....	20
2.2.1.	Energy transport.....	20
2.2.2.	Diffusive Mass Transport.....	23
2.3.	Welding metallurgy of stainless steels.....	30
2.3.1.	Stainless steel formation and weldability	30
2.3.2.	Tungsten-Inert Gas (TIG) Welding.....	33
2.3.3.	Weld solidification.....	35
2.3.4.	Partition Coefficient	37
2.3.5.	Weld chemical composition	42
2.3.6.	Hot cracking.....	47
2.4.	In situ weld monitoring	55
2.4.1.	Laser-induced breakdown spectroscopy (LIBS).....	58
2.4.2.	Radiation - matter interaction.....	61
2.4.3.	Characterization of laser-induced plasma.....	62
2.4.4.	Spectral processing and data quantification	63
3.	Summary of the literature.....	66
4.	Problem statement and objectives	68
5.	Experimental	72
5.1	Analyzed materials	72
5.1.1	Base materials	72
5.1.2	Filler materials.....	72
5.2	Experimental setup for in situ weld chemical composition monitoring	73
5.3	Characterization methods.....	79
5.3.1	Light optical microscopy.....	79
5.3.2	Scanning electron microscopy (SEM)	79
5.3.3	Spark-optical emission spectroscopy (OES).....	81
5.3.4	X-Ray (Radiography) Analysis	81
5.4	Preliminary Experiments: In situ alloying element detection using LIBS.....	82
5.4.1	Welding plasma as an analytical signal source.....	82
5.4.2	Influence of the welding parameters on the LIBS Signal.....	85
5.4.3	In situ detection of filler material addition during welding	97

6.	Results and discussion.....	110
6.1	Monitoring the alloying elements and parameters.....	110
6.1.1	LIBS Parameter investigation and optimization	110
6.1.2	Alloying element vaporization from the weld pool.....	121
6.2	Weld process monitoring during hot cracking of stainless steels using LIBS.....	127
6.2.1	Hot-cracking boundary conditions	127
6.2.2	Hot-Cracking, in situ chemical composition and in situ partition coefficient calculation 130	
6.2.3	Post-weld crack investigations.....	154
7.	Conclusions and future work.....	176
	List of Figures.....	179
	List of Tables.....	185
	References.....	186

Chapter 1

1. Introduction

Any flaw that compromises the usefulness of a weld is defined as a 'weld defect'. Welds tend to have defects due to various reasons. Process conditions remain at first place with 41%. According to Matthews [1], the main defects caused due to the process conditions are 'porosity', 'hot-cracking' and 'cold cracking'. These defects can be avoided by interfering with the process parameters.

Operator errors contain the second place with 32%. Within the framework of 'Industry 4.0', the manufacturing environment is evolving into automated cyber-physical systems and towards less human interference. Therefore, the automated systems need in-line process monitoring providing real time feedback for the intelligent manufacturing machines, to avoid potential weld defects, and thus improving the weld quality on site.

Chemical composition of a weld may lead to solidification related weld defects. Hence, the chemical composition of a weld may differentiate locally within the molten weld pool from the expected outcome due to above-mentioned or other various reasons depending on the external or internal factors. On one hand, alloying element burn-off (Cr, Ni, Mn etc.) during welding process may cause degradation of the part. The amount of the burnt-off material is controlled by the enthalpy of vaporization. On the other hand, a process flaw could cause undesired too fast or too slow material addition rate by filler rods or consumable electrodes, may also cause strongly deviated chemical compositions of the weld from the expected, hence causing weld defects.

To prevent weld defects such as hot cracks, it is necessary to detect them early in the welding process. This is achieved through the measurement of weld chemical composition, which can be used to identify the formation of hot cracks. By detecting these cracks early, the welding process can be adjusted in real-time to prevent further cracking and ensure the weld is of high quality.

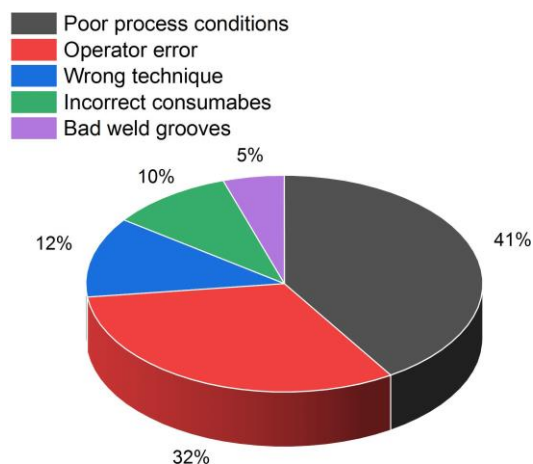


Figure 1-1: Main causes of weld defects[1]

There are currently no commercial systems available to measure the inline weld chemical composition. Conventional methods mainly evolve around destructive testing, such as cross sectioning the weld and conducting further measurements e.g., EDX, X-ray fluorescence or any other convenient spectroscopy method, can establish a spatially resolved chemical composition data on the sample. However, these methods would have pros and cons depending on the boundaries of the method itself. The main boundary of the weld chemical composition measurement methods would be, however, the methods being destructive and not applicable for onsite use.

Retrieving the online chemical composition data during the welding process could lead to eliminating the whole post-weld destructive investigations, hence reducing the risk of the parts failing during service and subsequently reducing quality control costs and time for the application area. In this sense, the improvements in laser technologies and laser-based spectroscopy methods are very promising to develop such systems for feasible application models due to their speed in terms of retrieving data as well as flexibility due to relatively lower costs of investment and return compared to laboratory scale equipment. Considering the online chemical composition information is retrieved from the molten weld pool, the data can be used to categorize the weld quality instantly. Moreover, the next step can be a feedback loop into the welding system to regulate the welding parameters to interfere with the weld quality during the welding process. Regulating the process parameters using the feedback data can allow regulating the chemical composition instantaneously during the welding process, thus instantaneously taking preventative actions against weld defects.

This study consists of building a prototype Laser-induced Breakdown Spectroscopy (LIBS) based chemical composition monitoring system for Tungsten-Inert Gas (TIG) welding process, to measure the alloying elements in the molten weld pool of hot-cracking susceptible materials, i.e. austenitic stainless steels. This study is the first step of a larger framework from creating a commercial smart welding system to assess the welding parameters by itself via continuous measurement of the weld chemical compositions during the welding process.

Chapter 2

2. Literature review

2.1. Genesis and development of steel

The history of modern steel industry began in 1850s with the invention of 'Bessemer process' [2], based on the principle of blowing air through the molten pig iron to oxidize the material and to remove the impurities. As of year 2020, steel still represents one of the most used materials in the world.

In essence, steel is an alloy of iron -matrix- and carbon. Steel is categorized by its chemical composition and physical properties, called 'steel grade'. Hence this categorization is undertaken by several institutions e.g. International Organisation for Standardization (ISO), American Society for Testing and Materials (ASTM), European Committee for Standardisation (CEN), using various designations. The properties of each steel grade are determined by the amount of carbon, as well as the level of impurities and additional alloying elements. According to the World Steel Association, there are over 3500 steel grades available.

Steel is frequently referred as the 'golden-standard' when compared to the other structural materials. It has been a growing and developing material, therefore, it has allowed constant and exciting discoveries in the context of iron and its alloys. This makes steel one of the most successful and cost-effective materials with over a billion tons of consumption annually[3].

Currently, metallurgists can combine approximately 170 years of steel-making knowledge of the metallurgical interrelationships with technological advancements and the modern production capabilities[4]. Furthermore, using the advanced computing power of modern computers and with utilizing artificial intelligence (AI), it is possible to model, simulate and produce very specific alloy designs for extremely specified applications.

The main goal of modern materials science can be identified as the theory-guided tailoring of materials. This includes optimizing the chemical composition and microstructure of the resulting alloy system to have improved properties for a sustainable technological advancement [5, 6]. Apart from these aspects, steel alloy design can also encompass economic reasons, including balancing the manufacturing, lifetime, maintenance and raw material costs, hence the safety factor[4].

Raw materials in context of steelmaking generally include iron ore, coal, coke, steel scrap and alloying elements e.g. chromium, nickel, molybdenum, magnesium. The cost of these raw materials is usually established by several factors e.g. available global resources in the market and recovery of those, global consumption and recycling.

2.1.1. Status quo of the global production and consumption

Over the past twenty years, there has been a global acceleration in steel production, which significantly increased the demand on the raw materials as well. Figure 2-1 shows the global crude steel production between 1950-2020. The increased production rates approximately start with the year 2000. The main reason of this growth has been mainly the economic developments in Asia. According to World Steel Association global crude steel production reached 1 billion tonnes by 2019[7]. There has not been any significant decrease since 1995.

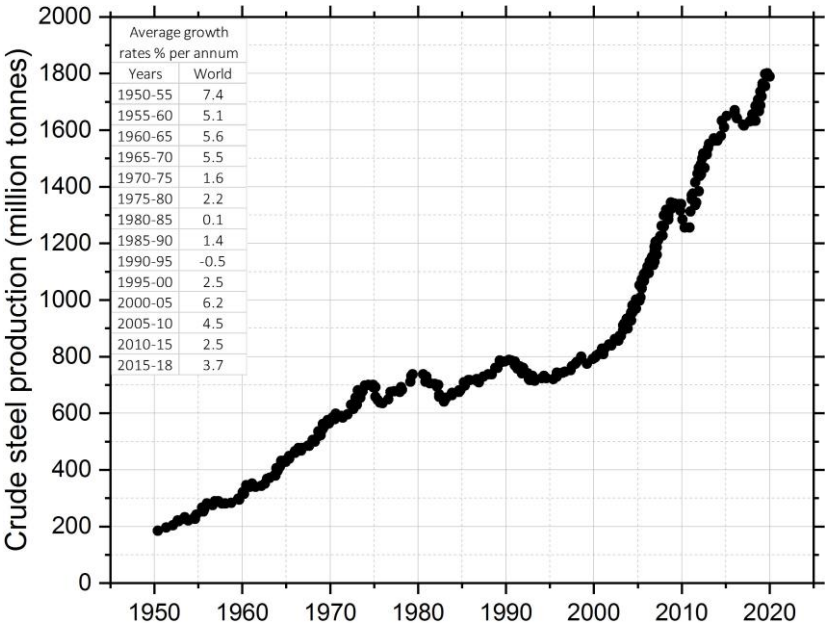


Figure 2-1: Worldwide crude steel production between 1950-2020 (Data source: World Steel Association) [7]

There have been some minor step-backs in the past twenty years as well, such as the decrease between 2008 -2010 due to the global economic crisis, having a negative influence on the global demand, consequently decreasing the overall production.

Overall trend of crude steel production is still increasing. Correspondingly, the demand on the raw materials is increasing. This situation, however, causes imbalanced and abrupt changes in the raw material prices. Metal prices change on daily basis depending on supply and demand, strategic importance, technological advancements and even the political climate in the producer country. Accordingly, it is not possible to estimate an accurate table of costs. However, it is possible to compare the relative prices of the major alloying elements of steel using iron as the base [8]. Figure 2-2 shows the approximate cost of major alloying elements relative to iron.

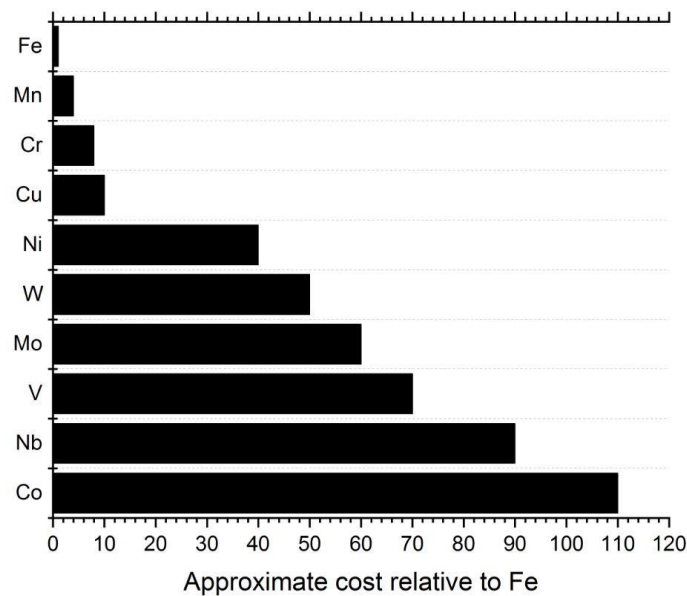


Figure 2-2: Approximate cost of major alloying elements relative to iron

The intensive cost pressure in the production of welded components, e.g. stainless steel -base metal- and welding consumables, results a variety of influencing factors. Stainless steels have a chromium content of at least 12% [9] up to 30% [3] and a nickel content of between 8% to 20% [3]. In the case of highly corrosive environment in the high temperature range, e.g. exhaust systems of motor vehicles, the nickel content must be increased again. However, this corrosion resistance can be affected during the welding process, among other process flaws such as elemental burn-off. The depletion of the above-mentioned alloying elements can impair the high-temperature corrosion resistance that is required and necessary for both component safety and safe operation in order to compensate for this burn-off behavior, a super-alloyed and thus extremely cost-intensive filler metal is often used in welding processes. The price development of the required alloying elements is therefore a major problem in the cost calculation of welding work with these steels.

Even though there is a certain flexibility in steel alloy design, the principal goal is to apply the most cost-effective design for the producers. Furthermore, even small market fluctuations of the alloying or micro-alloying elements could have an impact on the alloy design. Although the alloying elements can vary in a certain range, standards ensure that each grade of steel provides certain mechanical properties regardless of its producer[4]. Moreover, even though the mechanical properties satisfy the given standard's limits, the final product might not satisfy the same standard's alloying elements tolerance range in an attempt to reduce production costs.

2.1.2. Alloy steel

Although the general definitions and classifications in the field vary according to the country and the corresponding language, standard etc., alloy steels are defined as the type of steel

alloyed with several elements such as molybdenum, manganese, nickel, chromium, vanadium, silicon and boron. The main reason of this alloying practice is to increase the critical strength, hardness, wear and corrosion resistance and toughness values of the material. Considering the alloy steels, the amount of the alloying elements may vary between 1 and 50 wt%. Alloy steels can be subdivided into two groups, namely high alloy and low alloy steels. The commonly accepted boundary between low alloy and high alloy steel is usually considered 5 wt% alloying elements in the material [10]. Stainless steels are considered as a subgroup of high alloy steels.

A further way to categorize the alloys can be made according to the alloy composition and the resulting corrosion or high temperature properties. Farrar[8] categorizes the alloys as shown in Figure 2-3. According to this categorization, the alloy tree diagram provides an overview of the most important iron and nickel-based alloy groups and how they are linked with each other. The plain carbon steel is listed at the top as a starting point and towards down of the tree with increasing the alloy components and the resulting alloy groups are shown accordingly. The left-hand side of the tree shows the low and very low-carbon alloys designed mainly for corrosion resistance. The right-hand side of the alloy tree demonstrates the alloys contain controlled amounts of carbon or high-carbon alloys designed mainly for high temperature applications in various atmospheres.

Stainless steels find various application areas in many different industries e.g., the ubiquitous 18/8 Cr-Ni finds usage where sterility and appearance are important compared to corrosion resistance. This can contain usage in food, drink and pharmaceutical production where exposure is only restricted to weak acidic environment. Brewing, wine and medical equipment industries also use this type of alloys.

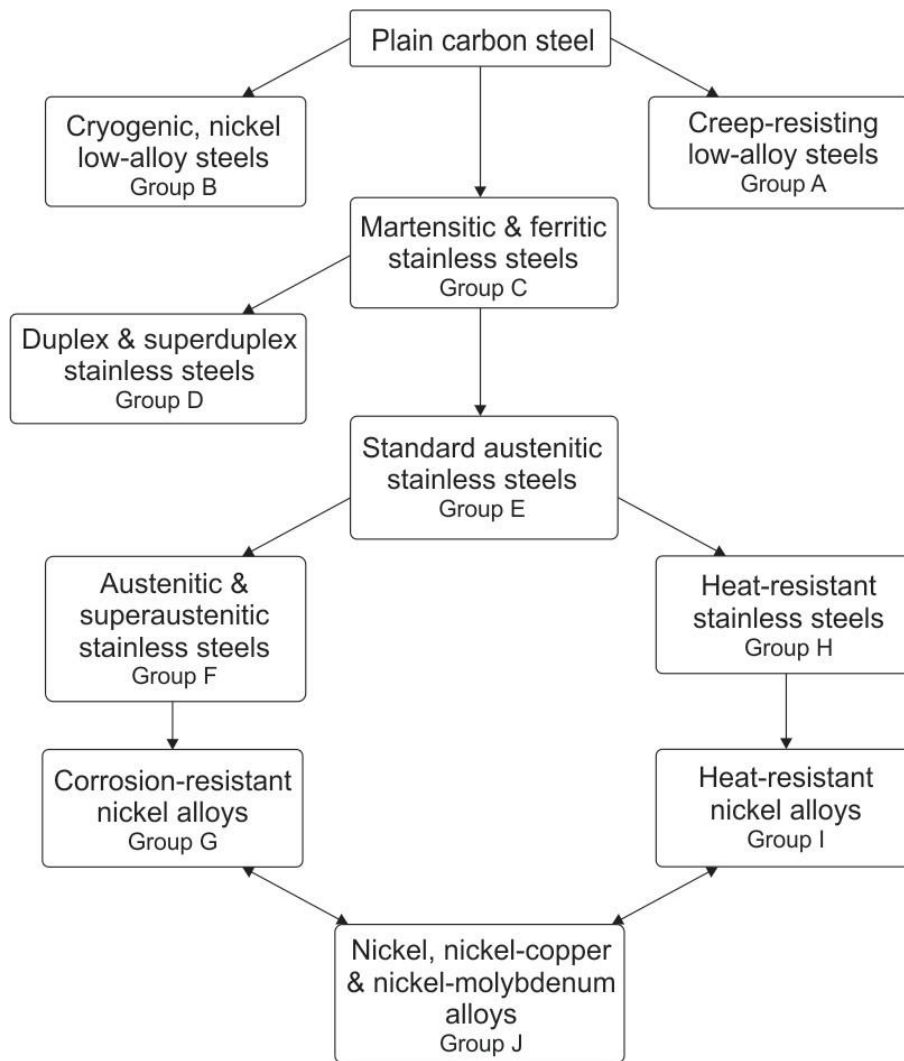


Figure 2-3: The alloy tree showing the interrelationships between the major alloy groups

As these alloys contain about 2.5% molybdenum, stainless steels may endure more corrosive environments. They are mainly used in chemical and petrochemical process plants, and thus are reasonably resistant to dilute acids at lower temperatures. A special and very successful application of these types are also offshore oil and gas platform modules, where maintenance and repainting costs can be significantly reduced[8].

Stainless steel

According to the DIN EN 10020:2000 [11], the definition of stainless steel is as follows: “Stainless steels are the steels that contain minimum mass fraction of chromium 10.5 wt% and a maximum carbon of 1.2 wt%.”

Stainless steels represent a group of high alloy steels based on Fe-Cr, Fe-Cr-C, and Fe- Cr-Ni systems[12]. The word 'steel' implies that iron composes the bulk of the material,

whereby 'stainless' means the non-appearance of staining, rusting or corroding, in the environments where 'non-stainless' steels would be susceptible to the problems e.g. in relatively pure and dry air. The utilization of the 'stainless' property in steels is achieved by the addition of at least about 11 wt% chromium into the alloy system. This amount of chromium can form an adherent and self-healing chromium oxide layer on the steel surface in relatively friendly environments. However, as the conditions deteriorate, and more hostile environments are concerned, e.g. humid, moist or polluted environments, higher chromium levels are required to avoid pitting and rusting [9].

DIN EN 10088 standard classifies stainless steel grades and divides the stainless steels under three subcategories, namely 'corrosion-resistant steels (Ger. Korrosionsbeständige Stähle)', 'heat-resistant steels (Ger. Hitzebeständige Stähle) ', and 'creep-resistant steels (Ger. Warmfeste Stähle) '. Chemical compositions for individual steel grades can be found in this standard. Further corresponding standards for the steel grades can be seen in Table 1.

Table 1: Overview of material standards for stainless steels [13, 14]

Corrosion-resistant steels	Heat-resistant steels	Creep-resistant steels
EN 10028-7		EN 10028-7
EN 10088-2		
EN 10088-3		
EN 10088-4		
EN 10088-5		
	EN 10095	
EN 10151		
EN 10216-5		EN 10216-5
EN 10217-7		
EN 10222-5		EN 10222-5
EN 10250-4		
EN 10263-5		
EN 10264-4	EN 10264-4	
EN 10269		EN 10269
EN 10270-3		
EN 10272		
EN 10296-2		
EN 10297-2		
		EN 10302
EN 10312		

DIN EN 10088-1 does not only categorize the stainless steel according to its application field. The categorization can also be made according to stainless steel's solidification mode and corresponding microstructure. According to their final crystalline structure, stainless steels can be sub-categorized into austenitic stainless steel, ferritic stainless steel, duplex stainless steel and martensitic stainless steel. Furthermore, the detailed review of the austenitic and ferritic stainless steels in context of welding metallurgy will be covered in the section 2.3 Welding metallurgy of stainless steels.

Austenitic stainless steels

Austenitic stainless steels can be considered as the most common and familiar type of stainless steel. They are essentially non-magnetic, have good formability properties and good weldability [12]. They enable utilization in cryogenic temperatures as well as high temperatures of furnaces or jet engines. Typically, they contain between about 16 to 25 wt% chromium, additionally they can contain nitrogen in solution, both contributing to their corrosion resistance property. These alloys would have been used even more widely, if the austenite stabilizing element nickel costs were lower [15].

Ferritic stainless steels

Ferritic stainless steels are the lowest cost option for high corrosion and oxidation environments. The ferritic stainless steels are essentially ferromagnetic. Their toughness values drop significantly for heavier sections; therefore, they are mostly useful in sheet form. This type of stainless steel can still economically displace the popular but expensive alternative EN grade 1.4301 alloy in many routine applications[12, 15].

Duplex stainless steels

Duplex stainless steels are the relatively newest family of stainless steel alloys [15]. They contain approximately 50% of austenite and 50% of ferrite and taking advantage of the desirable properties of the each phase [12]. They are strongly magnetic due to the existence of the ferrite phase. Duplex alloys can contain at least of 20% chromium; therefore, they are highly corrosion resistant. However they contain brittling phases and not suitable for high-temperatures[15]. One of the most important advantages of the duplex alloys is due to the lower nickel concentration, the economic costs are lower than the austenitic alloys from the same level of corrosion resistance. Due to the their greater strength values compared to the austenitic stainless steels, they can be utilized with lower amount of material required[15] and reduce production, utilization costs and carbon footprint.

Martensitic stainless steels

Martensitic stainless steels are the statistically smallest category of stainless steels in context of usage in volume. The main reason is the limited corrosion resistance due to the alloying element limitations to produce martensite structure, which is a diffusion-less transformation of austenite under special conditions [15]. However, they fill an important role as strong, hard and tough alloy with relatively good corrosion resistance, ferromagnetic and stable high-temperature alloy[12, 15].

2.2. Transport phenomena in materials

This section introduces the transport phenomena in materials. In the context of welding processes, transport phenomenon was reviewed under two main topics, namely in 2.2.1. Energy transport and in 2.2.2. Diffusive Mass Transport.

2.2.1. Energy transport

The flow of heat in welds

In general terms, the flow of heat in welds is for understanding the nature of the process and predict the resulting trends and temperature zones[18]. The following equations apply for the stationary heat sources. In an isotropic uniform solid system, the equation for the conduction of heat is as follows[18]:

$$\frac{\partial^2 T}{\partial x^2} + \frac{\partial^2 T}{\partial y^2} + \frac{\partial^2 T}{\partial z^2} - \frac{1}{\alpha} \frac{\partial T}{\partial t} = 0 \quad \text{Eq. 1}$$

or

$$\nabla^2 T - \frac{1}{\alpha} \frac{\partial T}{\partial t} = 0 \quad \text{Eq. 2}$$

where T is the temperature, t is the time and α is the diffusivity of heat for the solid in question. Diffusivity of heat is defined as the thermal conductivity divided by the specific heat per unit volume[18]:

$$\alpha = \frac{k}{\rho c} \quad \text{Eq. 3}$$

where k is thermal conductivity defined in Eq. 3, ρ is the density of the substance in question and c is the specific heat capacity.

For two-dimensional flow the formula is valid for a plate or sheet metal, considering that the heat flow across the surfaces is small enough i.e. no heat loss due to the radiative emission. In this case the temperature distribution of a plate with thickness of w can be written as [18]:

$$T = \frac{Q}{4\pi\omega kt} \exp(-r^2/4\alpha t) \quad \text{Eq. 4}$$

It is convenient to express temperature in terms of a reference radius r_0 , which representing the temperature at the boundary of the fused zone[18]. At this radius the peak temperature will be the melting point T_m , and the elapsed time t_0 is:

$$t_0 = \frac{r_0^2}{2D\alpha} \quad T_m = \frac{[Q_s]}{2^D(\pi\alpha t)^{D/2}} \exp\left(-\left(\frac{D}{2}\right)\right) \quad \text{Eq. 5}$$

where D representing the dimension of the heat source, i.e. point, line and plane heat source associated with respectively, three-, two- and one-dimensional.

If the case of an instantaneous line heat source considered, at the time t_0 the radial temperature distribution can be expresses as:

$$T = T_m \exp\left(1 - \frac{r^2}{r_0^2}\right) \quad \text{Eq. 6}$$

and similarly, the temperature as a function of time:

$$T = T_m \frac{t_0}{t} \exp\left(1 - \frac{t_0}{t}\right) \quad \text{Eq. 7}$$

Eq. 13 and 14 can be evaluated for steel with $T_m = 1500$ °C and were plotted in

Figure 2-4:

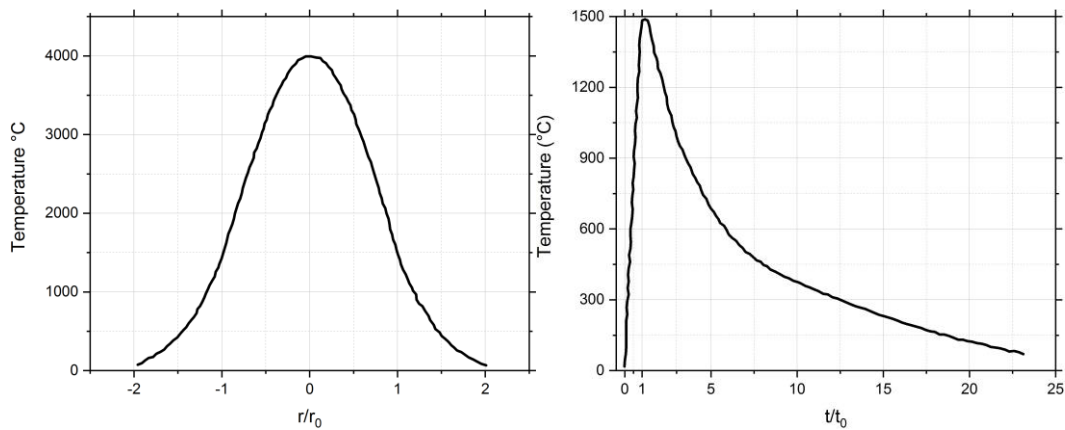


Figure 2-4: Spatial- and time-dependent temperature distributions of a hypothetical steel sample [18] Left: Temperature distribution due to a line heat source at time t_0 when the peak temperature at the radius $r=1$ is equal to 1500°C. Right: Time variation of temperature at radius $r=1$ due to a line heat source as the peak temperature at r_0 is 1500

The physical properties of some metals are given in

Table 2. Please note the thermal conductivity difference between the mild and austenitic steel. Even only comparing this data, one can argue that thermal properties of different types of steels can simply have an impact on the weldability properties of the questioned steel.

Table 2: Physical properties of the selected metals [18]

Metal	Mass Density ($kg\ m^{-3}$)	Specific Heat c ($J\ kg^{-1}\ K^{-1}$)	Thermal conductivity k ($J\ m^{-1}\ K^{-1}\ S^{-1}$)	Thermal diffusivity α ($m^2\ s^{-1}$)	Melting Point T_m ($^{\circ}C$)	Boiling Point T_b ($^{\circ}C$)
Aluminum	2.7×10^3	880	205	8.6×10^5	660	2400
Brass (60/40)	8.55×10^3	370	121	3.8	965	-
Copper	8.96×10^3	380	390	1.14	1083	2580
Nickel	8.9×10^3	444	91	2.3	1453	2820
Silver	10.5×10^3	232	418	1.7	981	2180
Steel, mild	7.85×10^3	450	50	1.4	1500	3000
Steel, austenitic	7.9×10^3	500	16	4.05	1500	3000
Titanium 6Al4V	4.4×10^3	610	5.8	2.2	1700	3300

Energy input into a weld

A source must provide energy, whether thermal (heat) or mechanical (pressure), for a welding process to take place. Different sources, regardless of their type, are suited for supplying both different amounts of energy and different intensities of energy[16]. Considering the relevant

and a simpler case of the thermal energy source, a large oxyacetylene torch flame can contain more thermal energy or heat, hence can supply more of that energy to a workpiece to heat it up than a smaller oxyacetylene torch flame. Both flames undergo the same basic chemical reaction and have the same maximum temperature. Yet, one source contains a different amount of energy than the other, but it is not more intense. This is known as the 'energy level' or the 'energy capacity', i.e. the available amount of energy in a heat source[16]. Nature of the energy source determines the units that energy level can be measured with e.g. calories for flame, Joules (J) as in internal energy, Watts (W) for an arc or electrical resistance, or a beam of electrons or photons (in laser systems) [16, 18].

For an electric arc under ideal conditions -without losing any energy in process-, the available heat at the source can be calculated by:

$$Q (W) = E I \quad \text{Eq. 8}$$

where E is the arc voltage and I is the arc current.

2.2.2. Diffusive Mass Transport

Mass transfer is defined by Aklahiri as 'transfer of a species from one location to another in a mixture of non-uniform composition'[19]. Although the species present in the solution move from one location to another, flow of a homogeneous solution do not represent any mass transfer since the concentration of the species do not change. For mass transfer, a concentration gradient of the present species in that system is essential[19].

Mass transport can be occurring due to different driving factors e.g. diffusion. This section will be covering the topic of mass transfer in context of welding processes. The diffusion phenomenon will be investigated and their relation to welding processes will be revealed in this section.

Diffusion

The generic term diffusion represents the movement of a substance from a high concentration region to a low concentration region. It is an omnipresent phenomenon and extremely important for various contexts in chemical, physical, and biological fields[20].

Depending on the external driving forces, e.g. temperature, pressure, and materials' own properties, e.g. crystal lattice structure, different types of diffusion mechanisms can be identified. Although in the most of the cases, the diffusion process is adequately explained by Fick's law[20], it is crucial to distinguish the particular type and mechanism of the diffusion in question[17]. Considering different types of diffusion mechanisms, the terms of self-diffusion, intrinsic diffusion, inter-diffusion, interstitial diffusion, vacancy diffusion, up-hill diffusion can

be seen in literature[17].

Self-diffusion

Self-diffusion can be considered as one the most fundamental aspects inside the lattice of a solid. Due to the continuous motion or the vibration of the atoms, there would be occasional unoccupied sites called vacancies. Focusing the attention on a particular vacancy, that site will eventually become occupied and consequently the neighboring site will become vacant. With this, a particular atom can slowly move and progress through the lattice. Alternatively, this particular vacancy may move randomly though the lattice. In both cases, the net effect is a random motion of atoms in the lattice[17]. This phenomenon is known as the self-diffusion.

The rate of an atom wandering through the lattice of a pure metal is called self-diffusion rate and can be measured by radioactive tracer atoms. Self-diffusion can also be observed in homogeneous systems, however, it should be considered that self-diffusion apply to homogeneous alloys with only no chemical composition gradients[17] Einstein had proposed:

$$D^* = B^* k_b T \quad \text{Eq. 9}$$

where D^* is the self-diffusion coefficient, B^* is the self-diffusion 'mobility', i.e. a measure of the ability of an atom to migrate within the structure without any external driving force[17] and Boltzmann constant¹[21, 22] and T is the temperature. From this equation it can be assumed that the D^* values depend on the physical properties of the questioned material and the temperature.

Diffusion under the influence of concentration gradient

Most of the materials processing situations include diffusion due to a concentration gradient, i.e. driving force is provided. Except some special circumstances, the diffusion coefficient used in the presence of this driving force is different than the self-diffusion coefficient[17]. Since this work includes stainless steels (or multi-component iron-based alloy systems) under welding conditions, it would be appropriate to investigate the diffusion on under the influence of a composition gradient

It is mainly presumed that if the solute atoms are considerably smaller in size than the solvent atoms, the interstitial mechanism dominates the diffusion process and the solvent atoms do not get displaced. Furthermore, this mechanism does not operate if the solute atoms' radius approach the solvent, hence this results in the solvent atoms being displaced by the diffusing solute atoms[17]. These mechanisms are called *intrinsic diffusion* and *interdiffusion* respectively. In both cases, the driving force for the diffusion to occur is mainly called *vacancy*

¹ The Boltzmann constant is the proportionality factor that corresponds to the average relative kinetic energy of the particles in a gas with the temperature of the gas

mechanism[17]. The theoretical background of the diffusion due to the concentration gradient is explained by Fick's law of diffusion

Fick's law of diffusion

Fick's first law of diffusion states that the species of A diffuses in the direction of decreasing concentration of A[17], i.e. a component diffuses downwards the concentration gradient[20]. Similarly heat flows by conduction in the direction of decreasing temperature[23]. Although the law can be written in various forms, in materials field it is usually written in terms of molar concentrations:

$$j_{Ax} = -D_A \left(\frac{\partial C_A}{\partial x} \right) \quad \text{Eq. 10}$$

where j_{Ax} is the molar flux of A in the x-direction, D_A is the diffusion coefficient or diffusivity, and C_A is the molar concentration of the species A.

The diffusion coefficient D_A appearing in Eq.10 is defined in the presence of a concentration gradient of A, hence it is a particular type, namely *intrinsic diffusion coefficient*.

Fick's second law predicts the resulting composition due to diffusion with respect to time[17]:

$$\frac{\partial C_A}{\partial t} = \frac{\partial}{\partial x} \left(D \cdot \frac{\partial C_B}{\partial x} \right) \quad \text{Eq. 11}$$

where C_A and C_B are the concentration of the substance A and B respectively, ∂x is the partial differential equation operator in x-direction.

Fick's second law can be rewritten in a plain form:

$$\frac{\partial C}{\partial t} = D \cdot \frac{\partial^2 C}{\partial x^2} \quad \text{Eq. 12}$$

indicating the accumulation is proportional to the diffusion coefficient D and second derivative of the concentration or the gradient of the species' mass fraction[23].

To conclude, *intrinsic diffusion* is the diffusivity of an element in the solution. Inter- or mutual diffusivity in solid is defined as the diffusivity of substance A in B and denoted as D_{AB} . For solid solutions, the inter- or mutual diffusivity is as follows[19, 24]:

$$D_{AB} = x_B D_A + x_A D_B \quad \text{Eq. 13}$$

where D_A and D_B are the intrinsic diffusivities of the substances A and B, and x_A and x_B are the

mole fractions of the substances A and B respectively.

Uphill diffusion

Fick's law indicates that the driving force for diffusion is the concentration gradient and it only takes place from higher concentration towards lower. Lawrence Stamper Darken had found out in 1948 that the concentration of one component may temporarily exceed its equilibrium value. This indicates in contrast to Fick's law, molecules diffuse in the direction of increasing rather than decreasing concentration[25]. This phenomenon is known as *uphill diffusion* and is a consequence of the thermodynamic non-idealities of multicomponent systems[20]. However, Fick's law is used mainly for practical analysis and the concept of uphill diffusion is used to explain the anomaly situations[19].

Temperature dependence of diffusion

In chemistry, the 'Arrhenius equation' adequately explains the temperature dependence of the rate of the questioned reaction. Since temperature is a form of energy and increasing the energy generally means the rate of reaction should increase as well, temperature has a vast influence on diffusion. Namely, the diffusion coefficient increases exponentially with the increasing temperature. If the equation is written for diffusion[17]:

$$D = D_0 e^{-Q/RT} \quad \text{Eq. 14}$$

where Q is the activation energy, T is the temperature, R is the universal gas constant, D_0 is the frequency factor, which is a constant.

Fluid flow and weld pool convection

Any fluid independent being in gaseous or liquid form are all subject to convection[16]. Convection for liquids can be defined as the bulk movement caused within a liquid under the driving force of density differences in that liquid[29]. Commonly, hot liquids expand, become less dense and consequently rise, where cool liquids contract, become denser and therefore sink[29].

Considering that there are many different active influencing factors during a welding process, convection of the liquid metal in the weld pool is a naturally expected incident. Convection in the weld pool has a significant effect on the pool's shape, mixing (homogeneity or heterogeneity as a result of macro-segregation), distribution of porosity as a result of gas dissolution and entrapment. Furthermore, it affects the evaporation of certain elements from the weld pool surface[29].

There are four types of active driving forces affecting on the weld pool and causing convection[27, 29], namely, (a) buoyancy or gravity force, (b) electromotive force EMF or

Lorentz force, (c) surface tension gradient force or *Marangoni* force and (d) the sheer stress induced by the plasma jet[27]. The predominant forces may depend on the employed heat source or the material being processed. For steels, to determine the shape and penetration of the solidified weld joint, it is suggested that the surface tension-driven Marangoni force dominates the weld pool material flow[30].

Buoyancy or gravity force

Increasing temperature causes the density of the liquid metal to decrease. Since the heat source is located above the center of the weld pool, liquid metal is warmer at the center (point a in Figure 2-5) and then at the boundary (point b in Figure 2-5). Gravity causes the heavier liquid at the boundary of the pool, consequently the liquid metal is transported along the boundary and rises up at the pool axis [27].

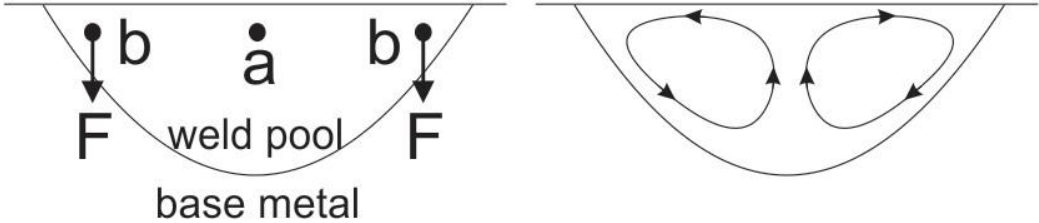


Figure 2-5: Buoyancy or gravity force and consequent material flow and convection[27]

EMF or Lorentz force

Figure 2-6 represents the example of TIG welding with DC electrode negative setting -used in this study and common practice for steel welds- The electric current in the workpiece converges near the center of the weld pool and towards the tungsten electrode.

This converging current field, hence its magnetic field induces a downward and inward Lorentz force[27], i.e. the effect is a result of the divergent current path in the weld pool and the magnetic field it generates[16]. As a result, the liquid metal is pushed down along the weld pool axis and rises along the pool boundary.

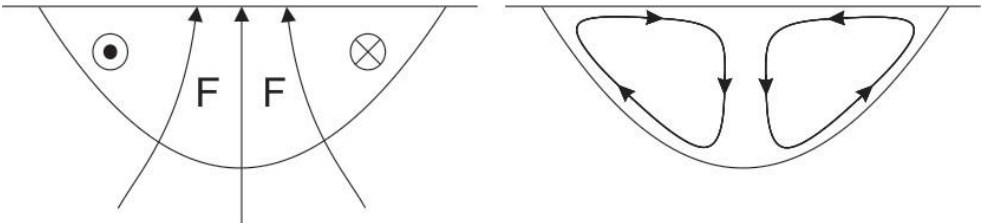


Figure 2-6: Electromotive EMF or Lorentz, force and consequent material flow and convection[27]

Surface tension gradient or Marangoni force

Whenever a temperature gradient exists in a liquid, a surface tension arises naturally[16].

Increasing temperature causes the surface tension of the liquid metal to decrease. Figure 2-7 demonstrates this situation, namely the warmer liquid metal with the lower surface tension at point a is pulled outwards by the cooler liquid metal with the higher surface tension at point b. As a consequence, the liquid metal flows from the center of the pool surface to the edge and return below the pool surface[27]. Surface tension induced convection can also be called Marangoni convection and as mentioned above, it is the dominating effect considering welding of steel workpieces.

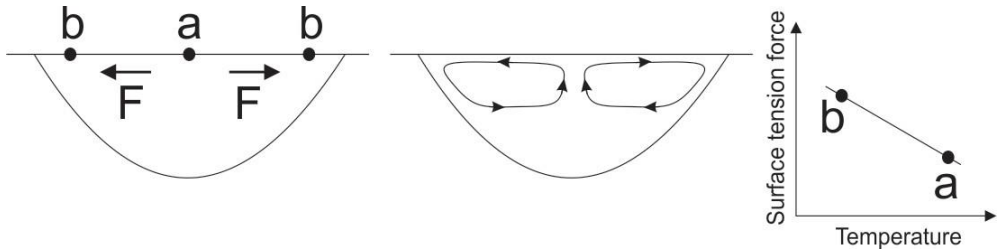


Figure 2-7: Surface tension gradient driven convection or Marangoni convection, and consequent material flow in the weld pool[27]

Weld pool convection has been a much concentrated topic and investigations have shown even small variations of welding process parameters can have a vast effect on the resulting weld pool shapes and microstructures[31]. Furthermore, the investigations using marker particles in the weld pool have shown that due to the Marangoni convection, extremely strong convection patterns and speeds between 10 to 100 cm/s have been observed[16, 32].

Shear stress induced by plasma jet

The arc plasma moves outwards at high speeds along the pool surface and induces an outward shear stress at the weld pool surface. This shear stress causes the liquid metal to be transported from the center of the pool towards the pool rim and return below the pool surface[27]. Figure 2-8 represents the shear stress induced by plasma jet. This type of convection has also been called “impinging” or “friction” force[16], since the sheer stress is induced by the momentum transfer through the friction between the impinging particles and metal atoms in the molten weld pool and the active particles can have varying momentum depending on the heat source, e.g. arc plasma, laser, electron beam.

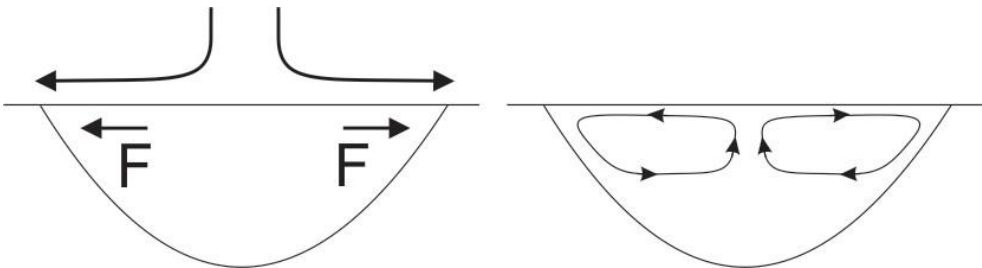


Figure 2-8: Shear stress induced by plasma jet and consequent material flow in the weld pool [27]

Alloy evaporation during welding

Welding processes employ high temperatures to melt the workpiece. Due to these high temperatures, the enthalpy of vaporization of an alloying element might be exceeded and consequently, metal evaporation may occur. This can be either due to exceeding the boiling temperature of the weld metal or causing the vapor pressure of a component in the weld metal to exceed its partial pressure in the surrounding atmosphere. Furthermore, significant amount of metal loss can occur from the surface of the weld pool, which is also aggregated by the weld pool convection[16].

Evaporation loss from the weld pool surface appears according to:

$$r_a = 44.33 P_a \left(\frac{M_a}{T} \right)^{1/2} \quad \text{Eq. 15}$$

where r_a is the rate of evaporation of element a, M_a is the atomic weight of element a, T is the temperature in K, and P_a is the equilibrium partial pressure of the element a in the gas phase above the weld. Considering various materials, the evaporation rate of some of the alloying elements can be higher than others, e.g. Mn for stainless steels, Mg for aluminum alloys, Zn for brasses [16].

Evaporation of the alloying elements is a potential problem for welding applications. The general negative effects of the alloying element loss due to the evaporation can be listed as [33], mechanical properties may be negatively influenced, arc stability can be impaired due to the compositional changes in the arc plasma, evaporation can place an upper limit on the temperature produced on the surface of the weld pool due to the evaporative cooling.

2.3. Welding metallurgy of stainless steels

The final microstructure and the properties of the welds are governed by a number of complex metallurgical reactions [34], in which the melting and solidification playing the significant roles to achieve a sound joint for fusion welding processes. Mainly, in conjunction with the solidification process, segregation and diffusion processes can result in local chemical compositional differences influencing the weldability and service performance of the end-product [35]. Many of these metallurgical processes e.g. phase transformations, precipitation reactions, recrystallization and grain growth, appear in the solid state. Furthermore, the extend of these reactions may vastly influence the final microstructure, hence altering the properties of the weldment weld metal and the heat-affected zone (HAZ) compared to the base material used [35], even causing the weldment to lack structural integrity, e.g. having various defects and cracking issues.

This section covers the general concepts of welding metallurgy in context of solidification process, weld chemical compositions and the consequent weld defect 'hot cracking' issue.

2.3.1. Stainless steel formation and weldability

It is essential to cover the basic metallurgy of iron, its allotropes and steel formation before understanding the stainless steel weldability and weld solidification. As it has been mentioned in previous sections, steel is essentially defined as an alloy of iron and carbon. Furthermore, at least three of iron allotropes can occur naturally in nature [3]. The phase diagram of pure iron is shown in Figure 2-9 displaying the allotropes of iron with respect to the temperature and pressure.

Body-centered cubic (bcc, α , ferrite), face-centered cubic (fcc, γ , austenite) and hexagonal close-packed (hcp, ϵ , hexaferrum) are the main allotropes of pure iron. δ iron can be defined as the high-temperature designation of α iron [3]. Furthermore, for a broad spectrum of steels, only α -ferrite and γ -austenite phases are relevant. Ferrite is stable from all temperatures up to 910°C -also known as the A_3 point-. It transforms into austenite at this temperature and would revert to ferrite at 1390°C. This phase is labelled as δ -ferrite, whereby it shows no difference in crystal structure to the α -ferrite. This δ -ferrite is stable up to 1536°C, where the melting occurs[3].

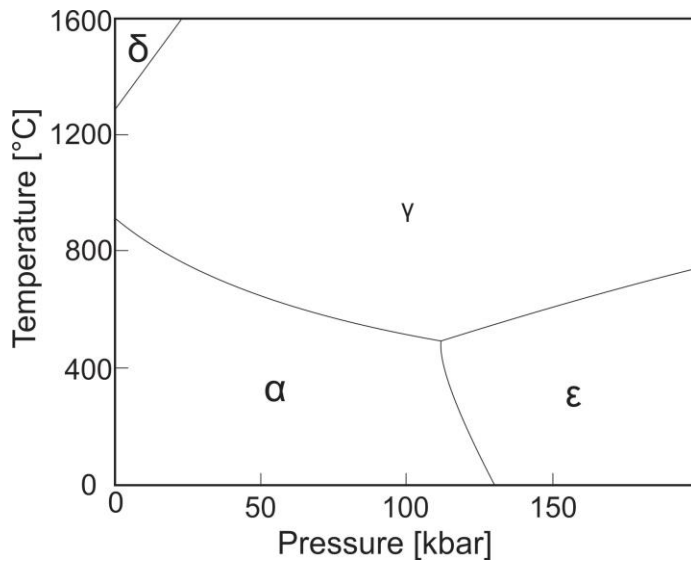


Figure 2-9: The allotropes of pure iron Triple point temperature and pressure values are 490°C and 110 kbars respectively [3]

To understand the steel formation, one of the indispensable tools is shown in Figure 2-10, also known as the 'iron-carbon phase diagram'. However, during the literature review, a common terminology mistake or misconception has been observed: The plotted diagram in Figure 2-10 is actually referred as 'iron-carbide (or cementite: a hard and brittle transition compound of C and Fe with the formula Fe_3C) phase diagram', which is plotted for the transient metastable phase of iron-carbide or cementite[36]. On the contrary, the 'iron-carbon phase diagram' terminology should only be used whenever the context is on stable phases, e.g. graphite. Theoretically, given the enough time, the thermodynamically metastable phase of iron-carbide or cementite will decay into iron and carbon, which would be the stable case. However, this decay would take infinite time at room temperature[37]. Therefore, the iron-cementite phases are mainly considered as stable at room temperature and such misconception in the terminology occurs.

To conclude, this literature review will use the terminology of 'iron-cementite' phase diagram, which is shown in Figure 2-10[38]. Please note that this diagram is only for illustrative purposes, and is not thermodynamically accurate

Considering the context of steel formation, the first important detail to notice in iron-cementite phase diagram is the range of steel defined at the bottom horizontal axis, namely the amount of carbon alloyed with iron. Steel is considered to have approx. 0 to 2 wt% of carbon, where cast iron contains approx. 2 to 6.67 wt% [37, 39].

To summarize the relevant critical boundary information from the iron-cementite diagram: The upper limit of the ferrite / cementite $\alpha+Fe_3C$ phase field (horizontal line at 723°C) is called A_1 boundary A_2 is the temperature iron loses its magnetism also called Curie point or

temperature[40]. A_3 is the boundary between the austenite (γ) and the austenite / ferrite ($\gamma+\alpha$) field.

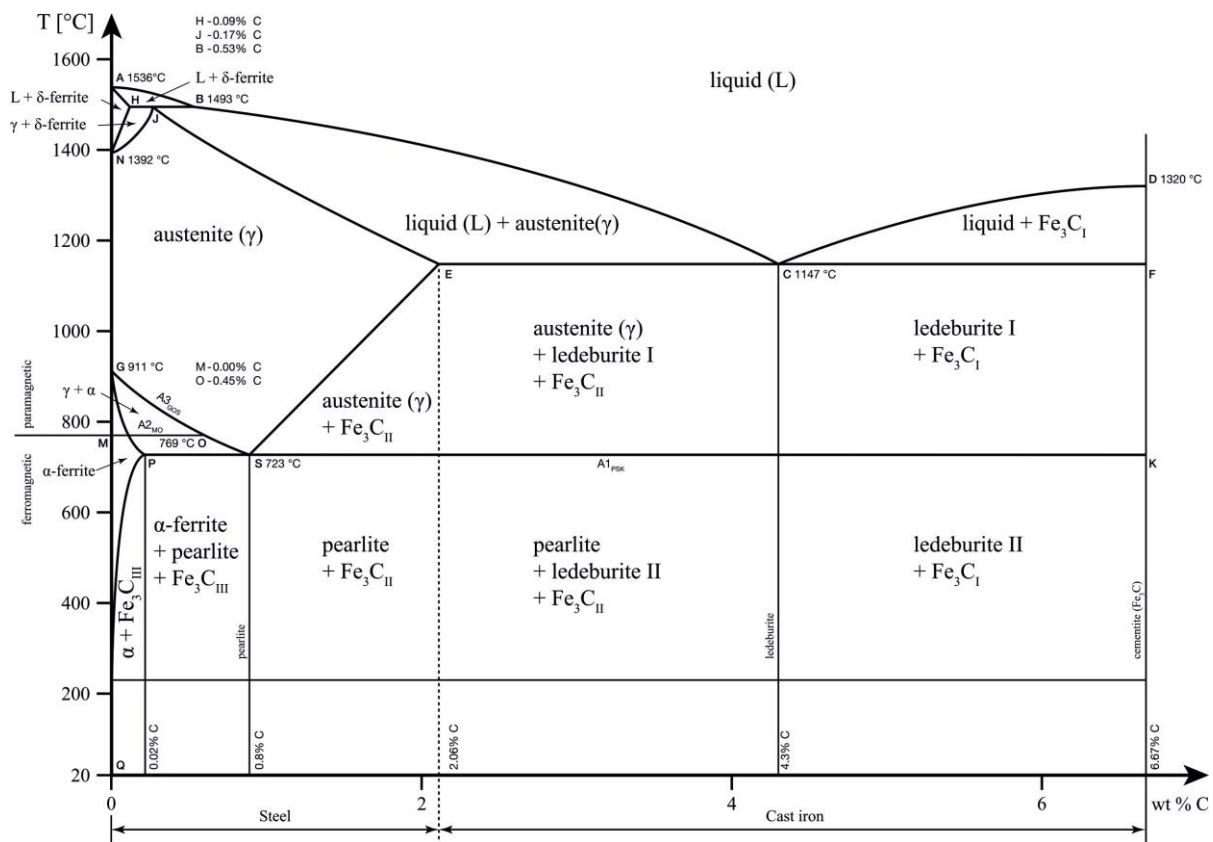


Figure 2-10: Iron-cementite metastable phase diagram modified and reprinted under Creative Commons License[38]

The stainless steels typically contain very low amounts of carbon. However, the other alloying elements have significant effects on the solidification behavior and the final microstructure of the material, especially for those undergoing a weld solidification process. The effect of the individual alloying elements on the stainless steel weld solidification microstructure has been reviewed in the following subsection of 2.3.5 Weld chemical composition

Before reviewing the further technical details of weld solidification of stainless steels, the term 'weldability' should be discussed. Yurioka [41] defines the steel weldability as how preferably a steel can be welded without weld defects and how satisfactorily a joint welded with a relevant steel can perform during service.

Considering different types of stainless steels, austenitic stainless steels can be welded relatively easily, however various weld metal and heat-affected zone (HAZ) defects might occur. Fully austenitic structures are more likely to have weld metal solidification cracking[42], i.e. are more hot cracking susceptible due to the formation of low melting point segregates in the weld metal, whereby a small amount of ferrite can stabilize these structures and has the capacity to dissolve harmful impurities[43].

Ferritic stainless steel welds exhibit exceptional stress corrosion cracking resistance and costs are lower compared to austenitic counterparts. However, they might have poor HAZ toughness due to the thermal cycles of welding process. Grain coarsening can lead to degradation of material properties, hence cracking in highly restrained joints[44].

Duplex stainless steels exhibit properties of both ferritic and austenitic stainless steels due to their balanced microstructures. They are easily weldable, however the heat input must be strictly monitored to obtain the correct weld metal structure[45]. Typical duplex stainless steel welding complication is the unbalanced resulting microstructure ratio of ferrite / austenite [46, 47].

Martensitic stainless steel welds can be realized by providing some precautions e.g. pre or post weld heat treatment, lower hydrogen containing processes such as (TIG) or metal-inert gas (MIG). They exhibit very hard martensitic structure in the weldment with low ductility and can be prone to hydrogen-assisted cracking (HAC) issue[48].

2.3.2. Tungsten-Inert Gas (TIG) Welding

Tungsten-inert gas (TIG) welding (or gas-tungsten arc welding - GTAW) is one of the most commonly used welding technologies for stainless steel, titanium alloys and non-ferrous metals in practice[26]. It uses a free burning electric arc between a non-consumable tungsten electrode and a workpiece (Figure 2-11). The strong heat-flux from the welding arc plasma forms the weld pool by partially melting the workpiece. An appropriate shielding gas is purged through a gas nozzle towards the weld pool surface to protect it from the atmosphere. Shielding gas consists of usually inert gases e.g. Argon, Helium, or a mixture of various other gases. The process can be undertaken either with or without using a filler rod. If the filler is not used, joints must be thin and have a close-fitting and square-butt configuration[16]. In case a filler rod is used, e.g. for joining thicker materials, it can be fed into the arc either manually or automatically[27].

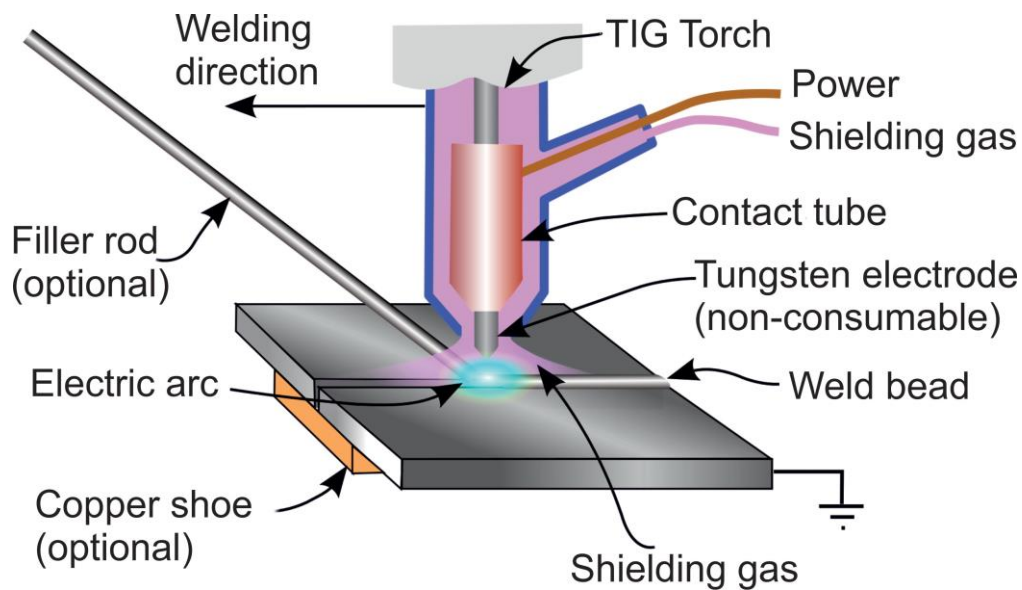


Figure 2-11: Schematic representation of tungsten-inert gas welding Modified and reprinted under Creative Commons License 2[28]

TIG welding process offers only limited heat inputs, therefore it has a shallow penetration and is mostly suitable for joining thin sections[26]. Although offering only lower heat inputs, TIG welding can be considered as one of the cleanest welding processes. Due to this property, it can be used to weld reactive metals e.g. titanium, zirconium, aluminum, magnesium. On the other hand, the deposition rate of TIG welding is relatively low. Excessive welding currents could negatively affect the tungsten electrode and cause melting. Hence, this could result in brittle tungsten inclusions in the weld metal. Deposition rate can be improved by preheating the filler materials[27].

Thus, the heat input in welding is defined as the quantity of energy introduced into the workpiece per unit length of weld[16]:

$$H = \frac{P}{v} \quad \text{Eq. 16}$$

where H is the net energy input (J/mm) and P is the total input power of the heat source (W). v is the travel or welding speed (mm/s).

In the case of an electric arc, Eq 17 can be rewritten as:

$$H = \frac{E I}{v} \quad \text{Eq. 17}$$

where E and I are calculated in volts and amperes respectively. v is considered in mm per second resulting in watt-second (or Joules) per mm.

2.3.3. Weld solidification

Each weldment consists of distinct microstructural zones. The shape and extent of these zones depend on the undertaken welding process and corresponding welding parameters. Since this work includes only fusion welding process in practice, namely the TIG welding, the specific zones are reviewed in respect to a fusion welded sample.

The fusion zone (FZ) is associated with the molten metal and solidification, where the heat-affected zone (HAZ) is the region of the material affected from the thermal cycles of the melting process. The unaffected base material lies beyond the HAZ, where the high temperatures cause no microstructural changes. These zones can be further divided into more specific zones, which is displayed in Figure 2-12 with the corresponding approx. temperature values in case of steels.

The FZ has been defined as such because it is the region where the complete melting and subsequent solidification occur, forming the weld -or joint-. The resulting microstructure in the FZ is a function of the chemical composition and the undergoing solidification conditions. Since all the metals are crystalline structures in nature and many of them retain cubic crystal lattices, the general solidification phenomenon applies to all the metals[35].

Any resulting microstructure and the properties of the HAZ are dependent of the thermal conditions undertaken during welding or by the post-weld heat treatment PWHT, e.g. considering aluminum alloys, the precipitation hardening or work hardening properties of the material can be radically eliminated in the HAZ by the thermal cycle from the welding; where for steels, any resulting phase transformation can result in a HAZ that has entirely different microstructure and properties from either the FZ or the base material[35].

In general, three different types of fusion zones are defined[35]. *Autogenous welds* are those where the fusion zone is formed by only melting and re-solidification of the base material without using a filler material. This type of welding process is often called “bead-on-plate welding” in practice and has been vastly used in this work. *Homogenous welds* are those where a filler material is used that matches the chemical composition of the base material. *Heterogenous welds* are conducted by filler materials those compositions are different from the base material.

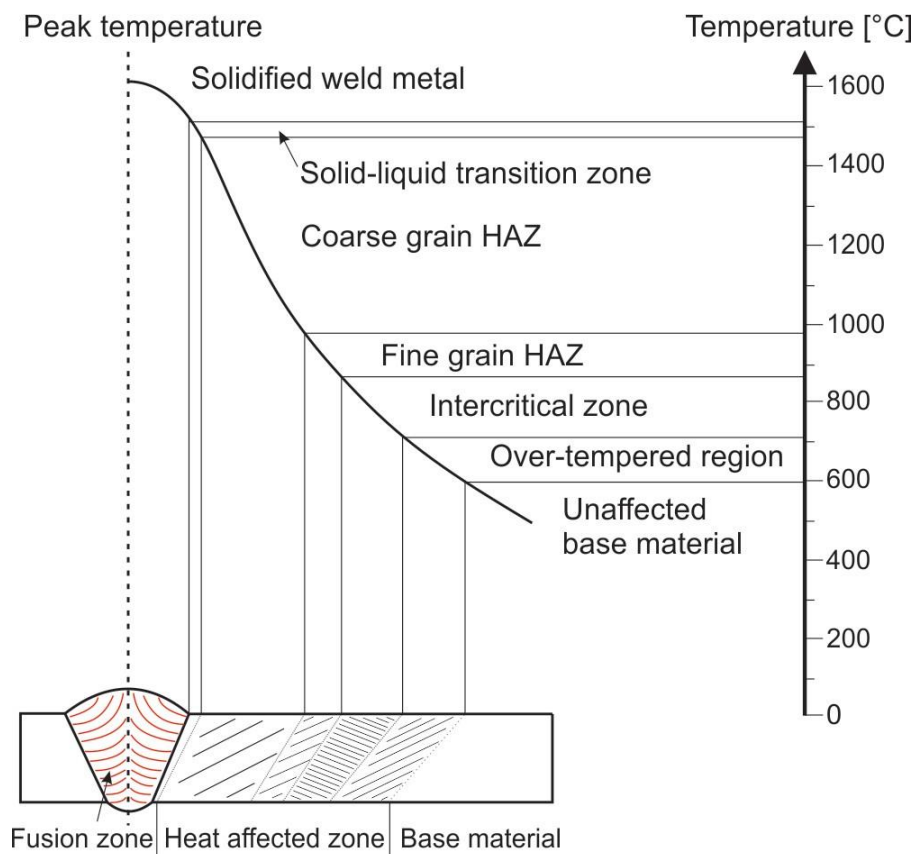


Figure 2-12: Weld microstructures and approximate temperatures in single fusion weld [49]. Data according to [50]

Solidification requires several conditions. First, solid species must nucleate within the liquid phase. As soon as the initial solid is formed, the liquid-solid transformation progresses. At this point, the heat of fusion generated by the transformation is removed, normally by conduction through the solid and away from the solidification front[35].

During an alloy solidification, the solute must be redistributed between the solid and liquid phases, while the chemical composition of the both phases change at the solidification front continuously with the decreasing temperature[35]. This redistribution will result in local changes in the chemical composition in the solidified structure, if the solid cannot reach its equilibrium composition, which is common in most of the metal casting and welding processes, i.e. when a uniform composition of liquid solidifies, the resultant solid is rarely in a uniform composition, hence the solute atoms undergo a redistribution during the solidification[27].

Metals typically undergo a decrease in their volume as they solidify[29]. Hence, this solidification shrinkage causes internal stresses to occur that may lead to solidification cracking, thus residual stresses remaining on the workpiece[35].

Here, the most important solidification parameter “partition coefficient” will be discussed in

the next sub-section.

2.3.4. Partition Coefficient

The partition coefficient k -also called segregation coefficient or distribution coefficient- is the ratio of the solid and liquid composition fraction in contact with each other at a given temperature in the solidification range:

$$k = C_S/C_L \quad \text{Eq. 18}$$

where the C_S and C_L are the composition of the solid and the liquid respectively.

Since the temperatures at the solidification front constantly change, the k is not constant and varies as a function of the temperature [35]. Figure 2-13 schematically demonstrates both positive and negative partition coefficient on hypothetical binary phase diagrams.

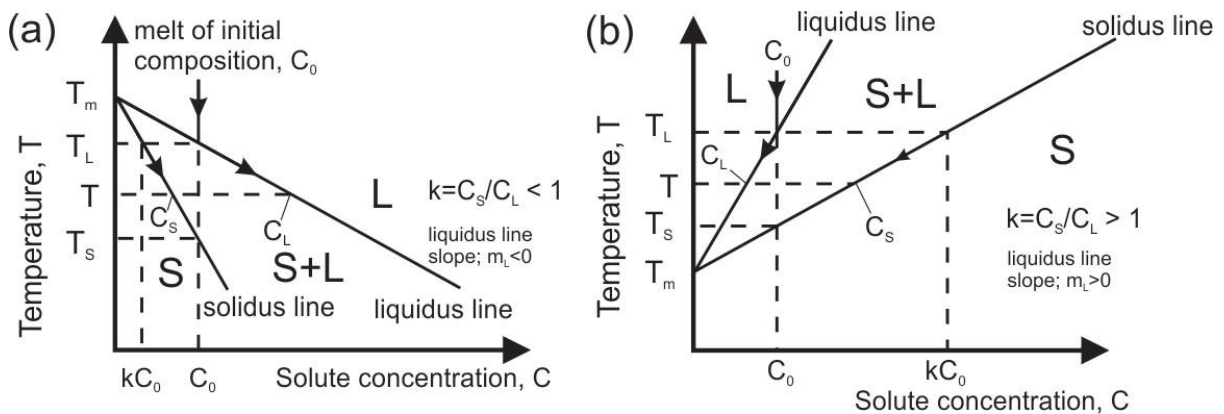


Figure 2-13: Portion of the partition coefficient displayed on a binary phase diagram [27]

According to Eq. 19 and considering the phase diagram in Figure 2-13a or the assumption of $k < 1$, the first solid to form will have the composition of $k C_0$ and for $T = T_L$, $C_L = C_0$. In this case the solid cannot contain as much solute as the liquid can, thus the solid rejects the solute into the liquid during solidification [27]. As a result, the solute content in the liquid continues to rise during solidification. Moreover, the solid grows naturally from the liquid part and therefore its solute content rises too.

In this case of solidification, the C_S and C_L both increase as the temperature of the solid-liquid interface drops.

In the case of $k > 1$ in Figure 2-13b, the solid can contain more solute than the liquid can, i.e. the solid absorbs the solute from the liquid during solidification and consequently the solute content in the liquid drops. Adversely to the initial situation in Figure 2-13a, solute content in the liquid continues to drop. In this case of solidification, the C_S and C_L both decrease as the temperature of the solid-liquid interface drops.

In a closed system the mass must be conserved, and thus:

$$f_s + f_L = 1 \quad \text{Eq. 19}$$

Where f_s and f_L mass fraction of solid and liquid respectively.

Using Scheil-Equation & Analysis[51], boundary condition for C_L becomes $C_L = C_0$ at $f_s = 0$, and thus composition of the liquid during solidification or composition of the solid during solidification can be calculated via the following equations respectively:

$$C_L = C_0(f_L)^{k-1} \quad \text{Eq. 20}$$

and,

$$C_S = kC_0(1 - f_s)^{k-1} \quad \text{Eq. 21}$$

To summarize, if solid segregation is expected during solidification, the average value of k is usually considered, i.e. if the value of $k < 1$, solute will partition to the liquid whereby the $k > 1$, solute will be depleted in the liquid. If the value approaches 1, solute redistribution during solidification is decreased.

Addition to the partition coefficient, the following parameters are considered highly useful in context of solidification:

Liquid temperature gradient G_L dictates the nature of the temperature field in advance of the solid-liquid interface[35]:

$$G_L = dT_L/dx \quad \text{Eq. 22}$$

This gradient is negative if there is some undercooling of the liquid has occurred before the solidification process, which is the case in most of the casting applications. However, during weld solidification, this gradient is mostly positive since the liquid metal is superheated by the electric arc[35].

Solidification growth rate (R) is governed by how fast the solid-liquid interface is moving during the solidification process [35]. Thermodynamically, the solid-liquid interface will form in the area of lower temperature and move towards the direction of higher temperature[23]. Combined with the G_L value, the local cooling rate at the solid liquid interface $G_L \cdot R$ can be determined, which has an influence on the solidification structure, e.g. dendrite² arm spacing:

$$R = dx/dt \quad G_L \cdot R = dT/dt \quad \text{Eq. 23}$$

² Growing tree-like characteristic structure of crystals as molten metal solidifies

Solidification nucleation and modes

Solidification process begins with nucleation; hence it is essential that solid nucleates in the liquid phase. This can occur both homogeneously where nucleation requires a critical size of solid to form within the liquid or heterogeneously whilst a nucleating particle or solid substrate already present in the liquid. In many cases heterogeneous nucleation accompanies homogeneous nucleation or entirely dominates it, which applies for welding processes [35].

Heterogeneous nucleation starts either from an existing solid substrate or from extrinsic particles, e.g. oxides, nitrides, sulphides etc. [35]. These heterogeneous sites are stable at or above the melting temperature of that alloy system, therefore, little to no constitutional supercooling -or undercooling- is required for nucleation to start [52, 53].

Heterogeneous nucleation starting off a solid substrate is called 'epitaxial nucleation'³ Heterogeneous nucleation during weld solidification is dominated by the epitaxial nucleation, which requires essentially no driving force or any undercooling[54]. Therefore, the solidification begins instantaneously after cooling below the liquidus temperature for that alloy system. Growth is most favorable if the growth directions are parallel to the heat flow or in normal direction to the solid-liquid interface [35].

The solid-liquid interface can form mainly four different microstructures during solidification. Pure metals usually solidify with a planar interface unless thermal undercooling is imposed[27]. However, alloys undergo the solidification process with various interface types depending on the solidification conditions and the material system involved, i.e. they can typically form the cellular, the columnar dendritic and the equiaxed dendritic solidification microstructures[52, 53]. Figure 2-14 shows the schematic illustration of various forms of weld solidification microstructures and corresponding constitutional supercooling conditions.

³ From the Greek word epitaxis, meaning 'to grow from'.

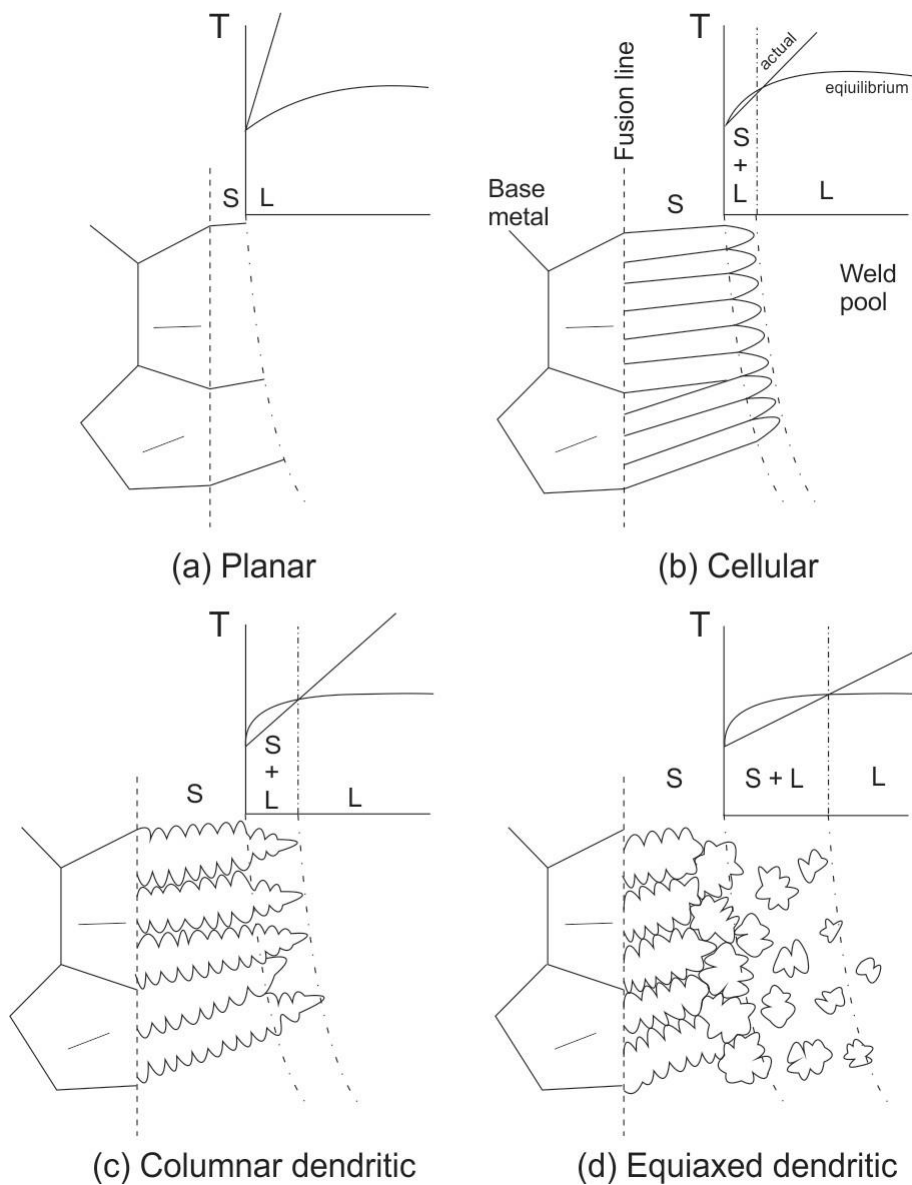


Figure 2-14: Schematic illustration of different forms of weld microstructure and corresponding supercooling conditions [52]

As it is seen in Figure 2-14, the characteristic of the microstructure is restrained by the degree of the constitutional supercooling, the actual temperature gradient and the expanse of the interface. The region where the solid columnar or equiaxed dendrites and liquid coexist is called *the mushy zone* [27], hence increasing amount of supercooling results in a larger range of the mushy zone. The temperature range of constitutional supercooling grows with faster solidification rate i.e., with a gentler actual temperature gradient [52, 53]

Constitutional supercooling

The theory of constitutional supercooling phenomenon -also called undercooling- was proposed in 1953 by Chalmer and co-workers [55, 56]. According to this theory, the following major points can be identified [55]:

- Impurities accumulate in the liquid adjacent to a growing solid-liquid interface during non-equilibrium freezing.
- This accumulation results in a layer of liquid below its equilibrium liquidus temperature, i.e. in unstable state.
- A spontaneous solidification is initiated in this unstable zone by the large crystal present, resulting in a formation of small projections on an initial plane.
- Impurities diffuse from the liquid at the tip of this projection to the surrounding liquid. This mechanism allows the solidification process at the tip of this projection to proceed at a higher temperature than at the plane interface. Therefore, the solidification occurs in the region around the base of this projection at a lower temperature than at the plane interface (2.14c, d).
- This temperature rises at the tip of the projection favors the condition of lateral heat flow from the projection towards the surrounding solid and liquid, hence promoting the growth of the projection.
- These factors above should result in a formation of a structure or an array of these projections on an initially plane solid-liquid interface during non-equilibrium solidification.

The temperature difference across the boundary layer can be defined as: $\Delta T = T_L - T_S$. (Figure 2-13). According to the supercooling theory, to achieve a planar stable solid-liquid interface, the actual temperature gradient G_L at the interface can be written as [27]:

$$\frac{G_L}{R} \geq \frac{\Delta T}{D_L} \quad \text{Eq. 24}$$

where D_L is the diffusion coefficient. Whenever this condition is not ensured, the planar solid-liquid interface transforms from planar to cellular and finally dendritic.

Considering the effect of the impurities on the supercooling phenomenon for an alloy system, the alloying elements or the solute atoms can be considered as impurities. The effect of solidification parameters such as temperature gradient (G_L), solidification growth rate (R) and increasing composition of the solute elements on the resulting microstructure is shown in Figure 2-15.

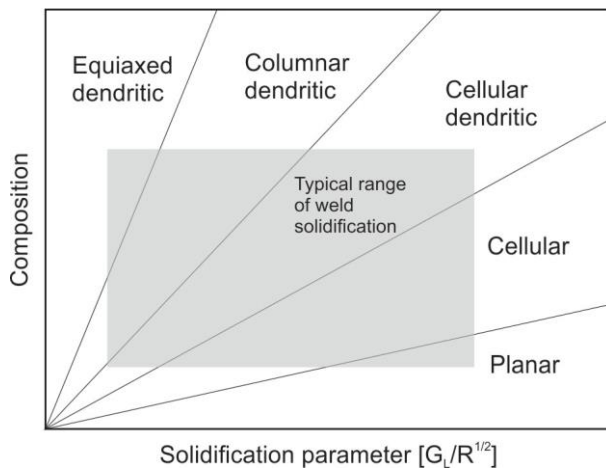


Figure 2-15: Effect of composition and solidification parameters on the resulting solidification mode [35] According to Borland [57]

All in all about the supercooling phenomenon, the following facts can be pointed out: A boundary layer of a liquid phase with solute rich concentration is thermodynamically stable only if it is above its liquidus temperature. If the temperature drops below the liquidus temperature, solid and liquid must coexist, i.e., the planar solid-liquid interface must break down to a dendritic or cellular structure so the solid cells can coexist with the intercellular or interdendritic liquid [27, 58]

2.3.5. Weld chemical composition

Stainless steels contain many different elements (other than C and Cr) in their composition, and thus the solidification behavior is highly dependent to the chemical composition[35]. These additions result in improving their various mechanical and corrosion properties as well as affecting the resulting microstructure[12]. This section reviews various elements' effects in context of stainless steel weld solidification. Constitution diagrams are also included in this section.

Chromium (Cr)

The main reason for chromium addition is to provide corrosion protection, which is especially effective in oxidizing environments. Chromium promotes an oxide layer formation on the steel surface that enables the main corrosion resistance property. The presence of chromium stabilizes the oxide since it has a much higher affinity for oxygen than the iron. In highly aggressive environments higher levels of chromium could be required in order to stabilize the oxide layer [12].

Chromium is also considered as a strong carbide forming element i.e. is able to form the carbides such as Cr_{23}C_6 , Cr_7C_3 and Cr_3C_2 [59]. Although the latter two not very common, they still could occur in stainless steels. Many cases, however, include only the mixed form of carbide $(\text{FeCr})_{23}\text{C}_6$, which is generally designated as M_{23}C_6 , where M is predominantly Cr but also may contain some fraction of Fe and Mo present in the alloy system [12].

Many of the intermetallic compounds that tend to embrittle the steel are also mainly caused by the chromium, i.e. the most common of them is being the sigma phase (σ) forming below 815°C [12]. Furthermore, the sigma phase is also considered as the most important of the secondary phases of stainless steels, with respect to its properties, e.g. mechanical properties, corrosion resistance, weldability, and thus is able to increase the mechanical strength but decrease elongation[60].

Chromium is a ferrite promoter, and thus for ferritic alloys, it is the primary alloying element to stabilize the ferritic microstructure[12].

Nickel (Ni)

Nickel principally promotes the austenite phase so the austenitic or austenitic-ferritic alloys can be produced. By addition of the nickel, the austenite phase field expands so the austenite phase is stable to the room temperature and below [59]. Nickel is not a strong carbide former and brittle intermetallic compounds are mainly not caused by this element [12].

Manganese (Mn)

Manganese is practically added to every stainless steel, where austenitic stainless steels contain around 1 to 2 wt% in their composition. Essentially, it was added to prevent *hot shortness*⁴ issue[12]. Manganese combines with sulphur much more easier than iron, i.e. sufficient amount of manganese forms the stable manganese sulphide (MnS), stabilizing the sulphur in the alloy system and preventing the hot shortness issue[12].

Manganese is an austenite former, similar to nickel, it expands the area of stable austenite

⁴ A form of solidification cracking that is associated with the formation of low melting point iron- sulfide eutectic species

phase to the lower temperatures, making it possible to contain at ambient temperatures Manganese could form mixed carbides of the type $(\text{FeMn})_3\text{C}$. However, for stainless steels these carbides are of no great importance[59].

Silicon (Si)

Similarly with manganese, silicon is also present in all stainless steels due to its deoxidation properties during melting, mostly between in the range 0.3 to 0.6 wt%, and thus greatly improving the corrosion resistance [12, 59].

For austenitic stainless steels, adding silicon up to 1 wt% have no effect on the phase balance, however, higher levels appear to promote ferrite phase. Furthermore, silicon is known to form several forms of embrittling compounds e.g. iron silicides FeSi , Fe_2Si , Fe_3Si , Fe_5Si_3 and the Cr_3Si intermetallic compound[12].

During solidification, silicon is known to form low melting eutectic constituents, particularly with nickel[12, 61]. Therefore, is usually held below 1 wt% to avoid solidification related problems.

Molybdenum (Mo)

Molybdenum is, along with chromium and nickel, another important alloying element for stainless steels. Hence, it promotes ferrite formation and can form intermetallic phases[59]. It is known to improve corrosion resistance and also elevated temperature strength for austenitic stainless steels [12].

Sulphur (S) and Phosphorus (P)

Sulphur and phosphorus are usually considered as impurity elements in the context of weld solidification. The main reason behind is that these elements can form low melting eutectic compounds during solidification and thus, even with addition of very small amounts can cause severe solidification cracking issues[35]. Sulphur and phosphorus mainly form the low melting liquid films that precipitate between the grain boundaries of newly formed crystals. This causes adhesion of grains and cause separations during shrinkage in the process of solidification, and thus the solidification cracks appear[59]. Sulphur and phosphorus are almost insoluble in iron, chromium and nickel -three main constituents of stainless steel- and both elements are strongly rejected into liquid during weld solidification of austenitic stainless steels[62, 63]. Therefore, they are considered as the most harmful elements for weld solidification[64]. Solidification cracking issues may likely to arise when the chemical composition of S + P is greater than 0.015 wt%[65].

From the weld solidification and respective microstructure point of view, the austenite and ferrite promoting -or stabilizing- elements are listed in Table 3 below [35]:

Table 3: Austenite and ferrite promoting -or stabilizing- elements

Ferrite promoting elements	Austenite promoting elements
Chromium	Nickel
Molybdenum	Manganese
Silicon	Carbon
Niobium	Nitrogen
Titanium	Copper
Aluminum	Cobalt
Vanadium	
Tungsten	

Constitution diagrams

Constitution diagrams have been the prediction tools for welders, engineers and various other end-users in the past 100 years, beginning in 1920 with the introduction of a nickel-chromium diagram for the prediction of occurring phases in the wrought and slowly cooled steels by Strauss and Maurer [35]. This design has been a model for many following diagrams to follow, with elemental variables on the x and y axes and showing the effect of those elements and their interactions on the resulting microstructure. An extensive chronological review on the topic has been done by Olson[66].

Schaeffler Diagram has been considered one of the most important of the constitution diagrams, and thus providing information about the expected microstructure due to the weld metal chemical compositions. Anton Schaeffler had developed the preceding research before him and applied it to the welding field. This has been considered as a major development for the prediction of weld metal microstructure. It includes the ferrite promoting elements with their corresponding coefficients as a Chromium-equivalent (Cr_{eq}), and austenite promoting elements as Nickel-equivalent (Ni_{eq}) with the same logic. These coefficients were established using empirical investigations. With the current technological developments, especially the application of artificial neural networks (ANN) in material sciences [67, 68], they are still being updated and the existing constitution diagrams are either being extended or becoming more precise in practice. The Schaeffler Diagram from 1949 can be seen in Figure 2-16.

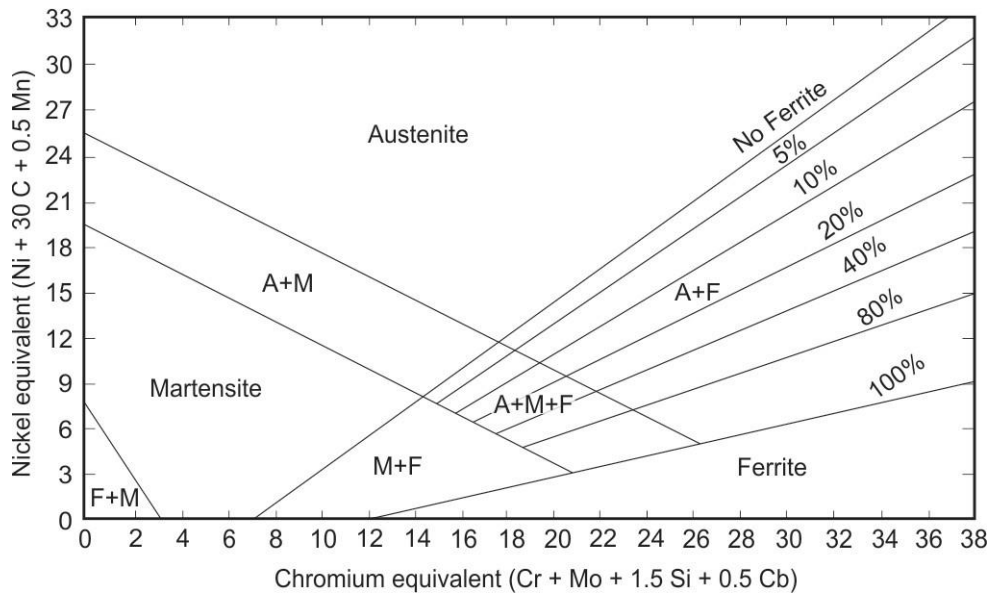


Figure 2-16: Schaeffler Diagram from 1949, which is still in use[69]. Please note that the element Niobium Nb was formerly called as Columbium Cb

Even this version of Schaeffler Diagram from 1949 is an updated version of the original one in terms of the equivalent coefficients, it also contains an important issue; although being one of the strongest austenite promoting elements, nitrogen is excluded from the nickel equivalent calculation. This was related to the difficulty of measuring the nitrogen content in steel back then [12]. The Cr_{eq} and Ni_{eq} formulas can be seen in Eq. 25 and 26 respectively:

$$Cr_{eq} = Cr + Mo + 1.5Si + 0.5Nb \quad \text{Eq. 25}$$

$$Ni_{eq} = Ni + 30C + 0.5Mn \quad \text{Eq. 26}$$

The corresponding elements' elemental concentration value (in wt%) should be used in these formulas in order to calculate the equivalent values.

With the time and technological developments further constitutional diagrams have been proposed and used. *DeLong Diagram* is the one that had been introduced in 1956 by DeLong and co-workers [70]. They had focused their work on austenitic stainless steels and thus only for the 300 series. One of the major improvements were the addition of nitrogen into the Ni_{eq} value and the improved precision of the isoferrite lines compared to the Schaeffler Diagram [35].

DeLong made further improvements to the diagram in 1973, and thus it included improvements to predict the delta ferrite present in the resulting microstructure. The major

upgrade was the term 'ferrite number (FN) ' [71, 72]. FN values are based on magnetic measurements, which can be conducted by the measurement device 'ferritoscope'.

During mid-1980s, the Subcommittee on Welding Stainless Steel of the Welding Research Council supported the activity and revision of the Schaeffler and DeLong diagrams to improve the accuracy of ferrite content prediction for stainless steel weld metal [35].

WRC-1988 and WRC-1992 diagrams [73] were developed within four years and the WRC-1992 is considered as the newest and the most accurate of these prediction tools to estimate the resulting FN for austenitic and duplex stainless steels[74]. The major constitution diagrams in chronological order and their corresponding Cr_{eq} and Ni_{eq} values are shown in Table 4.

Table 4: Constitutional diagrams in chronological order with the respective Cr_{eq} and Ni_{eq} formulas

Diagram Year	Equivalent Values	References
Schaeffler (1949)	$Cr_{eq} = Cr + Mo + 1.5 Si + 0.5 Nb$ $Ni_{eq} = Ni + 30 C + 0.5 Mn$	[69]
DeLong (1956)	$Cr_{eq} = Cr + Mo + 1.5 Si + 0.5 Nb$ $Ni_{eq} = Ni + 30 C + 30 N + 0.5 Mn$	[70]
Schoefer (1965)	$Cr_{eq} = Cr + 1.5 Si + Mo + Nb - 4.99$ $Ni_{eq} = Ni + 30 C + 0.5 Mn + 26 N - 0.02 + 2.77$	[75]
Hull (1973)	$Cr_{eq} = Cr + 1.21 Mo + 0.4 Si + 2.27 V + 0.72 W + 2.2 Ti + 0.14 Nb + 0.21 Ta + 2.4 Al$ $Ni_{eq} = Ni + 0.11 Mn - 0.006 Mn^2 + 0.41 Co + 0.44 Cu + 1.4 N + 24.5 C$	[76]
Carpenter (1985)	(uses only Ni_{eq}) $Ni_{eq} = Ni + 2 Mn + 30 C$	[77]
WRC-1988	$Cr_{eq} = Cr + Mo + 0.7 Nb$ $Ni_{eq} = Ni + 35C + 20 N$	[73]
WRC-1992	$Cr_{eq} = Cr + Mo + 0.7 Nb$ $Ni_{eq} = Ni + 35C + 20 N + 0.25 Cu$	[73, 78-80]

2.3.6. Hot cracking

Weld 'hot cracking' is generally referred to the cracking phenomena due to the liquid presence in the microstructure during its fabrication. It is usually correlated with the liquid films along the grain boundaries in the fusion zone (FZ) and the partially melted zone (PMZ) in the HAZ. These liquid films can endure the lower temperatures than their equilibrium solidus

temperatures of the bulk alloy, and thus extending the solidification range of that alloy [35]. In practice, most of the cases consist of alloys that may undergo temperatures during solidification well below the equilibrium solidus temperature range due to the effect of the solute atoms and impurity segregation.

According to Lippold [35], the term 'hot cracking' is used to describe a number of elevated temperature cracking phenomena, thus it is mainly used to identify three distinctive types of cracks, namely 'weld solidification cracking (SC)' occurring in the FZ and towards the end of solidification process, 'HAZ liquation cracking (LC)' occurring in the PMZ and 'weld metal liquation cracking' specific to reheated weld metal and occurring in multi-pass welds or repair welding.

American Welding Society (AWS) defines the term as 'cracking that occur between grains during the solidification process'. However, there are other types of cracks that may occur at elevated temperatures and during solidification process, e.g. 'ductility-dip cracks (DDC)' [81]. Furthermore, the definition of the term 'hot cracking' is rather vague and may be interpreted in various ways. This review includes only the relevant specific phenomenon '(weld) solidification cracking' in the following subsection.

In general, the hot cracking phenomenon may occur in many forms in both FZ and HAZ in many different forms e.g. root cracking, DDCs etc. An overview of the possible occurring hot cracks are shown in Figure 2-17.

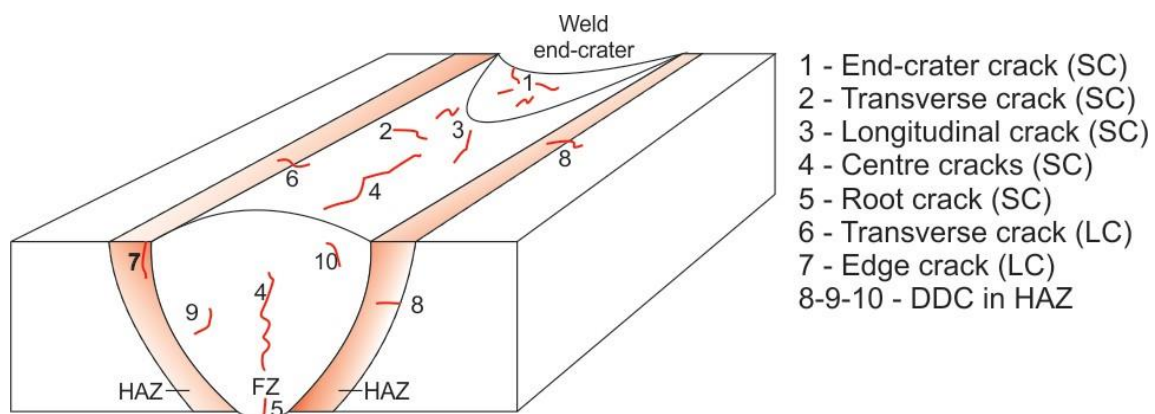


Figure 2-17: Classification of hot crack types in the FZ and HAZ [82, 83]

Solidification Cracking

Recent developments in technology, especially with increasing demand in product stability and quality in automation and manufacturing processes and thus with the 'Industry 4.0' framework, made the component safety concept especially important in the recent years. Similarly, increasing expectations occur with the advancements in material science, and thus

on new materials and alloys that are rather assessed as non-critical from the metallurgical point of view in terms of solidification cracking. However, it has been documented in the literature, that 'non-critical' designated alloys may have solidification cracks as well[84]. Especially during the welding and subsequent solidification process, the local chemical composition may vary due to the extended solidification range, solute atom and impurity segregation, which are the critical factors and drivers for solidification cracking.

Weld solidification cracking is usually associated with the low temperature melting liquid films along the grain boundaries that occur during the solidification process. Solidification cracking occurs due to the rupture of these liquid films, mostly in the region behind the weld pool where solid and liquid coexist, i.e. the mushy zone. The initiation of such cracks is a combination of many complex interactions between the metallurgical and mechanical interrelationships, and thus thermal-metallurgical interactions control the solidification microstructure where the thermal-mechanical interactions control the local and global stress and strains [34, 35]. Figure 2-18 represents the influencing factors between the main input parameters e.g. welding parameters or alloy composition, and the output effects of these parameters e.g. size of the mushy zone, thermal strain distribution.

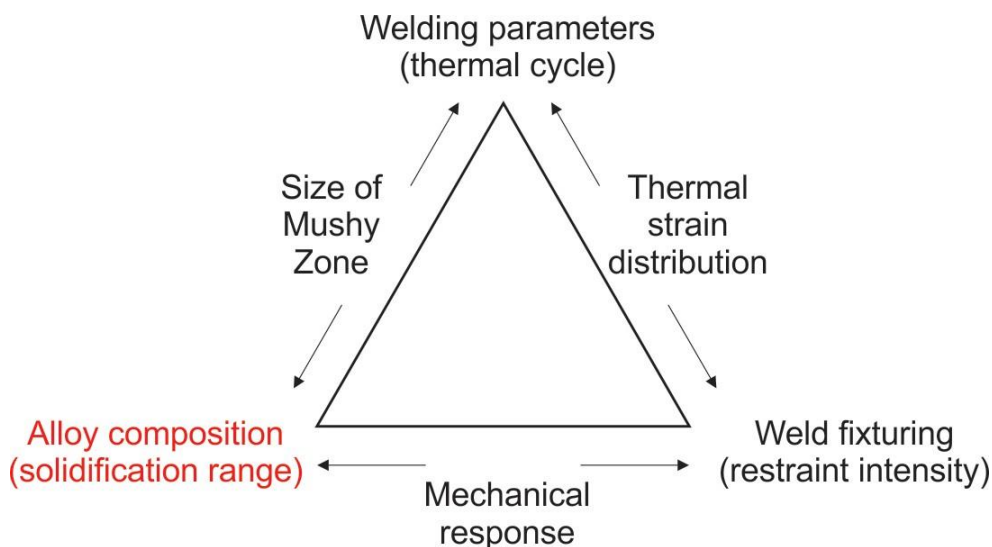


Figure 2-18: Interrelationships between the process parameters affecting the weld solidification cracking[34]

Various elements' effects on solidification process and thus on the resulting microstructure have been discussed in the section 2.3.5 Weld chemical composition. Here, the resulting weld microstructures, their properties and the theoretical background in context of austenitic stainless steel weld solidification cracking is covered.

Four main solidification modes may occur for the austenitic stainless steel weld metals. These four possibilities are shown on a pseudo-binary phase diagram of Fe-Cr-Ni system in Figure 2-19, i.e. A and AF modes associated with the primary austenite solidification where austenite

is the first phase to form during solidification. FA and F modes consist of delta ferrite as the primary phase to solidify. Austenitic stainless steel welds typically have γ -phase austenite (fcc) matrix with varying amounts of δ -ferrite (bcc). The amount of δ -ferrite in austenitic stainless steel weld must be strictly controlled, hence it is an essential component in the microstructure. More than 10 vol% δ -ferrite tends to reduce the ductility, toughness and corrosion resistance, increasing the ferrite phase properties and their influence, where less than 5 vol% δ -ferrite may result in solidification cracking [27].

Cr is a ferrite promoting element, where Ni is a strong austenite promoter. Since the austenitic stainless steels contain both of these elements -and also further alloying elements such as Mn, Mo, Si etc.-, it is possible to assess and predict the solidification cracking susceptibility of that alloy by the expected weld solidification microstructure using the chemical composition information of the base and input material.

In both Figure 2-19 and Figure 2-20, it can be seen that the weld solidification microstructure shifts towards primary ferrite if the Cr_{eq} increases, i.e. if the amount of ferrite promoting elements' wt% values increase. On the other hand, if the Ni_{eq} increases the solidification mode shifts towards primary austenite, i.e. similarly, the austenite promoting elements' chemical compositions increase

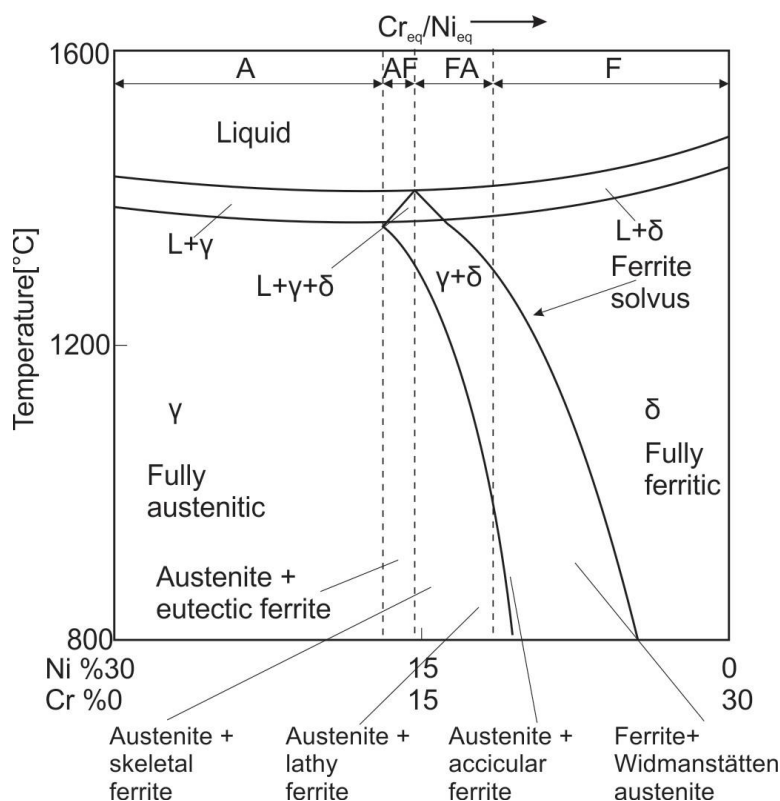


Figure 2-19: Solidification type on the pseudo-binary phase diagram for austenitic stainless steels [12, 64] A-fully austenitic, AF-primary austenite with ferrite as second phase, FA-primary ferrite with austenite as second phase, F-fully ferrite

The shift towards primary austenite solidification mode generally means increase in weld solidification cracking susceptibility. Although the austenitic stainless steels exhibit very good weldability properties, weld solidification cracking could be a considerable problem for these materials, since cracking susceptibility is primarily a function of the chemical composition [12]. As a general rule, the chemical compositions that result in primary austenite mode A and AF are the most susceptible to the solidification cracking (Figure 2-20). Moreover, the increasing impurity levels, particularly S and P elements, increase the cracking susceptibility dramatically. If the weld metal solidifies in primary austenite, welding conditions may also influence the cracking susceptibility negatively, i.e. high heat inputs and excessive welding speeds may promote teardrop shape weld pools resulting in solidification cracks [12].

Weld metals that solidify in FA mode have the most superior cracking susceptibility. In fact, the F mode is more susceptible than FA mode but still superior to A and AF modes. The primary reason for the FA mode's superiority in crack susceptibility is due to the presence of both phases ferrite and austenite mixture along the solidification grain boundaries (SGB⁵) at the end of the solidification, resisting wetting by liquid films and present a tortuous⁶ boundary along which cracks normally propagate and grow [12].

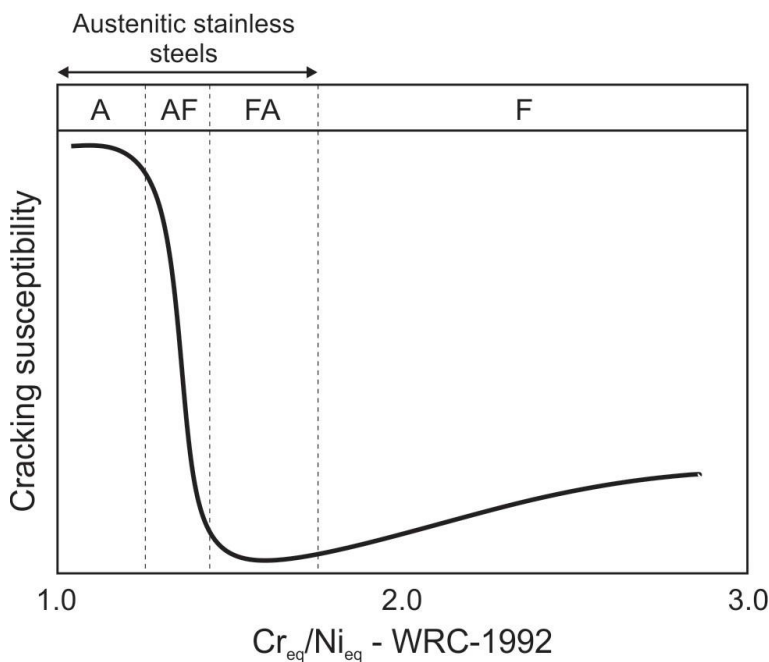


Figure 2-20: Weld solidification cracking susceptibility as a function of resulting weld microstructure [12].

The solidification behavior and possible resulting microstructure formation of the four modes are schematically shown in Figure 2-21. For the primary austenite solidification modes -A and

⁵ SGBs occur due to the intersection of packets, groups of sub-grains, and thus, they all have different growth orientation, resulting in boundaries with high angular misorientation -*high angle grain boundaries*-

⁶ not straight and smooth

AF- the partition ratio between liquid and primary austenite is generally between 0.7 to 0.8 for Cr and ca. 0.95 for Ni[85, 86]. Consequently, the growing primary solid is depleted in Cr, and therefore the interdendritic liquid is enriched in Cr. This enrichment of Cr in the interdendritic liquid is the reason of the shift from A to AF mode in the terminal stage of the solidification -or the shift from only fcc to fcc+bcc eutectic phase transformation-. The retained ferrite -or the eutectic bcc phase- may present itself with a divorced morphology in the interdendritic region. However the amount of the retained ferrite may decrease to some extent after solidification by diffusional bcc to fcc transformation[85, 86].

For the primary ferrite solidification modes -FA and F- the partition ratio between the liquid and primary ferrite is close to unity (between 0.95 to 1.05) for Cr, and between 0.7 to 0.8 for Ni[85, 86]. Consequently, the interdendritic liquid is enriched in Ni where the growing solid is enriched in Cr. Both primary and eutectic ferrite undergo the bcc-to-fcc transformation for the FA solidification mode as the temperature decreases. As a result the final microstructure contain the primary ferrite as the core of dendrites with vermicular, skeletal, or lacy morphology being surrounded by austenite[87, 88]. If there is any remained eutectic ferrite, it is expected to be located at dendrite boundaries[85]. The F mode undergoes a stable bcc reaction throughout the solidification process. Hence, it may transform in the terminal stage of solidification to Widmanstätten or lath-like plates (Figure 2-19 and Figure 2-21) [64, 85, 86].

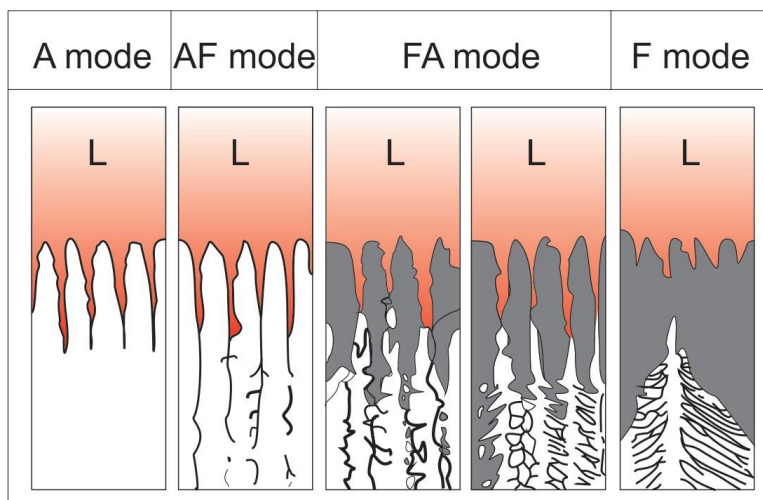


Figure 2-21: Schematics of the possible solidification modes of Fe base Cr-Ni alloys and austenitic stainless steels in welding processes [85]

According to Shankar et al. [64], the chemical composition affects the stainless steels' cracking tendency in two major ways:

First, as discussed above, the primary solidification mode is a function of the chemical composition, and thus the FA and F modes are beneficial for reducing cracking.

Hence, the nature of the solid-liquid interface is determined by the solidification mode. Second

effect of chemical composition is observed through segregation, and thus determining the wetting characteristics and the constitutional supercooling properties in the interdendritic solid-liquid interface area.

The hot cracking data from a number of studies including their own was represented by Kujanpaa et al. on a diagram representing the data for P + S vs Cr_{eq}/Ni_{eq} using the formulae from Schaeffler[64]. The relation between the impurity elements P + S, their chemical compositions and cracking susceptibility can be seen in Figure 2-22. It had been observed that the highly susceptible chemical compositions can be statistically divided by a curve with a lower limit of 0.01-0.015 wt % P + S. From the elemental equivalent side, the curve is limited by a value of 1.5 (Cr_{eq}/Ni_{eq}) up to where the primary austenitic solidification mode occur.

After discussing the main driving factors for solidification cracking, a very important question still remains unanswered i.e. 'what is theory behind hot cracking?'

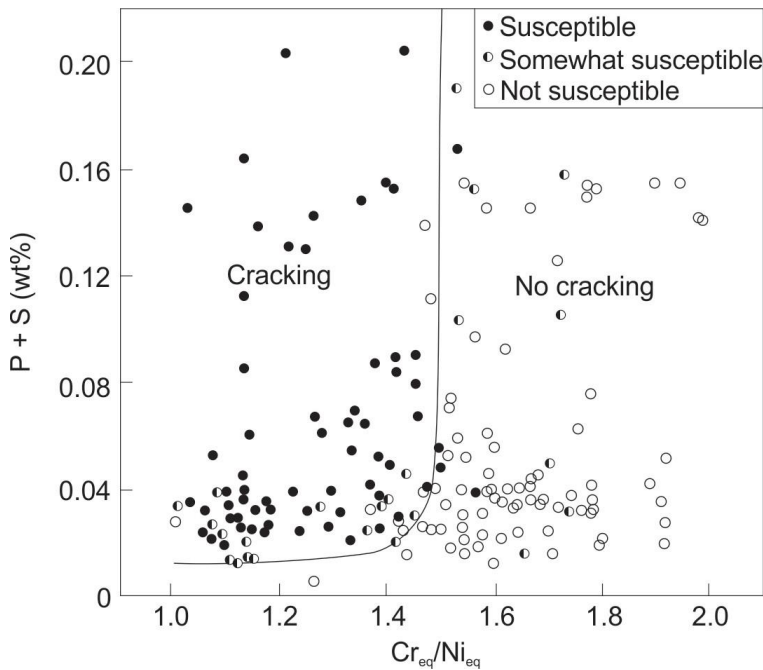


Figure 2-22: Solidification cracking behavior in austenitic stainless steel welds as a function of Cr_{eq}/Ni_{eq} ratio and P+S composition[89]

The solidification cracking mainly occurs due to the segregation of solutes to form low-melting eutectic phases, which during solidification cause shrinkage stresses, and thus causing the solidification cracking.

However, there has been several theories trying to explain this phenomenon in detail. Some of which included only the design and mechanical stress aspects whereas the others considered only the aspects of the alloy chemical composition and properties. The following theories have been proposed in chronological order: Pellini (1952) , Medovar (1954) , Borland (1960) and Holt (1992).

The initial theories only considered that the cracking phenomenon was associated only with segregation, hence it was thought that the cracking susceptibility increases only if the liquid-solid range of the alloy was increased. However, this initial theory was not satisfactory and not only there were exceptions to be seen in literature, but also the freezing range of an alloy was observed to be only one of many different factors influencing the hot cracking issue[64].

The 'Generalized Theory' was proposed by Borland and is considered as the first theory to satisfactorily explain the solidification phenomenon. Borland indicates that the solidification process can be divided into four stages that are arranged according to the distribution of the liquid and solid phases[64]. The process is explained in Figure 2-23 for a hypothetical binary alloy.

If the individual stages are described according to Borland[57], the stage 1 involves dispersed solid phase and continuous liquid phase, and thus both phases can accommodate their relative movement. In the stage 2, both liquid and solid are continuous, however the solid dendrites are interlocked and only the liquid has the capability of movement. Therefore, the liquid may still 'heal' the occurring cracks in this stage. Stage 3 involves an advanced stage of the solid crystal development and the liquid is not capable of free passage between the dendrites, and thus is only present in a very small quantity. During stage 3, if a stress exceeds the tolerance of that material, crack may propagate and cannot be filled by the remaining liquid phase. This stage -in which much of the cracking occur- is also called critical solidification range (CSR). Stage 4 is the end of solidification and no cracking related to the liquid phase is possible.

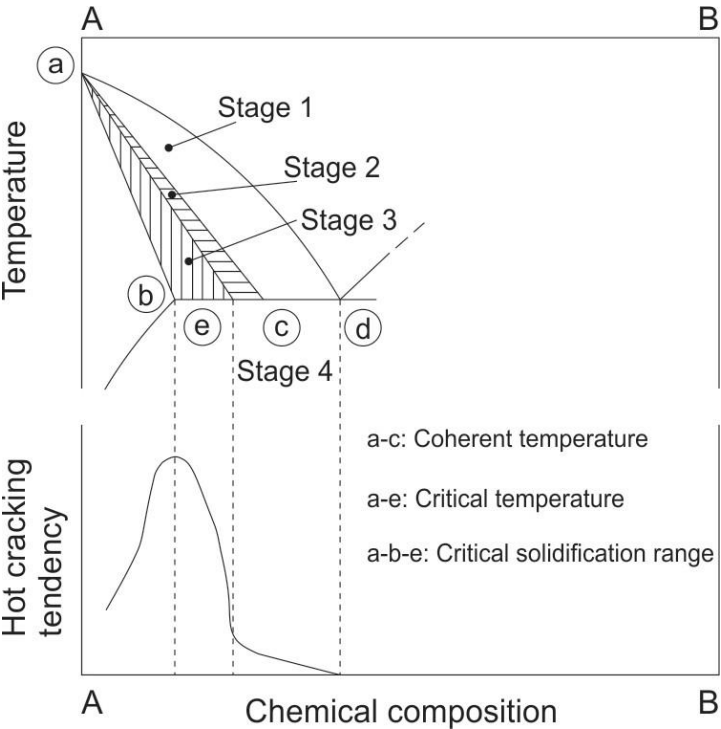


Figure 2-23: Effect of the constitutional properties on cracking susceptibility for binary alloys Generalized Theory [57]

The theory revealed the importance of wetting⁷ phenomenon in relation to cracking issue, and thus explaining the destructive effects of sulphur in stainless steels[57, 90]. The theory was modified in a recent review [91] in 1990 by Matsuda, and indicated that the crack initiation and propagation must be considered individually, i.e. the stage 3 in Generalized Theory was divided into sub-stages.

2.4. In situ weld monitoring

Most of the weld defects are inspected and thus detected after the solidification process and the weld is complete. However, these defects can hypothetically be detected during the process.

Local alloying element composition of the weld may affect the overall quality and even cause defects. By in situ monitoring of the chemical compositions, local elemental composition fluctuations can be monitored online during the process and by defining the tolerance limits for individual elements, chemical compositions may be kept in the tolerance band via interfering with the process parameters.

In situ weld defect monitoring using various inspection methods, e. g. measuring optical emissions directly from the welding arc, using in situ radiographic methods, using inline visual inspection by image processing or 3D laser scanning have previously been a topic of interest in the literature and industry:

Mirapeix et. al. [92] introduced a real-time arc weld quality monitoring concept based on electron temperature calculations by measuring the welding plasma. They detected various elemental emission lines during TIG welding of AISI 304 stainless steel, and thus systematically used several Ar emissions lines from 459 to 506 nm and Fe emission lines located between 372 nm to 416 nm to establish the Boltzmann-plots and calculate the plasma electron temperature. First, they have measured a reference weld without any defects, calculated the approximate plasma temperature ca. 9000 K with a stable trend through the experiment and plotted this over weld position. On the contrary, the welds they produced containing defects either by reducing the gas flow rate from 12 L/min to 6 L/min or increasing the welding arc current during the process demonstrated discontinued pattern of the welds, even rips and coinciding signal peaks at these spots.

Their further research [93] included a modification and optimization of the original line selection and temperature calculation model. They also used different material systems such as Inconel 718 and Ti-6Al-4V alloys apart from the AISI 304 stainless steel, and thus demonstrated the relationship between the electron temperature of the welding plasma and weld defects. During the absence of an external excitation source e.g. Laser in case of LIBS; X-

⁷ Ability of a liquid to maintain in contact with a solid surface, resulting from intermolecular interactions when the two are in contact.

rays in case of EDX; Ar emissions were the predominant species in their spectral range under analysis. They conclude their research with the following remark: 'An application of this method might lie in the framework of LIBS, where it might be used for a quantitative estimation of the composition of samples' [93].

Huber et. al. [94] argues that the most time- and cost saving production approach would be to investigate the welds simultaneously during the production. Although several visual inspection methods that can detect cracks or grooves may be utilized, any metallurgical fault cannot be avoided after the weld is complete, and thus this often results due to a critical chemical composition. To investigate the feasibility of such a concept, they investigated the metal evaporation processes during laser beam welding of EN-AW 6060 aluminum alloy by spectroscopic measurements. They were able to calculate the plasma electron temperature for deep penetration laser welding for the mentioned aluminum alloy at approx. 5000 K with an error of 15%. They also have demonstrated strong correlation between the plasma electron temperatures and the spectral emissions of the evaporated species from the deep penetration laser welding. Furthermore, they concluded that the detection of Si lines was not possible using a solid state laser e.g. Nd:YAG due to the relatively lower power outputs.

Zhang et. al. [95] developed a method for the real-time monitoring of weld perturbations and defects during pulsed gas tungsten arc welding (GTAW) of aluminum alloys using the spectroscopy signal and statistical feature selection from the spectrum bands of interest (SOI). They have concluded the emission lines of Ar II and Ar I between 584.945 nm and 608.410 nm have the best correlation with the seam oxidation, where the emission lines of Mn I and Mg I between 387.16 nm to 409 nm are strongly influenced by the defect of the arc crater. They have also concluded that the increase of the welding current influences the monitored signal intensity by increasing it due to the instant expansion of the plasma arc. They were able to distinguish the individual sensitivities of the monitored characteristic statistical features for the selected SOIs e.g. root mean square, variance and kurtosis values and concluded the variance feature was the most stable of them for the weld quality monitoring application.

Taparli et. al. [96] have conducted proof-of-principle in situ LIBS measurements during arc welding process of stainless steels. They performed experiments to demonstrate the feasibility of using LIBS as an in situ measurement method of the main alloying elements at a pre-set location behind the welding torch. Their work revealed the pseudo signal intensity increase effect due to the welding arc plasma. Post-weld application of LIBS was utilized by elemental mapping, and thus Mn-accumulation was observed at the edge of the HAZ. Their further research [97] investigated in situ monitoring of the metal vaporization during stationary TIG welding of EN grade 1.4435 stainless steel. They presented vaporized Mn above the weld pool during welding and subsequent condensation on the weld surface with the termination of the welding arc. The amount of the vaporized Mn and the thickness of the condensed layer was found to be in positive correlation with the increasing welding arc current especially at the weld center. Same group used LIBS method for post-weld chemical

composition investigations and detected the same vaporization pattern on bead-on-plate welds, and thus due to the relative movement of the welding torch, the Mn condensation took place at the edge of the FZ/HAZ by being swept away from due to turbulence at the above region of the weld pool. The chemical composition difference for Mn at the HAZ was approx. 0.7 wt% above the average of base material values [98].

Gött et. al. [99] have observed the temperature distributions of the welding arc using spectral diagnostics of pulsed TIG welding of steel, and thus detected a remarkable temperature minima in the arc center due to the pulsed arc modus. They have also observed these colder regions being dominated by the metal vapor and calculated the arc temperature of ca 9000 K, however the lack of temporal evolution of the metal vapor content was also highlighted by the author.

Gott et. al. [100] were able to combine high-speed digital imaging and spatially-resolved spectroscopy at 5000 fps during submerged arc welding process by inserting a thin-gauge steel tunnel apparatus into the flux material. Based on their observations, they were able to describe the process in detail concerning arc nature and behavior, size of the cavern, droplet, and arc in different polarity modes and welding currents (600 and 1000 A) for submerged arc single-wire welding. They have also detected that the main component of the cavern atmosphere was iron vapor and dissociated flux components. They have found that for all investigated process varieties, the oxygen content rises in droplet stage and drops into the molten bath, respectively, into the weld joint. The final oxygen content seems to be determined by welding polarity in a wide range. Lowest oxygen contents were achieved with a maximum percentage of cathode burning time on the electrode (DCEN and AC). They only observed slight changes in the chemical composition of the main alloying elements in the solidified weld joint due to the mentioned oxygen drop into the weld joint, and thus monitored and concluded a sound and nominal submerged arc welding process. Another interesting remark is the intensely self-absorbed emission lines of Na, Ca and Mn elements, which indicates the presence of these in the metal vapor. However, the reason behind this self-absorption should also originate due to the domination of the iron vapor in the cavity.

Independent from the context of hot cracking issue of welds, Smith II et. al. focused on the topic of cold cracking and investigated the detectable hydrogen content and distributions in high-strength steel welds using similar principle with laser-induced breakdown spectroscopy[101]. Samples were welded by varying H-containing shielding gas i.e. with 0.5%, 1.0% and 3% vol. in pure argon carrier gas at 22 mL/min flow rate They investigated the samples using laser ablation and gas chromatography. They also used LIBS method to compare the H-profile of HAZ and the FZ using the H-emission line at 656.2 nm, and thus observed higher H content in the FZ with increasing H content in the shielding gas. Their research results from the gas chromatography indicate the lowermost value of 2.4 ppm in 0.5% H₂/Ar shielding gas, however, they did not report on any limits of detection for both methods. Further reading on industrial applications of LIBS can be find elsewhere [102, 103] and H-measurements using

laser-ablation-principle can be found in the literature [104-107].

A general comparison of selected analytical elemental analysis techniques is shown in Table 5. Principally, in context of in situ weld quality monitoring, the LIBS technique can be counted as the most feasible among other analytical techniques. The main reasons are the relatively lower application costs and technical possibilities i.e. it is not possible to use synchrotron radiation to monitor a simple mobile welding application or conduct an EDX analysis without vacuum.

LIBS provides real time multi-elemental information from stand-off distances, which makes it exceptionally applicable in a manufacturing environment.

Table 5: Analytical techniques in comparison for elemental analysis [108]

Parameter	SEM / EDX	EPMA (Electron probe micro analysis)	X-Ray Fluorescence / Synchrotron	Laser Ablation ICP- MS	LIBS
Operation principle	Electrons	Electrons	X-rays	Laser ablation – mass spectrometry	Laser ablation – deionization radiation
Information depth	ca. 5 µm	<1 µm	ca. 100 µm	ca. 80 µm (user controlled)	ca. 50-100 µm (user controlled)
Sensitivity	1 ppm (0.1%)	100 ppm (0.01%)	100 ppm (0.01%)	<1 ppm (0.1%)	10-50ppm
Accuracy	Qualitative	Semi-quantitative	Semi-quantitative	Quantitative	Quantitative
Analysis speed	Fast	Slow	Very slow	Slow	Fast
Sample consumption	Non-destructive	Non-destructive	Non-destructive	Almost non-destructive	Almost non-destructive
In situ welding applicable	No	No	Not feasible	No	Yes

2.4.1. Laser-induced breakdown spectroscopy (LIBS)

Scientists became aware in the early 1800s that elements emit specific colors of light. With the development of the atomic theory, it has been revealed those colors, wavelengths or frequencies were actually unique signatures for each atom and ion. Thus, a spectrum has been perceived as the fingerprint of the emitting atomic species [109].

Laser spectroscopic methods are powerful tools for fundamental investigations and able determine several species simultaneously with the minimum equipment requirement.

Therefore, for technical applications, they are of special interest Laser-induced breakdown spectroscopy (LIBS) belongs to one of these methods[110]. Namely, LIBS is a type of atomic emission spectroscopy method, using laser pulse as an excitation source, and based on the principle of element specific light detection. The method is applicable to solid, liquid and gaseous state of the matter.

Figure 2-24 represents a typical LIBS setup. LIBS uses either single or multiple laser pulses as an excitation source to create a plasma that can be analyzed by a spectrometer. The existence of this plasma is a transient event where the peak temperatures are between 10000-15000 K if a 1064 nm laser⁸ is used⁹ [108]. The pulsed laser energy interacts with the target surface and thus chemical bonds break and produce electronically excited species e.g. atoms or ions. As these excited species return to their ground state, they emit radiation at specific wavelengths peculiar to the element. This radiation is also known as 'spectral fingerprint' [111] and thus can be transferred into a spectrometer, where it is resolved and analyzed.

Currently, LIBS finds itself vast application areas in a variety of research fields [103, 112], e.g. continuous steel casting monitoring in the steel industry, scrap sorting tasks, explosives detection, mining and mineral resource exploration, geology and environmental sciences, archaeology, biomedical applications on organic tissues and space exploration The 'Curiosity' rover and the mobile LIBS equipment 'ChemCam' has been in service since 6th August 2012 and has been considered as the latest milestone for the LIBS technology. It has conducted many successful measurements on Mars and thus contributed to our knowledge about the planet in significant extent. The next important milestone for the technology is considered as the 'Perseverance' rover and landed on Mars in February 2021. The Perseverance rover is carrying an improved LIBS equipment, 'SuperCam' to conduct further LIBS measurements on the red planet and send further enlightening information back home [113].

⁸ Wavelength of the pulsed laser light

⁹ Shorter-wavelength lasers would generate lower plasma temperatures

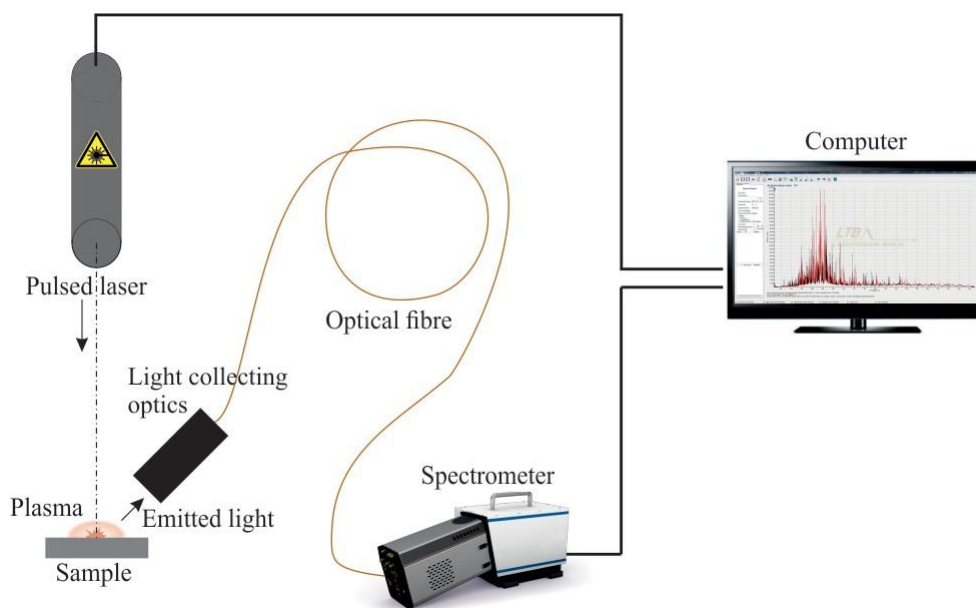


Figure 2-24: Schematic of a typical LIBS system

The advantages and disadvantages of the LIBS-technique are summarized in

Table 6. The frequently observed matrix effects¹⁰ [114], such as material separation or fragmentation, equipment dependency, non-reproducible LoDs in ppm range and mainly having no standardized application can be counted as the main disadvantages of the technique

Table 6: Advantages and disadvantages of the LIBS technique [115]

Pros	Cons
Simultaneous multi element detection possible	Ablation on the material, crater, particles
Solid, liquid, gas measurement possible	Plasma characteristics may depend on many factors, sample, environment.
Almost non-destructive	Calibration is highly dependent on the matrix of the reference materials
Very fast analysis	Limits of Detection are not entirely reproducible in ppm range
Measurement over distance possible by f/o and telescope lances	Method still not standardized
Space- and depth resolved analysis	Method still not standardized

¹⁰ Matrix dependency of an analytical signal

2.4.2. Radiation - matter interaction

Mechanism of the radiation-matter interaction, and thus the individual events during the brief lifetime of the laser-induced plasma are the necessary prerequisites for the general understanding of the LIBS method. Figure 2-25 shows a schematic representation of the various phases of the laser-induced plasma [116].

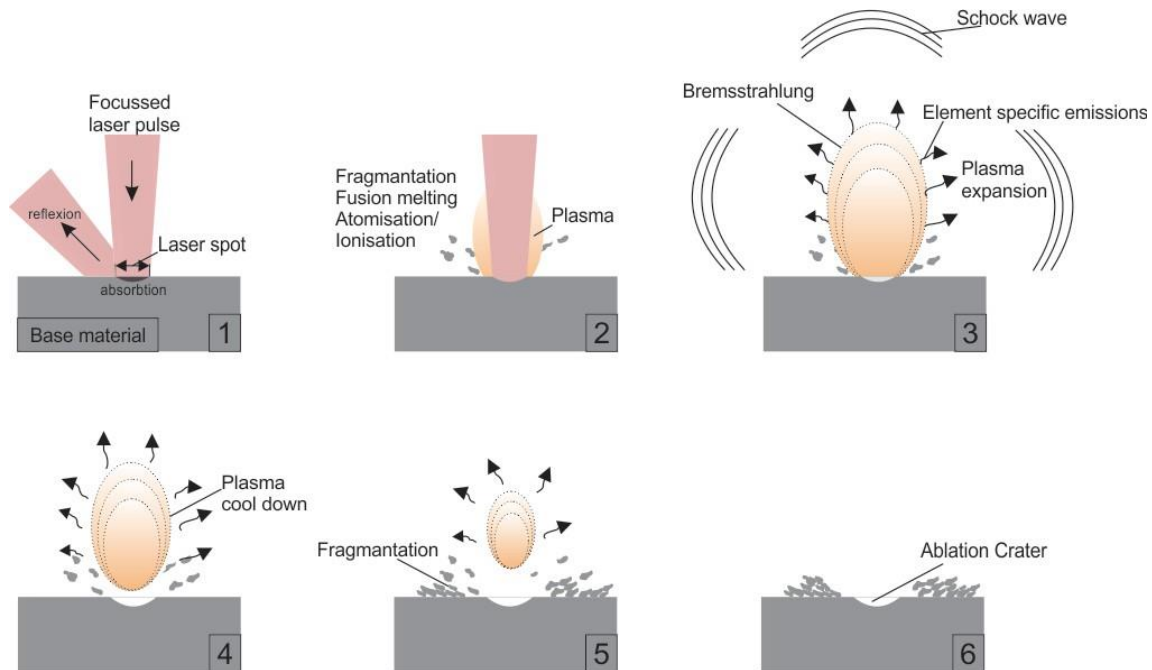


Figure 2-25: Schematic representation of the different phases of the laser-induced plasma 115

In the first phase (1), the pulsed laser radiation reaches the material surface. A part of the radiation is absorbed according to the thermo-optical properties of the target sample. The resulting sudden temperature increase causes a phase change both on the incident crater and in the surrounding area of the crater (also called heat-affected zone (HAZ)), i.e. phase change occurs from solid to gaseous state¹¹ and a material vapor is formed above the sample surface (phase 2) [110, 116, 117].

At this stage, sample material (in ng or μg scale depending on the laser energy) is partially or completely atomized and ionized due to the high temperature of between 10000-15000 K. The expansion of the formed plasma propagates a shock wave. The relaxation of the excited or charged particles in the plasma leads to the emission of electromagnetic radiation (phase 3). Initially, Bremsstrahlung dominates the spectrum in the form of broadband background radiation. After the first hundred nanoseconds, the background radiation decays and element-

¹¹ Sublimation

specific radiation of atoms, ions and molecules, can be detected (phase 3 and 4) [116, 117].

Finally, an ablation crater and single particles (μm to nm) around it remain (phase 5 and 6). The phase 3 and 4 are the decisive stages for element detection using LIBS, i.e. the element-specific radiation can be detected during these stages, and thus the peak intensity of the signal can be detected usually between 40-500 ns after the laser pulse [110, 116-119]. Using modern detector (e.g. CCD, ICCD etc.) technologies, the spectra can be captured with time-resolved precision¹², and thus this allows recording of the optimum spectra at the suitable stage e.g. without the unwanted background radiation or self-absorbed elemental lines.

2.4.3. Characterization of laser-induced plasma

The time dependent stages of the laser-induced plasmas enable the detection of element-specific radiation. After excitation with an energy above the ablation threshold¹³, different atoms or ions can be detected with a corresponding transition probability¹⁴[120], which are emitting photons.

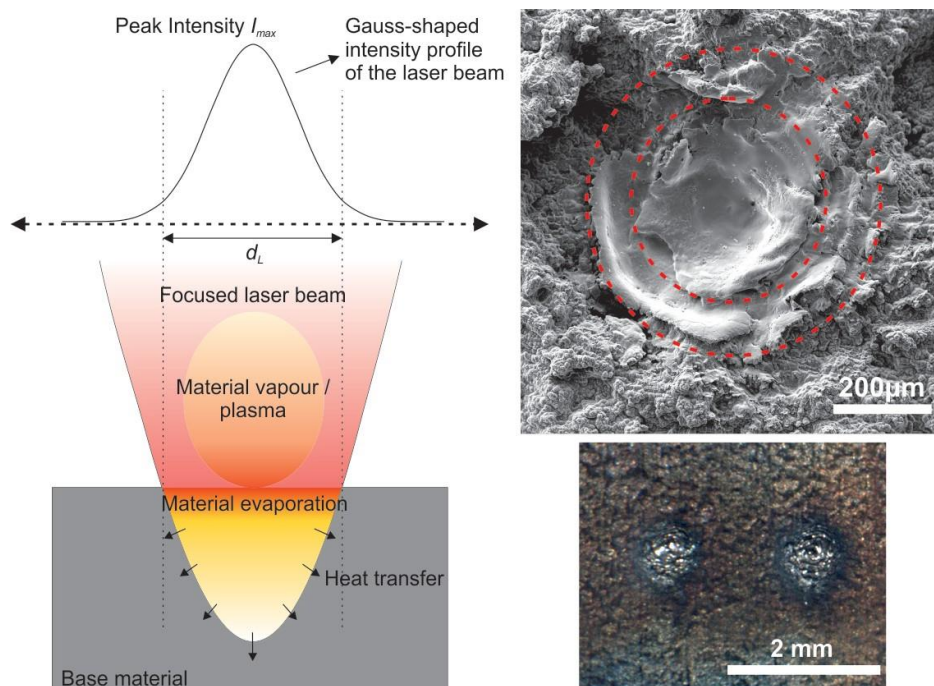


Figure 2-26: Illustration of the laser material interaction (left) [116] and SEM image of an ablation crater on a crack surface of a steel sample (right-top), image of the ablation craters from a LIBS line-scan (right-bottom).

Depending on the atomic structure, detection of various elements with different degrees of

¹² Possibility to capture the spectrum with an arbitrary time delay after the laser is pulsed

¹³ Critical fluence (optical energy per area per pulse) which results in material removal within theirradiated spot area

¹⁴ Transition probability (A_{ki}) is the number of downward transitions (photoemission) per second from an upper energy level k to a lower level i [119]. Also known as 'Einstein transition probability'.

accuracy is possible. The main influencing factors can be counted as [117], the experimental setup and equipment, the transition probability of the target elements, the excitation or ionization energy of the target element and the spectral wavelength range.

2.4.4. Spectral processing and data quantification

Various characteristic values can be derived based on the measured and recorded spectral lines. The atomic spectral line of iron Fe I 440.475 nm is shown as an example in Figure 2-27. Characteristic values relevant to the analysis are, the maximum intensity I_{max} and the integral area under the fit, the full width at half maximum FWHM, the background b_0 and the noise n_0 . The intensity of the background baseline in the spectra is caused mostly by the Bremsstrahlung radiation in the first nanoseconds of the plasma formation and can be corrected e.g., by a linear baseline correction. The noise, on the other hand, describes a signal fluctuation caused by e.g., the thermal noise of the spectrometer detector. This noise can also be compensated by averaging or filtering (data processing). To calculate the signal to background (S/B) or signal to noise (S/N) ratios, the maximum intensity of the selected elemental line is divided by the background, or the maximum intensity of the line is divided by the noise component respectively. The S/B or S/N ratios do not have a unit and used in arbitrary units (a.u.) to relatively quantify the optical signal quality.

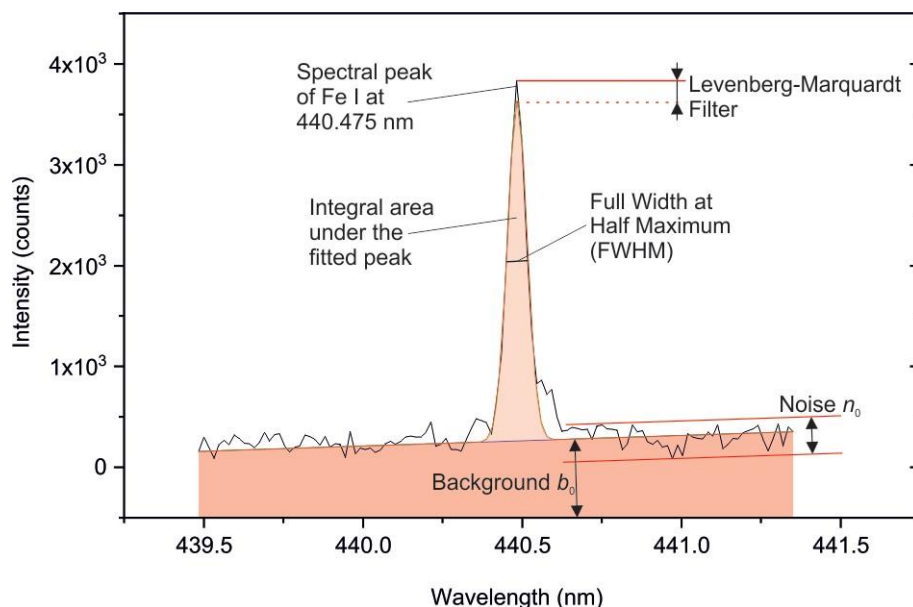


Figure 2-27: Display of the characteristic values I_{max} , FWHM, b_0 and n_0 at the spectral line of iron Fe 440 475 nm

The typical order of spectral processing includes the following stages: selection of the relevant peaks, baseline correction and subtraction, integrated peak area calculation and internal peak normalization through matrix element.

In order to obtain quantitative information about the elemental composition of the sample

using the experimentally recorded spectra of LIBS, methods of regression analysis are necessary. For this purpose a multitude of different methods are available [111]. Simple univariate regression (also known as linear regression) analysis to complex AI algorithms can be used for this purpose. Regardless of the method, the analysis requires corresponding input variables. These may include e.g., the measured spectra, characteristic values of spectral lines, integrated intensity values of the individual peaks and associated reference values for the respective element to be investigated.

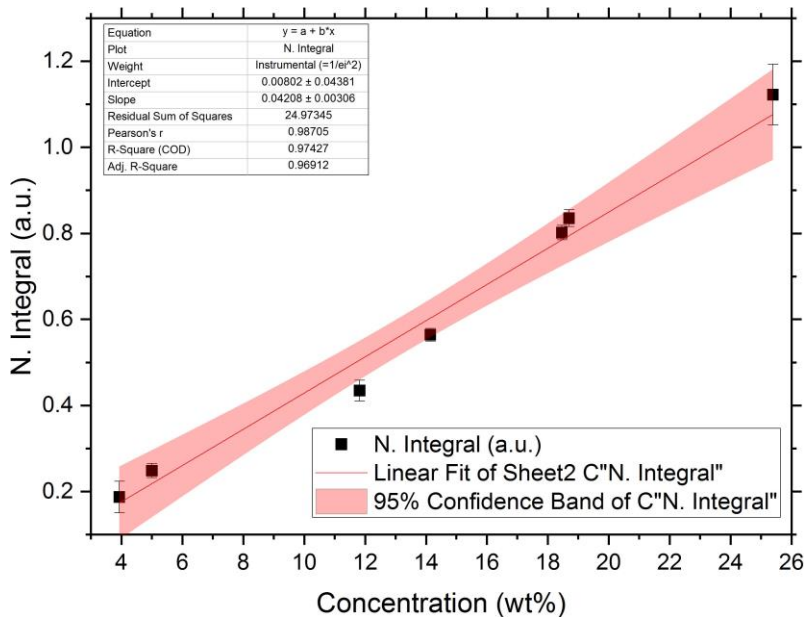


Figure 2-28: Characteristic univariate linear regression calibration model with 95% confidence band

When using univariate regression, a functional relationship between the reference values (x) and measured characteristic values (y) must be established by means of a linear or a non-linear model. A functional equation is then used to quantify unknown samples.

Figure 2-28 represents a typical calibration curve obtained by linear regression method. The x values represent the chemical concentration of the used certified reference material (CRM) and the corresponding y values are the measured intensities for that sample. Using these linear or non-linear relations from the known CRMs, a sample with unknown concentration can be measured and statistically determined.

All in all, the essentials of this chapter can be summarized with the following points:

- *Global steel production increased due to economic developments in Asia, and raw material prices fluctuate based on supply, demand, technological advancements, and political climate.*
- *Welding consumables for stainless steel can be costly due to depletion of alloying elements during the welding process and process conditions.*
- *Mass transfer involves species transfer in non-uniform composition, and diffusion is crucial to distinguish the type and mechanism of diffusion.*
- *Self-diffusion and concentration gradient diffusion occur due to the vibration of atoms and composition gradient, respectively, and Fick's law predicts diffusion flux and resulting composition over time.*
- *Fluid flow and weld pool convection affect welding processes and pool shape, mixing, porosity distribution, and metal evaporation.*
- *Final weld microstructure and properties depend on metallurgical reactions, solidification process, and chemical compositional differences, causing defects and cracking issues.*
- *Weldability refers to steel's ability to be welded without defects and how well a joint performs during service.*
- *Iron has three natural allotropes, and only alpha-ferrite and gamma-austenite are relevant for a broad spectrum of steels and in context of hot cracking issue.*
- *Stainless steel's solidification behavior and final microstructure are influenced by alloying elements, and zones of a weldment include the FZ, HAZ, and base material.*
- *Hot cracking and weld solidification cracking occur due to complex interactions between metallurgical and mechanical interrelationships during fabrication and solidification.*
- *Various methods have been used for in situ weld monitoring, including optical emissions, radiographic methods, image processing, 3D laser scanning, electron temperature calculations, spectroscopic measurements, and laser-induced breakdown spectroscopy (LIBS).*

Chapter 3

3. Summary of the literature

The modern steel industry began in the 1850s with the invention of the Bessemer process, which involved blowing air through molten pig iron to remove impurities. Today, steel is still one of the most widely used materials in the world, with over 3500 steel grades available. The properties of each grade are determined by the amount of carbon, impurities, and alloying elements. The global demand for steel and raw materials has increased significantly over the past twenty years, with production rates increasing since the year 2000 due to economic and technological developments. The cost of raw materials is determined by various factors, including global resources, consumption, and recycling. The intensive cost pressure in the production of welded components, such as stainless steel and welding consumables, results from a variety of factors. Even small market fluctuations in the alloying or micro-alloying elements could impact the alloy design. Although steel alloy design has a certain flexibility, the principal goal is to apply the most cost-effective design for producers while ensuring certain mechanical and chemical properties.

Welding metallurgy explores where the final microstructure and properties of the welds are determined by various metallurgical reactions, i.e. solidification, segregation, and diffusion processes. These reactions can lead to differences in local chemical composition that may affect the weldability and service performance of the end-product. The extent of these reactions can greatly influence the final microstructure, leading to changes in the properties of the weld metal and the heat-affected zone compared to the base material. The stainless steel weldability and solidification are dependent on the alloying elements present, and the term weldability is defined as the ability to weld steel without weld defects and satisfactory performance of the joint during service.

Solidification process involves several parameters and factors that influence the final microstructure and properties of the material. One of the critical parameters is the partition coefficient, which determines the distribution of solute between the solid and liquid phases during solidification. The partition coefficient varies with temperature and can be either positive or negative. A positive partition coefficient means that the solid absorbs solute from the liquid, while a negative partition coefficient means that the solid rejects solute into the liquid.

In addition to the partition coefficient, other factors such as liquid temperature gradient and solidification growth rate also play a crucial role in determining the microstructure of the solidified material. The liquid temperature gradient dictates the temperature field ahead of

the solid-liquid interface, while the solidification growth rate determines how fast the interface moves during the solidification process.

Hot cracking is the cracking issue that occurs during the fabrication process due to the presence of liquid in the microstructure. Hot cracking is mainly identified by three distinctive types of cracks: weld solidification cracking, HAZ liquation cracking, and weld metal liquation cracking. Solidification cracking occurs due to the rupture of low temperature melting liquid films along the grain boundaries that occur during the solidification process. Solidification cracking is influenced by several factors, including the chemical composition of the alloy, solute atoms, and impurity segregation. The amount of delta-ferrite in austenitic stainless steel weld must be strictly controlled since more than 10 vol% delta-ferrite tends to reduce the ductility, toughness, and corrosion resistance, whereas less than 5 vol% delta-ferrite may result in solidification cracking according to the literature. The weld solidification microstructure can be predicted by assessing the chemical composition of the base and input material.

Most of the weld defects are detected after the weld is complete. However, using in situ monitoring of chemical compositions, local elemental composition fluctuations can be monitored online during the process, hence this can lead to avoiding weld defects during process. Various methods of in-situ weld defect monitoring have been proposed, such as measuring optical emissions directly from the welding arc, inline visual inspection by image processing or 3D laser scanning. In conclusion, in situ monitoring of weld defects is a promising method for improving the quality of welding processes.

LIBS is a type of atomic emission spectroscopy method that uses laser pulses to create a plasma that can be analyzed by a spectrometer. The radiation emitted from the excited atomic species is element-specific and provides a spectral fingerprint that can be resolved and analyzed. LIBS finds vast application areas in a variety of research and industry fields such as steel industry, scrap sorting tasks, explosives detection, mining and mineral resource exploration, geology and environmental sciences, archaeology, biomedical applications, and space exploration. The advantages of LIBS include simultaneous multi-element detection, measurement over distance, and fast analysis. These advantages demonstrate a high potential for in situ weld and molten metal chemistry monitoring applications in respect to research and industry fields.

Chapter 4

4. Problem statement and objectives

Welding is a critical process in many industries, including manufacturing, construction, and automotive. Ensuring the quality of welds is essential to the safety and reliability of the final product. However, there are currently no commercial systems available to assess the chemical composition of welds in line. While destructive methods, such as cross sectioning and EDX or X-ray fluorescence analysis, can provide spatially resolved chemical composition information, they are not practical for on-site use. These methods are time-consuming, require specialized equipment and personnel, and destructing the sample, making them unable to be used for continuous quality control or real-time problem diagnosis.

Hot crack detection is possible during welding by measuring the weld chemical composition; this makes process control feasible, hence can enable preventative actions before the occurrence of any weld-defects.

The lack of a non-destructive and on-site method for weld chemical composition assessment presents a significant challenge. It hinders the ability to evaluate weld quality quickly and accurately, leading to potential delays and increased costs in manufacturing and other industries that rely on welds. In addition, the risk of faulty welds is increased when there is no way to continuously monitor and ensure the quality of the welds being produced. A solution that can assess weld chemical composition on site would improve efficiency, reduce costs, and minimize the risk of faulty welds.

The scientific and technical research questions of this study can be listed as:

1. Is it possible to measure the main alloying elements from distance without contact to the molten weld pool? Is LIBS feasible to deploy for this application? (*Technical*)
2. What is the boundary welding heat input energy to induce hot cracking for the selected sample geometry? (*Technical + Scientific*)
3. Which type of solidification modulus drives the hot-cracking formation for the selected high alloyed stainless steel, can this be detected online? (*Scientific*)
4. Is it possible to determine the elemental partition coefficient online during welding using the measured chemical composition? How does this correlate to the hot cracking behavior of the high alloyed stainless steel? (*Scientific*)
5. How do the alloying elements' chemical composition on the post-weld crack surface and

solidified weld pool differ from the base material reference measurements? (*Scientific*)

6. Does the intensity of the welding plasma interfere with the output LIBS signal and the measurement data? (*Technical*)

7. What is the response time of an online measurement via LIBS? Can one detect changes of the chemical composition in the weld pool instantly? (*Technical*)

8. Which spectral parameters influence detection of the alloying elements? How can they be optimized? (*Technical*)

9. Which elements could vaporize from the weld pool during welding of high-alloyed stainless steel? What happens to the mass vaporized after welding? (*Technical + Scientific*)

10. Do the welding parameters (welding heat input energy, shielding gas flow rate) affect the vaporization rate, hence the condensation rate? (*Technical + Scientific*)

To answer the listed research questions, the solution approach can be broken down to two main topics, namely the process development to cover technical research questions (prototyping and validation of initial design) and the process implementation and weld defect monitoring to cover scientific research questions (initial testing and method validation).

1. Process development (prototyping and validation of initial design):

(a) *Selection and utilization of the appropriate welding and experimental setup components for realization of the welding experiments.*

(b) *Selection and utilization of the appropriate LIBS components for in situ weld monitoring ability.*

(c) *Preliminary welding experiments of the selected stainless steel base materials with different sets of welding parameters.*

(d) *Observation of the welding parameters effects on the analytical LIBS signal. (Interference of the welding process on the measurement signal)*

(e) *In situ detection of external element addition using TIG filler rods.*

(f) *Qualitative in situ detection of the overall weld chemical compositions.*

2. Process implementation, weld defect induction and observation (initial testing and method validation):

(a) *LIBS system calibration by selection and measurement of appropriate CRMs.*

- (b) *Calibration of the LIBS system for the relevant elements in the alloy composition by univariate linear regression method. Quantification of the online measured weld chemical compositions.*
- (c) *In situ monitoring of the chemical compositions in the weld pool during the welding process.*
- (d) *Detection of alloying element vaporization from the weld pool.*
- (e) *Determining the hot cracking boundary conditions and in situ observation and compositional monitoring during the hot cracking phenomenon.*
- (f) *In situ partition coefficient calculation.*
- (g) *Post weld investigations for the characterization of the weld metal microstructure and possible impurity accumulation.*

In conclusion, the lack of a non-destructive and on site method for weld chemical composition assessment presents a significant challenge for the welding scientific community and industry. Thus assessment and preventing of the hot cracking phenomenon remains a scientific question in the field. The research questions listed above aimed to provide a solution to this problem, with a focus on both technical and scientific aspects. The solution approach involves two main topics, namely process development for prototyping and validation of the initial design, and process implementation and weld defect monitoring for initial testing and method validation. By addressing these research questions, the results will provide a foundation for the development of a non-destructive and on-site method for assessing weld chemical composition, which would improve efficiency, reduce costs, and minimize the risk of faulty welds in the manufacturing and other industries that rely on welds as well as answering significant weld solidification related questions. Moreover, the practical situation of hot cracking phenomenon was investigated thoroughly using the developed method.

Table 7: Work program of the experimental series.

Experimental Series	Base mat.	Filler mat.	Relevant Sections
1 - Welding plasma as an analytical signal	1.4404	-	5.4
Objectives: Initial experimental equipment set-up. Welding plasma as a replacement for laser signal source.			
2 - Influence of the welding parameters on the measurement signal	1.4435 1.4565	-	6.1
Objectives: Variation of welding parameters. Influence on the analytical measurement signal.			
3 - In situ detection of filler material addition during welding	1.4435	45703V	5.4
Objectives: In situ Cu-filler (external element) addition and detection.			
4 - In situ monitoring of the alloying elements	1.4404 1.4435	-	6.1
Objectives: Parameter investigation and optimization for the LIBS measurements.			
5 - Alloying element vaporization from the weld pool	1.4404 1.4435	-	6.1
Objectives: Accumulation phenomenon in the HAZ.			
6 - Process implementation and hot cracking of stainless steel	1.4404 1.4435	-	6.2
Objectives: Solidification cracking observation. In situ partition coefficient determination Effect of the impurity elements S and P. Post-weld crack investigation			

Chapter 5

5. Experimental

The following chapter presents the analyzed materials as well as the structure and procedure of the experiments performed. This is followed by a presentation of the experimental and measurement equipment used for welding processes and the chemical composition measurements using LIBS. Finally, the further characterization methods used to analyze the conducted welds are explained.

5.1 Analyzed materials

5.1.1 Base materials

Since this study focuses on stainless steels weld defects, various types of stainless steels grades and batches were used during the experimental stage to observe various material responses with varying chemical compositions. The chemical compositions of the base materials are determined by spark-optical emission spectroscopy control measurements. Table 8 shows the results of these analyses. The control measurements correspond to the tolerance requirements in the relevant standard (DIN EN 10088-1:2014, DIN EN 10088-2:2014 [13, 14]).

5.1.2 Filler materials

The chemical compositions of the welding filler metals are listed in

Table 9 according to the manufacturer's data sheet. In this study filler materials were used to influence the chemical compositions of the weld during the process and to examine the response of the LIBS monitoring system.

Table 8: Chemical compositions of the base materials in weight % (Spark-optical emission spectrometry). Balance wt% is Fe.

Material/batch	C	Si	Mn	P	S	Cr	Mo	Ni	Nb
1.4404/b.1	0.03	0.3	0.7	0.016	0.003	17.3	2.1	11.2	-
1.4404/b.2	0.03	0.3	1.4	0.023	0.005	17.0	2.0	10.2	-
1.4435/b.1	0.03	0.5	1.2	0.016	0.009	18.1	2.5	12.8	-
1.4435/b.2	0.03	0.5	1.5	0.012	0.005	18.0	2.4	12.6	-
1.4565	0.03	0.3	5.5	0.013	0.004	24.4	4.4	17.6	0.028

Table 9: Chemical compositions of the Cu-based filler material in weight % according to DIN EN 10204-2.2 (manufacturer data sheet).

Material	P	Fe	Zn	Sn	Pb	Al	Cu
Cu-based (45703W)	0.01 - 0.35	<0.1	<0.1	5.0-8.0	<0.02	<0.1	rest

5.2 Experimental setup for in situ weld chemical composition monitoring

The in situ weld monitoring concept was employed either during stationary welding spots or finishing weld beads by moving the base material using a linear motorized stage. The LIBS and the welding systems were controlled manually, thus, the first laser pulse was synced with the ignition of the welding arc for all the experimental series.

Stationary setup (Spot welds)

TIG stationary experiments were performed as individual spots on the base materials, i.e. neither the sample nor the welding torch were moved. This arc welding system contains a DC power supply and a TIG torch using pure tungsten electrode with 1.6 mm diameter. The distance from the base material to the electrode tip was set to 5 mm. The electrode tip extended approximately 3 mm from the ceramic gas nozzle. All the welding processes were performed with constant 16 l/min shielding Ar gas flow.

For the stationary set up, to monitor the effect of the resulting temperature from the welding arc, K-type thermocouples were used and placed in defined positions respective to the welding arc. Exact locations are given in the relevant results section 6.2.

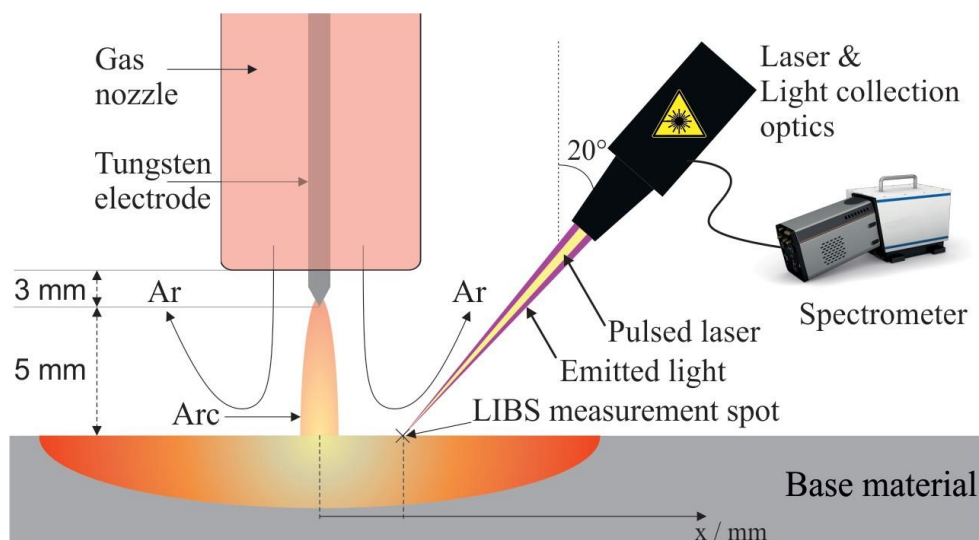


Figure 5-1: Schematic experimental setup for the stationary weld monitoring situation.

Movable setup (Bead-on-plate welds)

The in situ weld monitoring was employed by finishing weld beads up to 200 mm in length using a linear motorized stage with a linear movement resolution of 0.1 mm. To produce the weld beads, base materials were mounted on the linear stage and moved. Apart from the stage-mounted samples, the rest of the experimental setup remained static, i.e. welding was realized by the relative movement of the base material mounted on the linear stage. The stage and the LIBS system were controlled by an automatized pre-programmed software interface.

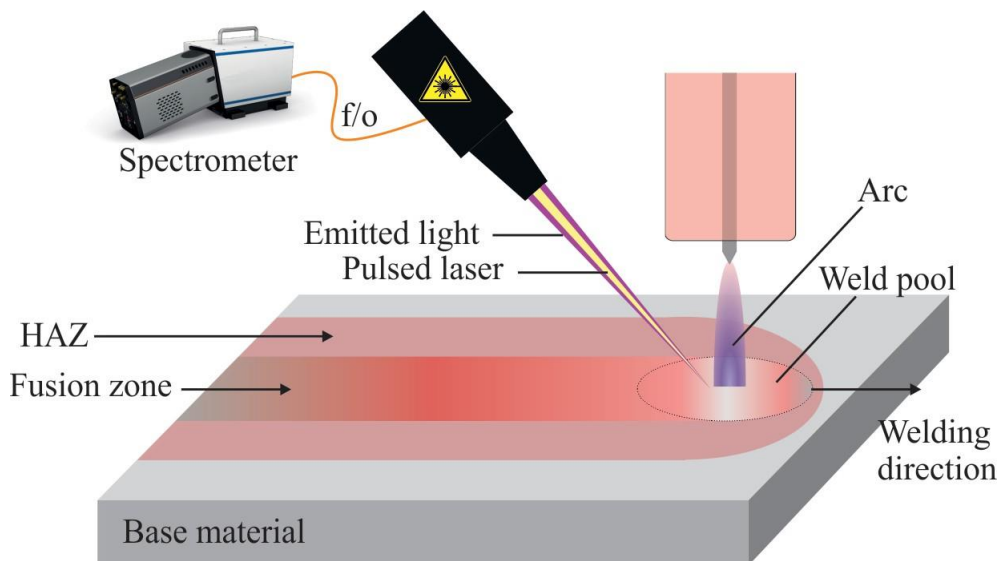


Figure 5-2: Schematic experimental setup for the moving weld monitoring situation. Weld pool is marked with dashed line for ease of visualization.

As the mounted sample on the motorized stage was moved and the welding process is underway, the LIBS measurements were conducted simultaneously. The LIBS process uses accumulated the laser pulses to increase the laser-induced plasma temperature and consequently the resulting signal intensity. Therefore, the spatial distribution of the chemical compositions depends on the welding speed, the amount of accumulated laser pulses and the laser repetition rate. This principle is explained in the following sub-section.

Within the process implementation for the final stage of the experiments, an infrared thermometer was used to detect the temperature from distance. The position of the temperature measurement was set to the relative same distance to the welding arc in perpendicular symmetry on the weld pool, to capture the same temperature of the LIBS measurement spot.

LIBS experiments

LIBS signal generation and evolution can be summarized as follows; pulsed laser beam is focused on the surface of the substance or sample material. Radiation is absorbed by the

substance and the material starts to evaporate. Within this vapor, a plasma is generated, leading to excitation of material constituents and spontaneous emission of radiation. As this plasma decays, element specific radiation is emitted [110].

These events follow a certain temporal order or happen in stages and are consist of time resolved phenomena; stages can be separated and can be distinguished or filtered by physical mechanisms built in the spectrometer and/or the optical path. Tinkering with some of the experimental parameters and optimizing them, one can improve the signal quality and the results. For these parameters, laser pulse accumulation amount, spectrometer signal delay time and gate width can be counted as the primary influencing factors. More information on the individual parameters can be found in elsewhere [110].

The LIBS system used in this study used a pulsed Nd:YAG laser working at 15 Hz and accumulated 20 pulses to acquire one spectrum. Accumulation of 20 laser pulses was the manufacturer recommended value and after experimental trials, it was allowing the user to generate a spectrum with the given setup. With this setting accumulating 20 laser pulses at 15 Hz interval resulted in recording a spectrum ca. every 1.2 seconds.

The further primary influencing factors or main physical mechanisms to control and distinguish the lifetime of the plasma are “Delay time” and “Gate width”. Delay time distinguishes the temporal observation beginning of the plasma from the time point it is created. The main reason for this mechanism is the noise generated by the spontaneous Bremsstrahlung generated at the early life of the plasma. In the LIBS applications, a certain amount of delay is usually applied to be able to initially eliminate the noise and distinguish the element-specific radiation.

The second important physical mechanism to improve the signal quality is the “gate-width”. Gate-width can be defined as the time the detector array is open for the incoming signal, in other words how long the detector is exposed to the incoming signal.

Investigation and optimization of the delay time and gate width parameters and their effect on the Signal-to-noise and Signal-to-background ratios are discussed in Section 5.4 Preliminary experiments.

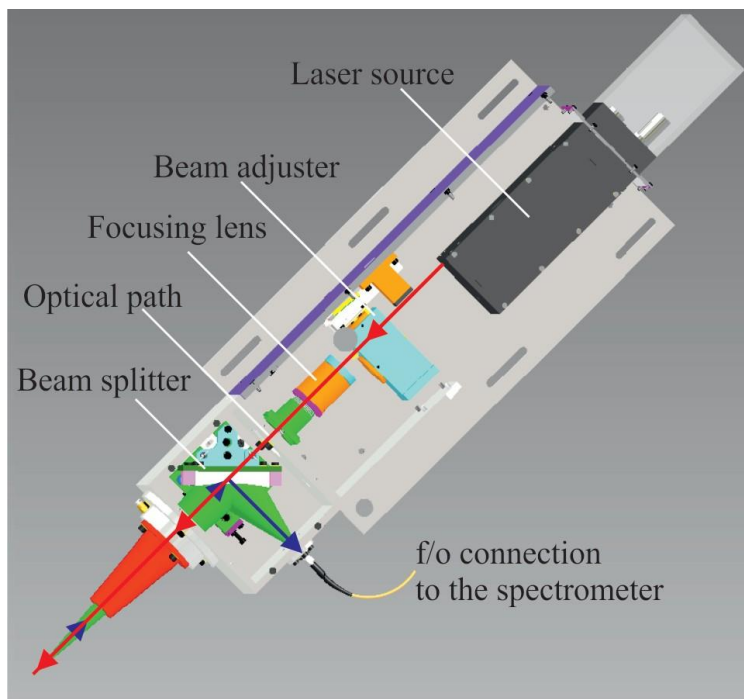


Figure 5-3: 3D CAD-drawing of the laser head with internal components and optical path representation.

Figure 5-3 demonstrates the Laser source and the optical path including the beam influencing components in 3D CAD (Computer Aided Design) drawing form. The purpose of this system is to house the laser source and to focus the laser beam on the sample surface; capture the emitted light and transport this information into the spectrometer via f/o cable connection for detection.

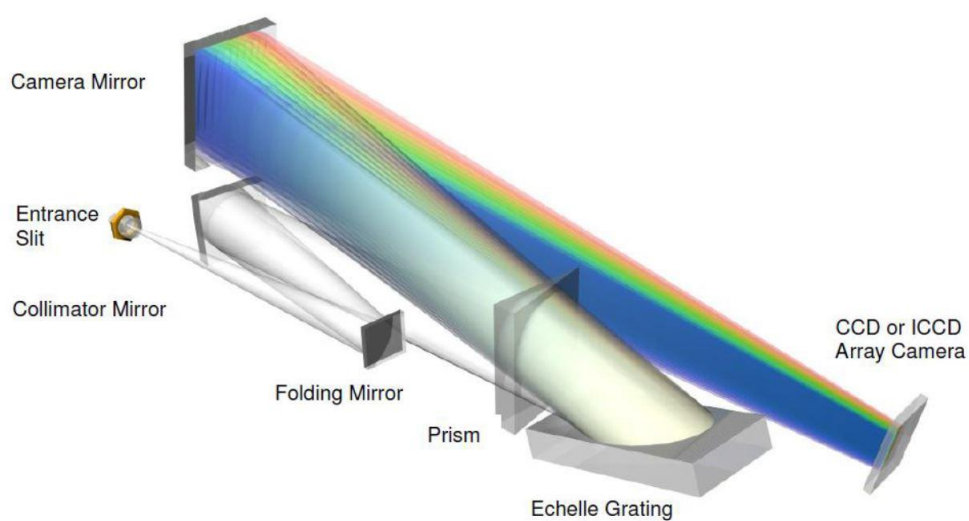


Figure 5-4: Optical setup Aryelle spectrometer [121].

Figure 5-4 demonstrates the schematical design of the Aryelle spectrometer and how the light

is transported or respectively went through different mirrors and prism systems. The incoming signal goes into the spectrometer via entrance slit and after going through several mirror mechanisms, it is broken down into the elemental characteristic lights via Echelle Grating and prism and reflected on the ICCD camera detector in this case.

Univariate calibration by linear regression

A univariate calibration model is a statistical model that is used to predict the value of a single variable (also known as a univariate variable) based on the values of one or more predictor variables. In other words, it is a model that is used to establish the relationship between a dependent variable and one or more independent variables.

Univariate calibration models are often used in the field of analytical chemistry, where they are used to predict the concentration of a specific chemical species in a sample based on the measured response of an analytical instrument, such as a spectrophotometer or a chromatograph [122].

Linear regression is a widely used technique for fitting univariate calibration models and is particularly useful when the relationship between the variables is approximately linear. It involves finding the line of best fit that minimizes the sum of the squared differences between the observed values of the dependent variable and the predicted values based on the independent variables. The slope of the line represents the strength of the relationship between the variables, and the intercept represents the value of the dependent variable when all of the independent variables are equal to zero [117, 122].

Table 10: Chemical compositions of the CRMs (in wt.%) used to establish the calibration models. All CRMs have iron matrix, i.e. balance wt% is Fe.

CRM / Producer	C	Si	Mn	P	S	Cr	Mo	Ni	Nb	Cu
BS19 / Brammer	1.5	1.4	8.5	0.030	0.006	3.9	2.0	1.4	-	0.5
271-1 / BAM	0.369	0.9	0.4	0.012	-	5.0	1.2	0.1	-	0.1
273-1 / BAM	0.033	0.4	0.8	0.013	-	14.7	0.2	4.8	0.2	3.0
295-1 / BAS	0.016	0.4	1.7	0.016	0.001	19.5	4.0	24.4	-	1.5
296-1 / BAS	0.116	0.2	0.6	0.017	0.002	11.8	1.7	2.7	-	0.1
475 / BAS	0.050	0.2	0.9	0.037	0.008	14.1	1.5	5.6	0.2	1.9
461-1 / BAS	0.010	0.3	0.7	0.005	0.005	14.7	-	6.1	-	-
462 / BAS	0.092	0.4	0.7	0.010	0.018	12.3	-	12.5	-	-
462-1 / BAS	0.035	0.4	0.7	0.005	0.004	11.8	-	12.8	-	-
463-1 / BAS	0.019	0.2	1.4	0.025	0.019	18.4	0.2	10.2	-	0.2
SS63 / BAS	0.066	0.4	0.7	0.016	0.020	18.7	-	9.5	-	0.1
SS64 / BAS	0.079	0.4	0.8	0.012	0.022	25.6	-	20.6	-	0.1
464-1 / BAS	0.086	0.5	0.8	0.020	0.028	25.4	-	20.0	-	-
1.4571 / SUS	0.020	0.6	1.9	0.030	0.030	16.6	2.0	11.1	-	0.4

The calibration measurements were conducted with the same stationary LIBS setup on the selected CRMs. Individual models for the elements Cr, Ni, Mn and Mo are given in the Section 6.3.

5.3 Characterization methods

5.3.1 Light optical microscopy

All the metallographic specimens were mechanically ground on SiC paper with 320, 500, 800, 1000 and 1200 μm grit size, subsequently polished using diamond spray with 6, 3 and 1 μm grit size and finished with OPS (Oxide-Polishing Suspension). The etching of the surfaces was performed by two different procedures¹⁵ depending on the base material to characterize the microstructure, weld defects or to highlight specific structure features and different phases.

Lichtenegger und Bloech I¹⁶ (LB I) includes the etchant prepared by 100 ml distilled water, 20 g ammonium hydrogen fluoride and 0.5 g potassium metabisulfite.

Boech und Wede II¹⁷ (B+V II) includes the etchant prepared by 50 ml distilled water, 50 ml hydrochloric acid, and 0.1 to 2 g potassium metabisulfite.

The optical microscopy was conducted using a Reicher-Jung Polyvar IET microscope with Leica DFC 290 camera. Macroscopic imaging of the welds was captured by Canon EOS 600D.

5.3.2 Scanning electron microscopy (SEM)

A scanning electron microscope (SEM) is a type of electron microscope in which the electron beam is accelerated, focused and subsequently scanned in a certain pattern over the object to be magnified. The interactions of the electrons with the object are used to create an image of the object. The electrons are excited and released from an electron source at the top of a main chamber. The primary electrons are released and accelerated with an energy in the magnitude of eV¹⁸. The specimen is placed in the chamber below this electron source and optical path. Due to the interaction between the primary electrons and the specimen atoms, a variety of elastic or inelastic collisions in the sample material can occur. As a result of these interactions, various emissions e.g. secondary or backscattered electrons, X-rays might occur. The origin of each signal comes from a specific interaction volume within the specimen (Figure 5-5), hence, can be directed to various detectors to create image and analyze various properties of the sample. To be able to control the source volume of information on the sample, one should take into account the following parameters: accelerating voltage, source

¹⁵ Individual procedure is indicated according to the used one for each micrograph in the Results and Discussion chapter.

¹⁶ Metallographische Anleitung zum Farbatzen nach dem Tauchverfahren, Teil II: Farbätzmittel nach Beraha und ihre Abwandlungen, E. Weck und E. Leistner, Deutscher Verlag für Schweißtechnik (DVS) GmbH - Düsseldorf 1983

¹⁷ Metallographische Anleitung zum Farbatzen nach dem Tauchverfahren, Teil III: Nichteisenmetalle, Hartmetalle und Eisenwerkstoffe, Nickel-Basis- und Kobalt-Basis-Legierungen, E. Weck und E. Leistner, Deutscher Verlag für Schweißtechnik (DVS) GmbH - Düsseldorf 1986

¹⁸ The amount of kinetic energy gained by a single electron accelerating from rest through an electric potential difference of one volt in vacuum. $1\text{eV} = 1.602176634 \cdot 10^{-19}\text{J}$

diameter and basic sample information i.e. microstructure, composition and crystal structure.

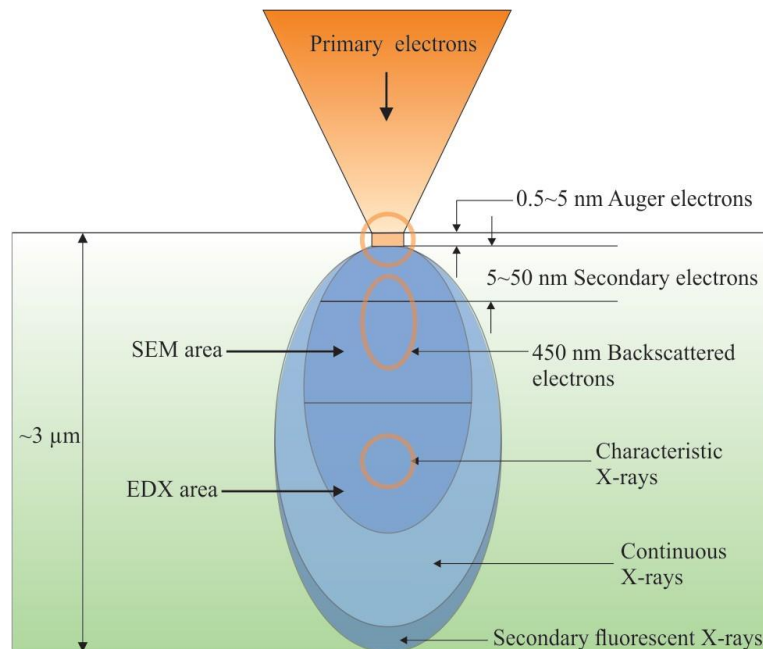


Figure 5-5: Schematic representation of the primary electron-sample interaction and the specific volumes of the emitted signals[123].

Cross-sections, crack surfaces and various other positions of the welds were observed using a Thermofischer Phenom L desktop scanning electron microscope. Depending on the equipped detector and the observed signal type, various information can be extracted from a SEM image. This SEM was equipped with back-scattered electron, secondary electron and an EDX detector. Electron source was able to apply an accelerating potential from 4.8 kV up to 20.5 kV. In the present work, the secondary electron detector was applied for observation of the different phases (austenite-ferrite) in higher magnification. Furthermore, crack surfaces were investigated using the backscattered electron detector to highlight the individual dendritic growth during the solidification process. EDX measurements were also conducted on various surfaces, e.g. crack surface, base material. Working parameters and different detectors are indicated in each SEM-image.

5.3.3 Spark-optical emission spectroscopy (OES)

Arc/spark optical emission spectroscopy is a traditional analytical method that being used in the field for decades and has been the leading technique and industry standard for elemental analysis for a long period of time. Currently, other methods e.g. ICP-OES, ICP MS are in comparison with this conventional method[124]. LIBS can be considered as an upgrade to this method in terms of excitation source.

Spark-optical emission spectroscopy measurements were conducted to compare and verify the in situ LIBS measured values. The mobile arc spark metal analyzer SPECTROTEST was employed for this purpose. Some of the main alloying elements and their limits-of-detection (LoD) values are shown in Table 11.

Table 11: LoD values for various alloying elements of the stainless steel using arc/spark OES method[124].

Element	LoD
Cr	0.53 mg/L
Ni	1.02 mg/L
Mn	1.33 mg/L
Mo	2 mg/L
P	~1 $\mu\text{g}/\text{mg}$

5.3.4 X-Ray (Radiography) Analysis

Radiography is an imaging technique using ionizing or non-ionizing radiation to view the internal form of an object. In the industrial environment, radiography is used as a novel non-destructive testing procedure using ionizing radiation (X-rays in this study) to inspect materials and components to locate and quantify degradation and related defects that might lead to failure of the components. It has an important usage in context of product quality and safety.

X-Ray radiography uses X-rays, produced by stationary or mobile X-ray generators. After crossing the specimen, photons are captured by a detector, such as a silver halide film, a phosphor plate or at panel detector. The examination can be performed in static 2D (named radiography), in real time 2D, (fluoroscopy) or in 3D after image reconstruction (computed tomography or CT).

The X-Ray radiography investigations were conducted according to DIN EN ISO 17636-2 standard using Titan 420 X-Ray Tube at 150 kV anode potential.

5.4 Preliminary Experiments: In situ alloying element detection using LIBS

5.4.1 Welding plasma as an analytical signal source

Arc welding processes cause a wide range of electromagnetic emissions and thus these emissions can be detected by a spectrometer. Each welding process in this study demonstrated characteristic signal count peak at the very beginning of the ignition of the welding arc and this peak signal decayed after the arc was stabilized in several seconds. However, it does not provide sufficient information to quantify the chemical composition of the weld pool, since the information is gathered from different sources in the beginning, e.g. electromagnetic radiation from the high-frequency (HF) start of the welding arc, infrared radiation; and after stabilization the gathered signal intensity was not sufficient with the current set up to resolve element-specific spectra [125]. The natural increase of the temperature also has a strong influence on the intensity count values as well. An internal standard normalization using an iron emission line is here not entirely feasible due to the varying dominant sources of the emissions. This type of normalization is employed -in the following sections- during the experiments that use a laser as an excitation source to induce its own information source, namely laser-induced plasma, where the instantaneous plasma temperature reaches up to 15000 K and generating dominant signal source.

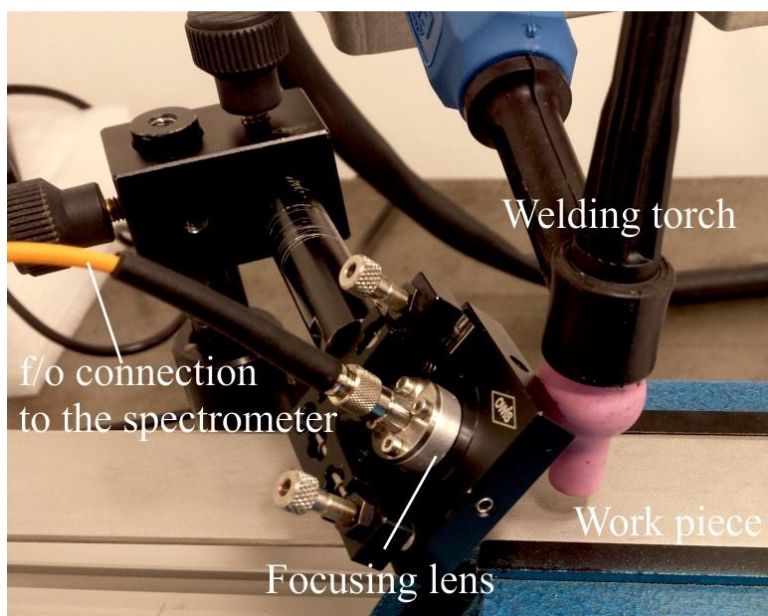


Figure 5-6: Detection set up without the laser source. Optics focusing directly on the sample surface where the welding arc meets the work piece below the electrode. Signal is carried to the spectrometer via fiber optic cable.

In this section base material 1.4404/b.1 was used in 3 mm plate thickness, two representative

experimental campaigns were put into comparison below for fundamental understanding of the problem statement with different welding currents. Two welding currents were used, namely 80A and 120A in constant welding speed of 10 cm/min and constant Ar gas flow rate of 16L/min. Increasing the welding current from 80A to 120A resulted in 0.672 and 1.022 kJ/mm input energy into the base material respectively. The signal collecting lens was focused on the base material where the tip of the welding electrode was directly above. Focusing optics were connected to the spectrometer for signal detection. Influence of the distant focusing locations were disregarded, since the decay of the signal in any trial spatial location was in many orders of magnitude than the used one and caused only in a background noise as resulting signal, hence didn't allow processing of the data. However, this information should be considered as a guideline for the further studies, that the detection of any elemental intensity lines without any external energy source (e.g., laser) should focus the optics where the welding arc hits the base material and pulling information from this specific location should be the main target.

Strong influence of the welding current on the detected signal was observed during the welding experiments. Increasing the welding current from 80A to 120A generated the difference in signal intensity counts. The detected peak signal intensity count of Fe I 373 nm line increased about one order of magnitude when the welding current was increased from 80A to 120A. However, this phenomenon was observed only for the matrix element iron. The alloying elements demonstrated different characteristic signal intensities between two different welding currents, however the general trend was an increase of the input signal counts with the increasing welding input energy (see Figure 5-7).

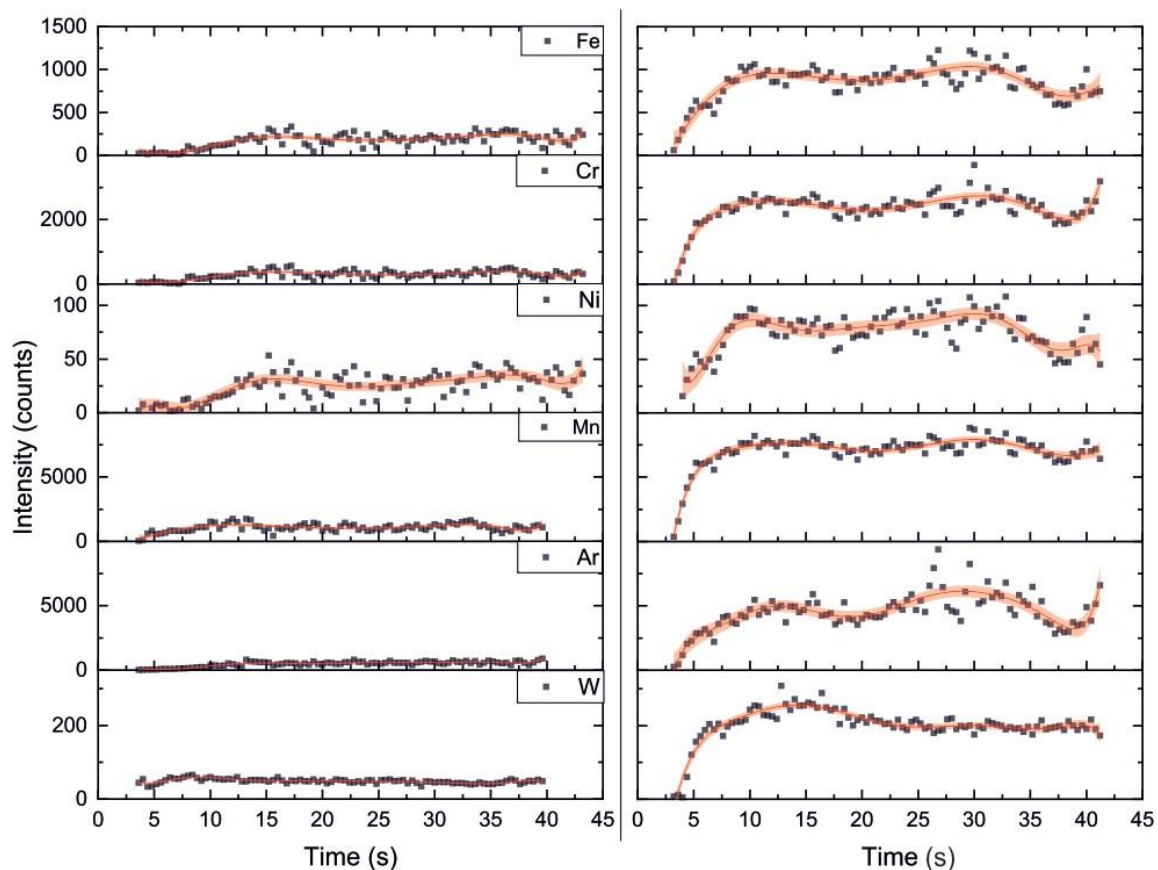


Figure 5-7: Recorded elemental intensity counts (Fe, Cr, Ni, Mn, Ar, W) during welding of 1.4404 base material. Left: 80A; Right: 120A. Welding Speed = 10 cm/min constant, Shielding gas flow rate = 16 L/min.

Figure 5-7 demonstrates the recorded intensity data points from both welding experiments mentioned above. Additional to the main alloying elements of Cr, Ni and Mn; Ar and W were also recorded to allow monitoring the potential effect of the shielding gas and the welding electrode emissions. Every element demonstrated different increasing rates with the increasing welding input energy, least in Ni resulting in lower signal-to-noise/background levels compared to the other monitored elements. This difference of increase for each element was cross-checked for any possible correlation between the ionization energies, physical melting points and electron transition potential between different levels of energies of the respective elements, however no significant correlation was observed between these physical attributes and the increasing rates of the welding current and incoming signal counts. Further data and investigations on the topic are required for deeper understanding of the subject.

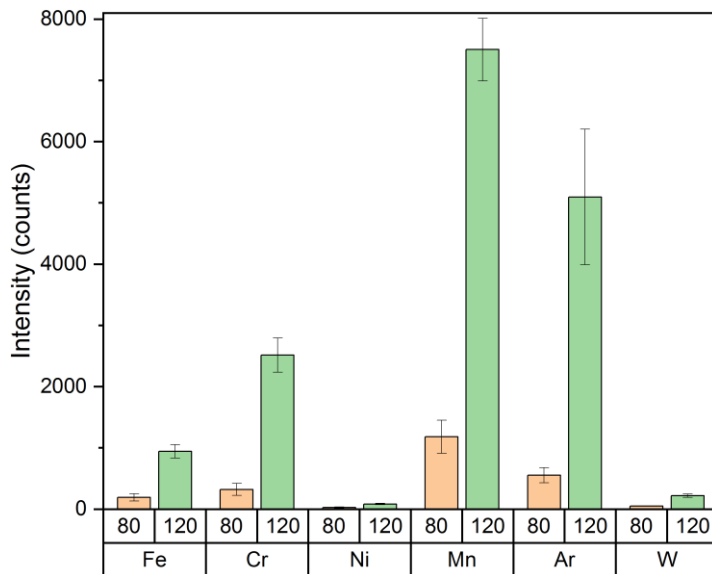


Figure 5-8: Average intensity counts between time interval 10-35s.

The different levels of incoming signal increase between the two welding currents, this was demonstrated in Figure 5-8. For this analysis, the average time interval from 10th second till 35th second of the welding process was selected where the signal mainly demonstrated a plateau characteristic and remained stable. Main reason for this selection was to disregard the influence from the start of the welding arc and the end of the welding process and get representative data for analysis.

The highest resolvable signal count was observed for the element Mn for both welding currents and followed by Cr. Hence the increase of the signal intensity counts were about eight times higher for both elements between 80A to 120A.

These demonstrated increase in the signal count are however not a result of a local chemical compositions increase or change, hence such drastic increase of any element in the molten metal in any stage of the bead-on-plate welding process is not expected to happen, since there are no drastic influencing external factors. On the contrary, this result indicates the requirement of a strong filtering and normalizing algorithm for further analysis and evaluation of the results from the spectroscopic information. More in depth information on the topic of spectroscopic analysis of the welding arc plasma and weld monitoring applications, readers are advised to refer the references[94, 126-128].

5.4.2 Influence of the welding parameters on the LIBS Signal

Before moving on to the further discussion on the results generated using LIBS, one must distinguish the difference between the terms “Intensity (count)” and “Relative -or normalized- Intensity (a.u.)” where this study often refers to. With “Intensity (count)”, the sole amount of the photons at a specific wavelength (elemental fingerprint) hitting the ICCD detector within the spectrometer is meant. With “Relative Intensity (a.u.)” the definition is slightly different

than the latter; when the intensity is relative, this means the recorded data has been processed in several ways: First the elemental signal counts were recorded, transformed into spectra -with background and noise removal from the spectra- and from the respective spectra, elemental peaks integrated, and their quantitative values below the peaks are calculated. Second, each quantitative value for an individual element was divided by the respective internal matrix element value in the data set undergoing the same algorithm described (Fe in this study due to stainless steel matrix) to minimize or eliminate the external (experimental) and internal (material) impacts on the experiment. Since two dimensionless values are divided to generate a filtered relative value, the units become arbitrary and only the sole amount of value become important. The most important of the main difference of counts vs. relative -normalized- intensity in this context: Counts cannot be used as a comparable information on the chemical composition where relative intensity in comparison within the same measurement or experiment can be used as a statement for the chemical composition change, amount or trend.

This study used the described normalization algorithm for all the results in the following sections. After the spectral processing, elemental line of the matrix material Fe I 373 nm was selected and used during the internal normalization. This eliminated the changing temperature effects on the sample material and its surface, mainly eliminating external temperature and experimental conditions and removing any matrix effects for further calculation of the quantified chemical compositions via calibration with reference samples. This type of spectral processing and internal normalization is considered as a typical step in optical emissions spectroscopy and a crucial step before quantifying the results and building a calibration model. For further information on the subject, readers should refer to [119, 129, 130].

This section investigates the welding current's influence on the incoming LIBS signal after applying the abovementioned spectral processing and normalization algorithms on stationary and moveable setups, namely spot and bead-on-plate welds respectively.

Welding current in stationary set-up

For the stationary welding process, main alloying elements Cr, Ni and Mn were monitored from different regions of the electromagnetic spectrum via LIBS. This was realized by focusing the target laser 5 mm next to the tip of the welding electrode on the sample surface. (See Figure 5-9)

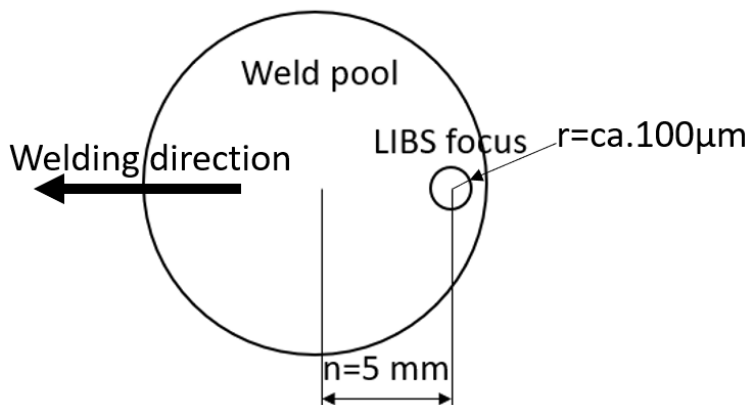


Figure 5-9: Schematic of the top view of the weld pool and LIBS focus point.

For chromium, the selected nine elemental lines were between 360-476nm range; for nickel also nine elemental lines between 232-357nm range and for manganese two elemental lines were at the 403nm range where manganese has triplet peaks in the electromagnetic spectrum. This study also generated information for further calibration processes since every elemental peak has a characteristic behavior in plasma. The reason for this selection was mainly due to their high relative intensity values, making data processing less prone to be influenced by external factors. Their detected peak positions also avoid overlapping with neighboring elemental lines and didn't demonstrate any self-absorption effects on the recorded spectra. Furthermore, the following metallurgical reasons can be listed for this selection: Fe is the main alloying element of the selected material. It is the matrix element of the alloying system. Cr and Ni are the main alloying elements containing ca. 18 wt% and 12 wt% respectively. Moreover, they are the main alloying elements of interest in this study associated with the hot cracking behavior of the weld metal. Lastly, chemical composition of Mn is known for varying during welding[97].

Further, all the selected emission lines have the same ionization states (all neutral -or state of "I"-, e.g., Cr I, Ni I, Fe I etc.), similar ionization energies, and similar upper energy levels, i.e., they show a similar response to the variations of the plasma temperature [131].

Figure 5-10 demonstrates the difference of relative intensities for the various Cr I lines and their percentage fraction through increasing welding current from 50A up to 160A. The main take from this experimental campaign is the difference between the calculated relative intensity values for any selected Cr line is max at 2% at lower welding currents. This value reduces to max. 1% at higher welding currents starting from 70A up to 160A. For Chromium, as the welding current increases, the incoming LIBS signal stability increases, and results become more repeatable, therefore the higher welding currents up to 160A (investigated range) give more stable results due to higher signal to noise/background ratio. In simpler words, higher welding currents produce more reliable data for LIBS analysis during welding and reducing measurement uncertainty.

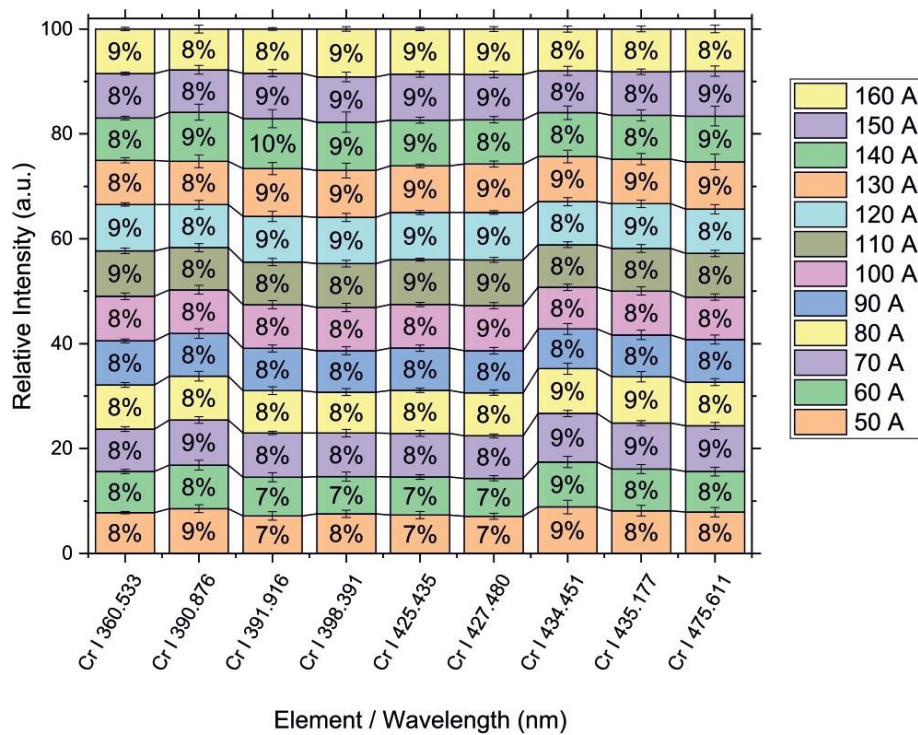


Figure 5-10: Relative intensities of the increasing welding currents vs. selected Cr I elemental lines. Average of the time interval 10-35s.

Same principle described in the previous paragraph was applied for the Ni I elemental lines. The results showed exact same trend for the selected Ni I lines between 232-357 nm range. The difference between the calculated relative intensity values for any selected Ni line is max at 2% at lower welding currents. This value reduces to max. 1% at higher welding currents starting from 70A up to 160A. For Nickel, as the welding current increase, the incoming LIBS signal stability increases.

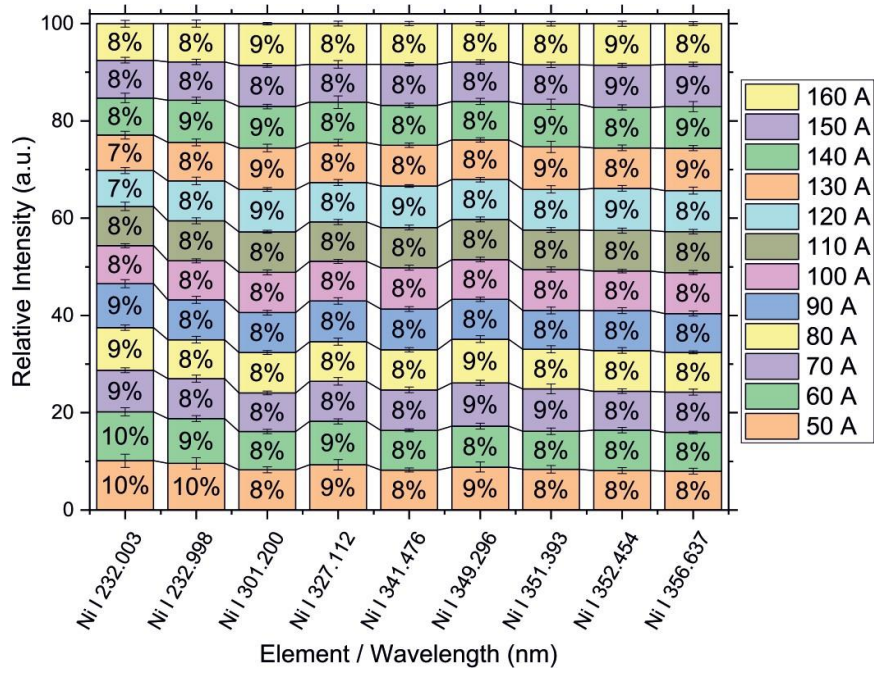


Figure 5-11: Relative intensities of the increasing welding currents vs. selected Ni I elemental lines. Average of the time interval 10-35s.

Same principle was applied for the Mn I elemental lines and the results showed more reliable trend for the selected Mn I lines. The difference between the calculated relative intensity values for any selected Mn line is max at 1% at lower welding currents. This value remains about at 1% at any selected welding current, highest repeatability at the highest selected welding current of 160A. For Mn, as the welding current increase, the incoming LIBS signal stability increases, and results become more repeatable, therefore the higher welding currents up to 160A provide more stable results due to higher signal to noise/background ratio and consequently reducing the measurement uncertainty.

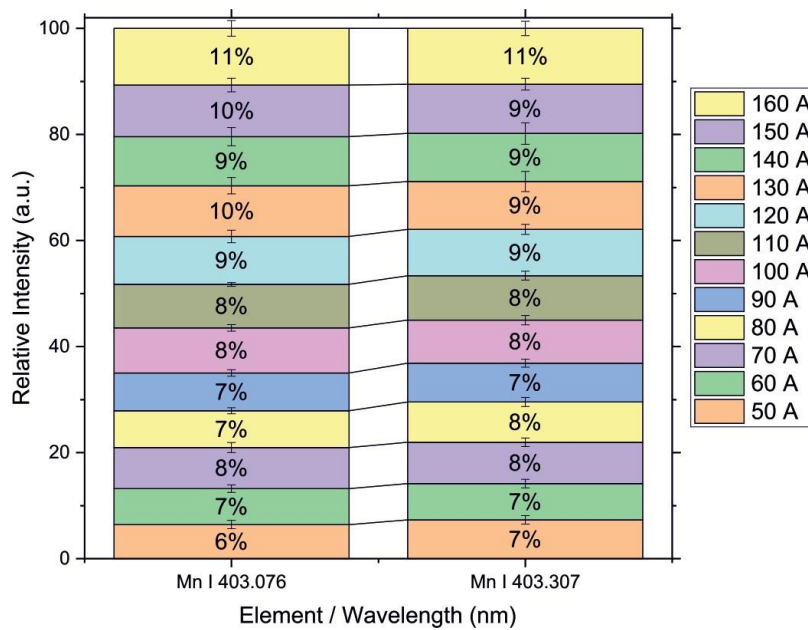


Figure 5-12: Relative intensities of the increasing welding currents vs. selected Mn I elemental lines. Average of the time interval 10-35s.

In order to validate the in situ measured LIBS data, the post-weld LIBS measurements were performed on the spot welds on varying distance to the welding arc. Same normalization algorithms were employed, and the normalized intensities compared against the spatial location on the finished spot welds with four different welding currents: 80A, 100A, 130A, 160A.

Spatial location of the LIBS focus point

In situ LIBS measurements were conducted during stationary welding on various locations to establish the effect of the measurement location on the normalized intensities. Therefore, min of 2 mm from the welding electrode tip was selected as starting point and the experiments were repeated under same conditions.

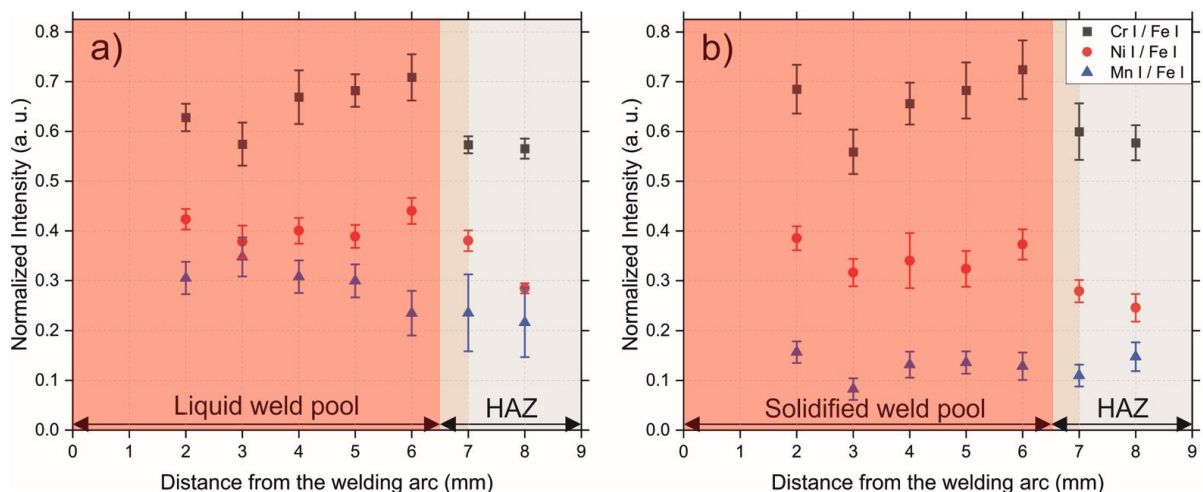


Figure 5-13: Spatially resolved (relative to the welding arc) relative -normalized- intensities of Cr I, Ni I and Mn I. a) recorded during welding: 0–14.4 s, b) After solidification: 73.8–91.8 s. Welding processes were performed at 160 A.[97]

Figure 5-13 shows the relative intensities for Cr, Ni and Mn recorded at differentiating positions on the base metal a) during welding and b) after solidification. There is no significant difference by comparing these two situations regarding the Cr and Ni intensities. Further, the values are generally lower at the HAZ compared to the weld pool for Cr and Ni in both situations. A different trend can be observed comparing the Mn normalized intensities for both situations. The values for Mn measured on the weld pool during welding (Figure 5-13a) are higher approx. factor of two than the ones measured after solidification (Figure 5-13b). It can be perceived by only looking at Figure 5-13a that the Mn demonstrates relatively higher chemical composition locally inside the weld pool compared to the HAZ. However, it is known from the literature [132-134] that Mn vaporizes during welding. This effect can be seen in Figure 5-13a by following the spatial distribution of the normalized intensities for Mn I emission line. Comparing the Mn relative intensities of the liquid weld pool during welding (Figure 5-13a) and the solidified weld pool after welding (Figure 5-13b) can reveal more details. In the latter one, a drastic decay of the Mn normalized intensities can be seen compared to the values in Figure 5-13a. It should be highlighted that the calculated values in Figure 5-13b indicate the measurements made in the last 18 seconds of the experiment, i.e., the weld is at this stage solidified and cooled down. Much of the condensed layer of Mn on the sample surface is also either removed or being removed by the laser shots. Such a difference does not manifest itself for Cr and Ni between the two situations[97].

After comparing the normalized intensities for $x = 2$ and $x = 3$ mm between both stages of the experiment, it can be assumed that chemical compositions of Cr and Ni vary locally in the weld pool. A metal vapor transportation model was proposed by Tashiro, et al. [133], hence they numerically and experimentally examined different regions of the welding arc temperatures and respective vapor pressures above the weld pool of pure iron. They validated their model by experimenting on the fumes collected during the welding process. Their conclusion was that the metal vapor from the weld pool escapes with the (welding) plasma arc flow from the bottom side of the arc column out to the atmosphere, cooling down and consequently condensing on the surface. Tanaka, et al. [135] demonstrated large amounts of Cr and Mn vapor exist in the welding arc plasma compared to the Fe vapor. Additionally, they noted that some amounts of Mn can evaporate due to its lower boiling point. Furthermore, Mn vapor from the weld pool surface could mix in the (welding) arc plasma through a convective circulation flow in the arc, which results in higher Mn and Cr compositions at the weld center[97].

These results indicate that LIBS is not only detecting the signal generated from the laser-induced plasma on the liquid metal surface but also detecting the signal from the vaporized elements on the optical path above the weld pool during welding. This effect is more present

for the Mn I emission line due to the physical properties of the Manganese -e.g., lower boiling point-. The final chemical composition of the solidified weld is not homogeneously distributed after the solidification is complete i.e., Cr and Ni tend to present the lowest concentrations in the HAZ[97].

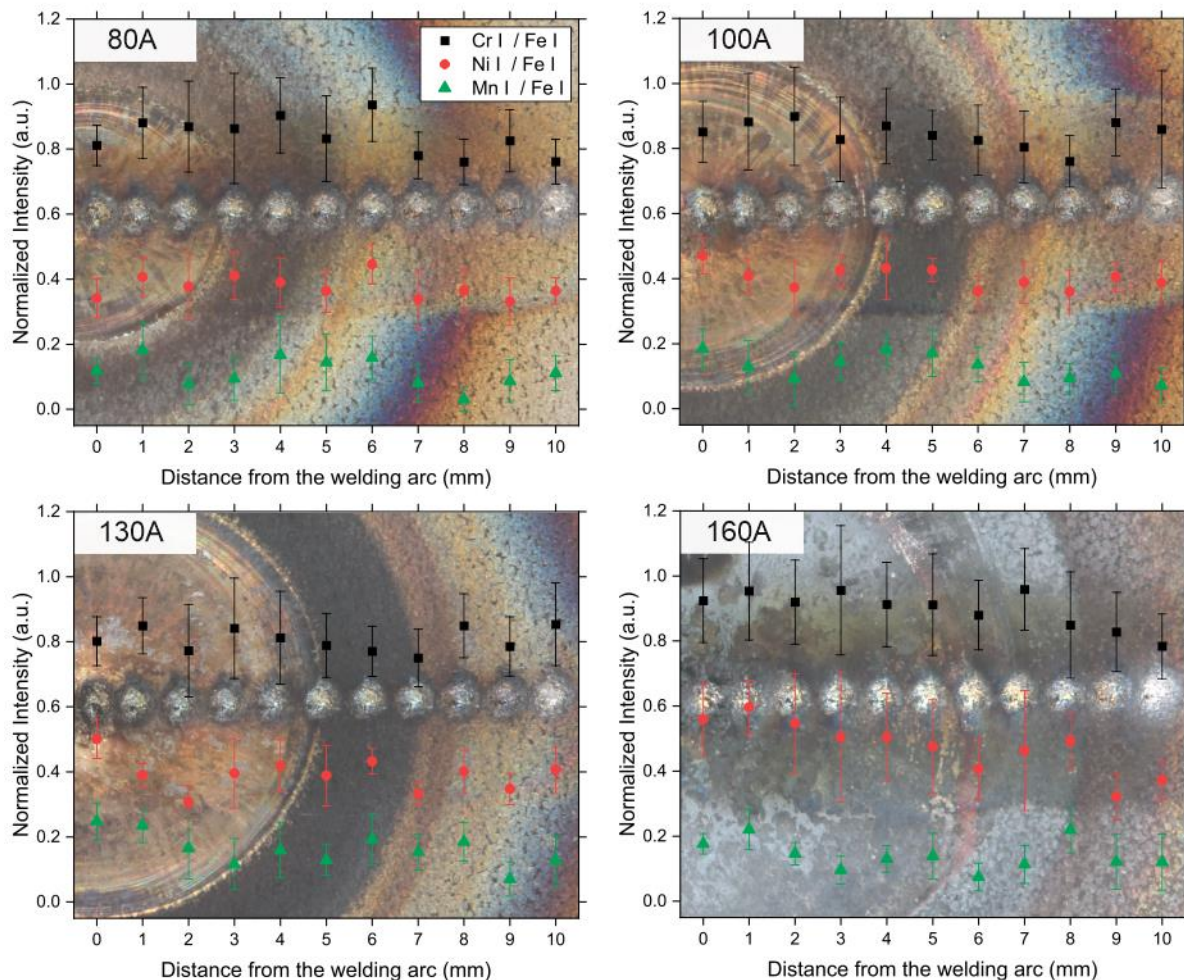


Figure 5-14: Post-weld spatially resolved normalized intensities of Cr I, Ni I and Mn I for different welding currents. LIBS measurements were conducted with 0.5 μ s delay time and 20 μ s gate width. The graphs are superimposed over photos of the respective spot weldments and the white spots are the respective LIBS measurement points.[97]

Post-weld investigations were performed to determine the correlation of the elemental distributions on the solidified weld spots with the online LIBS monitored welding experiments. Four selected weld spots were investigated from the welding currents between 80 A and 160 A (Figure 5-14). Normalized -relative- intensities were used to correlate the results to the local distributions of the alloying elements. 80 A and 100 A were the lowest welding current settings under investigation and showed no recognizable trend over the observed measurement points from the weld center towards HAZ. Cr I remained in a relatively stable at ca. 0.8 range from the weld center towards HAZ regardless of the welding current. Mn I and Ni I showed

the highest normalized intensity values at the weld center ($x = 0$ mm) hinting at an accumulation of the mentioned elements in the weld center at 130A and 160A. However, at 160A the weld spot grew relatively larger than the previous settings. Moreover, Ni showed a decreasing trend of normalized intensities from the weld center towards HAZ at 160A. Tanaka, et al. [135] had examined stainless steel welds via imaging spectroscopy and communicated that metal vapor includes several layers composed of metal atoms and ions; hence, where the metal vapor condenses could depend on different physical properties depending on the element e.g. ionization energy. Similarly, Park, et al. [136] suggested that different vapor pressures and vaporization rates of metals influence the distribution of the metal vapors above the weld surface. Their numerical simulations showed that Cr and Mn have accumulated and present higher mole fractions in the weld center. The post-weld LIBS assessment in this study validates the findings from the online LIBS monitored welding experiments; increasing the welding current results in larger volumes of weld spots and accumulation of Ni and Mn towards the weld center becomes more distinctive. This finding is in good correlation with the findings and simulations from Tanaka, et al. [135] and Park, et al. [136].

Welding current and speed in bead-on-plate set-up

To determine the influence of the welding current and welding speed on the detected LIBS signal, same principal was applied and varying experimental conditions and the outcome was compared respectively on different base materials.

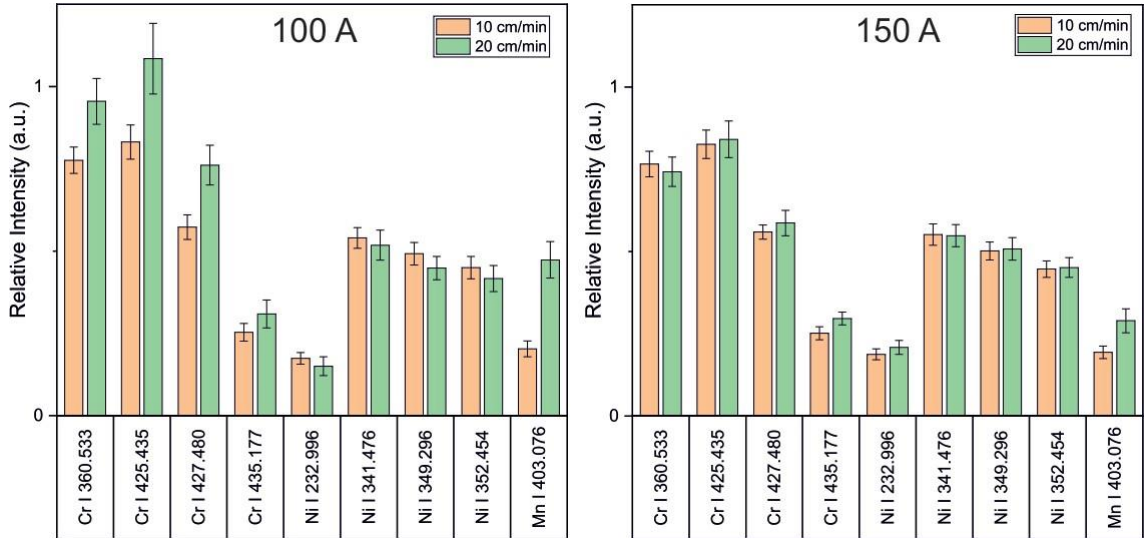


Figure 5-15: Bead-on-plate welding of 1.4435/b.2 base material with 4mm plate thickness. Left: 100A @10cm/min and 20cm/min; Right: 150A @10cm/min and 20cm/min. Constant shielding Ar gas flow rate 16 L/min. Values from the average of the time interval 10-35s.

For the base material 1.4435/b.2, the relative intensities of five Cr I, four Ni I and one Mn I lines were selected, processed and analyzed. Figure 5-15 summarizes this analysis. The calculated intensity values among all these three elements demonstrated similar values at 10

cm/min regardless of the welding current. During the bead-on-weld type of setup, no dramatic change of the chemical composition is expected and this result is in good correlation with the expected outcome.

As the welding speed is used at 20 cm/min, Cr demonstrated higher relative intensity values between 360-427nm band at 100A welding current and similarly Mn as well. This outcome is in good correlation with the elemental burn-off phenomenon, which is covered in the following Section 6.2. Principally, the lower the welding speed, higher the input energy; resulting in higher elemental burn-off from the molten weld pool. At slower welding speeds, the elemental intensity values are lower due to higher burn off from the surface of the base material.

As the welding current was used in 150A, this effect becomes less significant due to larger weld pool volume and higher speed of molten metal convection in the weld pool. As the convection speed of the molten metal in the weld pool gets faster, this generates a more homogeneous structure in smaller spatial resolution of the weld pool and the detection of elemental lines become more stable. In other words, at higher welding currents the effect of the welding speed becomes less significant or can eventually be disregarded for the examined material.

Figure 5-16 demonstrates the similar principal for the base material 1.4565. The reason for this repetition experiment to observe the same conditions for a material which has significantly higher Cr and Ni values compared to the latter one (1.4435). The individual chemical compositions of the used materials can be seen in Table 8 in Chapter 5.

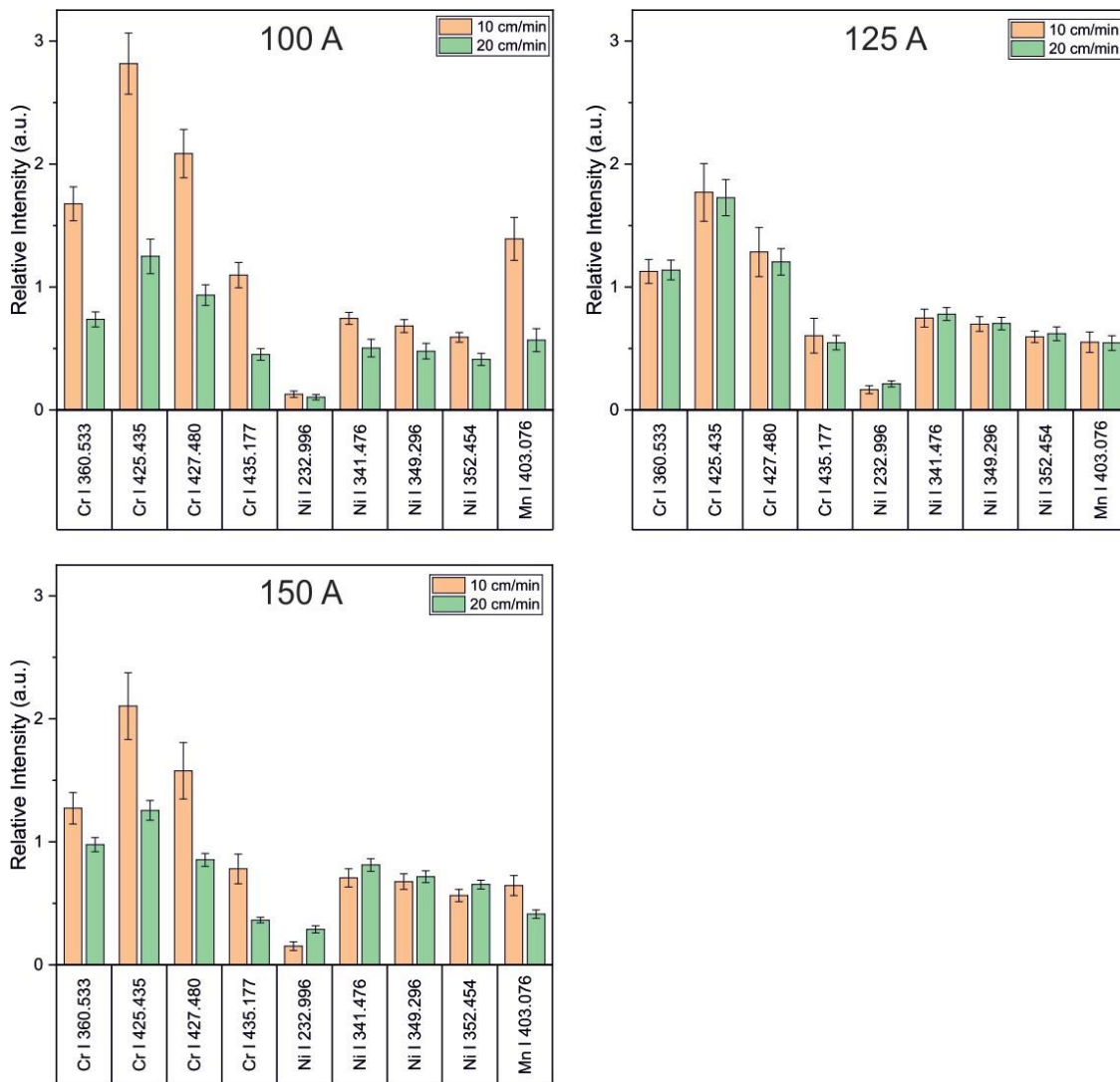


Figure 5-16: Bead-on-plate welding of 1.4565 base material with 6mm plate thickness. Left: 100A @10cm/min and 20cm/min; Right: 125A @10cm/min and 20cm/min; Bottom: 150A @10cm/min and 20cm/min. Constant shielding Ar gas flow rate 16 L/min. Values from the average of the time interval 10-35s.

In Figure 5-16, three different welding currents (100A, 125A and 150A) and two welding speeds (10 cm/min and 20 cm/min) were used and compared in respect to the relative intensities of the Cr, Ni and Mn lines. The base material 1.4565 has approx. 6wt% higher Cr, 5wt% Ni and 4wt%Mn higher than 1.4435/b.2 material. There is a qualitative difference of relative intensities when the values between Figure 5-15 and Figure 5-16 are compared. Furthermore, the calculated values of these elements in general show higher values for the base material 1.4565, which directly correlates with the higher amount of the chemical composition of this base material. In other words, the LIBS system is capable of detecting the elemental composition changes between two different materials during welding.

Another key finding from this analysis is the lower welding speed resulted in much higher

relative intensity values for Cr, especially at 100A and 150A. All in all, alloying element Ni showed to be least affected of these three elements through the experimental conditions, which is in good correlation with the highest physical boiling point of this element, therefore, to be the last one of these three to be affected from temperature and burn off conditions.

From the selected experimental conditions, the base material 1.4565 showed the highest stability among changing welding speed at 125A. However, this result does not correlate with the latter experimented material and in general, the LIBS system delivered higher reliable results at higher welding current settings. The individual effect of the differentiating welding arc currents and their direct influence on the elemental composition inside the welding arc plasma (in the plasma vapor) must be further investigated but not in scope of this study.

Shielding gas flow rates

In this part of the study, the effect of the shielding gas flow rate was put under investigation regarding the detected LIBS signal for Cr, Ni and Mn alloying elements. For this, constant 16L/min and 8L/min constant shielding Ar gas flow rates were chosen and implemented. The base material 1.4435/b.2 was used for these trials. Figure 5-17 demonstrates these experimental results for this investigation. For this investigation, same elemental lines for Cr, Ni and Mn were analyzed. The relative intensities between 8 and 16L/min did not show a significant trend in between, therefore the effect of the shielding gas flow rates was considered as negligible in this study.

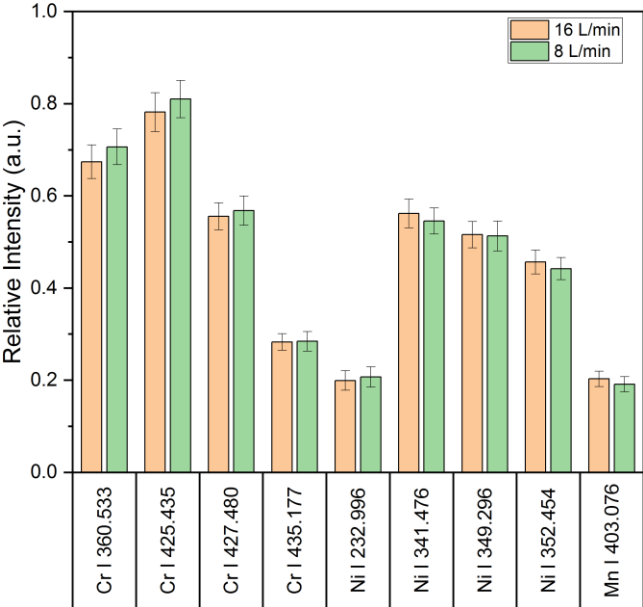


Figure 5-17: Bead-on-plate welding of 1.4435 base material with 4mm plate thickness. Welding arc current=100A @10cm/min Shielding Ar gas flow rate dropped from 16 L/min to 8L/min. Values averaged from the welding process.

5.4.3 In situ detection of filler material addition during welding

This section examines the effect of external element introduction into the molten weld pool during the welding process. This experimental process was monitored using the LIBS system and the observations of local changes of the chemical compositions were recorded and documented. For this purpose, an artificial experiment was designed to demonstrate the capability of the measurement system. The following section discusses the effect of addition of the copper filler wire, which only contributes from technical point of view, but not from scientific point of view.

Copper filler-wire

This section used the 1.4565 base material at varying welding process parameters. Each of the experiments' parameters are given in the individual respective figures. To assess the sole effect on the intensity counts, both monitoring graphs are plotted with "counts" and "relative intensity" values. To demonstrate the capability of the system, a copper-based filler wire (diameter = 2.5mm) material was chosen with intention, to introduce an element which was not present in the base material. Additionally, dissimilar materials would generate -principally- cracks due to the lower melting point of the intermetallic phases and consequent thermal stresses due to dissimilar material properties (between iron and copper). This would create a good case study to investigate the system capabilities as well as dissimilar material interface and the respective chemical compositions. The objective was achieved at the end of this experimental campaign and the results are displayed in the following pages. The copper wire was fed into the welding arc plasma manually where the welding process was automated via movable stage. For the data analysis, two copper elemental lines Cu I at 222 and 327nm were selected, where the typical Fe I line at 373 nm was used for monitoring and data normalization process.

Completed welds were investigated using X-ray radiography to detect the cracking behavior in the completed weld bead. Radiographs are shown with the completed welds in top view figures.

Figure 5-18 demonstrates the recorded results from the first trial of the experimental campaign. Figure 5-19 shows the top view of the completed weld joint along with the radiograph of the completed weld, where the copper filler addition is visible and marked along with the welding direction and the exact location of the LIBS measurement spot on the weld pool. The radiograph shows the initial cracks starting with the material addition as well as the end crater region. No visible cracks are detectable with the radiograph in the dissimilar material (copper) added weld. For both intensity count values and the relative intensity values from the Figure 5-18, one can immediately recognize the abrupt increase of the Cu signal at the mid of the weld joint -halfway through the weld joint-. Due to the manual addition of the filler wire, a quantified result is not possible to produce from this experiment. However, this

result immediately proves the instant detection capability of the system during the welding process.

This experiment was taken as a reference for the further examinations and followed up with the following inspections methods: first the weld joint was cross-sectioned in four different regions -marked with "1, 2, 3, 4" in the Figure 5-18- to investigate base material and the crack propagation microstructure. Furthermore, the micrograph sample from location 3 from this experiment was inspected with the SEM EDX analysis and the results are also given in the following pages. This investigation conducted to detect any correlations of the dilution rate of the weld pool and any potential local changes chemical compositions and correlation with the intensity values from the recorded LIBS signal.

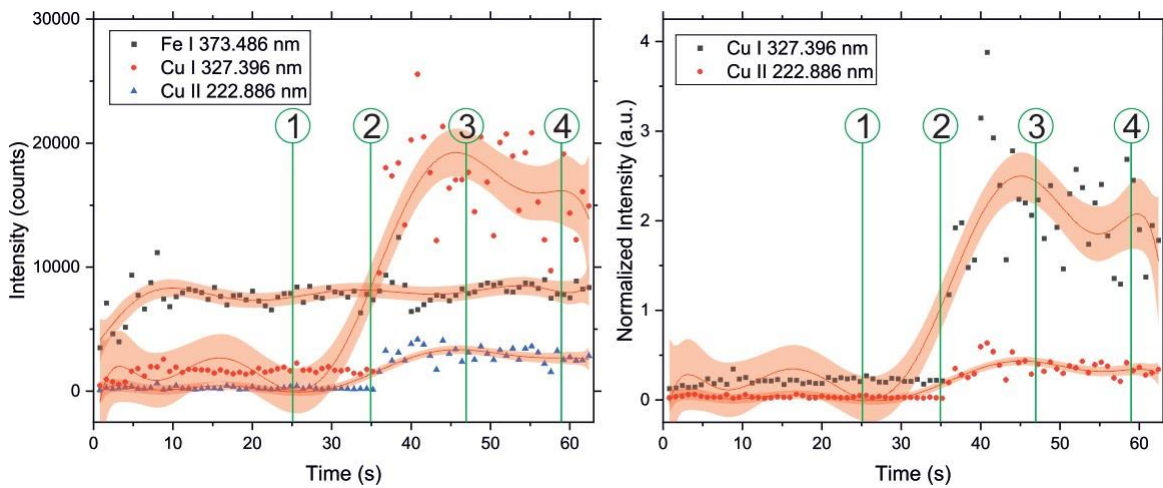
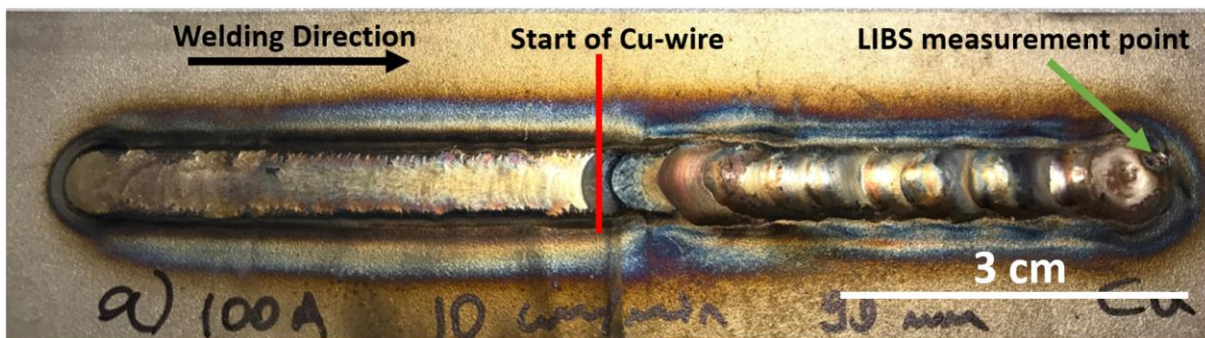


Figure 5-18: Welding arc current=100A @10cm/min; shielding Ar gas flow rate = 16 L/min. Micrograph positions are indicated in the corresponding position on the diagrams within the circled number. Weld bead length = 90mm; Cu filler addition @ 45 mm (mid-weld) / Cu Filler Material consumption: 29 mm Cu wire in 45/90 mm.



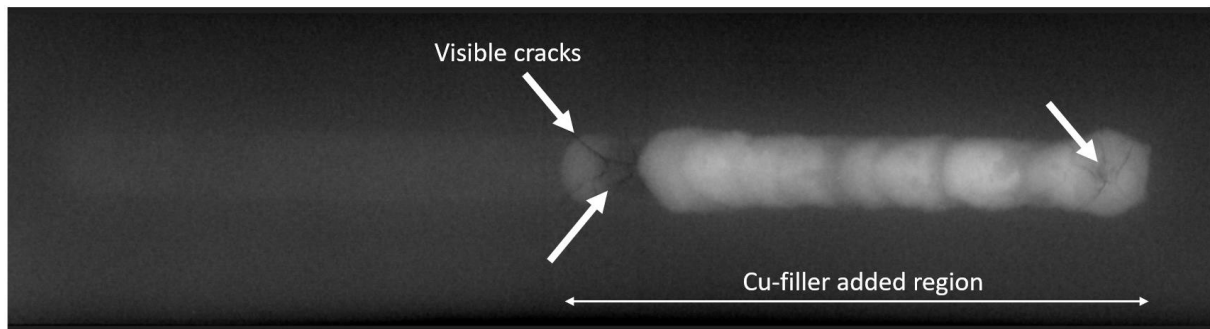


Figure 5-19: Top view of the completed weld bead (a) with Cu wire addition at 45mm. The radiograph of the completed weld is shown below the weld picture.

Figure 5-18 demonstrates the abrupt increase of the copper signal at the mid-range of the weld joint -approx. at 35th second of the experiment- for both intensity counts and relative intensities. This is the expected outcome of the in situ detection of the external element during welding experiment. After normalizing the copper values with the indicated Fe line at 373nm (Figure 5-18, right), the normalized intensities also show the same characteristic which for this experiment internally validates the result and the detection of the external element Cu.

The micrographs from the cross-sectioned samples show the different stages of the weld joint dilution and the clear interface between the base material and the filler copper wire material. The cracks are mostly starting at the filler-base material interface and in normal direction to the surface. This is a result of the low melting point intermetallic phases and the extreme thermal stress occurring due to different material properties, especially occurring at the copper-steel interface[137].

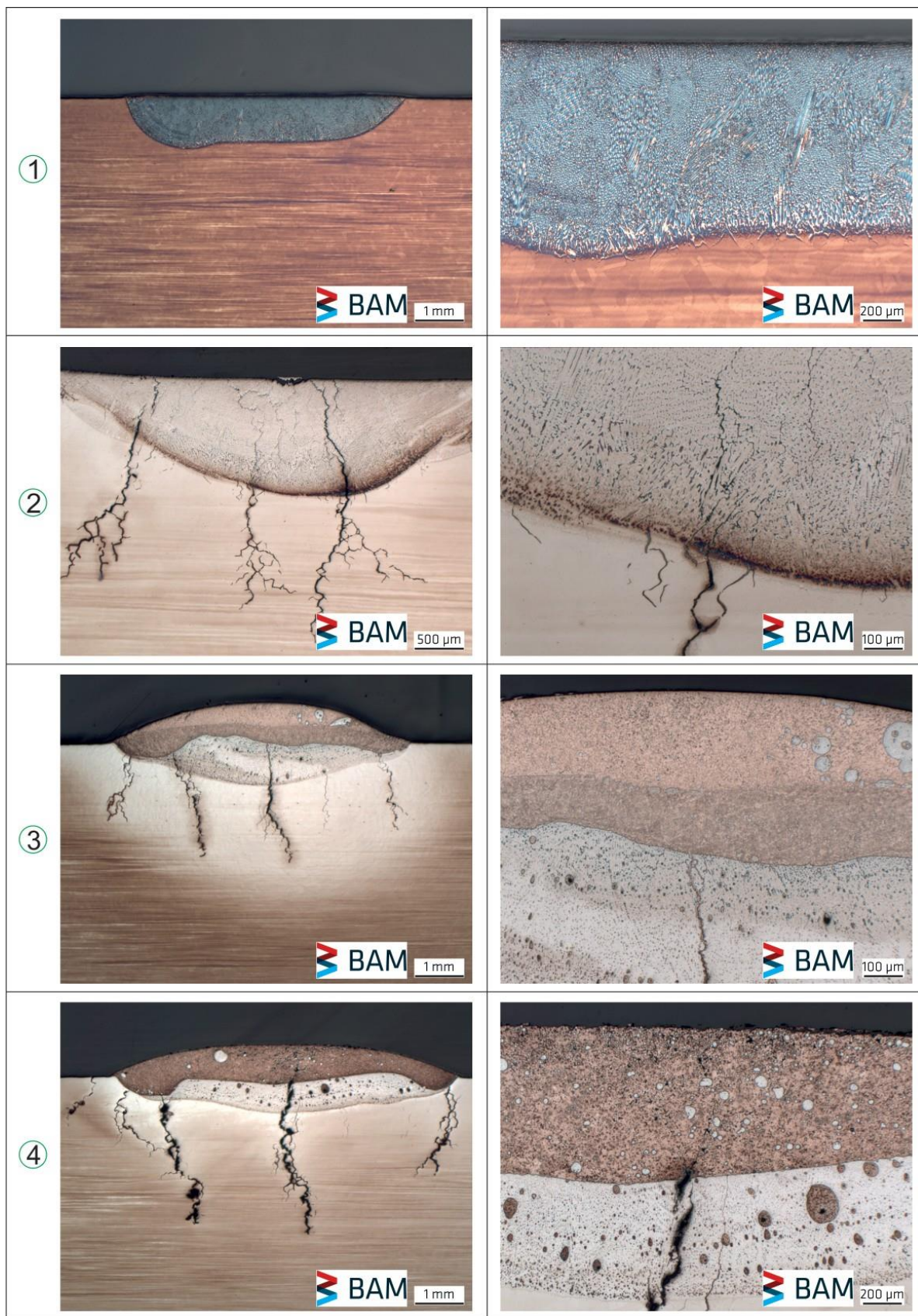


Figure 5-20: 100A, 10 cm/min. Micrograph positions are indicated in the corresponding position on the diagram within the circled number.

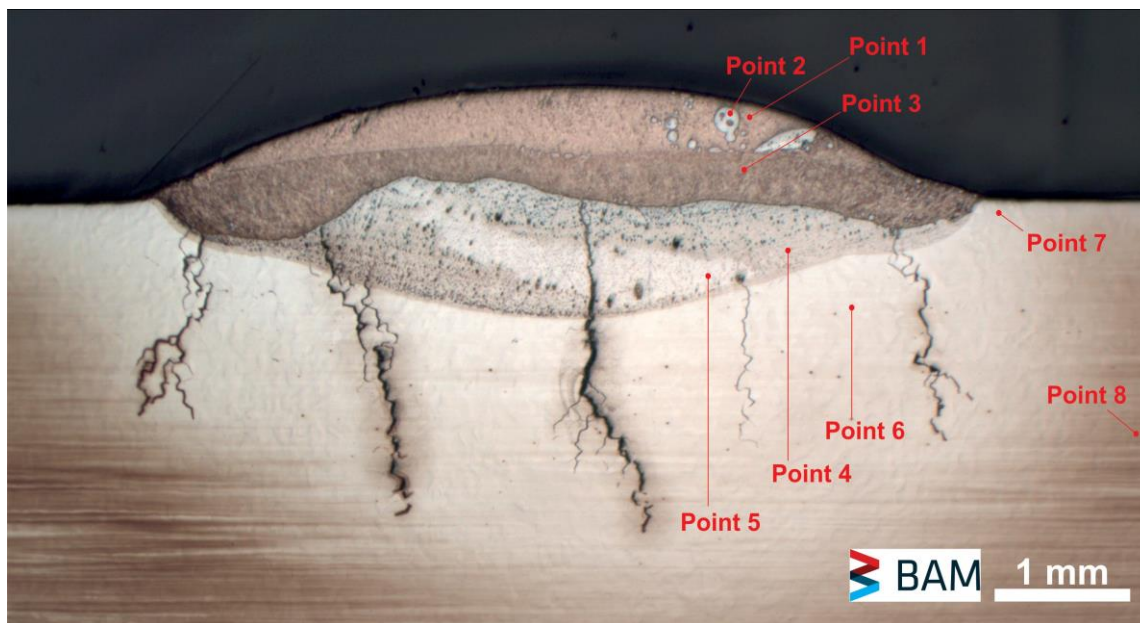


Figure 5-21: SEM-EDX analysis locations in Micrograph 3 from Figure 5-20.

Figure 5-21 shows the exact EDX measurement locations on the selected sample and

Table 12 demonstrates the EDX results. The measurement locations were selected due to the contrast difference detected on the micrograph and according to the points of interest. The closest measurement to the surface from Point 1 immediately validates the qualified result of the LIBS with high Cu relative intensities. At Point 2 the contrast of the micrograph is similar to the base material where the composition values also deviate, however still very similar to the base material especially regarding the alloying elements. The higher Cu amount via EDX measurement was observed at the surface area with 55wt% at Point 1 and 3. Point 4 measurement contains 10wt% Cu amount where the main alloying elements Cr and Ni are lower than the material data sheet. The hot cracks initiated mainly between the region of Point 3 and 4 where the Cu-Steel interface can be distinguished via the micrograph.

The EDX measurement validates the accumulation of Cu at the surface area of the weld joint. To have quantified wt% values via LIBS, respective calibration must be conducted with the system and requires further research. This experiment was conducted to validate the proof-of-principle concept of the external element detection and was a success in this sense.

Table 12: Chemical compositions of the marked positions from Figure 6.15 (SEM-EDX measurements).

Measurement	Si	Cr	Mn	Fe	Ni	Cu	Mo	Sn
1.4565 (data sheet)	0.2	24.3	5.6	47.9	17.5	-	4.5	-
Point 1	0.3	6.5	1.9	16.9	6.6	55.0	-	4.9
Point 2	0.3	21.9	2.6	39.8	11.9	13.5	5.5	1.0
Point 3	0.2	7.0	4.9	14.1	8.7	55.5	0.9	4.9
Point 4	0.4	22.9	3.3	41.1	12.6	10.0	5.0	0.8
Point 5	0.3	23.9	5.6	45.3	16.3	0.2	3.9	-
Point 6	0.3	23.7	6.1	45.1	16.3	0.6	4.2	-
Point 7	0.4	23.4	5.4	47.0	16.5	0.2	4.0	-
Point 8	0.4	23.7	5.7	44.9	16.0	0.1	4.0	-

Figure 5-22 demonstrates the repetition experiment of the previous weld joint and shows similar results, namely abrupt increase of the copper signal at the mid-range of the weld joint -approx. at 35th second of the experiment- for both intensity counts and relative intensities. After normalizing the copper values with the indicated Fe line at 373nm (Figure 5-22, right), the normalized intensities also show the same characteristic which for this experiment internally validates the result and the detection of the external element Cu. Here, one detail is important in comparison to Figure 5-18: The normalized intensities after the addition of the copper wire are about 5 times higher (approx. 10 for Cu I and 2.5 for Cu II) than the latter reported experiment. Reason for this outcome is qualitatively explained via the micrographs in the Figure 5-24.

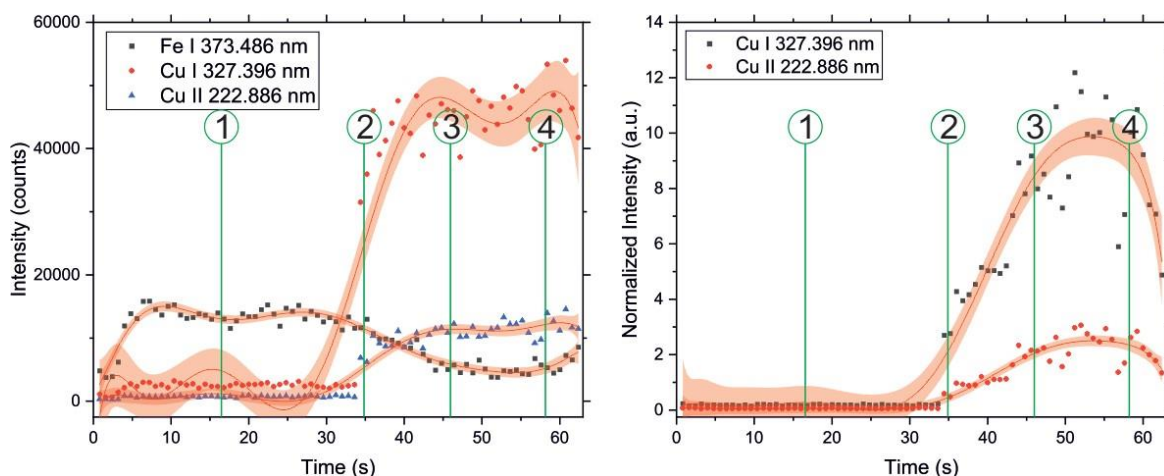


Figure 5-22: Welding arc current=100A @10cm/min; shielding Ar gas flow rate = 16 L/min. Micrograph positions are indicated in the corresponding position on the diagrams within the circled number. Weld bead length = 90mm; Cu filler addition @ 45 mm (mid-weld) / Cu Filler Material consumption: 55 mm Cu wire in 45/90 mm.

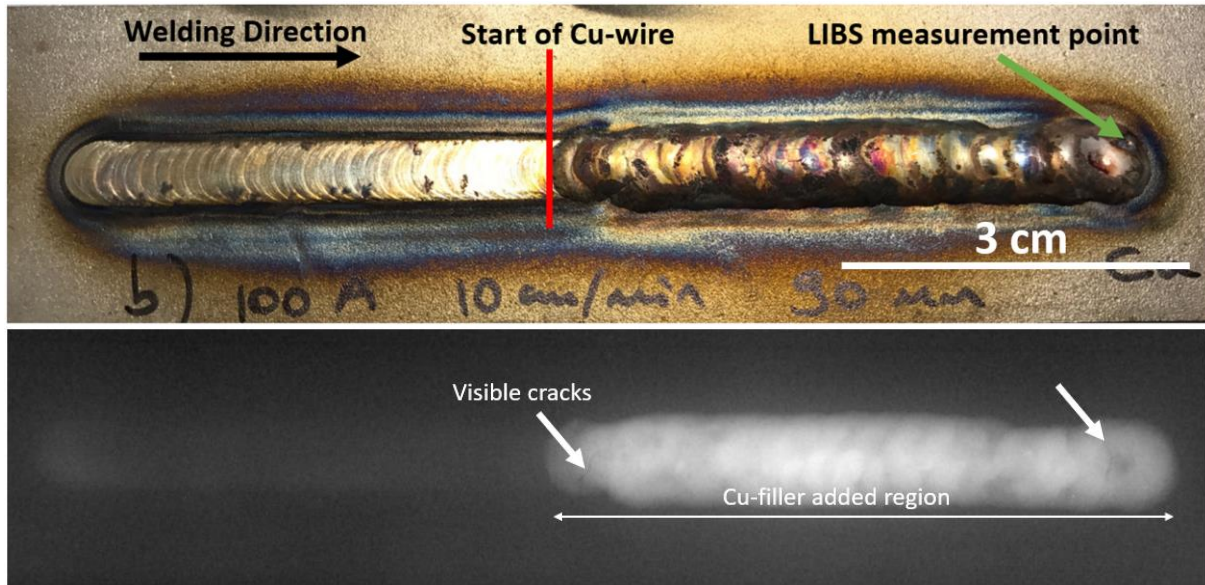


Figure 5-23: Top view of the completed weld bead (b) with Cu wire addition at 45mm. The radiograph of the completed weld is shown below the weld picture.

Figure 5-23 shows the completed weld from top view along with the radiograph of the weld complete weld bead. The cracks visible in the micrographs in Figure 5-24 from location 2 and 4 can be recognized in the radiograph.

The micrographs from the cross-sectioned samples in Figure 5-24 show the different stages of the weld joint dilution and the clear interface between the base material and the filler copper wire material. During this experiment, due to manual wire feeding conditions, the deposition of the copper wire had showed better weld quality also in cross-section micrographs. This can especially be seen in Figure 5-24/3 and 4 through the contrast of the weld joint. As the copper wire had better deposition on the surface and more homogeneous dilution, this resulted in approx. 5 times higher relative intensity values compared to the previous experiment under same conditions. This result again validates the capability of the LIBS system able to detect the qualitative changes of the chemical composition during welding, also non-ferrous material in this case.

The cracks in the material were observed to have originated at the interface between the filler and the base material, and they were oriented along the surface of the base material in a direction perpendicular to it. These cracks had an intergranular character (Figure 5-24/4 right)., which was likely due to the presence of low melting point intermetallic phases and the thermal stress that arose from the differences in material properties, particularly at the

interface between the copper and steel[137].

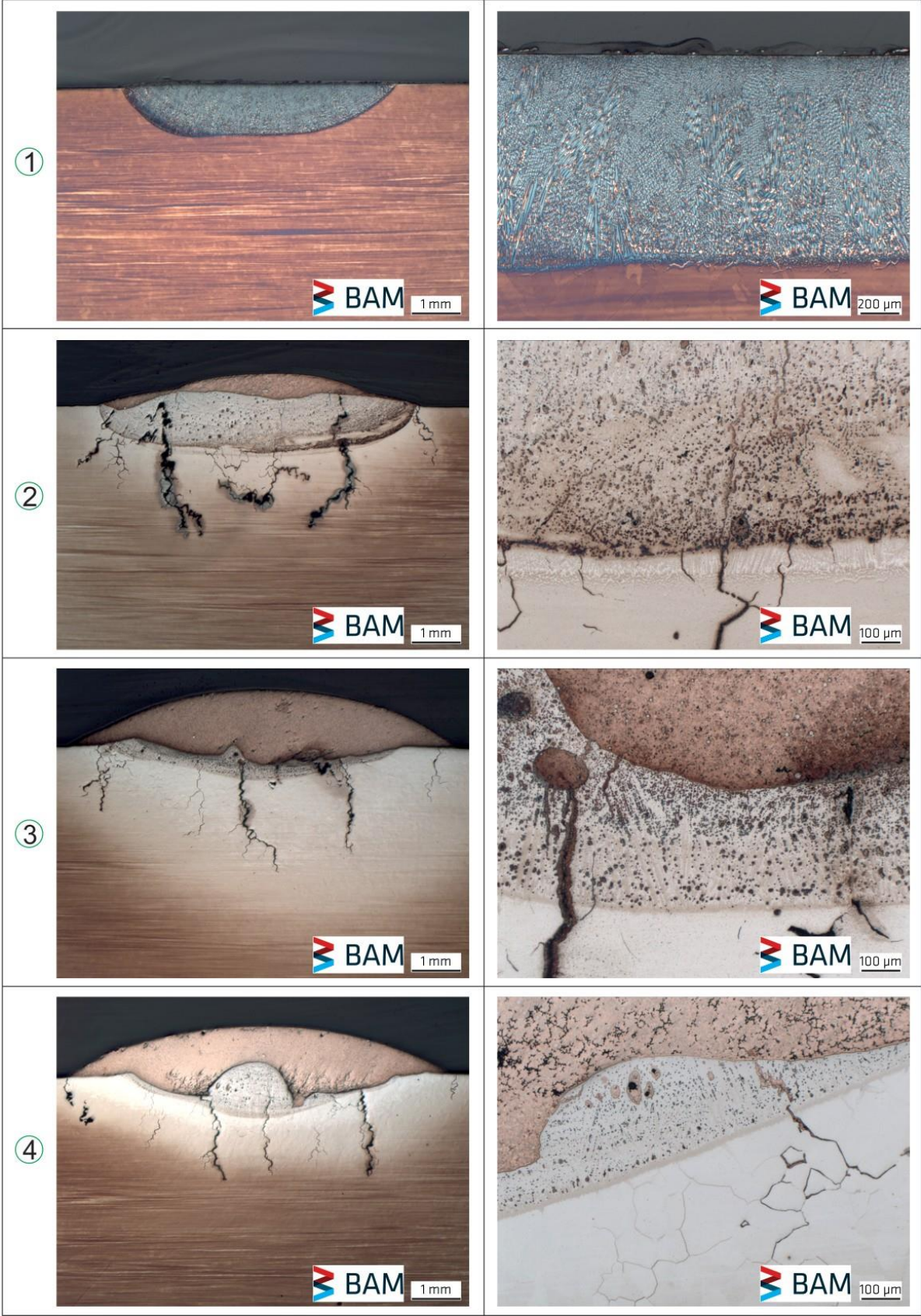


Figure 5-24: 100A, 10 cm/min. Micrograph positions are indicated in the corresponding

position on the diagram within the circled number.

Figure 5-25 demonstrates the repetition experiment of the copper wire trial at higher welding arc current, namely at 150A, to determine the effect of the arc current and the outcome of signal and the experimental influences. This experiment however showed very similar results, namely abrupt increase of the copper signal at the mid-range of the weld joint -approx. at 35th second of the experiment- for both intensity counts and relative intensities. After normalizing the copper values with the indicated Fe line at 373nm (Figure 5-25, right), the normalized intensities also show the same characteristic which for this experiment internally validates the result and the detection of the external element Cu. Here, the normalized intensities lie approx. at 2 and 0.5 a.u. for Cu I and Cu II lines respectively.

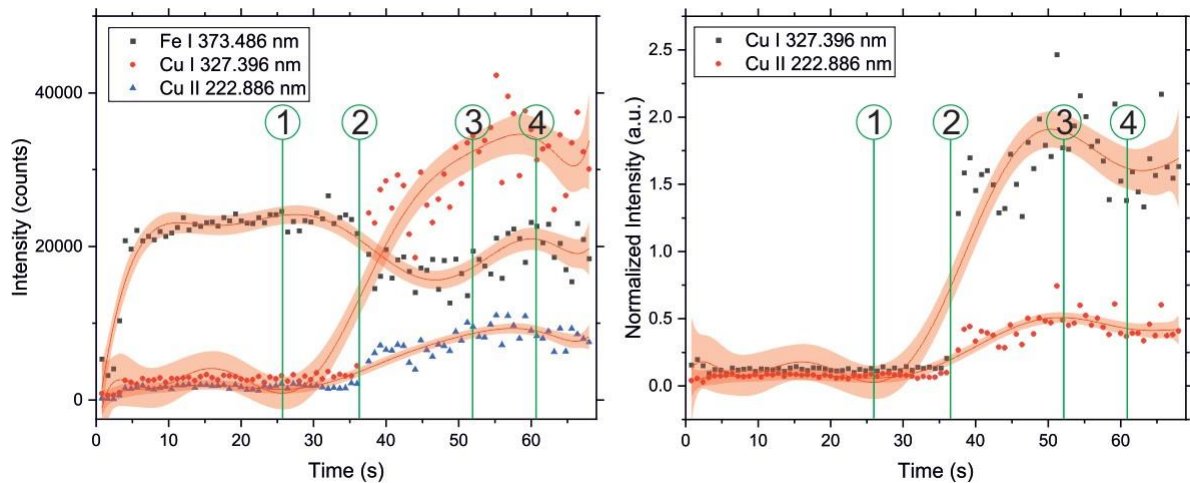


Figure 5-25: Welding arc current=150A @10cm/min; shielding Ar gas flow rate = 16 L/min. Micrograph positions are indicated in the corresponding position on the diagrams within the circled number. Weld bead length = 100mm; Cu filler addition @ 50 mm (mid-weld) / Cu Filler Material consumption: 43 mm Cu wire in 50/100 mm.

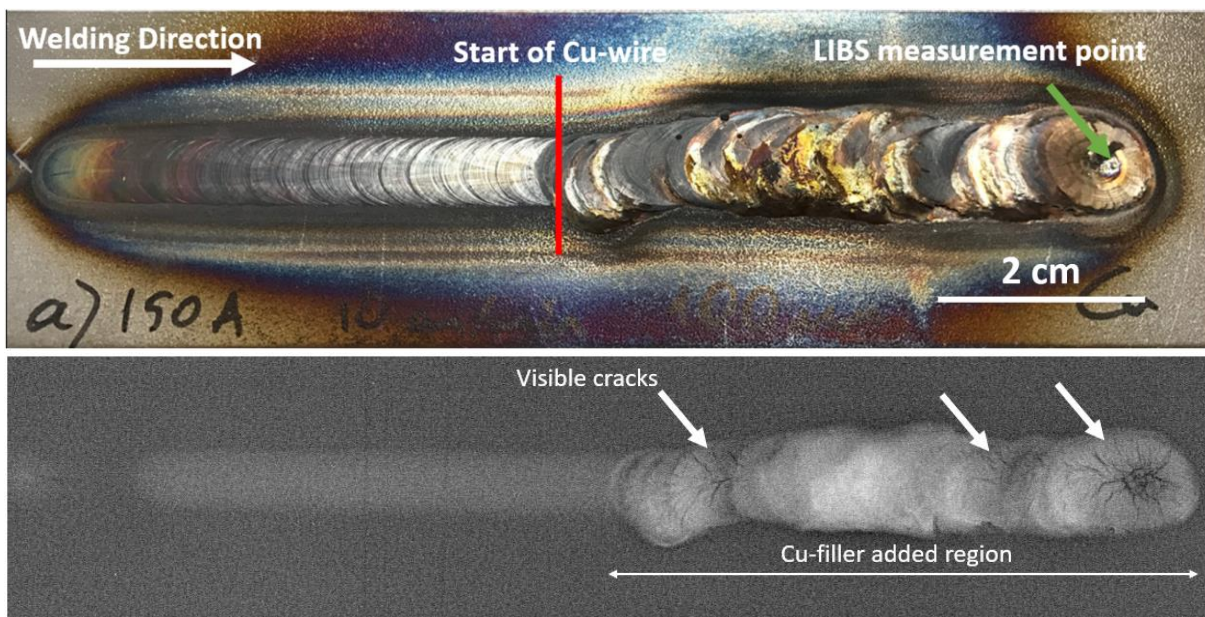


Figure 5-26: Top view of the completed weld bead (b) with Cu wire addition at 50mm. The radiograph of the completed weld is shown below the weld picture.

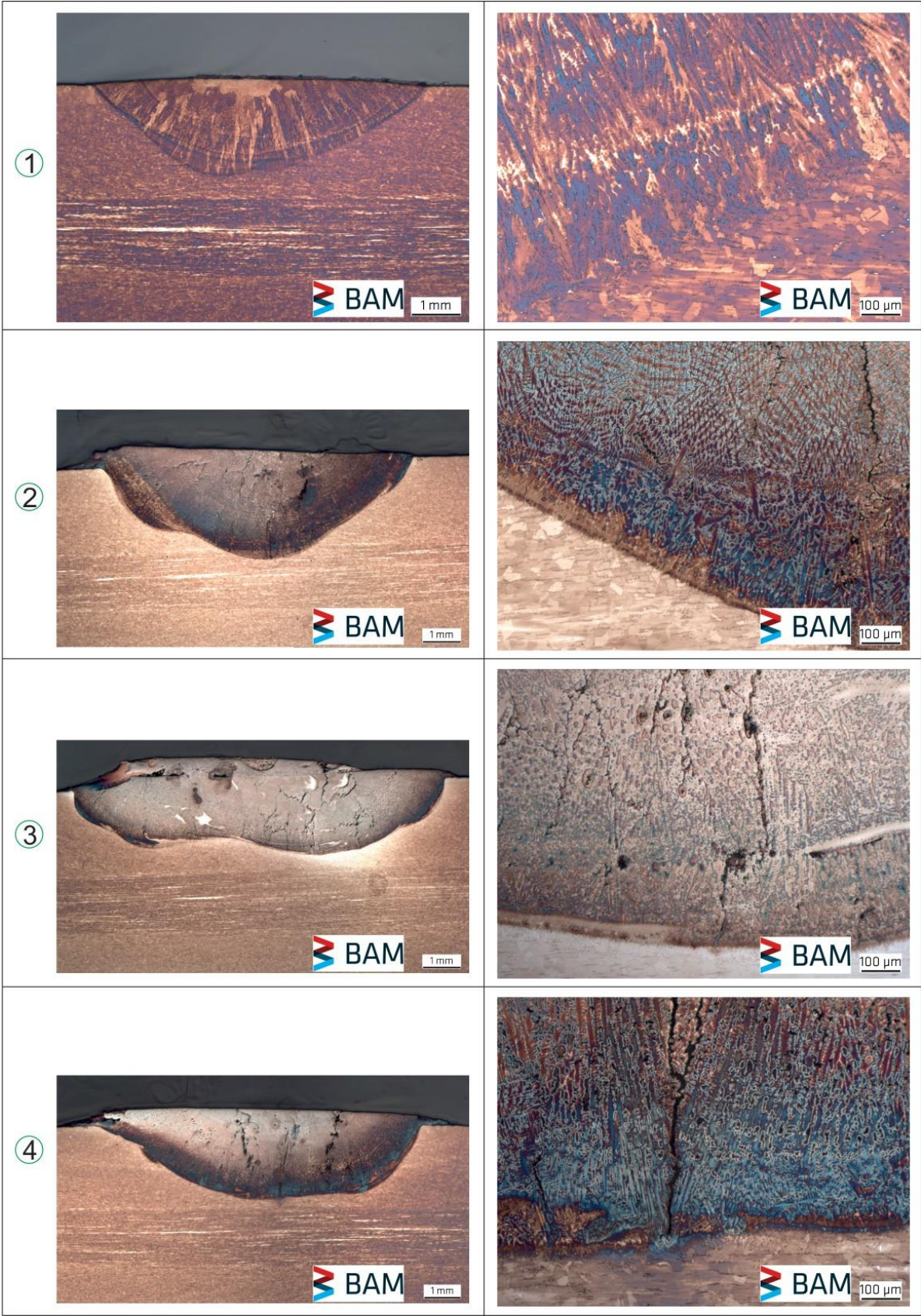


Figure 5-27: 150A, 10 cm/min. Micrograph positions are indicated in the corresponding position on the diagram within the circled number.

The micrographs from the cross-sectioned samples show the different stages of the weld joint dilution and the clear interface between the base material and the weld metal (Figure 5-27). At this welding current, manual feeding of the copper wire was debatably reduced the quality of the weld joint and resulted in uneven weld shapes and non-desired surface quality. However, the cracks were successfully propagated and the in situ LIBS measurements were conducted. Higher amount of welding arc current resulted in higher temperature of the molten weld pool, consequently higher speed of the convection of the molten metal, higher level of solubility and higher amount of dilution of the elements. This can be recognized by less contrast changes in the weld pool in the micrographs and visibility of the dendritic growth. Cracks were initiated along with the dendritic arms and mostly initiated among those with the solidification. This is an indicator of the hot crack formation due to the thermal stress during the solidification process[137]. However, since the LIBS system in this study detects the information from mainly the surface area of the weld pool, with the current data, it is not possible to validate the changes of the local composition changes in this scale e.g. at the dendritic arm space inside the weld pool. The future investigations on the topic can potentially solve this problem implementing machine learning data processing algorithms to calculate time and space resolved the complex chemical compositions among the solid-liquid interface and considering the complex mass transport and fluid flow properties in the molten weld pool during the solidification process.

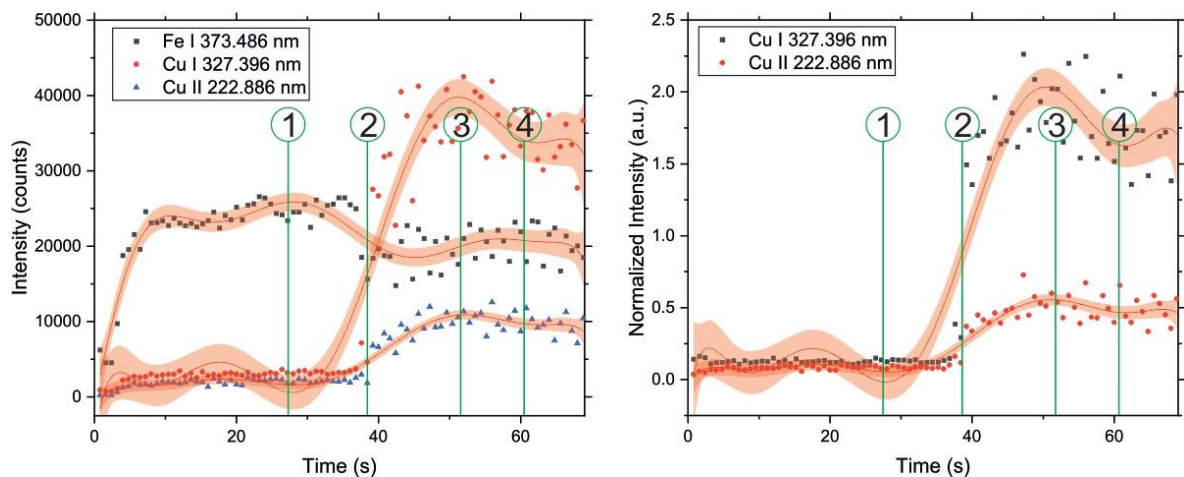


Figure 5-28: Welding arc current=150A @10cm/min; shielding Ar gas flow rate = 16 L/min. Micrograph positions are indicated in the corresponding position on the diagrams within the circled number. Weld bead length = 100mm; Cu filler addition @ 50 mm (mid-weld) / Cu Filler Material consumption: 50 mm Cu wire in 50/100 mm.

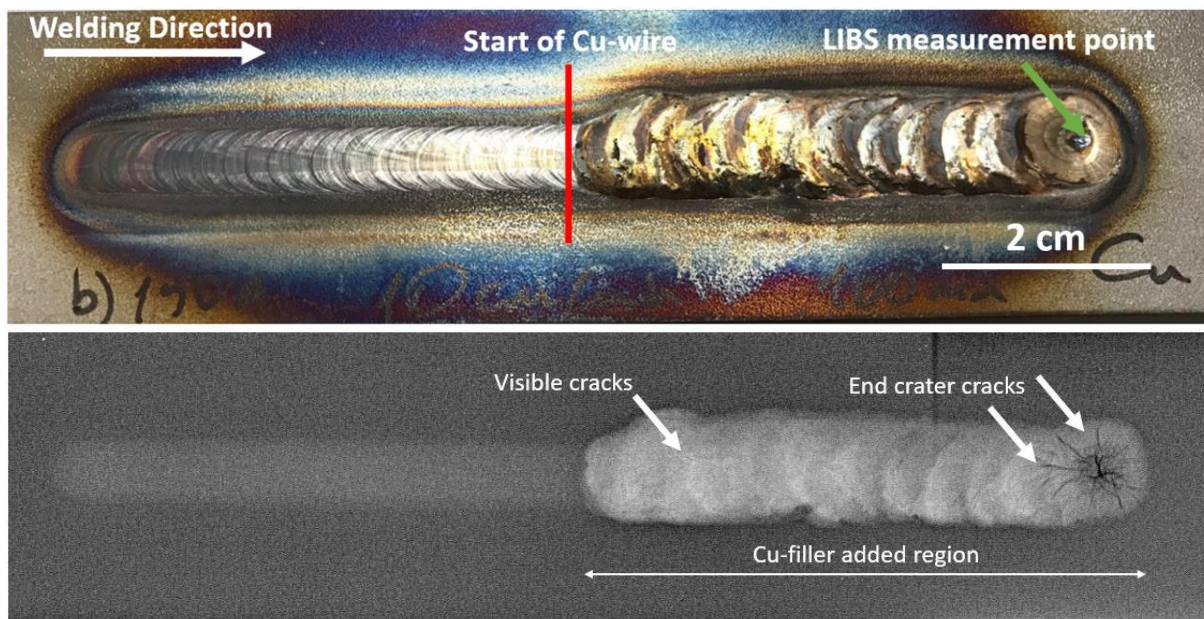


Figure 5-29: Top view of the completed weld bead (b) with Cu wire addition at 50mm. The radiograph of the completed weld is shown below the weld picture.

Figure 5-28 demonstrates the repetition the latter experiment of the copper wire trial at higher welding arc current. This experiment also showed very similar results to the previous one, namely abrupt increase of the copper signal at the mid-range of the weld joint -approx. at 35th second of the experiment- for both intensity counts and relative intensities. After normalizing the copper values with the indicated Fe line at 373nm (Figure 5-28, right), the normalized intensities also show the same characteristic which for this experiment internally validates the result and the detection of the external element Cu. Here, the normalized intensities also lie approx. at 2 and 0.5 for Cu I and Cu II lines respectively.

The micrographs from the cross-sectioned samples show the different stages of the weld joint dilution and the interface between the base material and the weld metal (Figure 5-30). At this welding current, manual feeding of the copper wire produced lower quality weld joint and resulted in uneven weld shapes and non-desired surface quality, similarly to the previous trial. However, the cracks were propagated and the in situ LIBS measurements were conducted. Increasing the welding arc current leads to a higher temperature of the weld pool, which in turn causes the molten metal to convect more quickly, increases the solubility of elements in the weld pool, and leads to more dilution of elements. This can be observed in microscopy images as a lack of contrast changes in the weld pool and the visibility of dendritic growth. Cracks were found to form within the weld pool, particularly along the dendritic arms and during solidification. This suggests that the formation of these cracks, known as hot cracks, is a result of thermal stress occurring during the solidification process.[137]. Similarly, it is impossible to extend the surface chemical composition information of the weld pool to the weld root at this stage of the study.

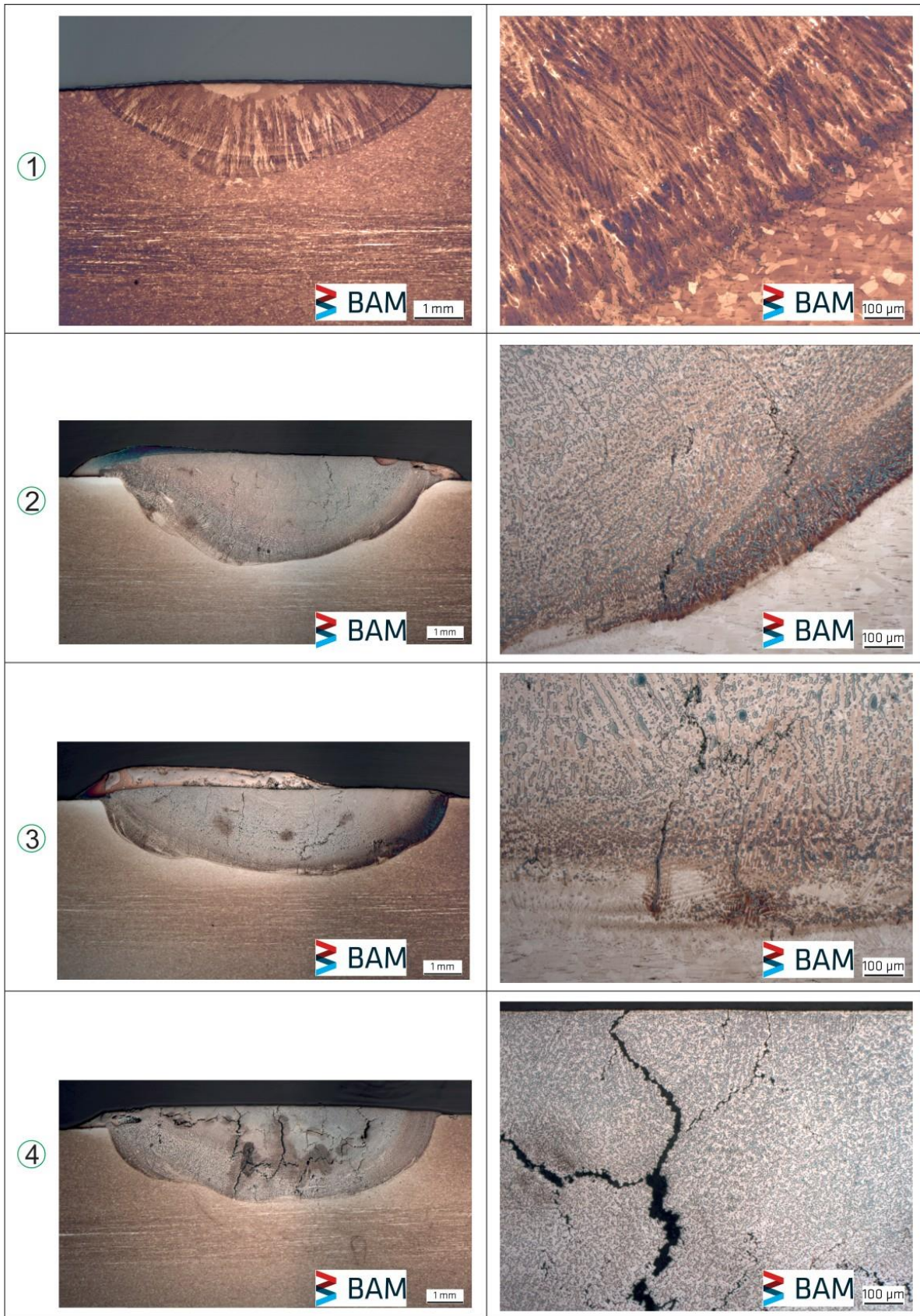


Figure 5-30: 150A, 10 cm/min. Micrograph positions are indicated in the corresponding position on the diagram within the circled number. Repetition experiment.

Chapter 6

6. Results and discussion

6.1 Monitoring the alloying elements and parameters

6.1.1 LIBS Parameter investigation and optimization

The main identifiers of the optical signal quality were discussed in Section 2.4., namely the Signal to background (S/B) and signal to noise (S/N) ratios. In this section, these two identifiers were further investigated and optimized with the two main physical detection parameters of “gate width” and “delay time” of the LIBS system.

This parameter study was conducted on the elemental lines of Fe, Cr, Ni and Mn as the main alloying elements on the base material 1.4435/b2 (See Table 8 for chemical composition). Initially, for each element, different characteristic lines were selected based on their applicability from the NIST atomic spectral database.

The following elemental lines in Table 13 were selected for further processing and the data analysis during the process implementation in the Section 6.3. The main reasons of the selection of these lines were due to their high relative intensity values. Their detected peak positions avoided overlapping with any other relevant elemental lines or signal intensity, hence they didn't show any self-absorption effects on the recorded spectra.

Table 13:List of the selected emission lines and the spectroscopic parameters based on NIST database, observed wavelength (λ), lower (E_i) and upper energy (E_k) levels. .

Element / λ (nm)	E_i (eV)	E_k (eV)
Fe I 373.486	0.85	4.17
Cr I 359.350	0.00	3.44
Ni I 349.296	0.10	3.65
Mn I 403.076	0.00	3.07

Before the selection of these individual elemental lines, for each element, potential elemental lines in the same characteristic properties were also investigated for their S/B and S/N performance, which are shown in the following figures from Figure 6-1 to Figure 6-16. The listed lines in the above table showed the highest performance in terms of these two parameters apart from the Mn I 403 nm. The reason of this deviating selection for process implementation was due to practical reasons, ease of data processing from scripting point of view and the recommendations of the literature for the typical Mn I triplet lines at the 403 nm region of the electromagnetic spectrum [138].

Signal-to-background

Initially the signal-to-background ratio was investigated via varying the gate width values from 0 μs to 200 μs at fixed delay time value of 0.5 μs . For this purpose, four potential Fe I lines were selected and checked for performance, namely at 373nm, 381nm, 430nm and 440nm. From these, the 373nm line showed the highest S/B ratio in any given condition. For any given elemental line, the S/B ratio showed a plateau characteristic after about 25 μs gate width time.

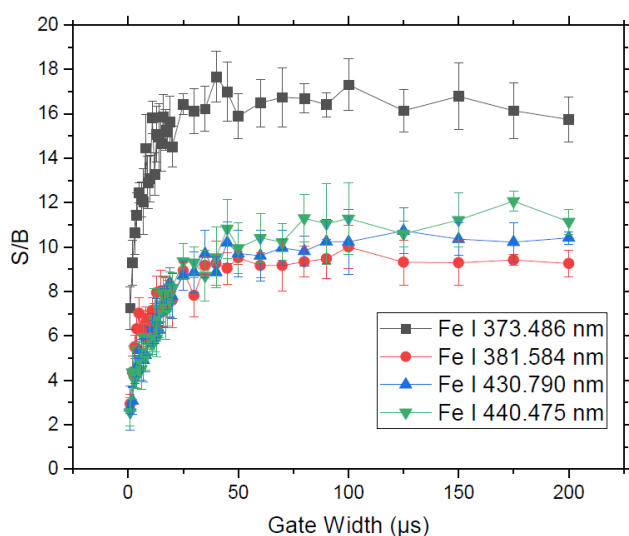


Figure 6-1: Signal-to-background for Fe lines. S/B as function of gate width at constant delay time = 0.5 μs for the selected emission lines. Individual lines between data points were added as guide-to-the-eye.

Same principle was applied for Cr I elemental lines, for the 359nm, 425nm and 428nm. From these, the 359nm line showed the highest S/B ratio in any given condition. For any given elemental line, the S/B ratio showed a plateau characteristic after about 25 μs gate width time.

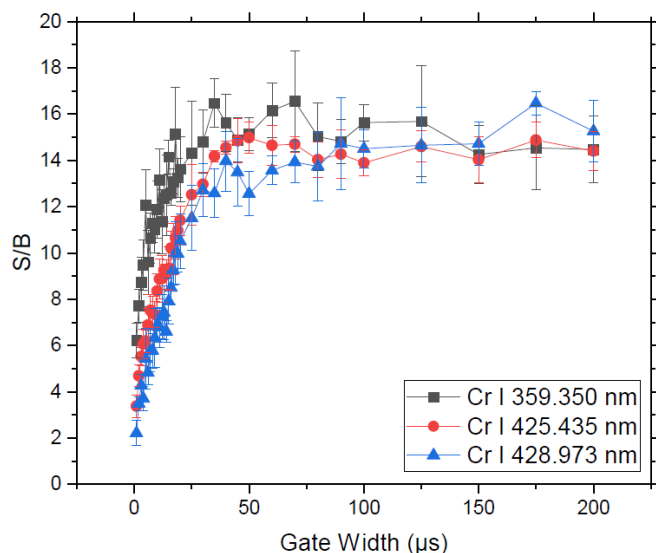


Figure 6-2: Signal-to-background for Cr lines. S/B as function of gate width at constant delay time = 0.5 μs for the selected emission lines. Individual lines between data points were added as guide-to-the-eye.

Same principle was applied for Ni I elemental lines, for the 341nm and 349nm. From these, the 349nm line showed the highest S/B ratio in any given condition. For any given elemental line, the S/B ratio showed a plateau characteristic after about 25 μs gate width time as the previous elements.

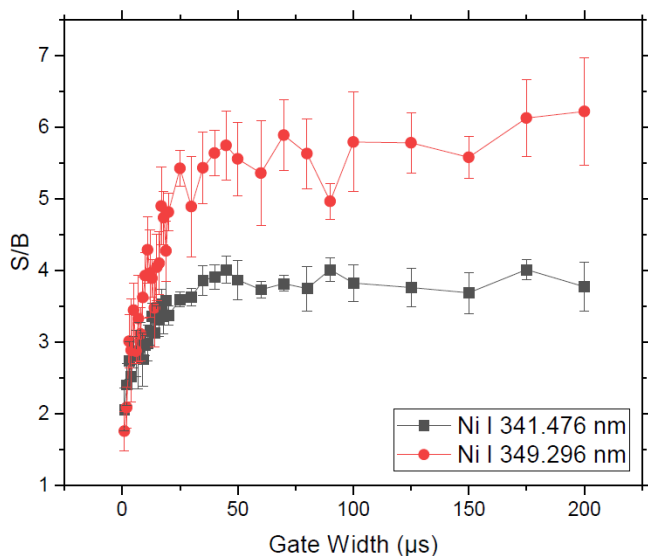


Figure 6-3: Signal-to-background for Ni lines. S/B as function of gate width at constant delay time = 0.5 μs for the selected emission lines. Individual lines between data points were added as guide-to-the-eye.

Same principle was applied for Mn I elemental lines, for the 403.076nm, 403.298nm, 403.449nm and 406.353nm. From these, the 406nm line showed the highest S/B ratio in any given condition. However, this line was not selected for further data processing as mentioned in the beginning of this subsection. The second high performing line at 403.076 was selected and used. For any given elemental line, the S/B ratio showed a plateau characteristic after about 25 μs gate width time as the previous elements.

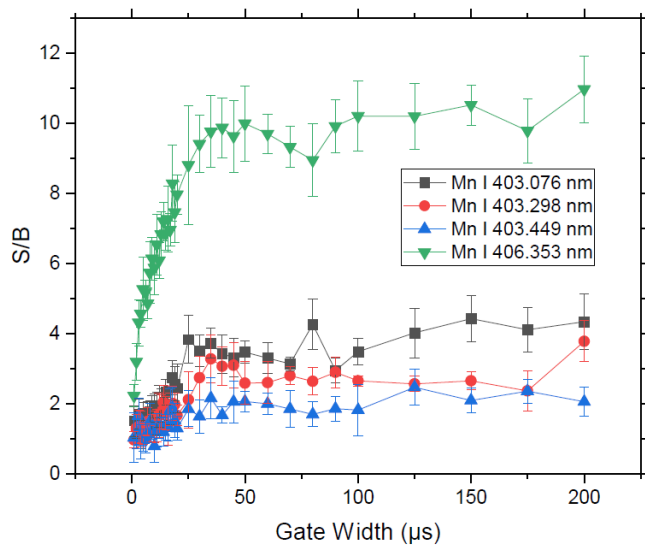


Figure 6-4: Signal-to-background for In lines. S/B as function of gate width at constant delay time = 0.5 μs for the selected emission lines. Individual lines between data points were added as guide-to-the-eye.

After establishing a trend in the gate width values, the delay time was varied to establish the correct value for this parameter. During this study, fixed value of 20 μs for gate width was utilized. With the same principle, four Fe I lines were selected and checked for performance, namely at 373nm, 381nm, 430nm and 440nm. From these, the 373nm line showed similarly the highest S/B ratio in any given condition. For any given elemental line, the S/B ratio showed a plateau characteristic after about 1 μs delay time.

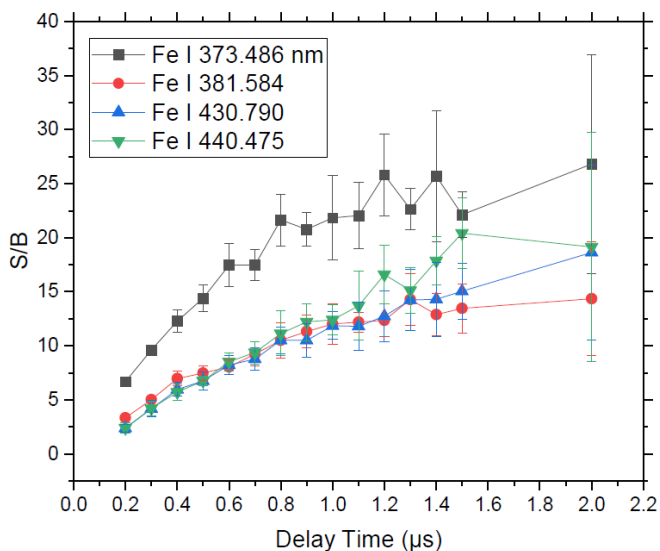


Figure 6-5: S/B as function of delay time at constant gate width = 20 μs . Individual lines between data points were added as guide-to-the-eye.

The same approach was used to analyze the Cr I elemental lines at wavelengths of 359 nm, 425 nm, and 428 nm. Of these, the 359 nm line had the highest signal-to-background (S/B) ratio under any conditions. For any given elemental line, the S/B ratio tended to reach a plateau after a delay time of around 1 μ s.

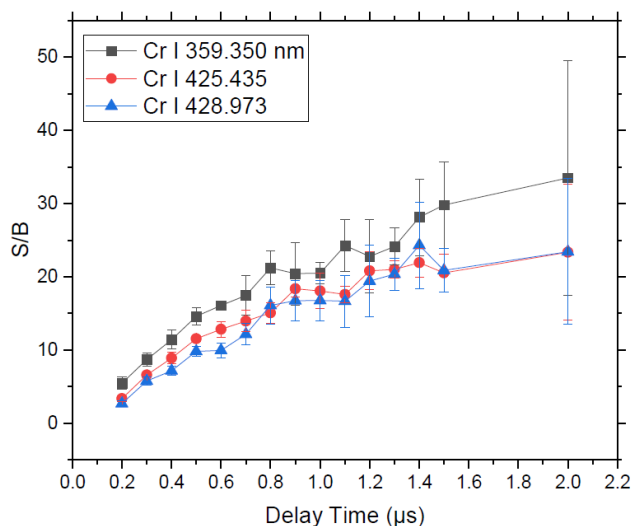


Figure 6-6: S/B as function of delay time at constant gate width = 20 μ s. Individual lines between data points were added as guide-to-the-eye.

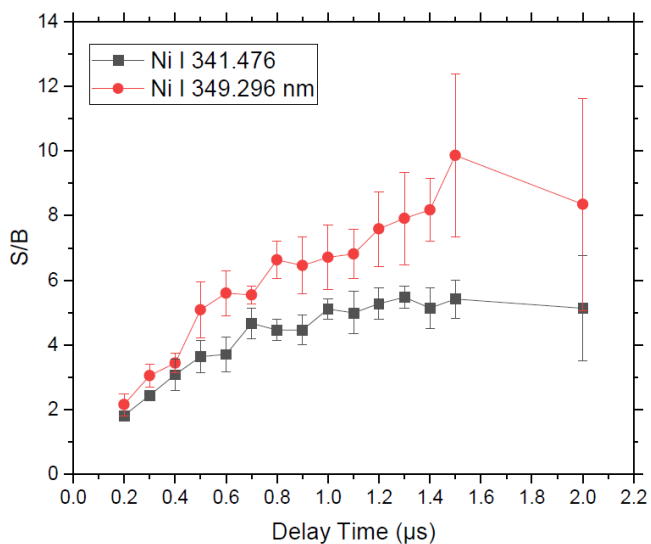


Figure 6-7: S/B as function of delay time at constant gate width = 20 μ s. Individual lines between data points were added as guide-to-the-eye.

The same method was used to analyze the Ni I elemental lines at 341 nm and 349 nm. The 349 nm line had the highest S/B ratio under any conditions and continued to increase to approximately 10. S/B ratio for 341nm line reached a plateau after a delay time of around 1 μ s where 349nm line continued to increase to S/B level between 8 to 10 by 1.4 to 1.5 μ s region.

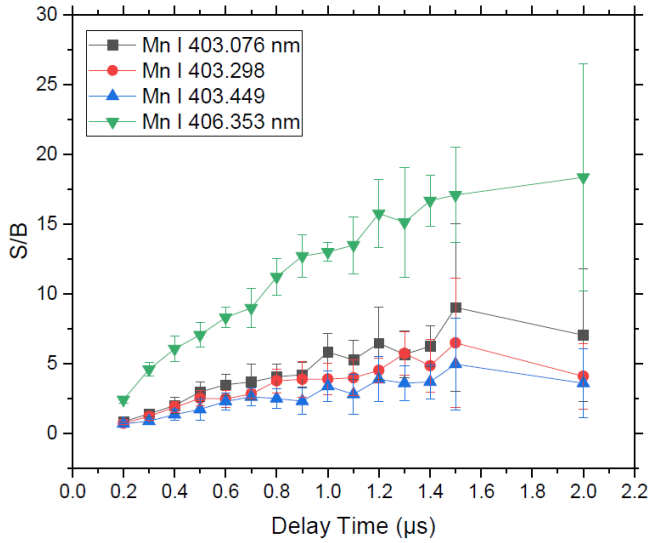


Figure 6-8: S/B as function of delay time at constant gate width = 20 μs . Individual lines between data points were added as guide-to-the-eye.

The same technique was used to analyze the Mn I elemental lines at 403.076 nm, 403.298 nm, 403.449 nm, and 406.353 nm. The 406 nm line had the highest S/B ratio under any conditions, but it was not selected for further data processing as mentioned earlier in the section. The second highest performing line at 403.076 nm was selected instead. Like the previous elements, the S/B ratio for any given elemental line reached a plateau after a delay time of around 1 μs . However, in contrast to the previous measurements, the 406 nm line showed an increasing trend rather than a plateau, although the deviation between the measurements as indicated by the error bars also increased with longer delay times, leading to an increase in the error of the processed data for subsequent stages of the measurements.

Signal-to-noise

After evaluating the signal-to-background ratios, the same approach was used to analyze the signal-to-noise ratios. The signal-to-noise ratio was studied by varying the gate width values from 0 μs to 200 μs at a fixed delay time of 0.5 μs . Four Fe I lines were evaluated for their performance at 373 nm, 381 nm, 430 nm, and 440 nm. The 373 nm line had the highest S/N ratio under any conditions. For any given elemental line, the S/N ratio reached a plateau after a gate width time of around 25 μs .

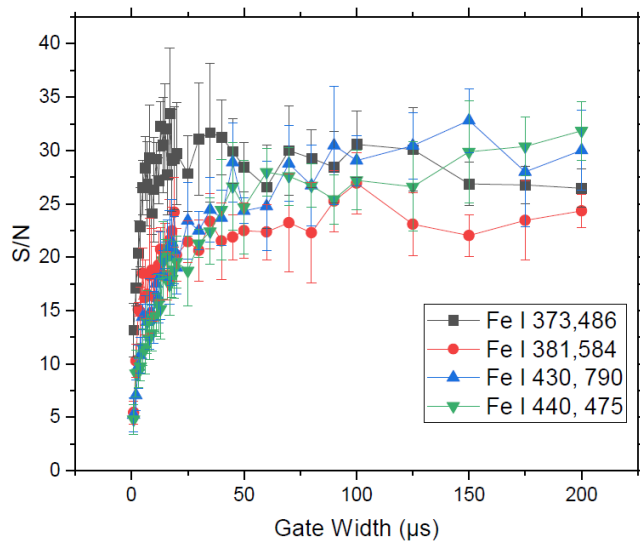


Figure 6-9: Signal-to-noise for Fe lines. S/N as function of gate width at constant delay time = $0.5 \mu\text{s}$ for the selected emission lines. Individual lines between data points were added as guide-to-the-eye.

The same approach was used to analyze the Cr I elemental lines at 359 nm, 425 nm, and 428 nm. Of these, the 359 nm line had the highest signal-to-noise (S/N) ratio under any conditions. For any given elemental line, the S/N ratio reached a plateau after a gate width time of around $25 \mu\text{s}$.

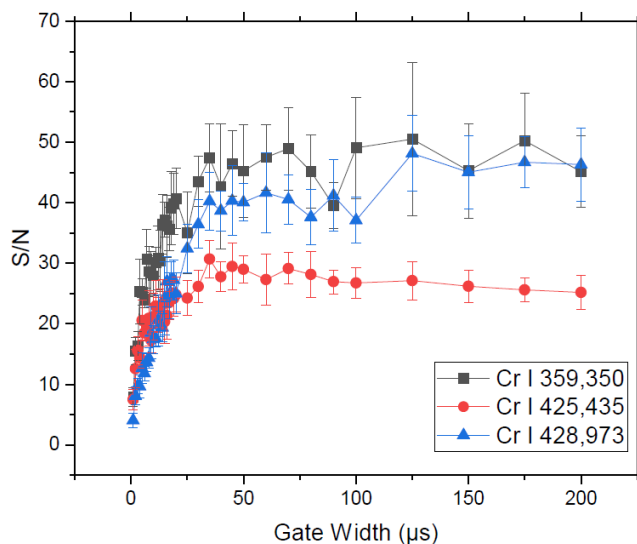


Figure 6-10: Signal-to-noise for Cr lines. S/N as function of gate width at constant delay time = $0.5 \mu\text{s}$ for the selected emission lines. Individual lines between data points were added as guide-to-the-eye.

The same method was used to analyze the Ni I elemental lines at 341 nm and 349 nm. The 349 nm line had the highest signal-to-noise (S/N) ratio under any conditions. Similar to the

previous elements, the S/N ratio for any given elemental line reached a plateau after a gate width time of around 25 μs .

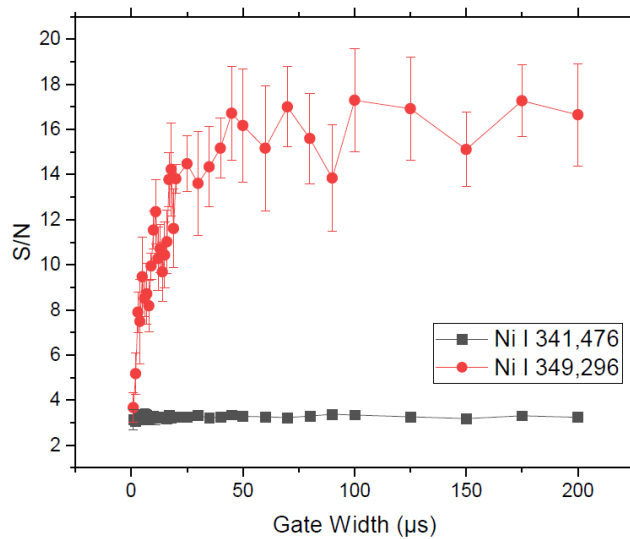


Figure 6-11: Signal-to-noise for Ni lines. S/N as function of gate width at constant delay time = 0.5 μs for the selected emission lines. Individual lines between data points were added as guide-to-the-eye.

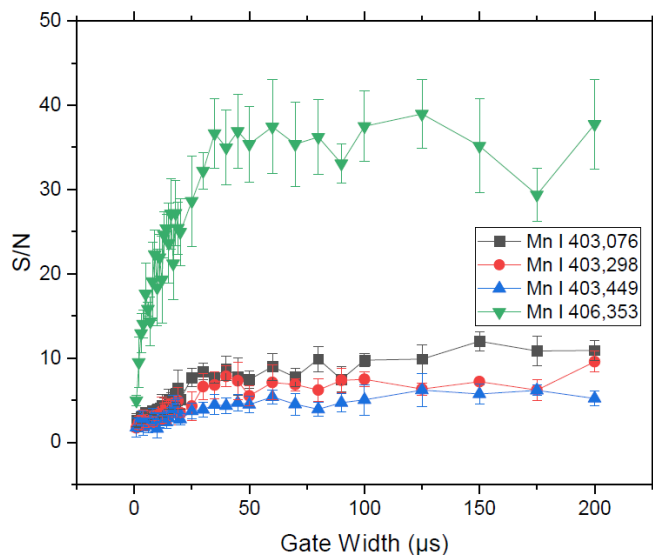


Figure 6-12: Signal-to-noise for In lines. S/N as function of gate width at constant delay time = 0.5 μs for the selected emission lines. Individual lines between data points were added as guide-to-the-eye.

Same principle was applied for Mn I elemental lines, for the 403.076nm, 403.298nm, 403.449nm and 406.353nm. From these, the 406nm line showed, similarly as the S/B, the highest S/N ratio in any given condition. However, this line was not selected for further data processing as mentioned in the beginning of this subsection. The second high performing line

at 403.076 was utilized. For any given elemental line, the S/N ratio showed a plateau characteristic after about 25 μs gate width time as the previous elements.

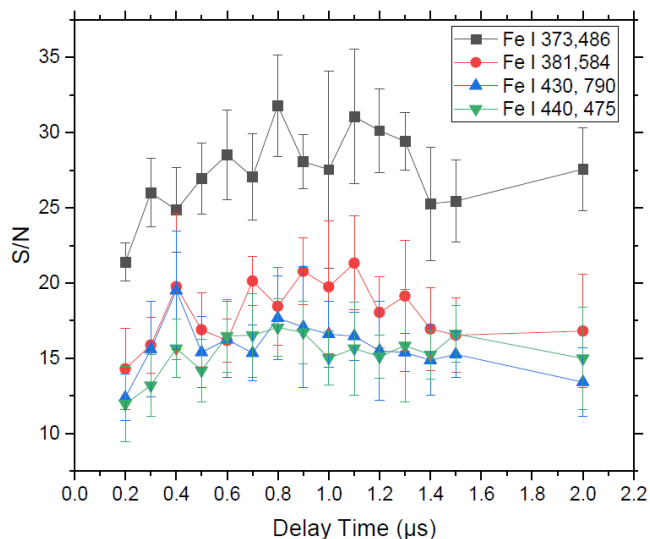


Figure 6-13: Signal-to-noise for Fe lines. S/N as function of gate width at constant delay time = 0.5 μs for the selected emission lines. Individual lines between data points were added as guide-to-the-eye.

Applying the same principle as the S/B ratios, after establishing a trend in the gate width values, the delay time was varied to determine the correct value for this parameter. During this study, fixed value of 20 μs for gate width was utilized. Using the same principle, four Fe I lines were selected and checked for performance, namely at 373nm, 381nm, 430nm and 440nm. From these, the 373nm line showed similarly the highest S/N ratio in any given condition. For any given elemental line, the S/N ratio showed a plateau characteristic after about 0.5 μs delay time.

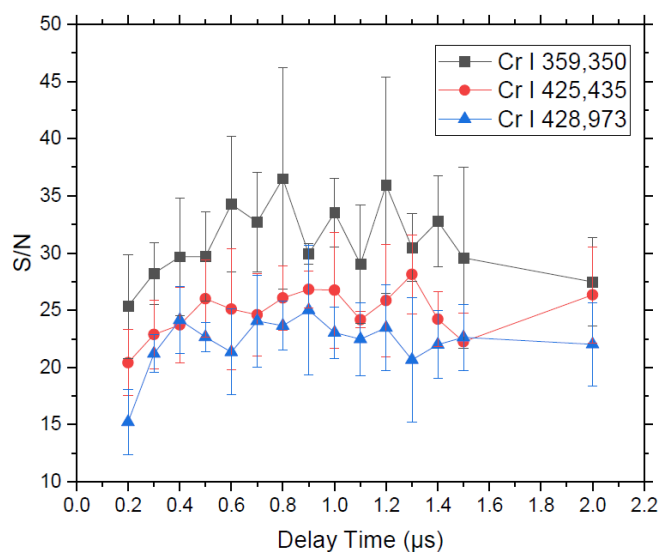


Figure 6-14: Signal-to-noise for Cr lines. S/N as function of gate width at constant delay time = 0.5 μs for the selected emission lines. Individual lines between data points were added as guide-to-the-eye.

The same approach was used to analyze the Cr I elemental lines at 359 nm, 425 nm, and 428 nm. Of these, the 359 nm line had the highest signal-to-noise (S/N) ratio under any conditions. For any given elemental line, the S/N ratio reached a plateau after a delay time of around 0.5 μs .

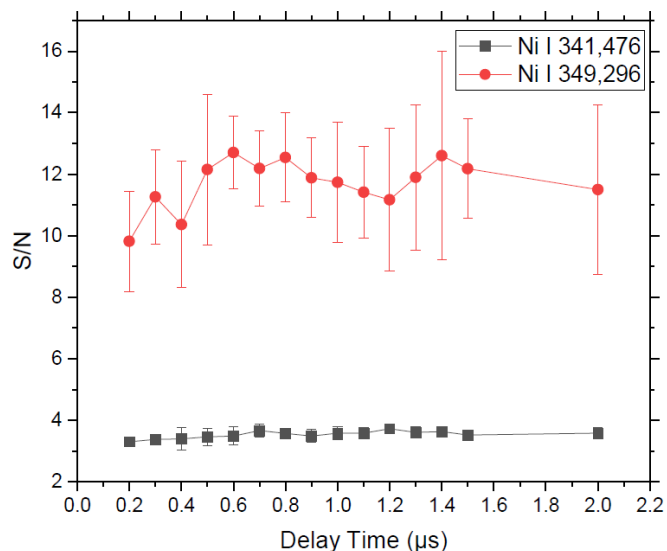


Figure 6-15: Signal-to-noise for Ni lines. S/N as function of gate width at constant delay time = 0.5 μs for the selected emission lines. Individual lines between data points were added as guide-to-the-eye.

Same principle was utilized for Ni I elemental lines, for the 341nm and 349nm. From these, the 349nm line showed the highest S/N ratio in any given condition. For any given elemental

line, the S/N ratio showed a plateau characteristic after about 0.5 μs delay time as the previous elements.

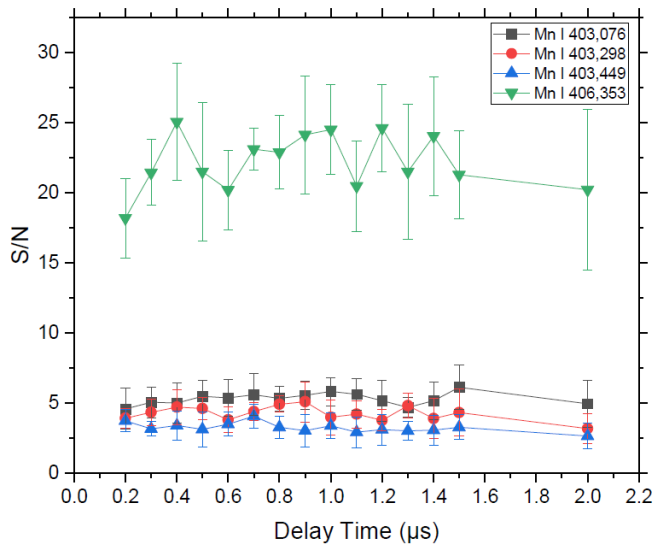


Figure 6-16: Signal-to-noise for In lines. S/N as function of gate width at constant delay time = 0.5 μs for the selected emission lines. Individual lines between data points were added as guide-to-the-eye.

Same principle was applied for Mn I elemental lines during the S/N study, for the 403.076nm, 403.298nm, 403.449nm and 406.353nm. From these, the 406nm line showed the highest S/N ratio in any given condition. However, similarly with the gate width variation, this line was not selected for further data processing as mentioned in the beginning of this subsection. The second high performing line at 403.076 was selected and used. For any given elemental line, the S/N ratio showed a plateau characteristic after about 0.5 μs delay time as the previous elements.

The cross examination of the parameters and the resulting S/B and S/N ratios given a good overview of the LIBS parameters for the data processing and acquiring a clean spectrum. The selected parameters for the further tests were delay time = 0.5 μs ; gate width = 20 μs .

6.1.2 Alloying element vaporization from the weld pool

One of the first and unexpected findings of during the prototyping and initial testing stage was to observe higher content of Manganese at the Heat-Affected-Zone of the finished welds. This phenomenon can be seen in Figure 6-17. The observation of this phenomenon drove the project to investigate in depth and more systematically, namely the effect of welding parameters on this phenomenon is shown in this section.

Manganese accumulation at the HAZ

During a post-weld LIBS investigation on welded samples of 1.4404/b.2 material, a 16mm × 16mm (width x length) surface mapping – a limited segment of the weld seam – was conducted in order to extend and show the possible applications of LIBS for the surface control of the welds. This random check caused the finding mentioned above. The base material Cr and Mn chemical compositions are 17.0 and 1.4 wt% respectively (Table 8).

The finished weld shown in Figure 6-17 was a bead-on-plate TIG welding, conducted at 60 A with 10 cm/min welding speed and 12 l/min Ar gas flow. LIBS mapping was performed with 0.1 mm spatial resolution, 10 laser pulses accumulated for each measurement spot at 25 Hz Nd:YAG laser, using the Aryelle 200 spectrometer (LTB Berlin). The LIBS mapping was performed on the mid-region of the weld seam to resolve a representative area for the whole weld. For this study, Mn II line was recorded at 294.92 nm. Higher Mn intensity counts at the edges of the weld seam, i.e. Mn accumulations in the HAZ is present.

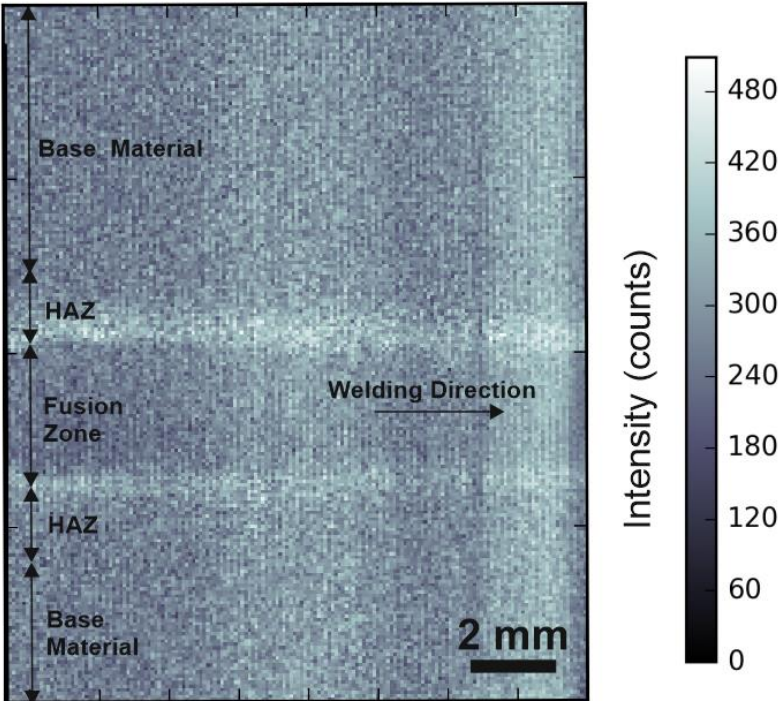


Figure 6-17: The surface of the welded sample was analyzed using laser-induced breakdown spectroscopy (LIBS) mapping to identify the distribution of manganese on the surface, with a particular focus on the accumulation of manganese in the heat-affected zone (HAZ). [96]

These findings were validated by investigating the results systematically. Figure 6-18 shows three fitted and processed spectra overlapped on the diagram from the Mn I approx. 402.8 nm to 403.8 nm triplet lines region recorded for the base material, weld bead and heat-affected-zone. (Welding parameters: Welding current = 65A; Welding speed = 10 cm/min - Heat input= 491 J/mm-; shielding gas flow rate = 18 l/min). The weld bead and base material peak intensity count remains about the half of the heat-affected zone peak intensity count at approximately 7500 counts, 4500 counts and 3000 counts respectively, validating the mapping result shown in Figure 6-17. Furthermore, these findings were quantified using the same calibration model, given in Section 6.2 in Figure 6-23 and Figure 6-25.

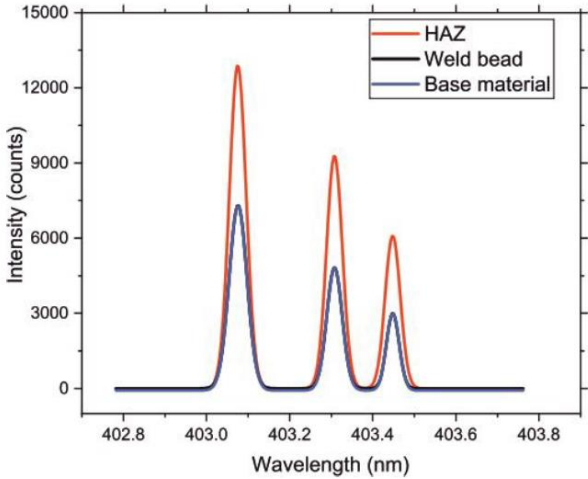


Figure 6-18: The fitted Mn I triplet peaks around 403 nm. The curves for the "weld bead" and "base material" overlapped due to their similar chemical compositions. The welding parameters used were a welding current of 65 A, a welding speed of 10 cm/min (which resulted in a heat input of 491 J/mm), and a shielding gas flow rate of 18 l/min. The material used was EN 1.4404 / 327005. Reproduced with permission.[98]

The calibration model was applied on a conducted line scan of the finished weld and showing quantified results in wt% for all three regions of the finished weld bead in perpendicular direction results in a chemical composition vs. position profile.

In Figure 6-18, there are three spectra plotted, yet two of them overlap; the black curve (measured spectrum from the weld bead) and the blue curve (measured spectrum from the base material) are not visible separately due to this overlap. The reason for this is given in Figure 6-19, i.e. the Mn content at the base material and the weld bead are similar and deviating in the same interval between approx. 16.5-18 wt%, where Mn content for the HAZ demonstrates a peak compared to the weld bead and the base material. This result confirms

the higher Mn content at the border of the FZ. Hence, Mn was accumulated on the HAZ as a result of the welding process[98].

Figure 6-19 reveals a different trend for Cr, hence, the Cr chemical compositions present the lowest values on the weld bead or the FZ with approx. 16.5wt%; and increasing trend towards the base material (towards the rim of the base material) reaching about 18wt%. This finding indicates a potential Cr depletion in the solidified weld metal. This can be explained by a possible vaporization of this alloying element or potential burn-off. However, any visible local accumulation of Cr at any specific location was not observed.

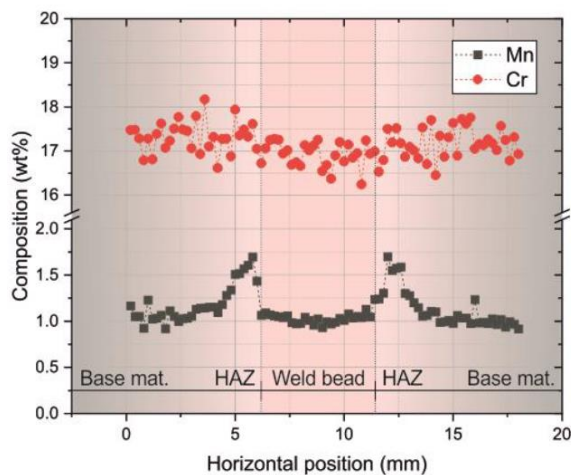


Figure 6-19: The distribution of chromium and manganese elements was studied using a line-scan with laser-induced breakdown spectroscopy (LIBS) perpendicular to the welding direction. The measurements were made at specific points along the line to determine the spatial distribution of the elements. Reproduced with permission. [98]

This observation of the higher Mn content in the HAZ raised the question if there is an oxide formation at the edge of the finished weld bead was the actual case, i.e. where more oxygen being present for molecular formation at the edges of the argon flow causing the a Mn-oxide layer[96]. This hypothesis is supported by the literature, hence, Tashiro demonstrated the fume formation mechanism via numerical simulations and showed that the Mn can deplete and solidify on neighboring regions of the TIG weld beads [133]. Additionally, Tanaka investigated the layering regions of the metal vapor under helium TIG arc plasma using imaging spectroscopy, supporting the findings of increased vaporization of the manganese element under welding condition and reaching the neighboring area of the weld bead via convective air flow in and around the arc plasma[135].

Effect of the welding heat input

The previous subsection has explained a potential Mn accumulation phenomenon at the HAZ. This subsection reveals the same phenomenon in relation to the welding heat input for the alloying elements Mn and Cr in same base material 1.4404/b.2. Increasing welding heat inputs

were generated by modifying the relevant welding parameters, namely welding current and speed.

Figure 6-20 presents the Mn (left) and Cr (right) wt%-compositions as a function of welding heat input. Figure 6-20 shows the chemical composition of the Cr and Mn elements measured in three predefined regions on the finished welds (base material, HAZ and weld bead (FZ)).

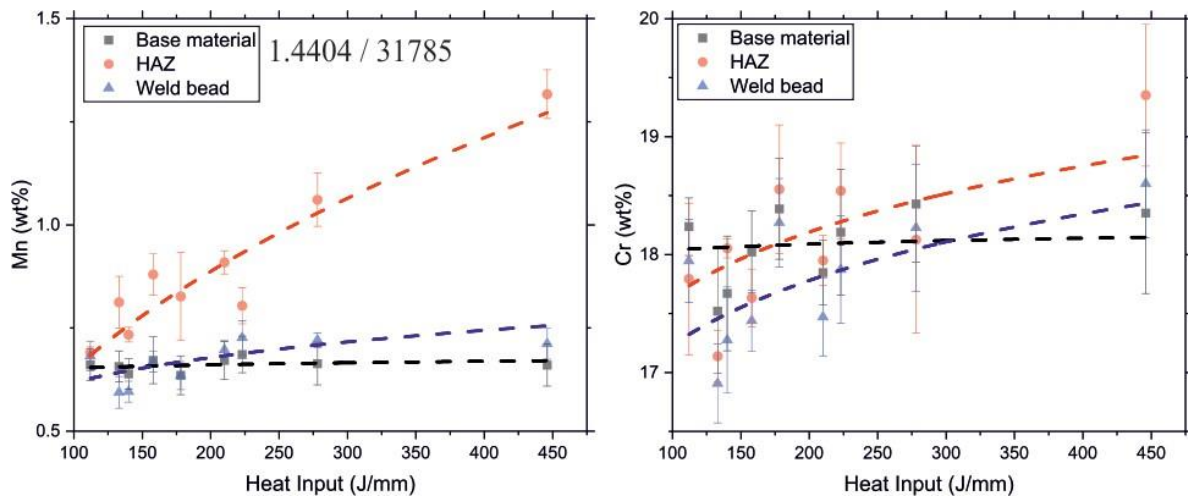


Figure 6-20: The chemical compositions of manganese (left) and chromium (right) at the base material, heat-affected zone (HAZ), and weld bead were plotted as a function of the welding heat input. Dashed lines were included as visual aids. Dashed lines are guide-to-the-eye. Reproduced with permission. [98]

Figure 6-20 shows an observation of approx. 0.5 wt% increase of the resulting surface chemical compositions for both Mn and Cr on the HAZ with the increasing the heat input from 110 J/mm up to 450 J/mm. Similarly, the increasing trend for Mn and Cr compositions along with the increasing heat input is observed on the weld bead (FZ). However, the increasing trend for Cr (blue dashed lines) is steeper compared to Mn at the weld bead. Measurements conducted on the base material didn't show any significant composition variations as function of the heat input (black dashed lines). It was reported by Khan et al. that increasing the power input during laser welding of stainless steels would increase the vaporization rate of alloying elements [139]. Khan's results are in good agreement with the findings in Figure 6-20, hence, the Mn composition at the HAZ increased with the higher welding heat input. Consequently, the amount of the condensed Mn on the weld surface after weld situation is also increased. Same principal applies for the elemental Cr, however in a different region on the weld surface. Tanaka et al. had showed that Cr is mainly present in the welding arc plasma through its lower ionization energy[135]. There remains the possibility also shown in the literature that the vaporized Cr could be carried to the TIG welding electrode [134], which was reported as the finding of higher Cr composition directly above the weld bead region or on the FZ region[98].

Effect of the shielding gas flow rate

This last subsection investigates the chemical composition changes of Mn and Cr for the sample material 1.4435/b1 at constant heat input (491 J/mm) as a function of the shielding gas (Ar) flow rate. Figure 6-21(left) shows the accumulated Mn content at the HAZ for any given flow rate with approx. 0.2 wt% positive difference. The deciding difference displays itself at the strongest applied gas flow rate (20 l/min) and with approx. 1 wt% increase to the other measured Mn at the base material and the weld bead (FZ) to the slower gas flow rates. This finding indicates that the vaporized Mn from the weld pool is swept away from the area above the FZ faster. Following, it was carried onto the HAZ, i.e. accumulated on the HAZ at faster rate and therefore resulting in approx. 1wt% more composition.

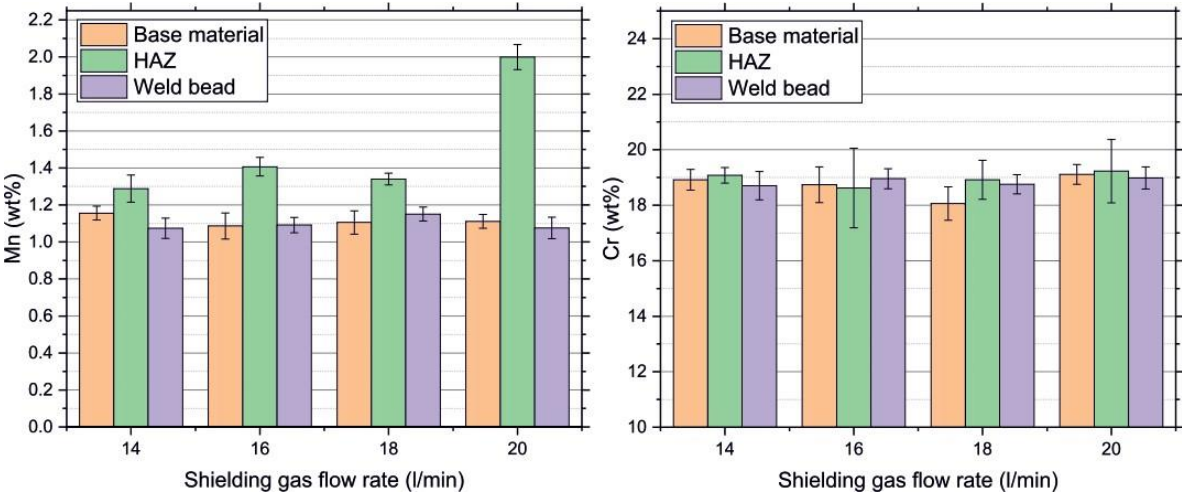


Figure 6-21: The chemical compositions of manganese (left) and chromium (right) at the base material, heat-affected zone (HAZ), and weld bead were plotted as a function of the welding heat input. Dashed lines are guide- to-the-eye. Reproduced with permission.[98].

This result indicates that the transport model of the alloying elements in the welding arc plasma is directly related to the weld shielding gas flow rate. Considering the rate of Manganese vaporization from the weld pool is independent of the gas flow rate, moreover, is directly related to the weld pool temperature via input energy, it is possible to interpret this higher Mn content at 20 l/min setting is due to the faster transport kinetics in the welding arc plasma: not due to the higher vaporization rate from the weld pool[98].

In Figure 6-21 (right) one can see that Cr has followed relatively stable results by approx. 19wt% throughout all selected flow rate settings for this sample material, yet still about 1wt% higher than the given base material composition. According to this trial, it can be concluded that the measured chemical composition of the Cr in various weld regions do not depend on the shielding gas flow rate or the heat input.

Moreover, if the latent enthalpy of vaporization values for Mn and Cr to be compared, it would make this assumption more comprehensible. Mn requires 225 kJ/mol to vaporize where Cr needs 347 J/mol[140]. These values support the possible Mn vaporization and consequent condensation to happen thermodynamically relatively easier compared to Cr. Huber et al. reported that the weld pool temperature has a higher impact on the metal vapor generation and the excitation degree of the individual alloying elements from the weld pool[94]. In this study, the welding heat input possibly remains below a critical level for chromium, therefore Cr composition does not change over the different regions via shielding gas flow rate increase.

6.2 Weld process monitoring during hot cracking of stainless steels using LIBS

6.2.1 Hot-cracking boundary conditions

In this section welding samples were systematically investigated against their hot cracking susceptibility properties, their local chemical compositions during welding and post weld chemical compositions and metallographic structures. For this purpose, same geometry samples were welded using bead-on-weld method; varying welding parameters resulted in centerline hot cracking forms of the welds when the input energy was increased to about 0.8 kJ/mm for both inspected materials, namely 1.4404 and 1.4435.

For all the welding experiments, 160A welding current was used. Various input energy levels between 0.4 – 0.8 kJ/mm into the base material were achieved via varying the welding speed. Figure 6-22 shows the various welding speeds and the outcome (crack / no crack) of these conditions on the final weld product.

Additionally in these series of experiments, the weld pool temperature was measured via an infrared thermometer at the same position to the LIBS measurement spot respective to the welding arc in the weld pool. The temperature measurements were aimed to provide more data on the solidification status of the weld pool.

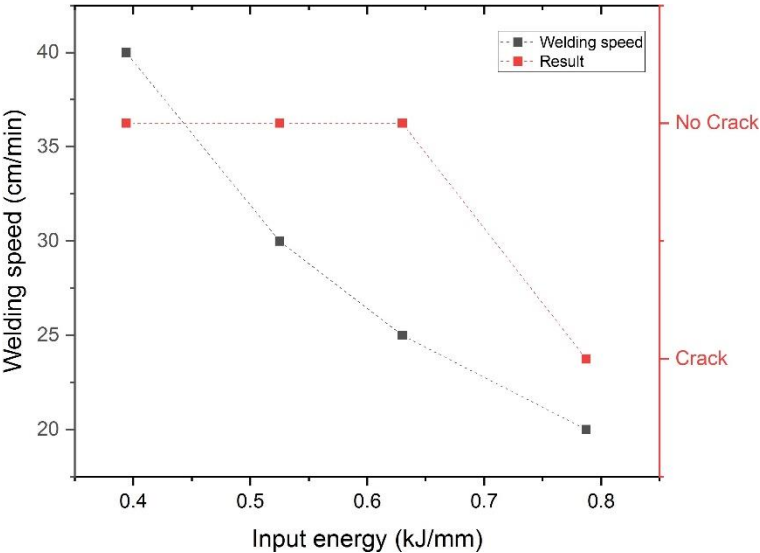


Figure 6-22: Different weld input energies and end condition of the finished product. Similar result for both 1.4404 and 1.4435. 1.4404 created wavy form and showed relatively less susceptibility to cracking. 1.4435 demonstrated higher susceptibility to center line cracking. 160A constant welding current, same sample geometry.

Elemental line selection and calibration models

After initial trials on the welding parameters, 20 cm/min and 160A resulting in approx. 0.8 kJ/mm input energy as reference hot crack propagation welding parameter on the sample geometry for the rest of the series. Nine samples welded and monitored in total, compared with cold LIBS measurements; final weld transverse line scans and weld end crater local chemical composition including metallographic samples and SEM/EDX investigations included.

Before moving on to the online monitored experiments, the selected elemental lines and the calibration model built for the quantified LIBS chemical compositions measurements are as follows:

Table 14: Selected elemental lines for the calibration model and online process monitoring.

Line	Peak Intensity (nm)
Fe I	373,486
Cr I	359,350
Ni I	349,296
Mo I	386,411
Mn I	403,076
P I	213,546

During the welding experiments and during the post-weld analyses, calibration of the Cr, Ni, Mn and Mo elements via the elemental lines in Table 14 were used. In some cases of the online monitoring of the elements, mainly -Mo, Mn, P-, due to the lower recorded relative intensities and low signal to background ratios, the monitoring was only possible using the normalized intensities, hence no quantified results. Moreover, for the lower alloying elements, quantified calibration models were not possible to establish due to the lack of commercial reference materials at lower compositions. As a rule of thumb, increasing the sample size of the reference samples and measurements will increase the confidence level of the calibration model, hence reducing the error margin of the measurements. Future studies must encompass ground up reference material production to fully integrate the calibration model into the measurement system. Figure 6-23, Figure 6-24, Figure 6-25 and Figure 6-26 show the univariate calibration curves with 95% confidence band for the Cr, Ni, Mn and Mo respectively. More information on the calibration model can be found in Section 2.4.

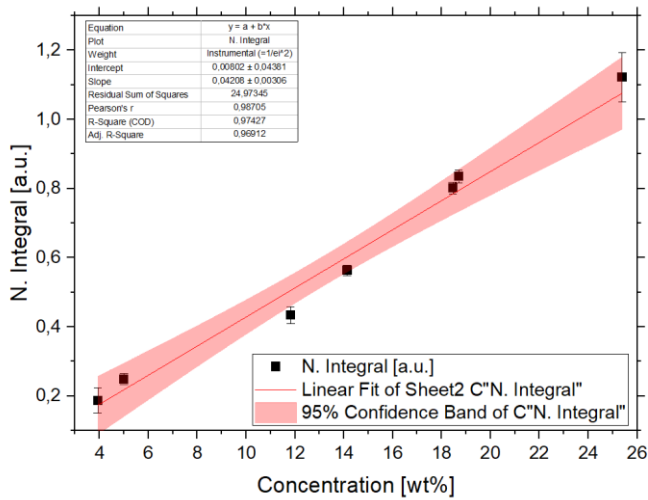


Figure 6-23: Univariate calibration curve model for Cr with 95% confidence band marked in red. $R^2=0.97$. Used Certified Reference Materials (CRMs): BS 19, 271-1, BS 36B, BAS 475, 232-1 (AKP133), SS 468-1, SS 463-1, BAS 295-1, SS 464-1

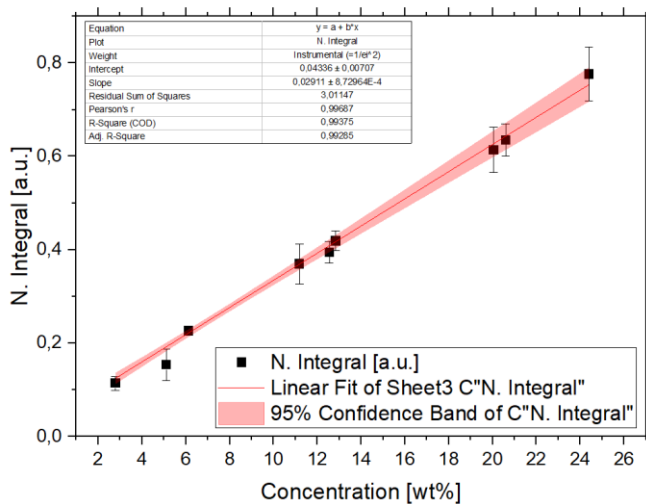


Figure 6-24: Univariate calibration curve model for Ni with 95% confidence band marked in red. $R^2=0.99$. Used Certified Reference Materials (CRMs): BAS 296-1, 273-1, SS 461-1, SUS 1.4571, SS 462, SS 462-1, SS 464-1, SS 64, BAS 295-1

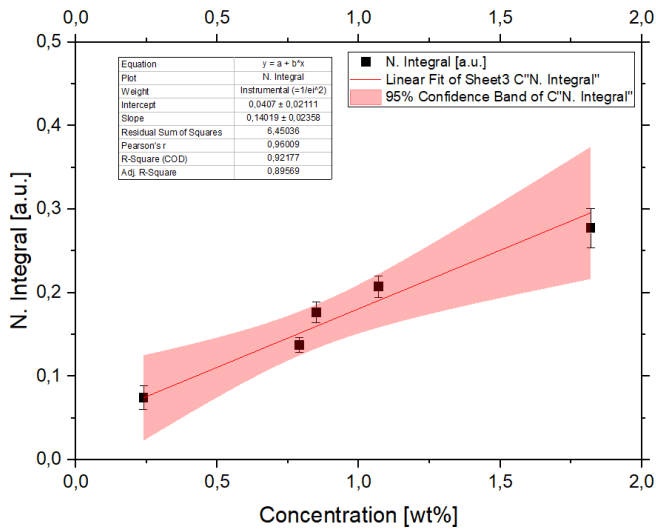


Figure 6-25: Univariate calibration curve model for Mn with 95% confidence band marked in red. $R^2=0.92$. Used Certified Reference Materials (CRMs): SUS 1.4034, SS 63, SS 64, SUS 1.4306, SUS 1.4541

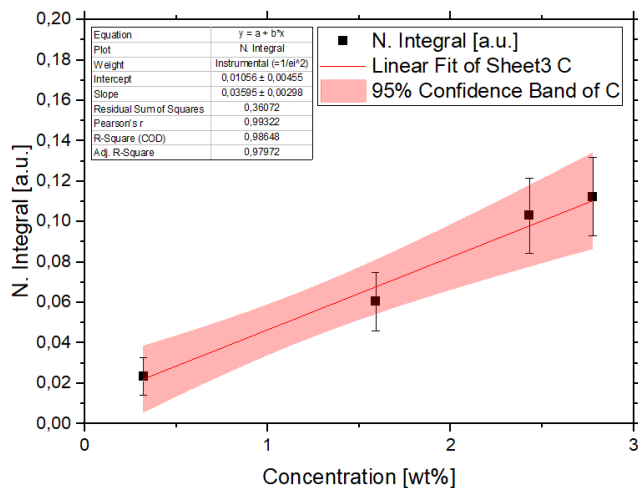


Figure 6-26: Univariate calibration curve model for Mo with 95% confidence band marked in red. $R^2=0.98$. Used Certified Reference Materials (CRMs): SUS 1.4541, BAS 475, SS 66, SS 466-2

6.2.2 Hot-cracking, in situ chemical composition and in situ partition coefficient calculation

For the ease of navigation between the results/samples in this section, the following table is given for comparison and end condition of the welds. The terminology “All crack” is used if the sample showed a solidification crack all among the weld bead, “half crack” is used for the samples which showed solidification weld in a segment of the weld and “no crack” situation is self-explanatory. To determine the end-conditions of each sample, please refer to the top-view pictures given for each sample.

Table 15: Sample identification, input parameters and end condition.

Sample ID	Material	Weld heat input [kJ/mm]	End condition	In situ partition coefficient [Y/N]
Sample 1	1.4435 / b.2	0.40	No Crack	N
Sample 2	1.4435 / b.2	0.80	All Crack	N
Sample 3	1.4435 / b.2	0.53	No Crack	Y
Sample 4	1.4435 / b.2	0.62	No Crack	N
Sample 5	1.4435 / b.2	0.80	All Crack	Y
Sample 6	1.4404 / b.1	0.80	No Crack	Y
Sample 7	1.4404 / b.1	0.80	Half-Crack	Y
Sample 8	1.4435 / b.2	0.80	All Crack	N
Sample 9	1.4435 / b.2	0.80	All Crack	N

Sample 1: 1.4435/b2

Sample 1 was welded at 0.4 kJ/mm and therefore with no solidification cracking observed. The finished weld can be seen in Figure 6-27 from top view. Table 16 shows the nominal Cr and Ni chemical compositions measured on the base material via LIBS, namely “cold measurements” without the welding situation.

Table 16: Cold LIBS measurements on the base material (no welding) 1.4435/b2 (Material thickness = 3mm)

Element	Mean Value (wt%)	Standard Deviation
Cr	17.22	0.58
Ni	10.31	0.83

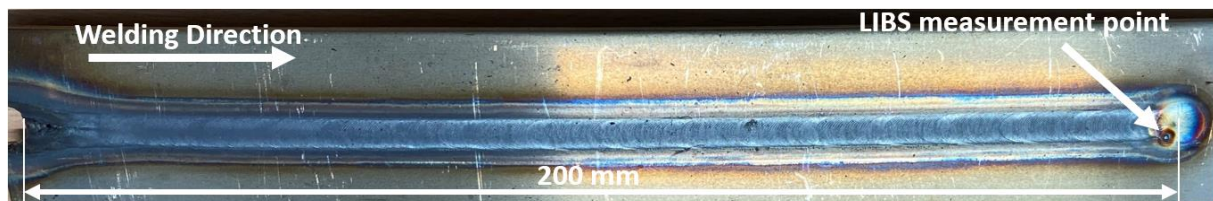


Figure 6-27: Finished weld seam of the Sample 1, LIBS measurement spot on the weld end crater is marked.

Figure 6-27 demonstrates the finished work piece with the bead-on-plate TIG weld in 200 mm length, with marked welding direction towards right, the LIBS measurement spot marked on the end crater. The LIBS measurement was conducted in 2 mm distance from the welding electrode. Temperature measurement was done at the same spot in symmetrical respective to the welding electrode, to eliminate the effect of the LIBS plasma and capture the weld pool temperature only.

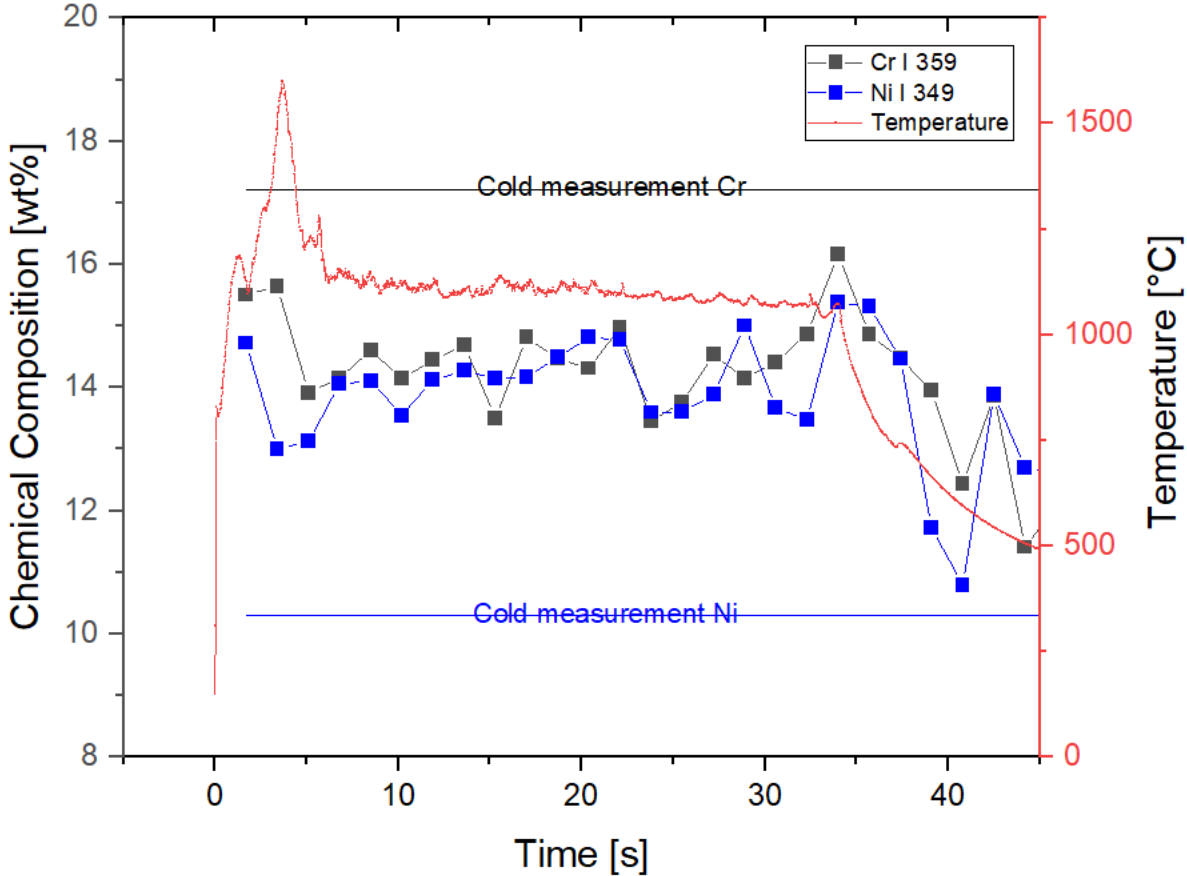


Figure 6-28: Sample 1 online weld monitoring of element Cr and Ni over time along with the temperature measurement on the same spot to the LIBS point respective to the welding arc position.

Figure 6-28 shows the in situ Cr (black) and Ni (blue) chemical compositions in wt% via LIBS and the temperature measurements via infrared thermometer from the same respective position. The temperature curve also shows the welding process with increasing temperature slightly above 1500°C until the weld pool is created and then relative movement of the workpiece starts to conduct the bead-on-weld bead. The welding process was completed approx. at 34th second and the temperature curve starts to decay as the solidification immediately initiates in the weld end crater.

Figure 6-28 demonstrated that the in situ Cr values in the weld pool in 2 mm distance from the weld electrode remained at level of 15wt%, 2.2wt% lower than the base material nominal

value -cold measurement-, and approx. at 14wt% for Ni where it is about 3.5wt% higher than the base material nominal value. This discrepancy of the in situ recorded value and the base material value raises immediately several questions such as Cr elemental burn-off from the weld pool during welding, where higher Ni content in the weld pool cannot be correlated with the burn-off phenomenon or local chemical composition change due to changing partition coefficient of these elements. Lower Cr value could be a result of a declining partition coefficient which results in the Cr element being rejected from the liquid solution in the measurement spot where higher Nickel can be explained with increasing partition coefficient where solute is more present in the solution, resulting in higher Ni content than the nominal value.

Sample 2: 1.4435/b2

Sample 2 was welded at approx. 0.8 kJ/mm and therefore with solidification cracking observed, namely a centerline cracking among the whole weld bead was visible. The finished weld can be seen in Figure 6-29 from top view. Table 16 showed the nominal Cr and Ni chemical compositions measured on the base material via LIBS, namely “cold measurements” without the welding situation on this base material.

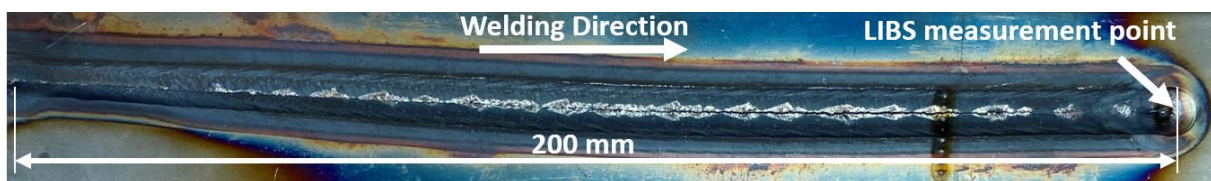


Figure 6-29: Finished weld seam of the Sample 1, LIBS measurement spot on the weld end crater is marked.

Figure 6-29 demonstrates the finished work piece with the bead-on-plate TIG weld in 200 mm length, with marked welding direction towards right, end crater of the weld and the LIBS measurement spot marked on the end crater. The LIBS measurement was conducted in 2 mm distance from the welding electrode. Infrared temperature measurement was done at the same spot in symmetrical respect to the welding electrode, to eliminate the effect of the LIBS plasma and capture the weld pool temperature only. In this sample, a centerline cracking is visible among the whole weld in 200 mm length. The input energy reached a threshold to initiate the solidification cracking due to thermo-mechanical conditions discussed in Section 2.3.

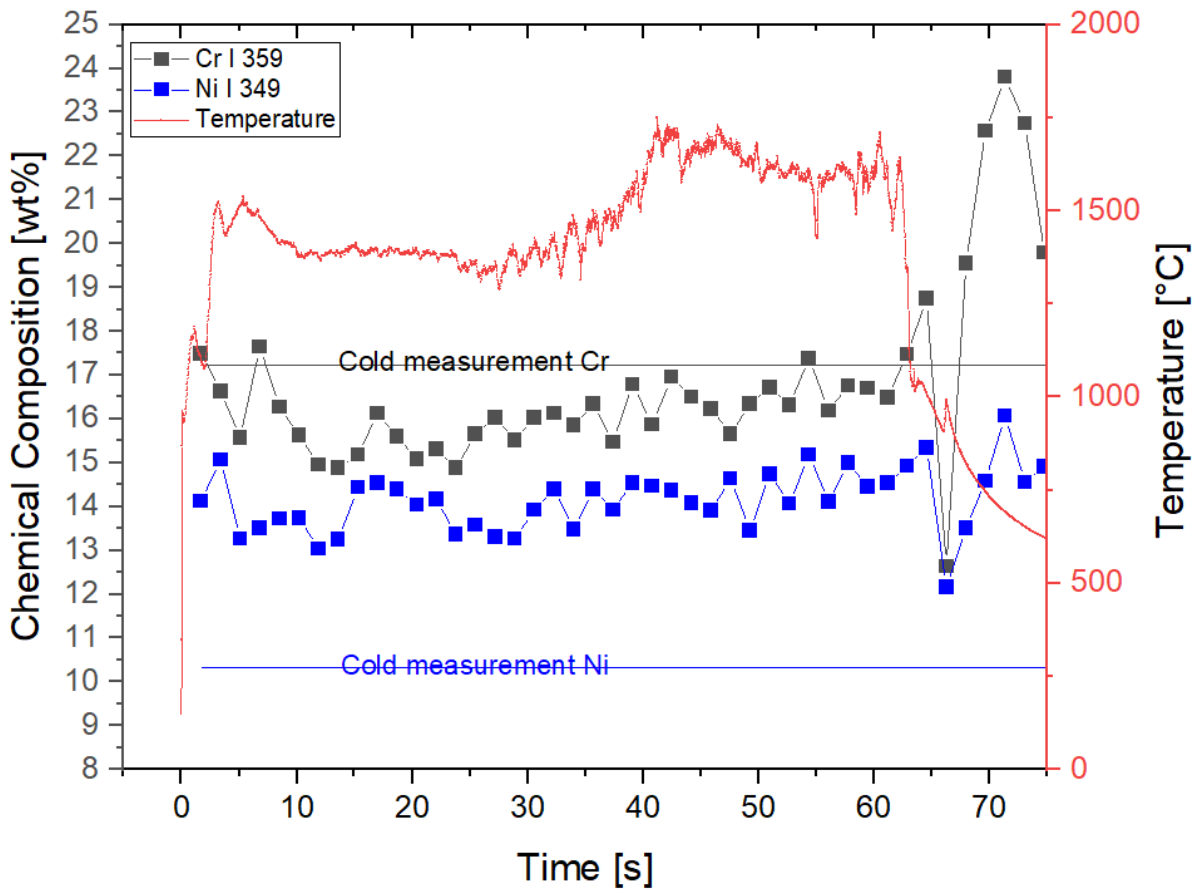


Figure 6-30: Sample 2 online weld monitoring of element Cr and Ni over time along with the temperature measurement on the same spot to the LIBS point respective to the welding arc position.

Along with the thermo-mechanical conditions, the focus of this study remains on the alloying elements of the molten weld pool in this cracking situation. Figure 6-30 shows the in situ Cr (black) and Ni (blue) chemical compositions in wt% via LIBS and the temperature measurements via infrared thermometer from the same respective position in symmetry to welding electrode. The temperature curve clearly shows the welding process with increasing temperature slightly above 1500°C until the weld pool is created and then relative movement of the workpiece to conduct the bead-on-weld bead. The temperature curve shows an additional increase to above 1700°C while approaching 40th second of the welding process. This additional increase was due to the crack initiation and the physical bending of the sample; hence the temperature measurement height & focus of the infrared thermometer being compromised at this point.

The welding process was completed approx. at 64th second and the temperature curve starts to decay as the solidification immediately initiates in the weld end crater. This welding trial with the initiated crack demonstrated that the in situ Cr values in the weld pool in 2 mm distance from the weld electrode started at level of approx. 16wt%, 1.2wt% lower than the base material nominal value, showed an increase during welding process and as the centerline

crack followed the weld pool as the solidification initiated in the mushy zone, and reached approx. at 18wt% as the solidification of the end crater was complete. The values after the temperature curve reduced below 600°C are neglected due to fast oxide formation on the surface of the material and generating measurement artefacts.

For Ni where the lower value of the online measurements are about 3wt% higher than the base material nominal value -following the same trend as Sample 1- also showed an increasing trend and reached approx. 15wt% at the measurement location in the end crater of the weld pool. This discrepancy of the in situ recorded value is potentially a local difference of the partition coefficient and is further analyzed in the next subsection in comparison with post weld analysis discussion.

Sample 3: 1.4435/b2

Sample 3 was welded at approx. 0.53 kJ/mm and therefore no solidification cracking was initiated. The finished weld can be seen in Figure 6-31 from top view. Table 16 showed the nominal Cr and Ni chemical compositions measured on the base material via LIBS, namely “cold measurements” without the welding situation on this base material.



Figure 6-31: Finished weld seam of the Sample 3, LIBS measurement spot on the weld end crater is marked.

Figure 6-31 demonstrates the finished work piece with the bead-on-plate TIG weld in 200 mm length, with marked welding direction towards right, end crater of the weld and the LIBS measurement spot marked on the end crater. The LIBS measurement was conducted in 2 mm distance from the welding electrode. Infrared temperature measurement was done at the same spot in symmetrical respect to the welding electrode, to eliminate the effect of the LIBS plasma and capture the weld pool temperature only. In this sample, the input energy did not reach the threshold to initiate the solidification cracking due to thermo-mechanical conditions discussed in Section 2.3. or the main alloying elements didn't demonstrate any anomaly to initiate a solidification cracking under the observed conditions.

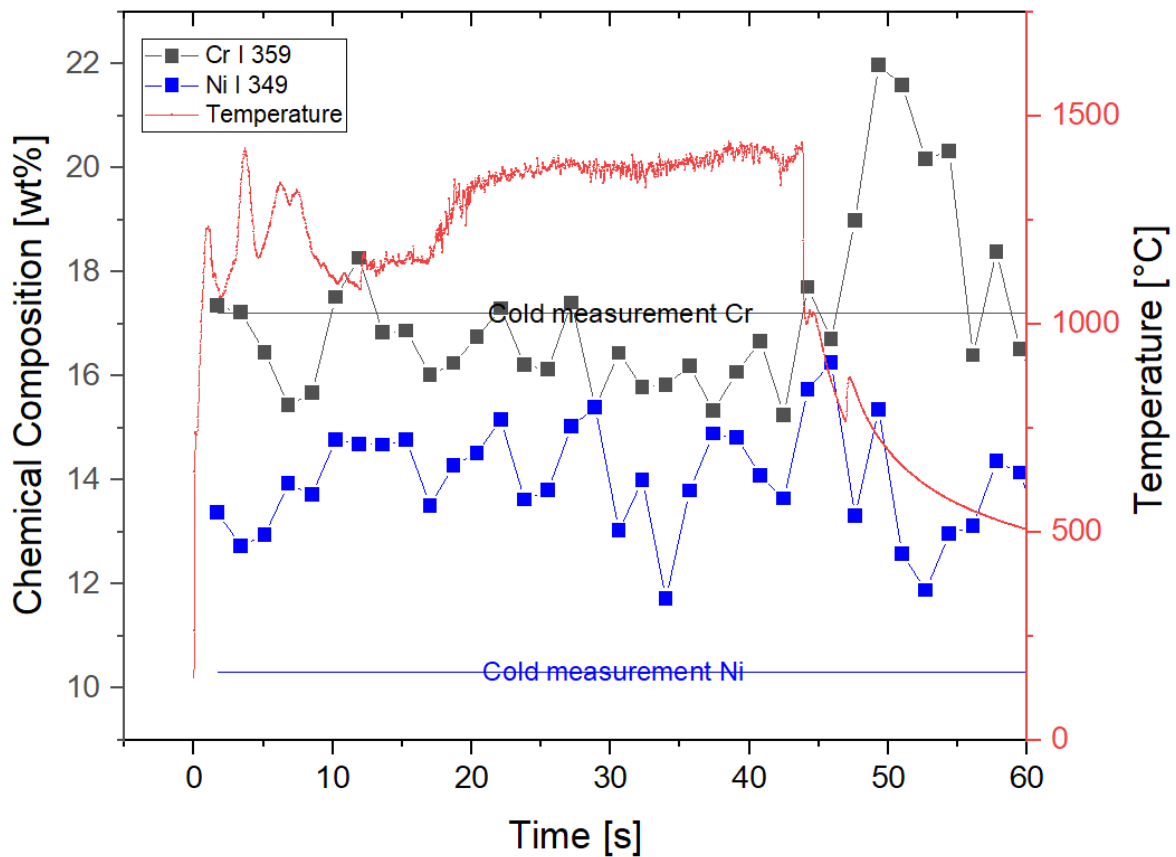


Figure 6-32: Sample 3, Online weld monitoring of element Cr and Ni over time along with the temperature measurement on the same spot to the LIBS point respective to the welding arc position.

Figure 6-32 shows the in situ Cr (left) and Ni (right) chemical compositions in wt% (black data points) via LIBS and the temperature measurements via infrared thermometer from the same respective position. The temperature curve also shows the welding process with increasing temperature near 1500°C at about 20th second. One can observe fluctuation on the temperature curve until the weld pool is created and then relative movement of the workpiece to conduct the bead-on-weld bead, this is an outcome of the moveable setup, hence the high speed convection of the material in the molten weld pool due to arc plasma jet created by the welding process. The welding process was completed approx. at 40th second and the temperature curve starts to decay as the solidification immediately initiates in the weld end crater in the terminal stage of the welding process.

Figure 6-32 demonstrated that the in situ Cr values in the weld pool in 2 mm distance from the weld electrode remained between 15wt% minimum and 18wt% maximum neglecting the values after the solidification was completed -50th second-. The average of the trend remains about 17wt% where the base material nominal value remains at 17.2wt%. For Ni, approx. the online LIBS measurement remained at about 14wt% for where it is about 3.5wt% higher than the base material nominal value.

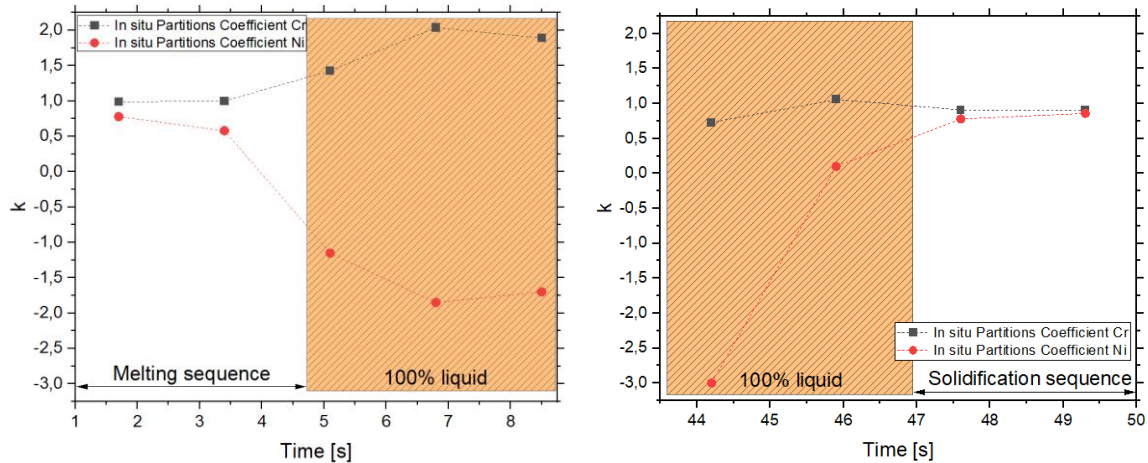


Figure 6-33: Sample 3 In situ partitions coefficient calculation. Left: first 9 seconds of the welding process. Right: The terminal stage of the welding process between 42nd and 50th seconds.

This sample was further analyzed for in situ partition coefficient calculations. To calculate, the Scheil equation was utilized with the following assumptions[141] [142] [143]:

- No diffusion occurs in solid phases after they are formed.
- Infinitely fast diffusion occurs in the liquid at all temperatures via of a high diffusion coefficient, thermal convection, Marangoni force, etc.
- Equilibrium exists at the solid-liquid interface, and so compositions from the phase diagram are valid
- The model can be only valid in transition states, namely during melting and solidification sequences

With these assumptions, a model was built to calculate the partition coefficient using the online chemical composition values. Since the model is valid only in transition states, the values under 100% liquid phase in Figure 6-33 must be considered under attention. According to the diagram, the k_{Cr} and k_{Ni} remain about 1 and 0.6 to 0.5 respectively. During liquid, Cr shows an increase where Ni decays in partitioning in the solution. This trend, however, correlates with the reduced measured values of Cr and increased measured values of the Ni, namely Cr is rejected from solution with $k > 1$ values where Ni is trapped in the solution with $k < 1$ values.

Same trend continues in the solidification sequence, yet in this case also the Cr chemical composition values shows an increasing trend after the welding process is complete. One can see the k values for both elements remain below 1 after solidification and this causing both elements' increasing partitions in the solution. This model shows also the calculated values are in good agreement with the literature, where the nominal k values under equilibrium

condition for Cr and Ni remain at 0.89 and 1,02 respectively[144].

Sample 4: 1.4435/b2

Sample 4 was welded at approx. 0.62 kJ/mm and therefore no solidification cracking observed. The finished weld can be seen in Figure 6-31 from top view. Table 16 showed the nominal Cr and Ni chemical compositions measured on the base material via LIBS, namely “cold measurements” without the welding situation on this base material.

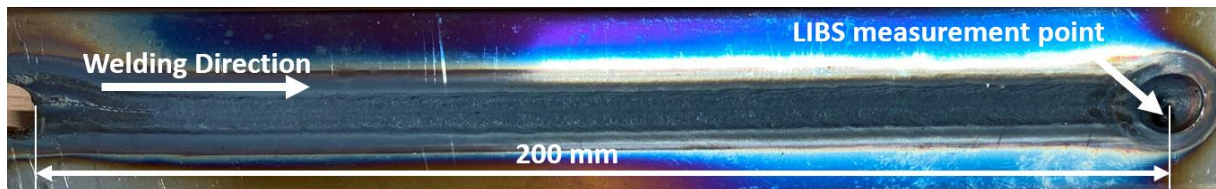


Figure 6-34: Finished weld seam of the Sample 4, LIBS measurement spot on the weld end crater is marked.

Figure 6-34 demonstrates the finished work piece with the bead-on-plate TIG weld in 200 mm length, with marked welding direction towards right, end crater of the weld and the LIBS measurement spot marked on the end crater. The LIBS measurement was conducted in 2 mm distance from the welding electrode. Infrared temperature measurement was done at the same spot in symmetrical respective to the welding electrode, to eliminate the effect of the LIBS plasma and capture the weld pool temperature only. In this sample, the input energy did not reach the threshold to initiate the solidification cracking due to thermo-mechanical conditions discussed in Section 2.3. or the main alloying elements didn't demonstrate any anomaly to initiate a solidification cracking under the observed conditions.

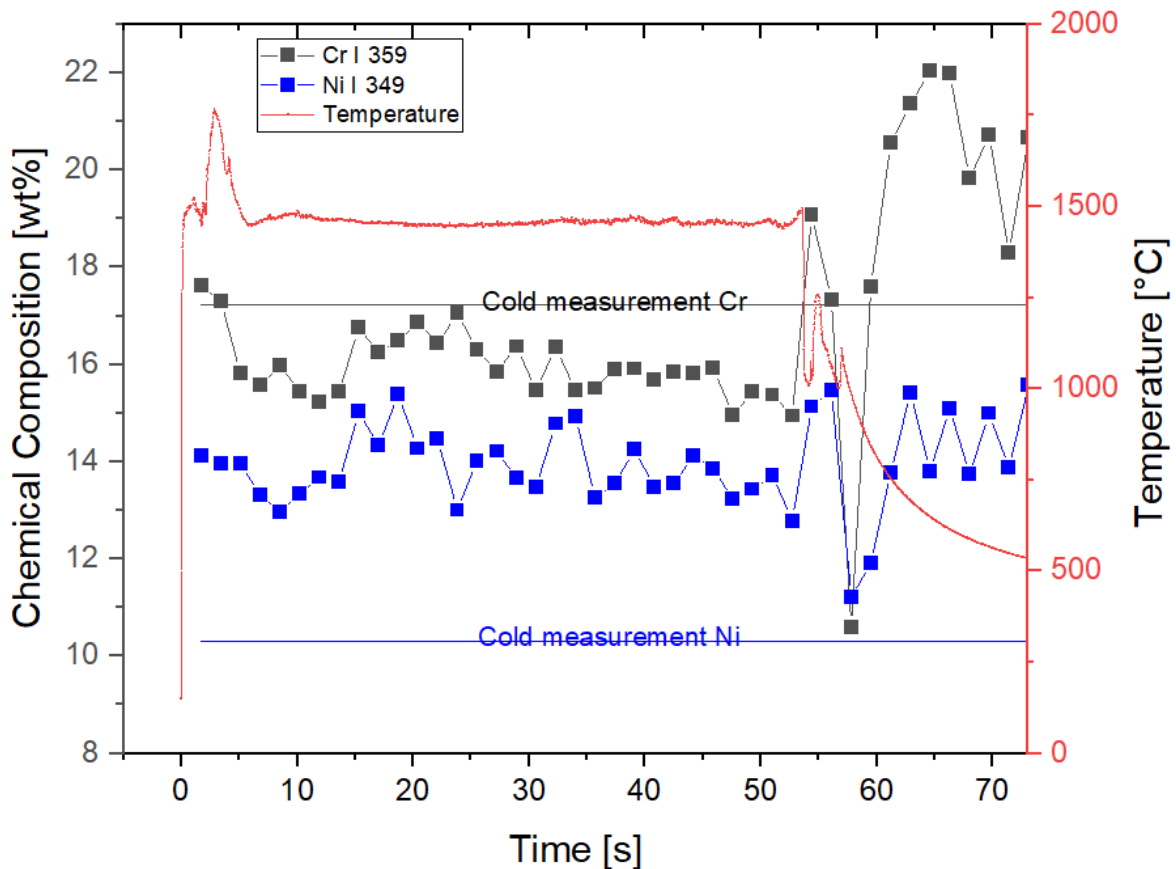


Figure 6-35: Sample 4, Online weld monitoring of element Cr and Ni over time along with the temperature measurement on the same spot to the LIBS point respective to the welding arc position.

Figure 6-35 shows the in situ Cr (black) and Ni (blue) chemical compositions in wt% via LIBS and the temperature measurements via infrared thermometer from the same respective position. The temperature curve shows the welding process starts about 1700°C in the weld pool in the beginning and remains stable at near 1500°C until the end of the process. The welding process was completed approx. at 55th second and the temperature curve starts to decay as the solidification immediately initiates in the weld end crater.

Figure 6-35 demonstrated that the in situ Cr values in the weld pool in 2 mm distance from the weld electrode remained between 15wt% minimum and 17.5wt% maximum, neglecting the values after the solidification was completed. The average of the trend remains about 16wt% where the base material nominal value remains at 17.22wt%. For Ni, approx. the online LIBS measurement fluctuated between 13wt% and 15wt% for where it is about 4wt% higher than the base material nominal value.

Although the Ni values showed higher content than the cold measurements, and Ni being an austenite promoter and therefore a potential crack propagator, this sample didn't show any solidification cracks. One can also observe that Cr values are being closer to nominal values, hence closer to the equilibrium conditions, this helps the material to remain intact during

solidification, thus undergoing a ferritic solidification as a driver.

Sample 5: 1.4435

Sample 5 was welded at approx. 0.8 kJ/mm and therefore with solidification cracking observed namely a centerline cracking among the whole weld bead was visible. The finished weld can be seen in Figure 6-36 from top view. Table 16 showed the nominal Cr and Ni chemical compositions measured on the base material via LIBS, namely “cold measurements” without the welding situation on this base material.

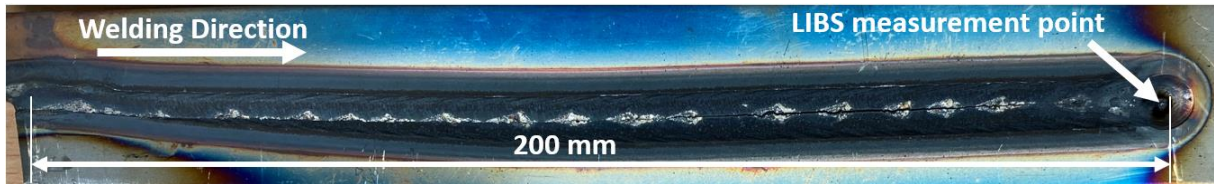


Figure 6-36: Finished weld seam of the Sample 4, LIBS measurement spot on the weld end crater is marked.

Figure 6-36 shows the finished workpiece with a 200 mm long bead-on-plate TIG weld, with the marked welding direction towards the right and the end crater of the weld marked. The LIBS measurement was taken at a spot 2 mm away from the welding electrode. The infrared temperature measurement was also taken at the same spot, symmetrical with respect to the welding electrode, to eliminate the effect of the LIBS plasma and only capture the temperature of the weld pool. In this sample, a centerline cracking is visible throughout the 200 mm long weld. The input energy reached a level that caused solidification cracking due to the thermo-mechanical conditions discussed in Section 2.3.

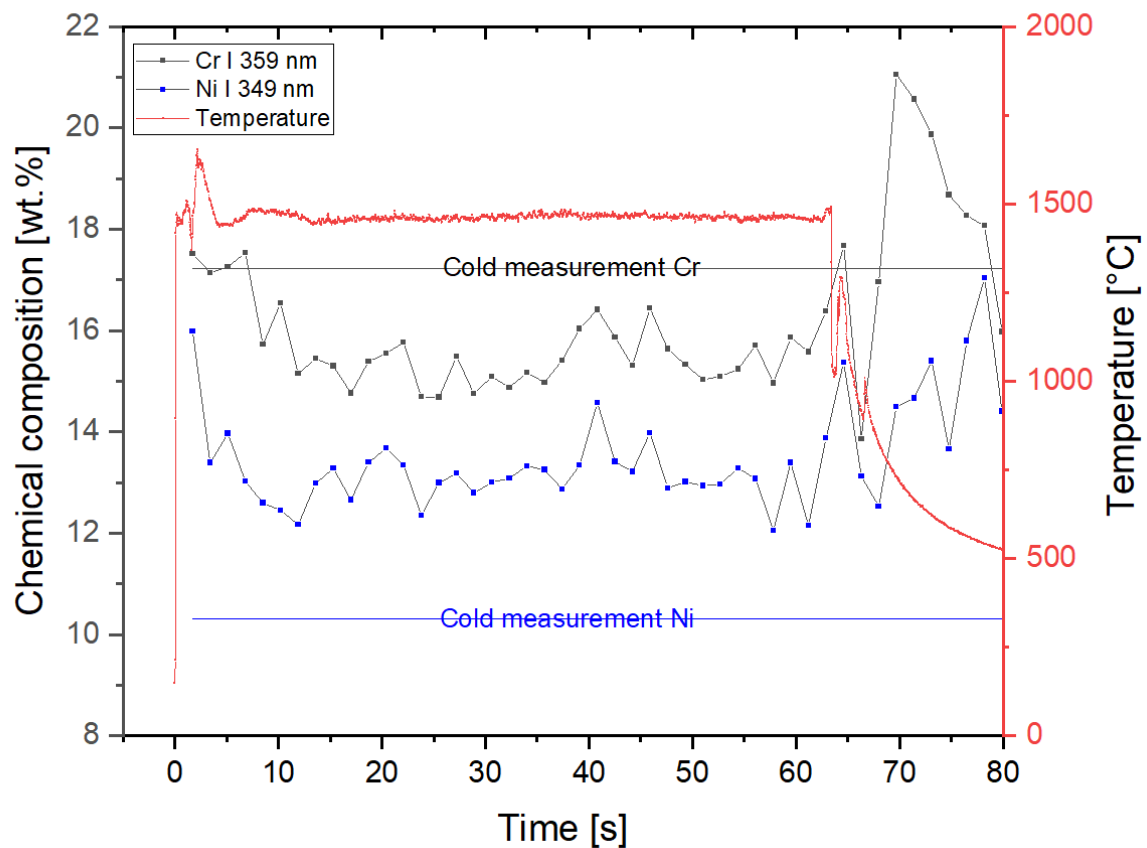


Figure 6-37: Sample 5 Cr and Ni with highlighted area

Along with the thermo-mechanical conditions reached to initiate a centerline cracking or solidification cracking, Sample 5 also showed the same characteristic and repeating behavior of the solidification cracking. Figure 6-37 shows the in situ Cr (black) and Ni (blue) chemical compositions in wt% via LIBS and the temperature measurements via infrared thermometer from the same respective position. The temperature curve shows the welding process with increasing temperature slightly above 1500°C until the weld pool is created and then relative movement of the workpiece to conduct the bead-on-weld process. The temperature curve shows a relatively stable curve at approx. 1500°C in the weld pool at the measurement location.

The welding process was completed approx. at 64th second and the temperature curve starts to decay as the solidification immediately initiates in the weld end crater. This welding trial with the initiated crack demonstrated that the in situ Cr values in the weld pool in 2 mm distance from the weld electrode started at level of approx. 18wt% and showed an initial decay and plateau at approx. 16wt% during welding process and as the centerline crack followed the weld pool as the solidification initiated among the mushy zone. The values after the temperature curve reduced below 600°C are neglected due to fast oxide formation on the surface of the material and generating measurement artefacts.

For Ni where the lower value of the online measurements are about 2wt% higher than the

base material nominal value also showed an increasing trend and reached approx. 13wt% at the measurement location during process and in the weld pool.

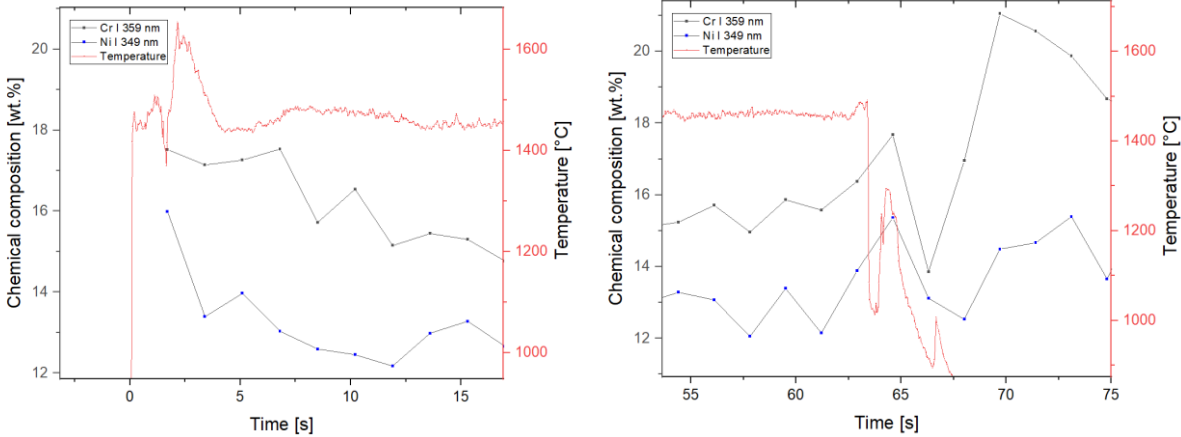


Figure 6-38: Sample 5 Cr and Ni, first 15 s in higher magnification.

Figure 6-38 shows the 0-15s (left) and 55-75s (right) intervals of the experiment in higher magnification. The diagram on the left side shows the decay of the chemical compositions for both Cr and Ni elements during the weld pool creation via heat input. This decay could be a result of possible burn-off of the mentioned alloying elements during the generation of the weld pool due to excessive heat input in the same location. However the individual partition coefficient change of the alloying elements is another possible explanation if this dramatic difference in the reading of the chemical compositions. The finding supporting this hypothesis is the stabilization of the chemical composition trends after the 10th second with the relative movement and stabilization of the weld pool temperatures.

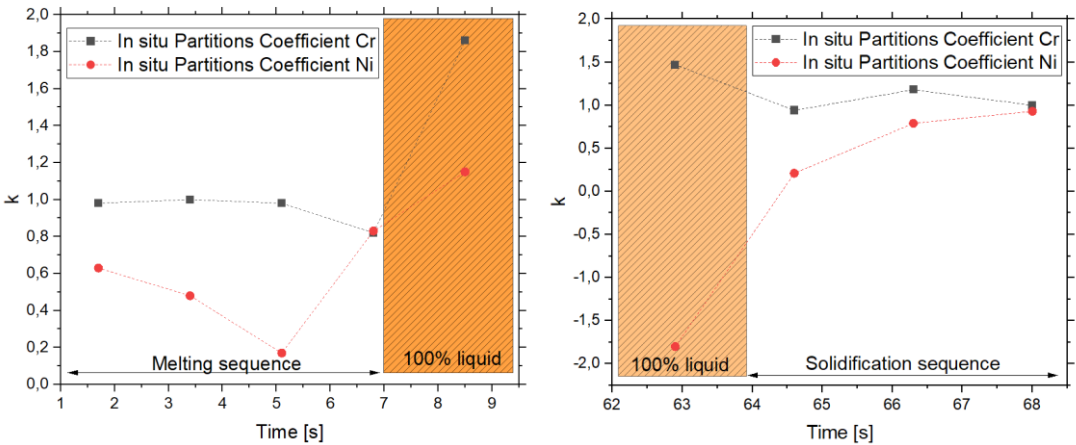


Figure 6-39: Sample 5 In situ partitions coefficient calculation. Left: first 10 seconds of the welding process. Right: The terminal stage of the welding process between 62nd and 69th seconds.

With the assumptions given in Sample 3 and using the same model, in situ partition coefficients were calculated via online LIBS chemical compositions.

According to the diagram, the k_{Cr} and k_{Ni} remain about 1.25-0.8 and 0.65 to 0.10 respectively. This trend correlates with the reduced measured values of Cr and increased measured values of the Ni than the nominal values, namely Cr is rejected from solution with $k > 1$ values where Ni is trapped in the solution with $k < 1$ values. During the melting sequence, the k_{Ni} value shows an increase towards the 100% liquid region, this is also in good agreement with inducing primary austenitic solidification by creating the main matrix enriched with Ni element. These results are also in good agreement with the metallographic samples and SEM measurements in the next sub-section.

Same trend continues in the solidification sequence, yet in this case also the Cr chemical composition values show a significant increasing trend after the welding process is complete. One can see the k values for both elements finish below 1 after solidification and this causing both elements' increasing partitions in the solution. This model shows also the calculated values are in good agreement with the literature, where the nominal k values under equilibrium condition for Cr and Ni remain at 0.89 and 1,02 respectively[144].

Sample 6: 1.4404/b1

Sample 6 was a material change (1.4404) with lower Ni values, a trial compared to the previous hot cracking process implementation experiments. It was welded at approx. 0.8 kJ/mm and expected to demonstrate a solidification cracking, yet there was no cracking observed as an outlier. The reason for this was related to the lower amount of austenite promoting alloying elements, i.e. lower Ni measures at 9.14wt%, and solidification occurring under primary ferritic conditions and decreasing the hot cracking susceptibility in general. The finished weld can be seen in Figure 6-40 from top view. Table 17 shows the nominal Cr and Ni chemical compositions measured on the base material via LIBS, namely “cold measurements” without the welding situation on this base material.

Table 17: Cold LIBS measurements on the base material (no welding) 1.4404/b1 (Material thickness = 3mm)

Element	Mean Value (wt%)	Standard Deviation
Cr	17.34	1.45
Ni	9.14	1.28

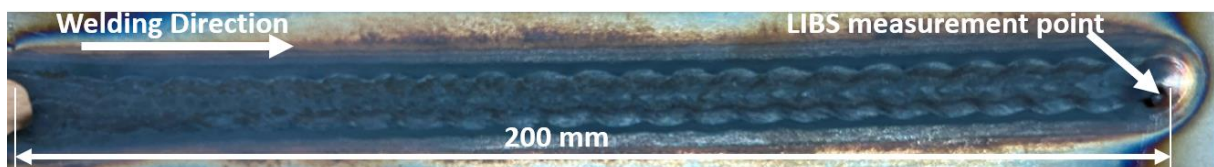


Figure 6-40: Finished weld seam of the Sample 4, LIBS measurement spot on the weld end crater is marked.

Figure 6-40 demonstrates the finished work piece with the bead-on-plate TIG weld in 200 mm length, with marked welding direction towards right, end crater of the weld and the LIBS

measurement spot marked on the end crater. The LIBS measurement was conducted in 2 mm distance from the welding electrode. Infrared temperature measurement was done at the same spot in symmetrical respective to the welding electrode, to eliminate the effect of the LIBS plasma and capture the weld pool temperature only. This sample showed an outlier situation for cracking behavior, although the input energy should reach the threshold to initiate the solidification cracking due to thermo-mechanical conditions discussed in Section 2.3., the crack propagation did not start. The main alloying elements of Cr, Ni, Mn, Mo and impurity element P were monitored during the welding process via LIBS.

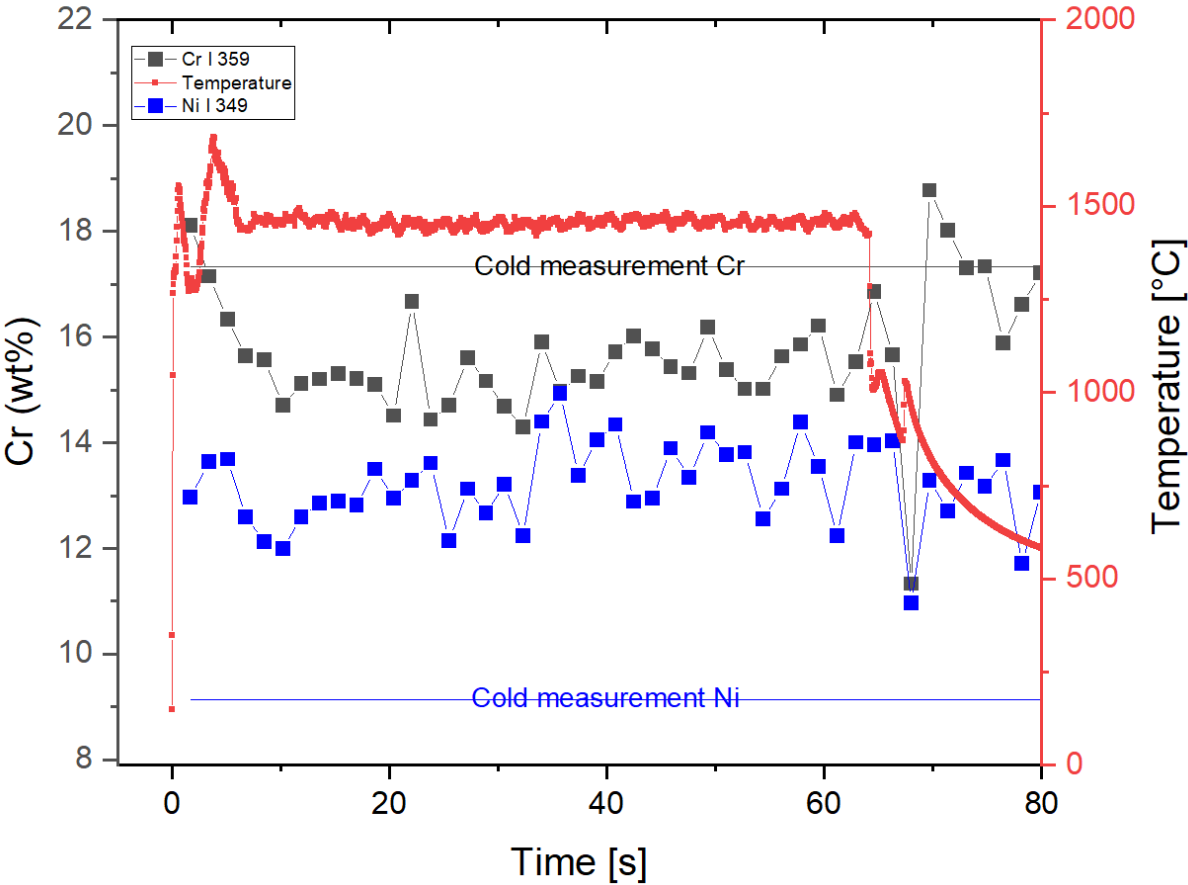


Figure 6-41: Sample 6 Cr and Ni online weld monitoring of element Cr and Ni over time along with the temperature measurement on the same spot to the LIBS point respective to the welding arc position

Figure 6-41 shows the in situ Cr (black) and Ni (blue) chemical compositions in wt% via LIBS and the temperature measurements via infrared thermometer from the same respective position. The temperature curve clearly shows the welding process with increasing temperature above 1500°C until the weld pool is created and then relative movement of the workpiece to conduct the bead-on-weld bead. The temperature curve shows a relatively stable trend at approx. 1500°C in the weld pool at the measurement location.

The welding process was completed approx. at 64th second and the temperature curve starts

to decay as the solidification immediately initiates in the weld end crater. This welding trial without the initiated crack demonstrated that the in situ Cr values in the weld pool in 2 mm distance from the weld electrode started at level of approx. 15 to 16wt% and showed an initial decay and plateau at approx. 15wt% during welding process, which is about 2wt% lower than the nominal cold measurement for Cr. This could be a possible elemental burn-off during welding or as discussed in the previous samples, a local change in the chemical composition due to local change of the partition coefficients of the alloying elements, yet this claim needs validation. No crack formation was observed in this trial; however a wavy form of weld bead was observed (see Figure 6-40).

For Ni where the lower value of the online measurement is about 3.5wt% higher than the base material nominal value, also showed an increasing trend and reached approx. 14wt% at the measurement location at approx. 30th second of welding.

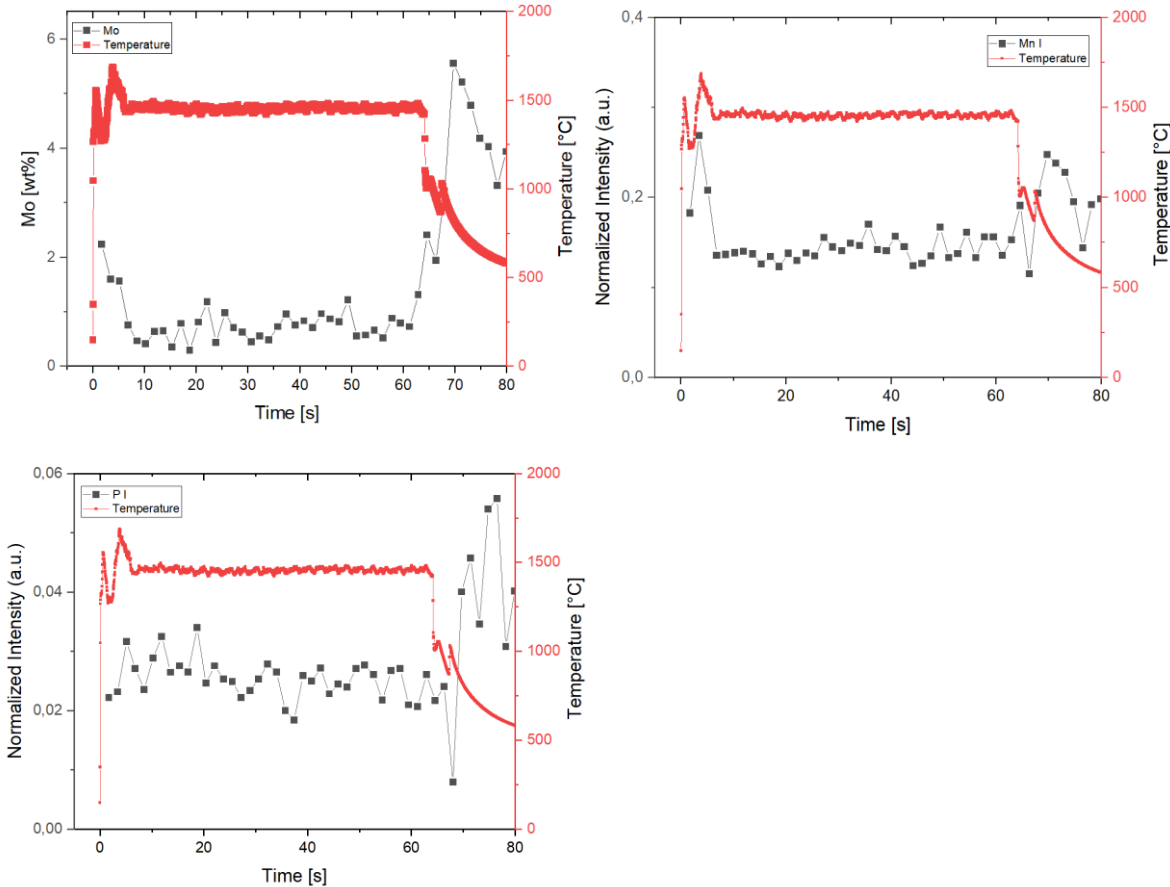


Figure 6-42: Sample 6 Mo chemical composition at 386 nm, Mn in a.u.at 403nm, P in a.u. at 213 nm.

Figure 6-42 demonstrates Mo, Mn and P online measurements, with Mo calibrated samples (with wt% calculation) and Mn and P non-calibrated normalized intensities for the Sample 6. Mo measurements show an initial decay after the sample movement begins during welding. The chemical composition of Mo stabilizes at average of 0.5wt%. The chemical composition curve of the Mo significantly increases after the welding process is complete and reaches

about 5.7wt% and remains at average of 4.1wt% after the solidification is complete. For Mn and P elements, the normalized intensity lines do not show significant outliers and remain with the same trends it was seen for the rest of the alloying elements. Mn curve remains in a plateau shape during the welding process at approx. 0.1 (a.u.). Since the calibration model was not applied (not applicable) for this sample, it is not possible to calculate the wt% value for Mn and P in this case. However, the plateau shape of the data points show a stable values for these elements during the welding process. The existence of P in this case is debatable or can be declared as below the limits of detection, due to very lower amounts expected in the base material alloy and no suitable calibration sample with the small amount of P to prove the existence of P occurrence in the weld bead. Also no significant change in the un-calibrated signal was observed for this element.

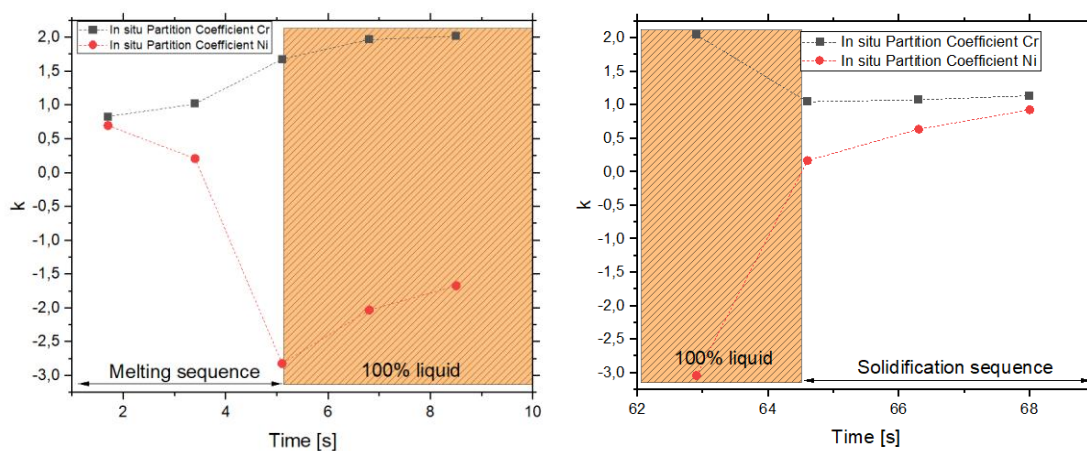


Figure 6-43: Sample 6 In situ partitions coefficient calculation. Left: first 10 seconds of the welding process. Right: The terminal stage of the welding process between 62nd and 69th seconds.

According to the diagram in Figure 6-43, the k_{Cr} and k_{Ni} remain about 0.8-1.6 and 0.75 towards negative trend respectively. During liquid, Cr shows an increase where Ni increase in partitioning in the solution. This trend correlates with the decaying measured values of Cr starting at higher than nominal and increased measured values of the Ni than nominal in general, namely Cr is rejected from solution with $k > 1$ values where Ni is trapped in the solution with $k < 1$ values.

k_{Cr} remains at about 1 during solidification sequence, where the online chemical composition values are close to nominal values, yet in this case also the Cr chemical composition values show an increasing trend after the welding process is complete. One can see the k values for Ni remain below 1 after solidification and this causing Ni increasing partition in the solution and closing the measured chemical composition to nominal values.

Sample 7: 1.4404/b1

Sample 7 was a repetition of the same material (1.4404) and previous trial. It was welded at

approx. 0.8 kJ/mm and expected to demonstrate a solidification cracking, The cracking was observed in the first approx. 80mm of the weld bead. The reason for this was similar to the previous trial and related to the lower amount of austenite promoting alloying elements and solidification occurring mainly under ferritic conditions and decreasing the hot cracking susceptibility. The finished weld can be seen in Figure 6-44 from top view with this material observed characteristic wavy form. Table 17 was given for the nominal Cr and Ni chemical compositions measured on the base material via LIBS.

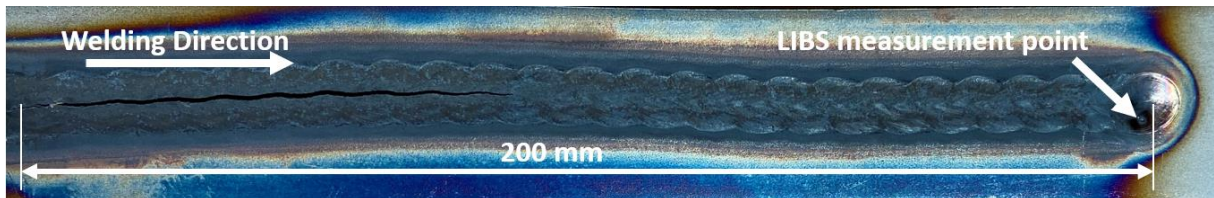


Figure 6-44: Finished weld seam of the Sample 7, LIBS measurement spot on the weld end crater is marked.

Figure 6-44 demonstrates the finished work piece with the bead-on-plate TIG weld in 200 mm length, with marked welding direction towards right, end crater of the weld and the LIBS measurement spot marked on the end crater. The LIBS measurement was conducted in 2 mm distance from the welding electrode. Infrared temperature measurement was done at the same spot in symmetrical respective to the welding electrode, to eliminate the effect of the LIBS plasma and capture the weld pool temperature only. The main alloying elements of Cr, Ni, Mn, Mo and impurity element P was during the welding process via LIBS monitored.

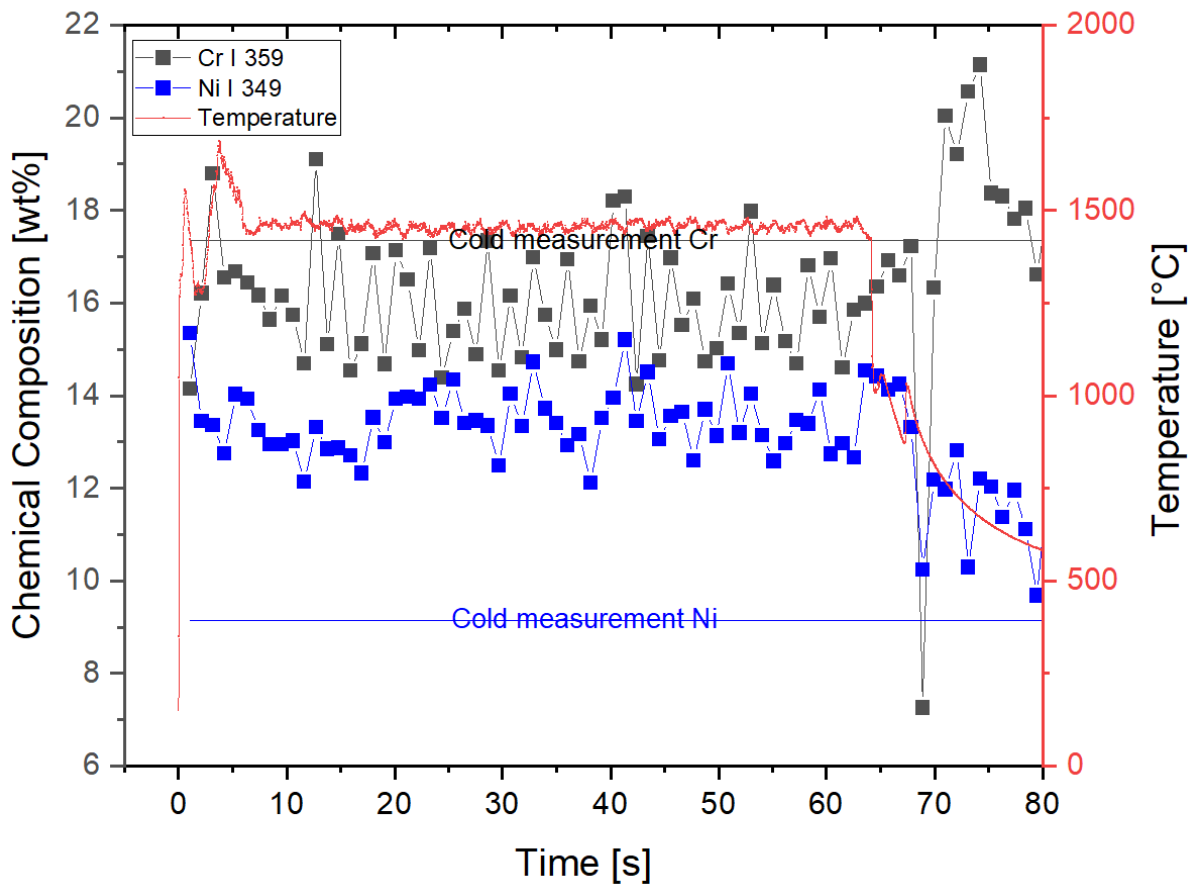


Figure 6-45: Sample 7 Cr and Ni online weld monitoring of element Cr and Ni over time along with the temperature measurement on the same spot to the LIBS point respective to the welding arc position

Figure 6-45 shows the in situ Cr (black) and Ni (blue) chemical compositions in wt% via LIBS and the temperature measurements via infrared thermometer from the same respective position. The temperature curve shows the welding process with increasing temperature slightly above 1500°C until the weld pool is created following with the relative movement of the workpiece to start the bead-on-weld. The temperature curve shows a stable curve at approx. 1500°C in the weld pool at the measurement location.

The welding process was completed approx. at 64th second and the temperature curve starts to decay as the solidification immediately initiates in the weld end crater. This welding trial with the initiated crack demonstrated that the in situ Cr values in the weld pool in 2 mm distance from the weld electrode started at level of approx. 14wt% and fluctuated between 15-17wt% during welding process. The center line crack formation was observed in this trial during the first 80mm of the weld; the wavy form of weld bead was also present.

For Ni where the lower value of the online measurement is about 3wt% higher than the base material nominal value, also showed an increasing trend and reached approx. 14wt% at the measurement location at approx. 20th second of welding, where this also coincides with the

end of the centerline cracking. The average of the Cr measurements are also closer to the cold measurement values after about 15th second of the welding, which is also in good agreement with promoting a primary ferritic solidification modulus and eliminating the initial solidification cracking.

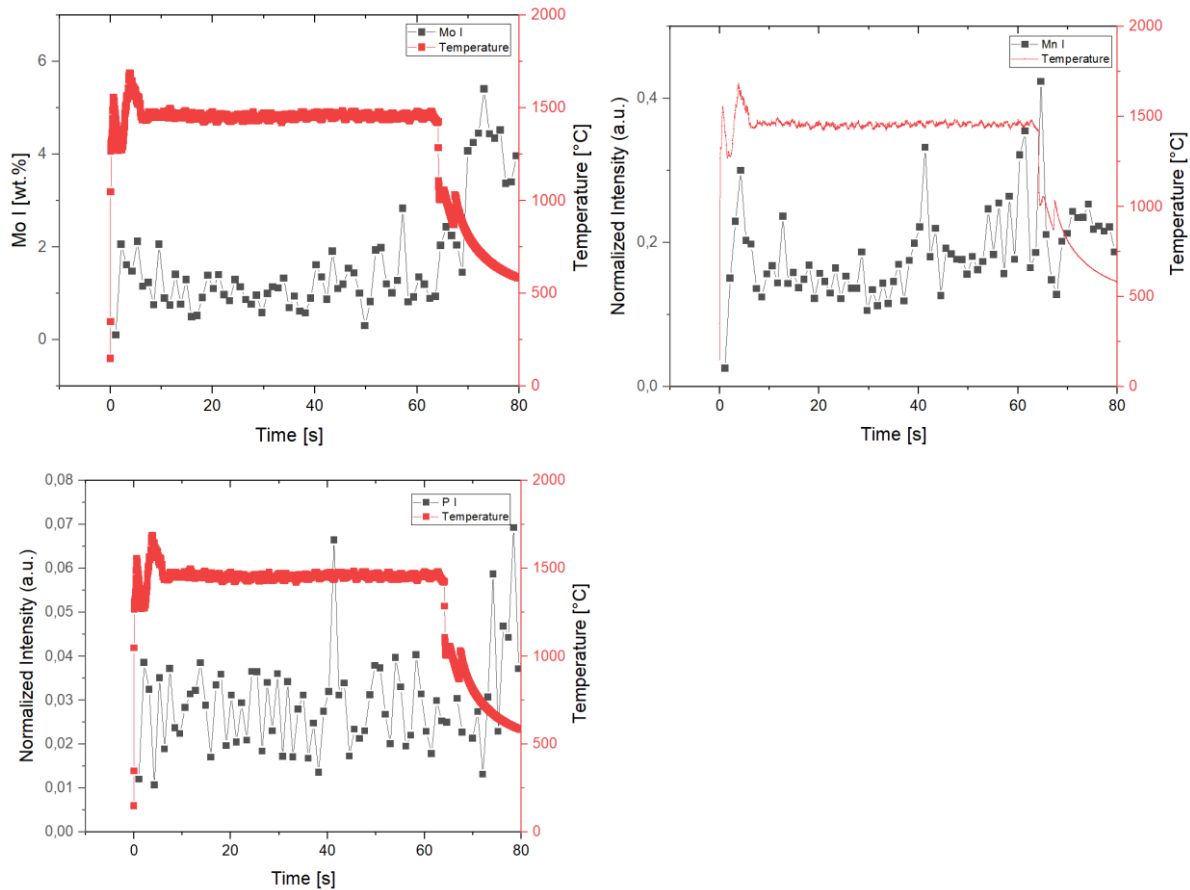


Figure 6-46: chemical composition at 386 nm, Mn in a.u.at 403nm, P in a.u. at 213 nm

Figure 6-46 demonstrates Mo, Mn and P online measurements, with Mo calibrated samples (with wt% calculation) and Mn and P non-calibrated normalized intensities for the Sample 7. Mo measurements show an initial decay after the sample movement begins during welding. Different to Sample 6, in this measurement the chemical composition of Mo stabilizes at average of 1wt% and fluctuates more than the latter sample trial. The chemical composition curve of the Mo significantly increases after the welding process is complete and reaches also about 5.7wt% and remains at average of 4.1wt% after the solidification is complete -similar behavior as Sample 6-.

For Mn and P elements, the normalized intensity lines do not show significant outliers and remain with the same trends it was seen for the rest of the alloying elements also similar to Sample 6. Mn remains in a plateau shape during the welding process at slightly above 0.1 level (a.u.). The plateau shape of the data points indicates a stable wt% values for these elements during the welding process. No significant change in the un-calibrated signal of P was

observed, namely it lies between 0.01 and 0.04 (a.u.) level.

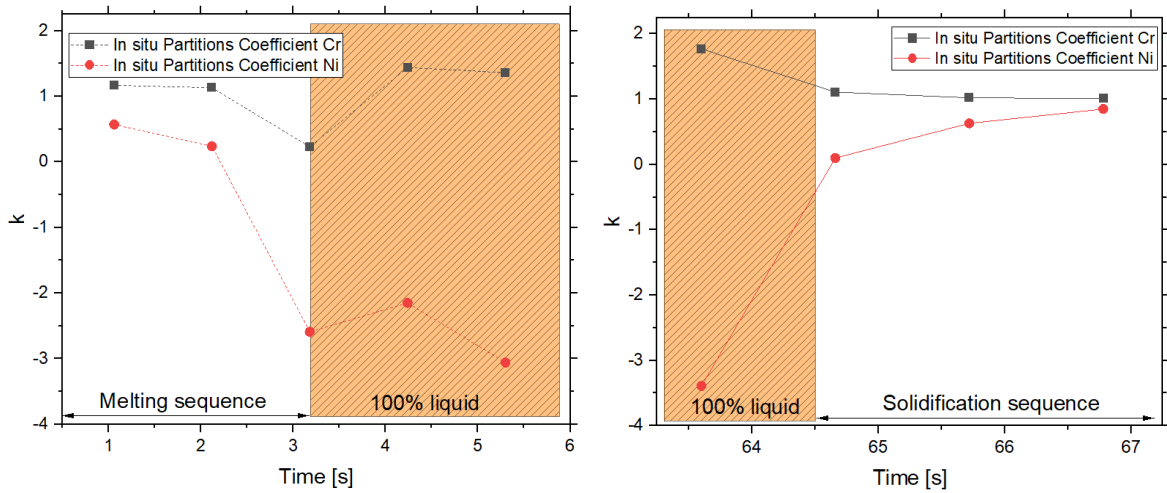


Figure 6-47: Sample 7 In situ partitions coefficient calculation. Left: first 6 seconds of the welding process. Right: The terminal stage of the welding process between 63rd and 67th seconds.

According to the diagram in Figure 6-47, the k_{Cr} and k_{Ni} remain about 1.2-0.4 and 0.70 towards negative trend respectively during melting sequence. During liquid, Cr shows an increase where Ni increase in partitioning in the solution. This trend, correlates with the increasing measured values of Cr in the melt hence, increased measured values of the Ni than nominal in general, namely Cr is rejected from solution with $k > 1$ values and this trend changes by system reducing it below 1 to capture more Cr to reach equilibrium conditions where Ni is trapped in the solution with $k < 1$ values. This indicates also that system is working thermodynamically towards to reach an equilibrium state and compensate the cracking situation by increasing the Cr value in the liquid phase to initiate a primary ferritic solidification modus.

k_{Cr} remains at about 1 during solidification sequence, where the online chemical composition values are closer to nominal values than the melting sequence, yet in this case also the Cr chemical composition values show an increasing trend after the welding process is complete. One can see the k values for Ni remain below 1 after solidification but increasing and this causing Ni's increasing partition in the solution and reaching the closer measured chemical composition to the nominal Ni-values.

Sample 8: 1.4435/b2

Sample 8 was welded at approx. 0.8 kJ/mm, was a repetition of the Sample 5 conditions and therefore with solidification cracking observed namely a centerline cracking among the whole weld bead was visible. The finished weld can be seen in Figure 6-48 from top view. Table 16 showed the nominal Cr and Ni chemical compositions measured on the base material via LIBS, namely "cold measurements" without the welding situation on this base material.

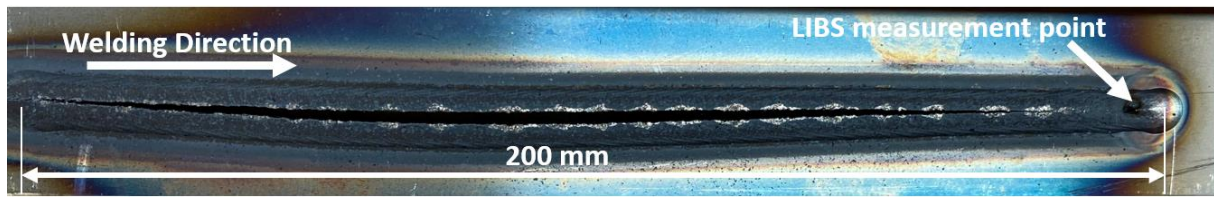


Figure 6-48: Finished weld seam of the Sample 8, LIBS measurement spot on the weld end crater is marked.

Figure 6-48 demonstrates the finished work piece with the bead-on-plate TIG weld in 200 mm length, with marked welding direction towards right, end crater of the weld and the LIBS measurement spot marked on the end crater. The LIBS measurement was conducted in 2 mm behind the welding electrode. Infrared temperature measurement was done at the same spot in symmetrical respect to the welding electrode. In this sample, a centerline cracking is, similarly to sample 5, visible among the whole weld in 200 mm length. The input energy reached the threshold to initiate the solidification cracking.

Sample 8 also showed the same characteristic and repeating behavior of the solidification cracking. Figure 6-49 shows the in situ Cr (black) and Ni (blue) chemical compositions in wt% via LIBS and the temperature measurements via infrared thermometer from the same respective position. In this sample the temperature curve clearly shows the welding process with reaching temperature slightly above 1500°C until the weld pool is created and then relative movement of the workpiece starts to conduct the bead-on-weld bead. The temperature curve shows a decay during welding process and ends at approx. 1200°C in the end crater.

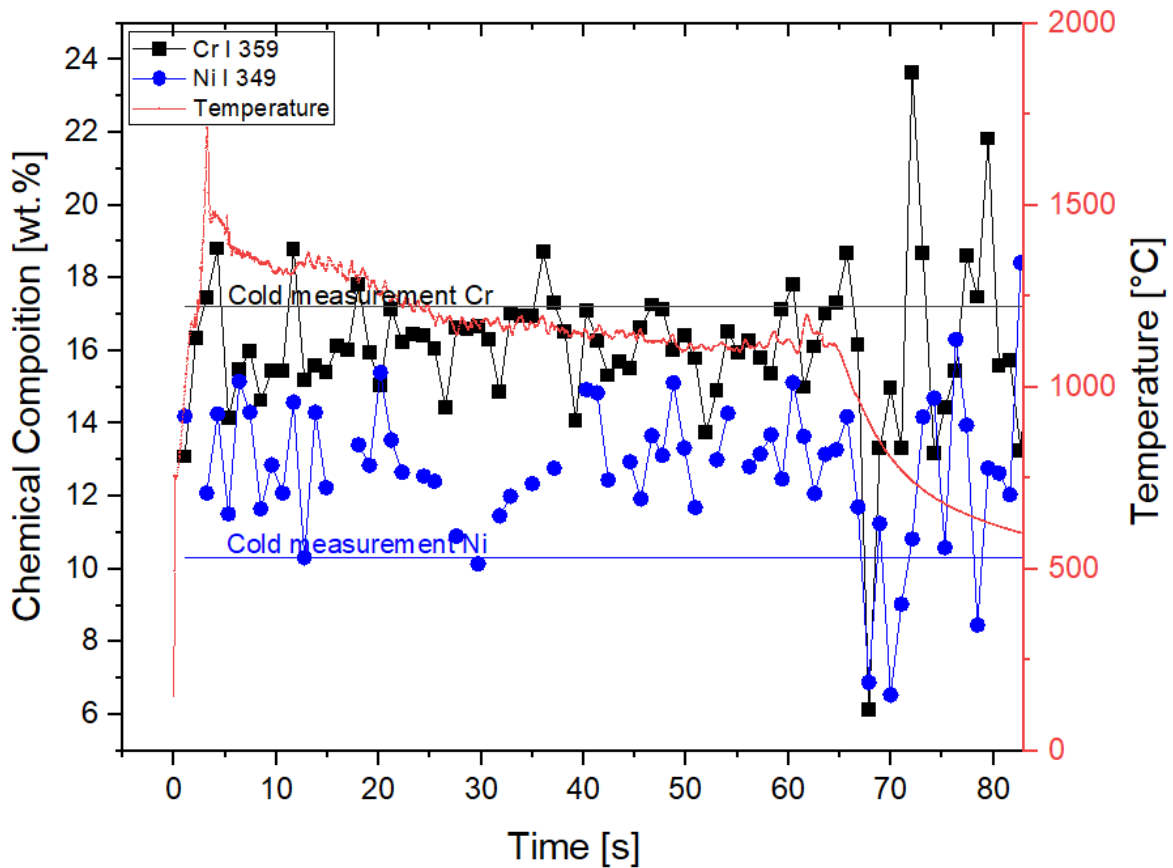


Figure 6-49: Sample 8 Cr and Ni online weld monitoring of element Cr and Ni over time along with the temperature measurement on the same spot to the LIBS point respective to the welding arc position

The welding process was completed approx. at 64th second and the temperature curve starts to decay as the solidification immediately initiates in the weld end crater. This welding trial with the initiated crack demonstrated that the in situ Cr values in the weld pool in 2 mm behind from the weld electrode started at level of approx. 16wt% and showed relatively stable plateau at approx. 16-17wt% during welding process and as the centerline crack followed the weld pool with the solidification initiated among the mushy zone.

For Ni where the lower value of the online measurements are similarly about 2wt% higher than the base material nominal value also showed a fluctuating trend, reached approx. 15wt% max. and 10.3wt% min. at the measurement location during process and in the weld pool.

Sample 9: 1.4435/b2

Sample 9 was welded at approx. 0.8 kJ/mm, was a repetition of the conditions from Sample 5 and 8, therefore with solidification cracking observed namely a centerline cracking among the whole weld bead was visible. The finished weld can be seen in Figure 6-50 from top view. Table 16 showed the nominal Cr and Ni chemical compositions measured on the base material via LIBS, namely “cold measurements” without the welding situation on this base material.

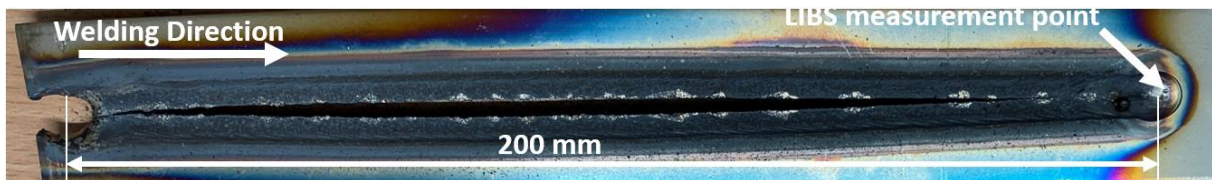


Figure 6-50: Finished weld seam of the Sample 8, LIBS measurement spot on the weld end crater is marked.

Figure 6-50 demonstrates the finished work piece with the bead-on-plate TIG weld in 200 mm length, with marked welding direction towards right, end crater of the weld and the LIBS measurement spot marked on the end crater. The LIBS measurement was conducted in 2 mm behind the welding electrode. Infrared temperature measurement was done at the same spot in symmetrical respective to the welding electrode. In this sample, a centerline cracking is , similarly to sample 5 and 8, visible among the whole weld in 200 mm length.

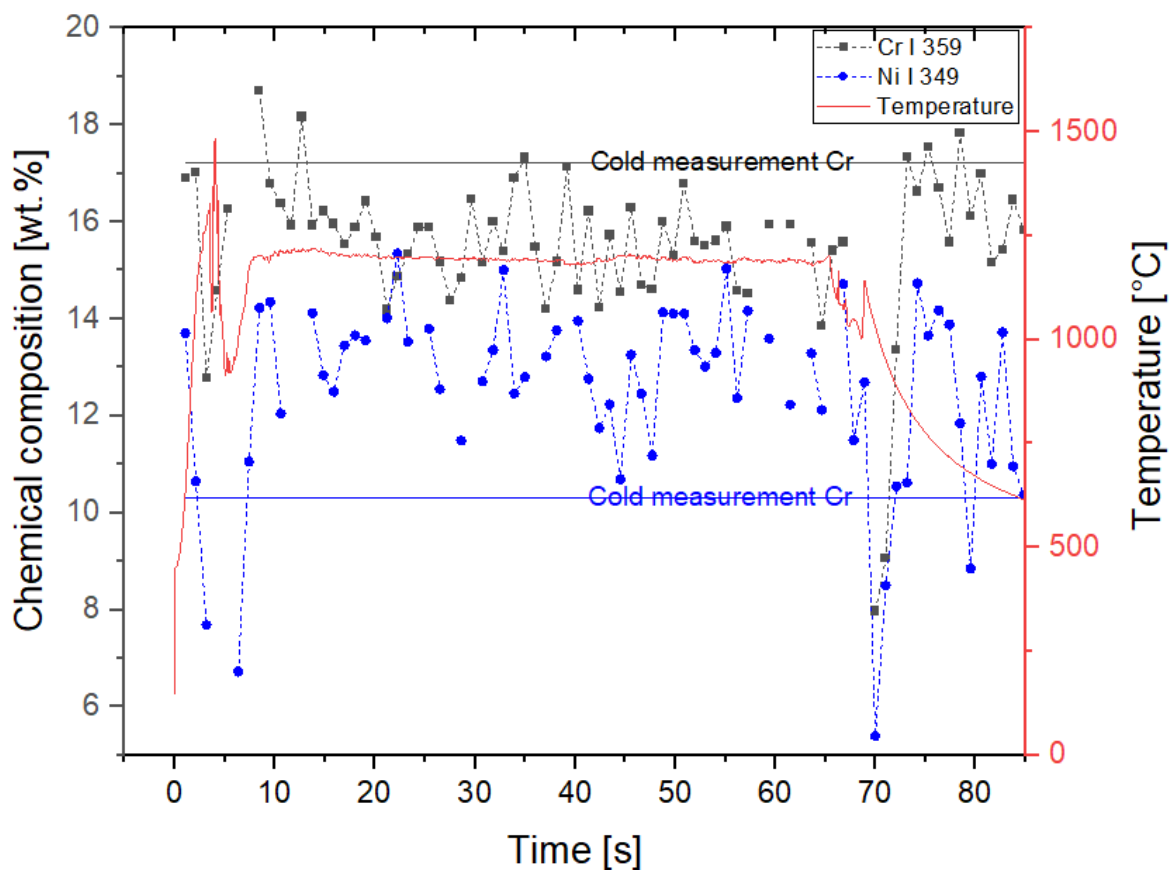


Figure 6-51 Sample 9 Cr and Ni online weld monitoring of element Cr and Ni over time along with the temperature measurement on the same spot to the LIBS point respective to the welding arc position

Sample 8 also showed the same characteristic and repeating behavior of the solidification cracking. Figure 6-51 shows the in situ Cr (black) and Ni (blue) chemical compositions in wt% via LIBS and the temperature measurements via infrared thermometer from the same

respective position. In this sample the temperature curve clearly shows the welding process with reaching temperature stable about 1200°C until the weld pool is created and then relative movement of the workpiece starts to conduct the bead-on-weld bead.

The welding process was completed approx. at 64th second and the temperature curve starts to decay as the solidification immediately initiates in the weld end crater. This welding trial with the initiated crack demonstrated that the in situ Cr values in the weld pool in 2 mm behind from the weld electrode started at level of approx. 16wt% and showed fluctuation between 15-18wt% during welding process and as the centerline crack followed the weld pool with the solidification initiated among the mushy zone.

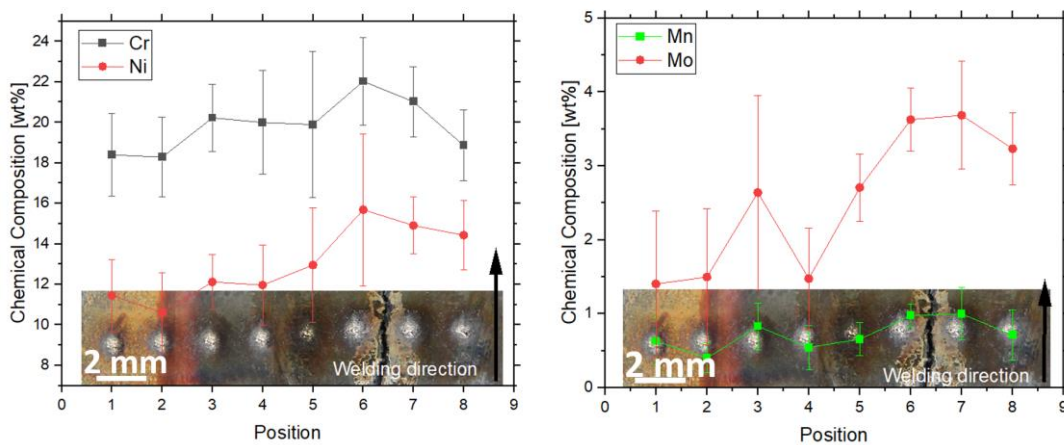
For Ni where the lower value of the online measurements are similarly about 3wt% higher than the base material nominal value also showed a fluctuating trend, reached approx. 15wt% max. and 10.3wt% min. (without outliers below 10wt%) at the measurement location during process and in the weld pool.

6.2.3 Post-weld crack investigations

Post-weld crack investigations were conducted using the ex situ setup of the LIBS system. The investigation was focused mainly on the chemical compositions of the transverse line scans from the completed and cracked welds, crack surfaces and weld end-crater chemical compositions to reveal spatial distribution of the individual alloying elements and any possible correlation with the in situ measured data. The line scans were conducted in the middle section of the weld length (approx. 100mm from the beginning) to have representative data for the whole weld bead.

Sample 2:

LIBS Linescan



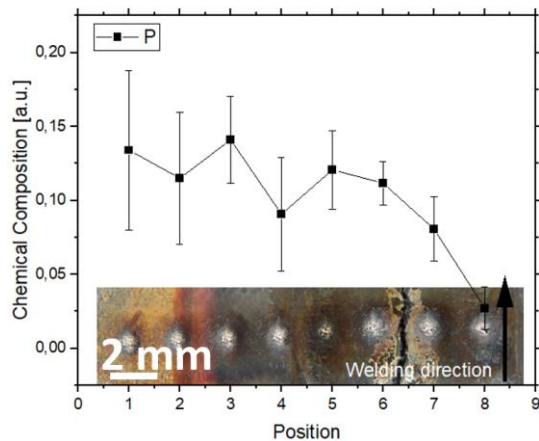


Figure 6-52: Sample 2 Post-weld LIBS line scan for Cr, Ni, Mn, Mo in wt%, and P in a.u. units across the weld bead and crack edges. Position 6 and 7 are the measurements taken at the crack edges

Figure 6-52 is presenting data for eight positions from Sample 2, and for each position, it shows the Cr, Ni, Mn, Mo content in weight percent (wt%), P in arbitrary units (a.u.) and the standard deviation (St. Dev.) of each position. The center line cracking can be seen between data points 6 and 7. Welding direction is toward up in the figure.

Figure 6-52 Top left: The chromium content ranges from 18.3 wt% in position 1 to 22.0 wt% in position 6. The standard deviation of the chromium content ranges from 1.9 in position 2 to 3.6 in position 5. The highest chromium content was observed at the position 6 and 7 where the cracking occurs in between. The nickel content ranges from 10.6 wt% in position 2 to 15.6 wt% in position 6. The standard deviation of the nickel content ranges from 1.3 in position 3 to 3.7 in position 6. Similarly to Cr, highest observed Ni content was observed in position 6 and 7.

Figure 6-52 Top right: the manganese content ranges from 0.6 wt% in position 1 to 0.9 wt% in position 7. The standard deviation of the manganese content ranges max. approx. at 0.3. For the molybdenum data, the molybdenum content ranges from 1.4 wt% in position 1 to 3.6 wt% in position 7. The standard deviation of the molybdenum content ranges from 0.9 in position 1 to 0.7 in position 7. Similar to other alloying elements, the higher composition of Mo was observed at the crack edges.

Higher content of the alloying elements nearing the crack edges are in good agreement with local changing of the chemical compositions, thus partition coefficient of the individual elements during solidification.

Figure 6-52 bottom is showing data for eight positions, with values for phosphorus (P) in arbitrary units (a.u.) and standard deviation (St. Dev.) for each position. The phosphorus content ranges from 0.13 a.u. in position 1 to 0.02 a.u. in position 8. The standard deviation of the phosphorus content ranges from 0.05 in position 1 to 0.01 in position 8. The phosphorus content decreases as the position increases, and the standard deviation of the phosphorus

content also decreases as the position number increases. This suggests that the phosphorus content is generally decreasing across the line scan and weld transverse direction and the spread of the phosphorus content is also decreasing. However, it's worth noting that this trend may not necessarily hold true for positions outside of the ones shown in the graph.

As a general trend for Sample 2 and elements Cr, Ni, Mn and Mo, they seem to have a higher content across the weld center line across the crack edges. This doesn't apply for the P content measured in a.u.

Crack surface LIBS analysis

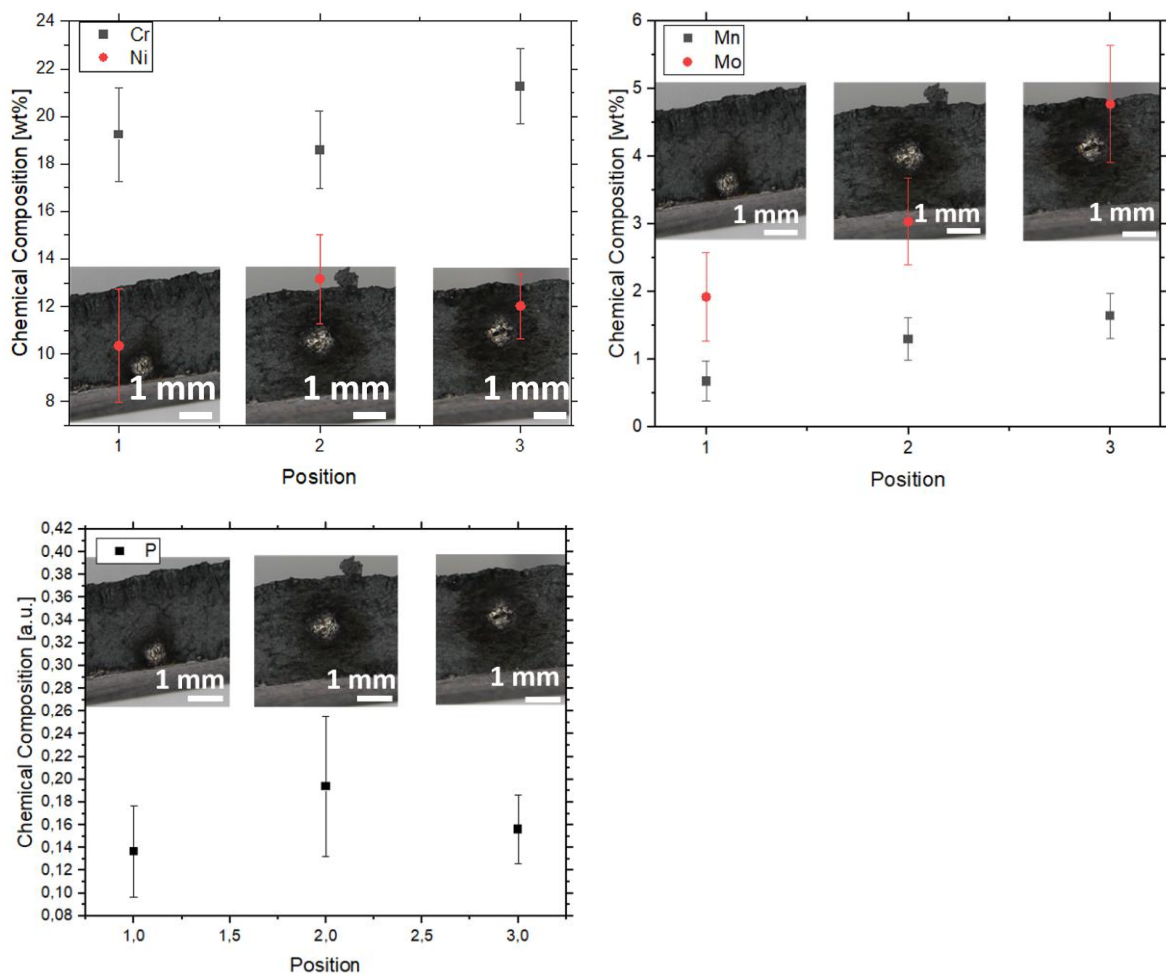


Figure 6-53: Sample 2 Post-weld Crack surface LIBS analysis

Figure 6-53 shows the crack surface measurements taken on three different positions for the alloying elements. The position 1 is close to bottom side of the work piece where the second and third positions were at the mid-range of the work piece and weld center crack. The graphs are presenting data for three positions, providing information about the weight percent of Cr, Ni, Mn, Mo in wt% and P in a.u. in that position, as well as the standard deviation for each of these measurements.

Figure 6-53 top left shows that in position 1, the composition of chromium is 19.2wt%, with a standard deviation of 1.9. The composition of nickel in this position is 10.3wt%, with a standard deviation of 2.3. The data for position 2, with the composition of chromium being 18.5 wt% and the of nickel being 13.1 wt%. The standard deviations for these measurements are 1.6 and 1.8, respectively. The third position shows data for chromium composition being 21.2 wt% and the nickel being 12.0 wt%. The standard deviations for these measurements are 1.5 and 1.3, respectively.

Figure 6-53 top right is showing data for three positions, with values for Mn content in weight percent (wt%) and standard deviation (St. Dev.) for each position, as well as values for Mo content in weight percent (wt%) and standard deviation (St. Dev.) for each position.

For the manganese data, the manganese content ranges from 0.6 wt% in position 1 to 1.6 wt% in position 3. The standard deviation of the manganese content ranges from 0.2 in position 1 to 0.3 in position 3. For the molybdenum data, the molybdenum content ranges from 1.9 wt% in position 1 to 4.7 wt% in position 3. The standard deviation of the molybdenum content ranges from 0.6 in position 1 to 0.8 in position 3. It seems that the manganese and molybdenum content both increase at the position 2 and 3, and the standard deviation of both the manganese and molybdenum content also increases at position 2 and 3. This suggests that the manganese and molybdenum content are both generally increasing from bottom to surface of the work piece on the crack surface and the spread of the manganese and molybdenum is also increasing looking at the standard deviations.

Figure 6-53 bottom is showing data with values for phosphorus (P) content in in arbitrary units (a.u.) and standard deviation for each position. The phosphorus content ranges from 0.13 a.u. in position 1 to 0.15 a.u. in position 3. The standard deviation of the phosphorus content ranges from 0.04 in position 1 to 0.03 in position 3. The phosphorus content is generally increasing at position 2 and 3, the standard deviation of the phosphorus content is at highest in position 2 and decreasing as the position number increases to 3. It is also important to mention that P content is relatively higher than the sample surface, which can be seen in the surface line scans, indicating a potential accumulation of the impurity elements on the crack surface, in good agreement with the solidification theory.

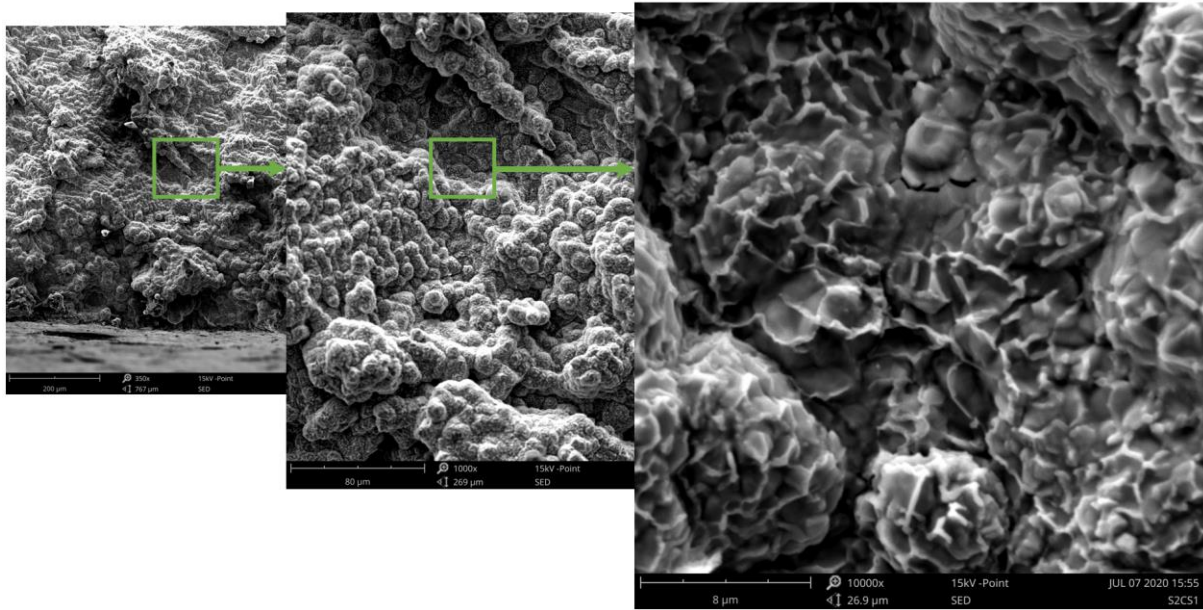


Figure 6-54: Sample 2 Crack surface SEM analysis. Dendritic formation is visible on the crack surface.

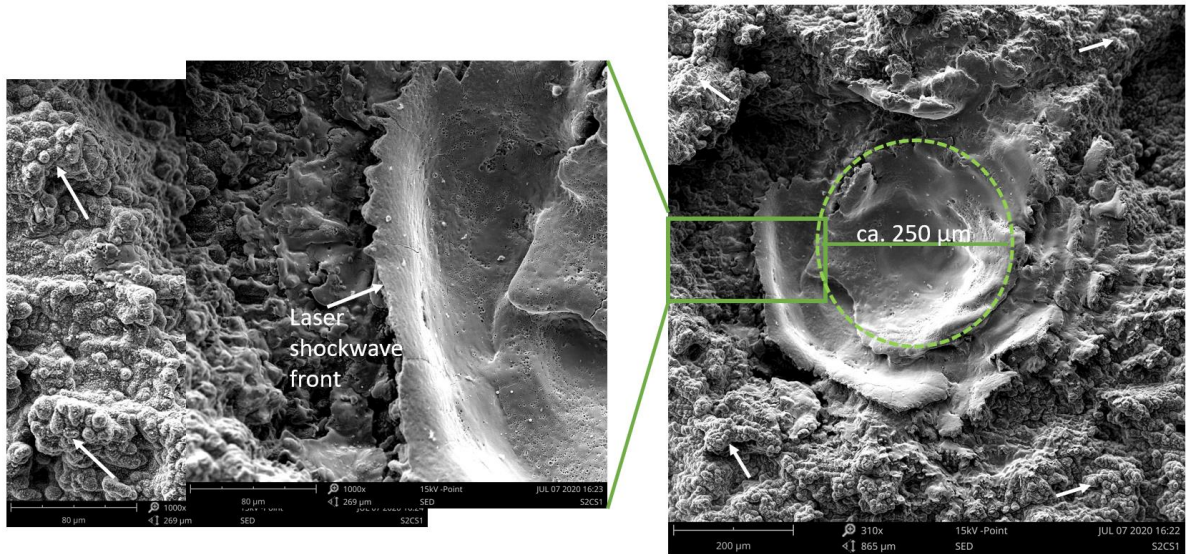


Figure 6-55: Sample 2 crack surface SEM analysis with the LIBS measurement spot. LIBS measurement spot can be seen along with the laser shockwave formation.

Figure 6-54 and Figure 6-55 demonstrate the SEM images of the crack surface and the LIBS measurement spot using secondary electron detector. These images clearly show the columnar dendritic growth and respective solidification front at the crack surface. LIBS measurement spot consists of approx. 250μm circumference to receive the online chemical composition measurement data.

Sample 7:

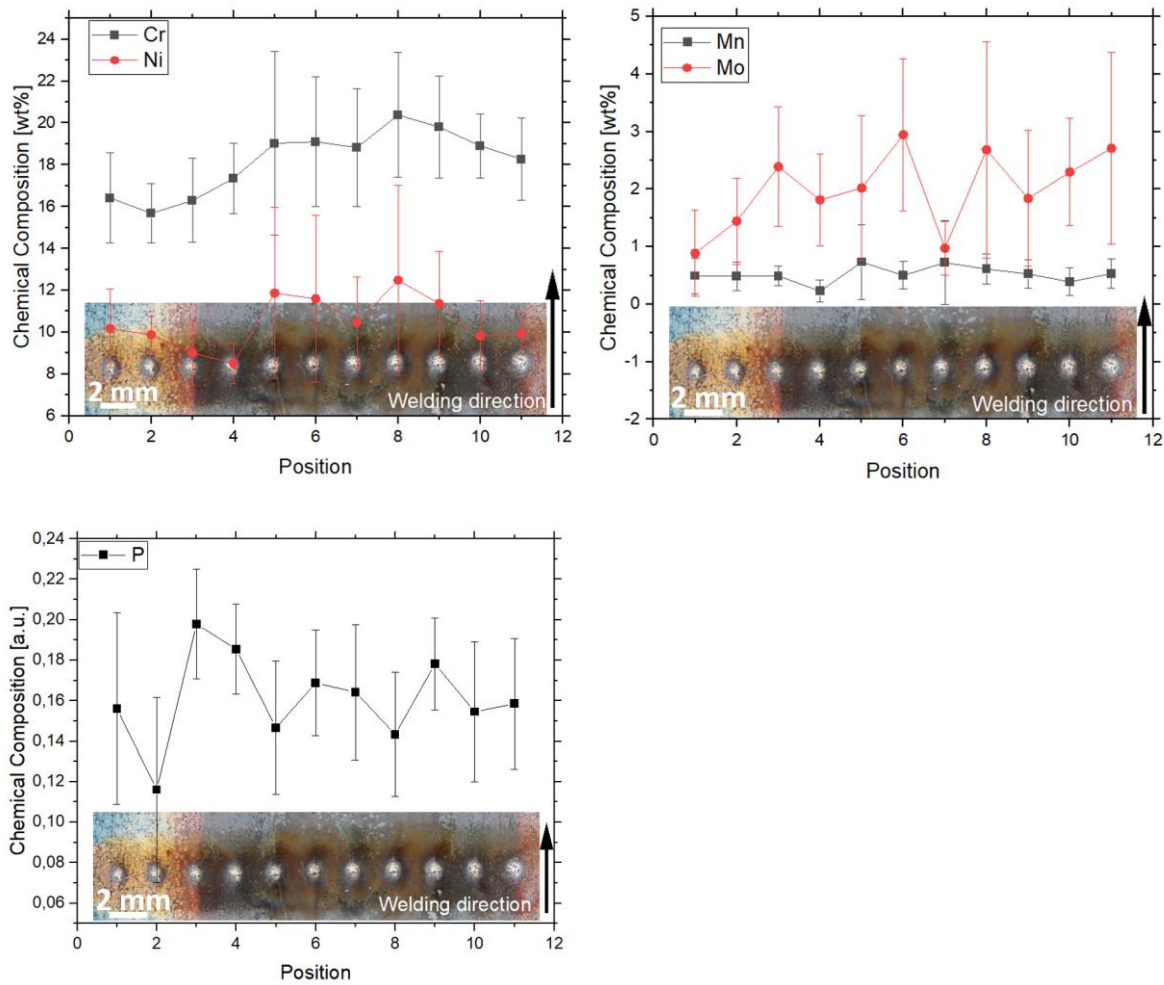


Figure 6-56: Sample 7 Post-weld line scan 1 no crack situation

Figure 6-56 is presenting data for eleven positions from Sample 7, and for each position, it shows the Cr, Ni, Mn, Mo content in weight percent (wt%), P in arbitrary units (a.u.) and the standard deviation (St. Dev.) of the respective position. This is the representative measurement for no crack situation made on the sample.

Figure 6-56 top left is showing data for eleven positions, with values for Cr content in weight percent (wt%) and standard deviation (St. Dev.) for each position, as well as values for Ni content in weight percent (wt%) and standard deviation (St. Dev.) for each position.

For the chromium data, the chromium chemical composition ranges from 16.4 wt% in position 1 to 20.3 wt% in position 8 at the weld center, in good agreement with the primary ferritic solidification modulus and hindering cracking. The standard deviation of the chromium content ranges from 2.1 in position 1 to 4.3 in position 5.

For the nickel data, the nickel content ranges from 10.1 wt% in position 1 to 12.4 wt% in position 8. The standard deviation of the nickel content ranges from 1.8 in position 1 to 4.5 in position 8.

Standard deviation is a measure of the spread or dispersion of a set of data, namely chemical composition in this context. It seems that the chromium and nickel content both increase as the position number increases, but the standard deviation of both the chromium and nickel content increases as the position number increases. This suggests that the chromium and nickel content are both generally increasing across the positions, but the spread of the chromium and nickel content is also increasing among the measurement points.

Figure 6-56 top right is showing data for eleven positions, with values for Mn content in weight percent (wt%) and standard deviation for each position, as well as values for Mo content in weight percent (wt%) and standard deviation for each position.

For the manganese data, the manganese content ranges from 0.4 wt% in position 1 to 0.7 wt% in position 7. The standard deviation of the manganese content ranges from 0.3 in position 1 to 0.7 in position 7. The molybdenum content ranges from 0.8 wt% in position 1 to 2.9 wt% in position 6. The standard deviation of the molybdenum content ranges from 0.7 in position 1 to 1.6 in position 11.

The manganese content tends to increase as the position number increases, but the standard deviation of the manganese content is relatively high and varies from 0.3 in position 1 to 0.7 in position 7. Similarly, the molybdenum content also tends to increase as the position number increases, but the standard deviation of the molybdenum content is also relatively high and varies from 0.7 in position 1 to 1.6 in position 11. This indicates that the manganese and molybdenum content both tend to increase across the positions, but the spread of the manganese and molybdenum content is high.

Figure 6-56 bottom is showing data for eleven positions, with values for P content in arbitrary units (a.u.) and standard deviation for each position.

The phosphorus content ranges from 0.15 a.u. in position 1 to 0.17 a.u. in position 9. The standard deviation of the phosphorus content ranges from 0.04 in position 1 to 0.03 in position 10, in general showing a stable trend across the weld in transverse direction.

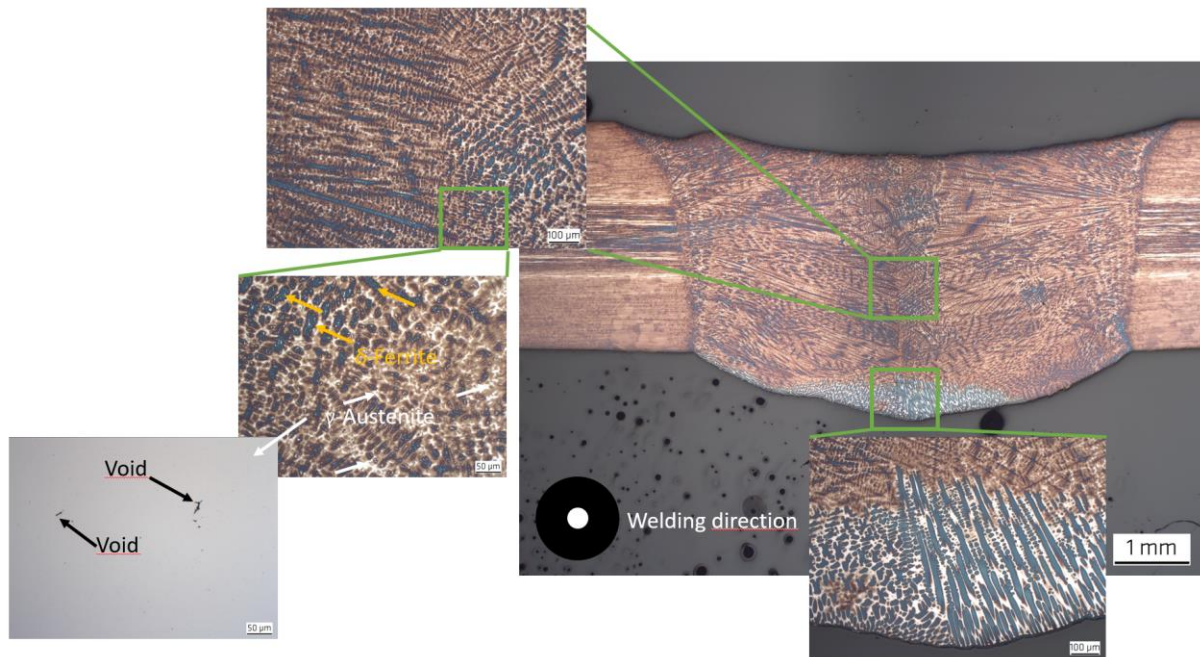


Figure 6-57: Sample 7 No crack situation metallography cross-section. Dendritic formation is visible in the fusion zone. Voids form due to liquid phase not able to fill the dendrite spacings during solidification.

Figure 6-57 shows a metallographic etched cross section from the weld without a crack situation. The cross-section picture demonstrates several conditions as columnar dendritic growth towards the weld center. In general this situation shows a main ferritic matrix and columnar dendritic growth, thus austenitic phase distributed across the dendrite spacings. This can be observed in high-magnified section of the picture.

Weld root shows a clear dendritic growth towards weld center and surface due to the temperature gradient across the fusion zone. In this area the two phases are clearly visible.

Moreover, in an unetched sample, some voids are visible, which were the result of the rapid cooling of the weld metal, hence the low melt eutectic phases not able to reach the voids and filling these dendrite spacings. However, the amount didn't reach the boundary condition to induce a solidification cracking for this sample.

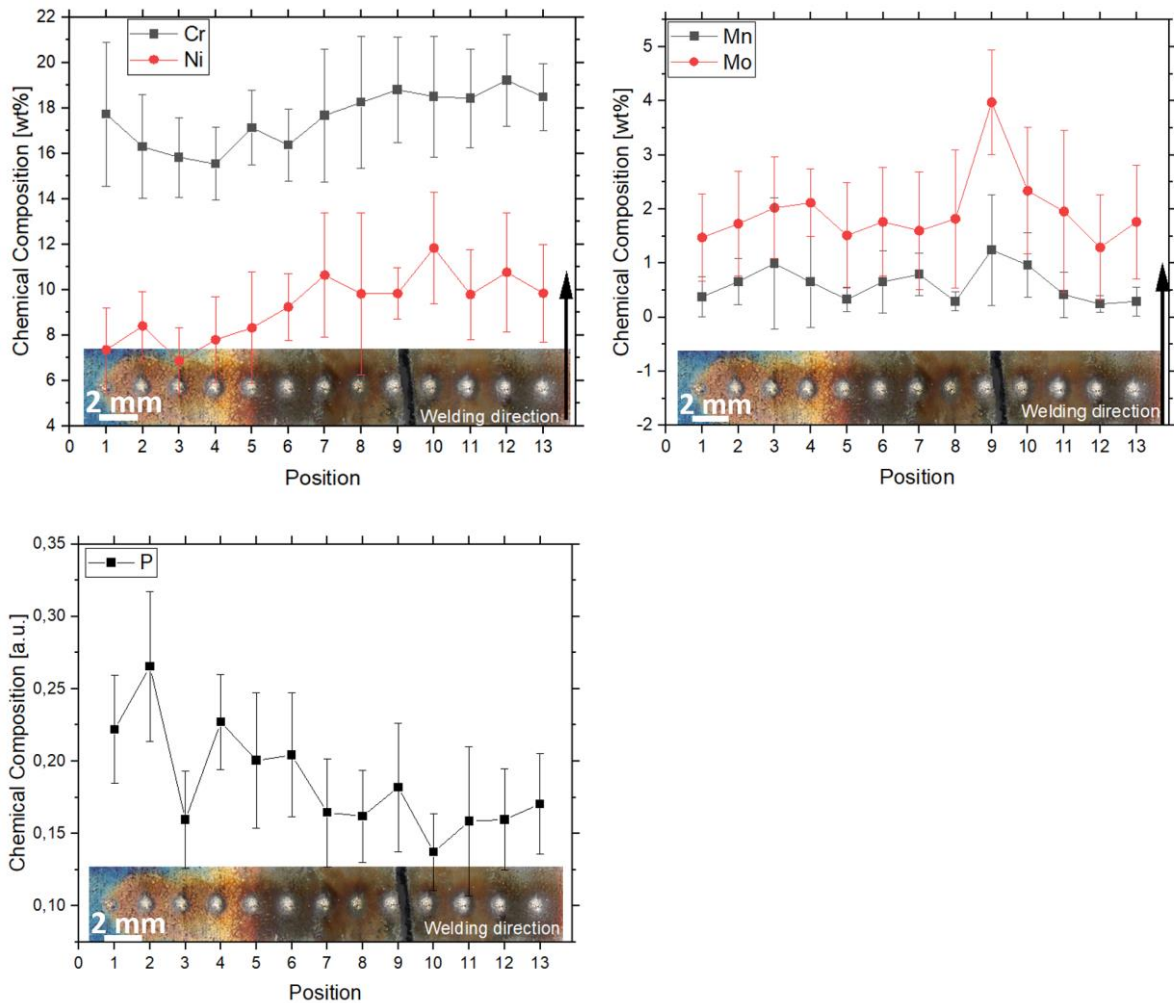


Figure 6-58: Sample 7 Post-weld line scan 2 crack situation

Figure 6-58 top left is presenting data for thirteen positions from Sample 7, and for each position, it shows the Cr, Ni, Mn, Mo content in weight percent (wt%), P in arbitrary units (a.u.) and the standard deviation (St. Dev.) of the respective position. This is the representative measurement from cracked situation observed on the sample. The centerline crack can be seen in the middle of the 9th and 10th measurement spots.

The chromium content ranges from 17.7 wt% in position 1 to 19.2 wt% in position 12. The standard deviation of the chromium content ranges from 3.1 in position 1 to 1.4 in position 13. The nickel content ranges from 7.3 wt% in position 1 to 10.7 wt% in position 12. The standard deviation of the nickel content ranges from 1.8 in position 1 to 2.6 in position 12.

It seems that the chromium content generally increases as the position number increases. Similarly, the nickel content generally increases as the position number increases.

Figure 6-58 top right shows data on the Mn and Mo content, along with their corresponding standard deviations, at different positions.

For Mn, the content generally increases as the position number increases, with the highest

value of 1.24 at position 9. The standard deviation of the manganese content is relatively high, ranging from 0.37 at position 1 to 1.02 at position 9.

For Mo, the content also generally increases as the position number increases, with the highest value of 3.97 at position 9. The standard deviation of the molybdenum content is also relatively high, ranging from 0.81 at position 1 to 1.50 at position 11.

This suggests that while there may be a general trend of increasing manganese and molybdenum content across the positions, the spread of the manganese and molybdenum content is high as well.

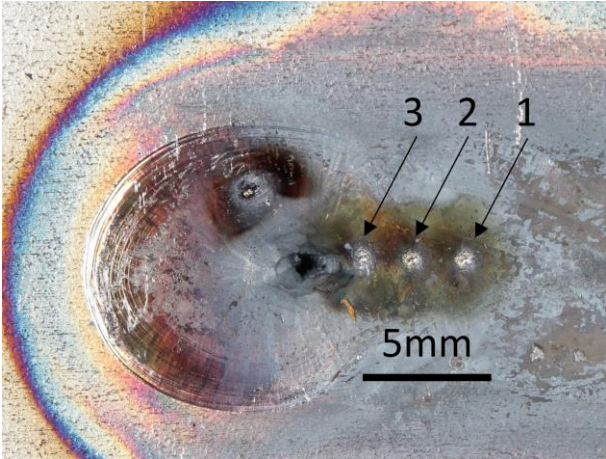
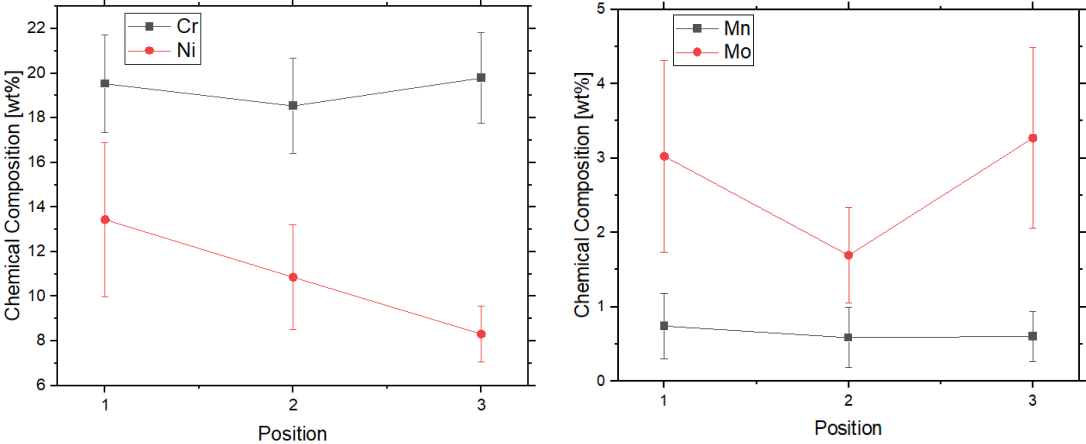


Figure 6-59: Sample 7 End crater LIBS measurement positions

Figure 6-59 shows the end crater of the Sample 7 and three positions of the post-weld LIBS measurement locations. The chemical composition measurements are given in Figure 6-60 below. This measurement was conducted to show alloying elements distribution especially in the mushy zone after solidification of the weld end crater was complete with 2 mm spatial distance between the measurement locations. Position 3 is exactly 2 mm behind on a central axis of the weld bead where the weld electrode tip was pointed at the work piece.



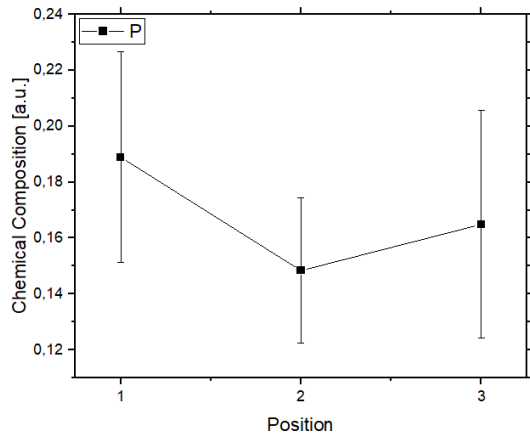


Figure 6-60: Sample 7 End crater LIBS analysis

Figure 6-60 top left shows three positions with corresponding values for Cr content and Ni content. The Cr content ranges from 19.5 to 19.8 wt%, with a standard deviation ranging from 2.0 to 2.1 wt%. The Ni content ranges from 8.3 to 13.4 wt%, with a standard deviation ranging from 1.2 to 3.4 wt%. Overall, the Cr content appears to be slightly higher in position 3 compared to positions 1 and 2, while the Ni content appears to be highest in position 1 and lowest in position 3, meaning the Ni content decreased as the measurement position get closer to the heat origin point where the welding arc hits the work piece. The standard deviation for both Cr and Ni is relatively high, indicating that there is a significant spread in the values for these elements.

The Mn content and Mo content are both given in Figure 6-60 top right in weight percent (wt%) and the standard deviation (St. Dev.) for each element is also provided. It appears that the Mn content is generally decreasing as the position number increases, with the lowest Mn content in position 3 and the highest content in position 1. The standard deviation for Mn is relatively low, ranging from 0.34 in position 3 to 0.44 in position 1. The Mo content also generally decreases as the position number increases, with the lowest Mo content in position 2 and the highest content in position 1. The standard deviation for Mo is relatively high, ranging from 1.22 in position 3 to 1.29 in position 1. Overall, the trend for both Mn and Mo is a decrease in content as the position number increases, thus getting closer to the heat origin, but there is a significant amount of variability in the Mo content.

Figure 6-60 bottom shows the phosphorus content in arbitrary units. The first position has the highest phosphorus content with a value of 0.188 a.u. being the closest measurement point from the heat origin and a standard deviation of 0.037 a.u. The second position has the lowest phosphorus content with a value of 0.148 a.u. and a standard deviation of 0.026 a.u. The third position has a phosphorus content of 0.164 a.u. and a standard deviation of 0.040 a.u. Overall, there is a slight decrease in phosphorus content from the first position to the second position, but the third position has a slightly higher phosphorus content than the second position. The standard deviations for the phosphorus content are all relatively small, indicating that the phosphorus content is relatively consistent within each position. This could indicate a possible

higher P content and transportation towards the edge of the mushy zone and supporting the hypothesis of contributing to the weld center crack propagation via impurity elements.

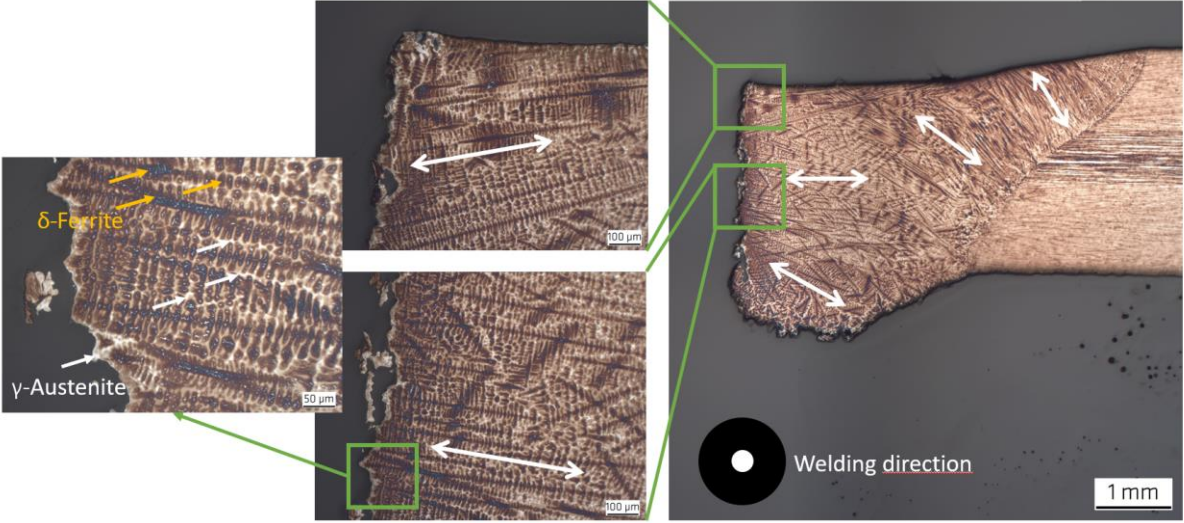


Figure 6-61: Sample 7 Crack situation metallography cross-section. Dendritic arm formation as primary ferrite in austenitic matrix towards weld center is visible in the fusion zone. Weld center consist of a thin austenitic film at the crack surface

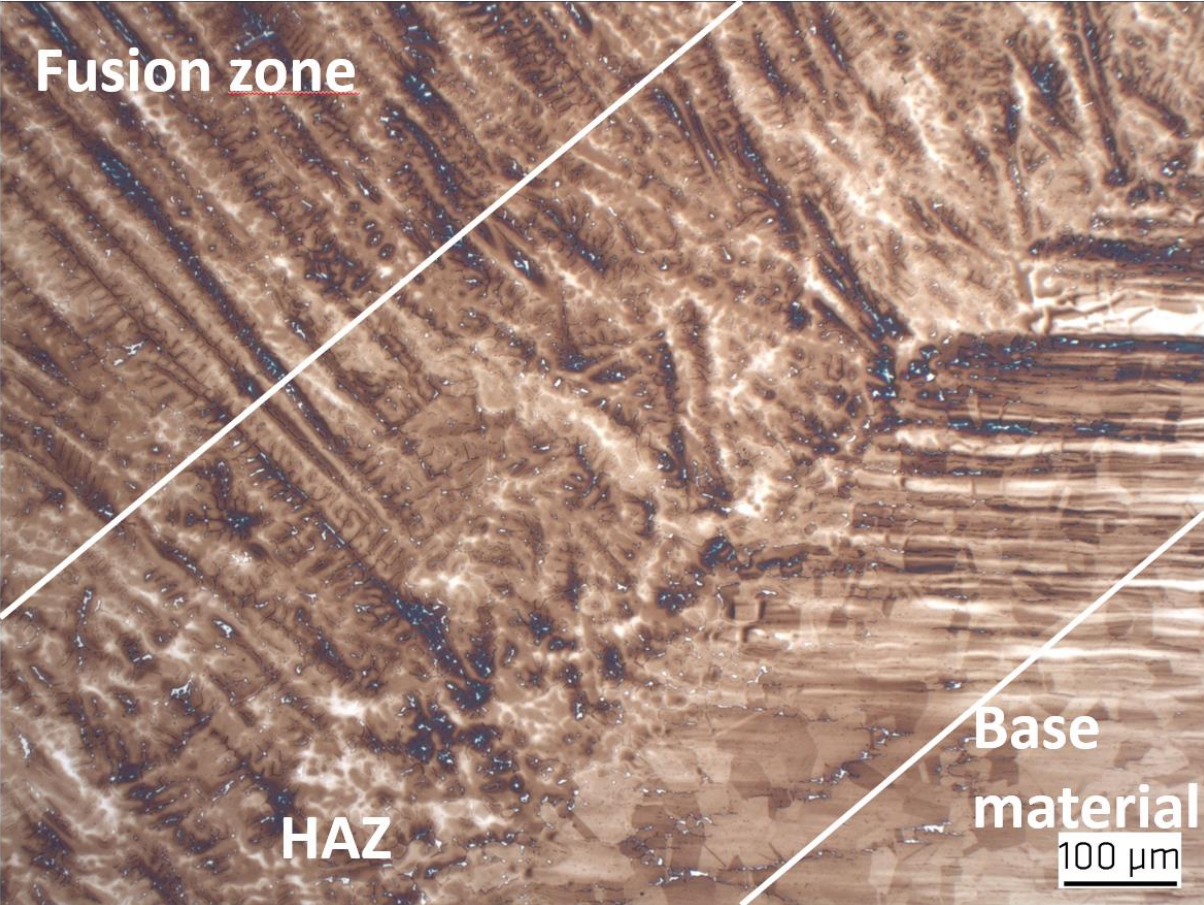


Figure 6-62: Sample 7 Metallography cross-section of the fusion zone – base material transition zone. Dendritic formation is visible in the fusion zone where base metal shows equiaxed grains.

Figure 6-61 and Figure 6-62 demonstrate metallographic cross sections from the same sample. Figure 6-61 demonstrates the cracked sample in etched form, revealing the solidification structure and columnar dendritic formation. The austenitic matrix seems to dominate this section of the weld, which is in good agreement with a primary austenitic solidification mode for this weld. The liquid film form at the crack surface is noteworthy, where the split of the sample took place at the terminal stage of the solidification sequence.

Figure 6-62 shows the transition zone of the weld root from the fusion zone to base material, where the equiaxed grain structure of the base material and dendritic grain structure of the fusion zone after the solidification sequence can be observed.

Furthermore, these sections were investigated with SEM and EDX analysis for further verification of the local changes of the chemical compositions on polished surfaces of the cracks.

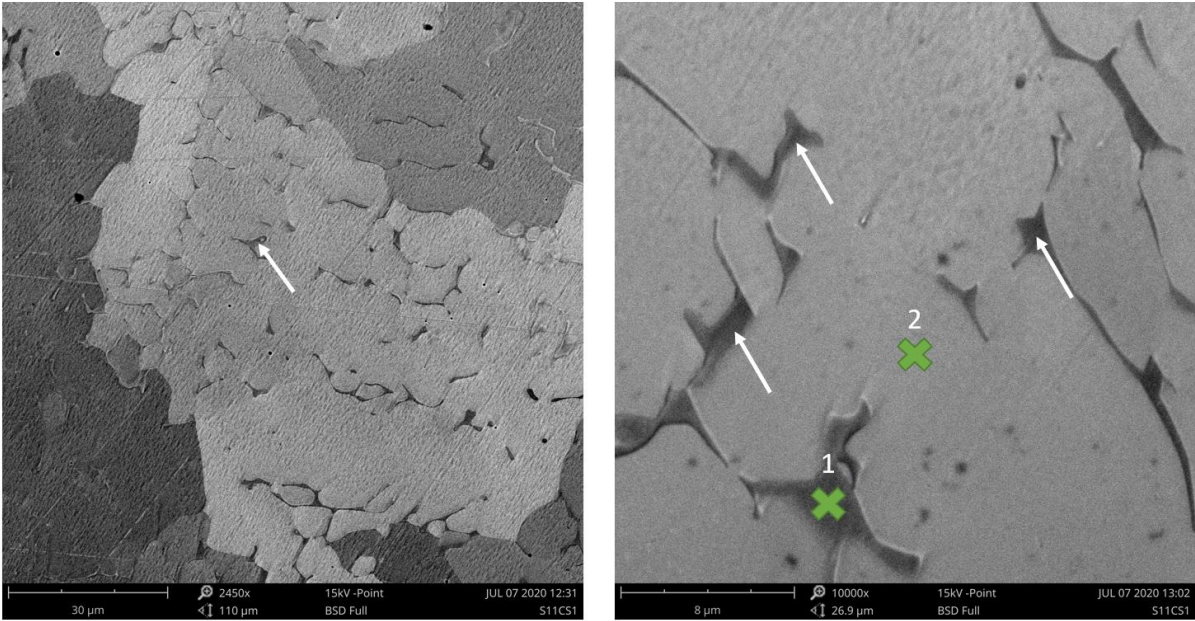


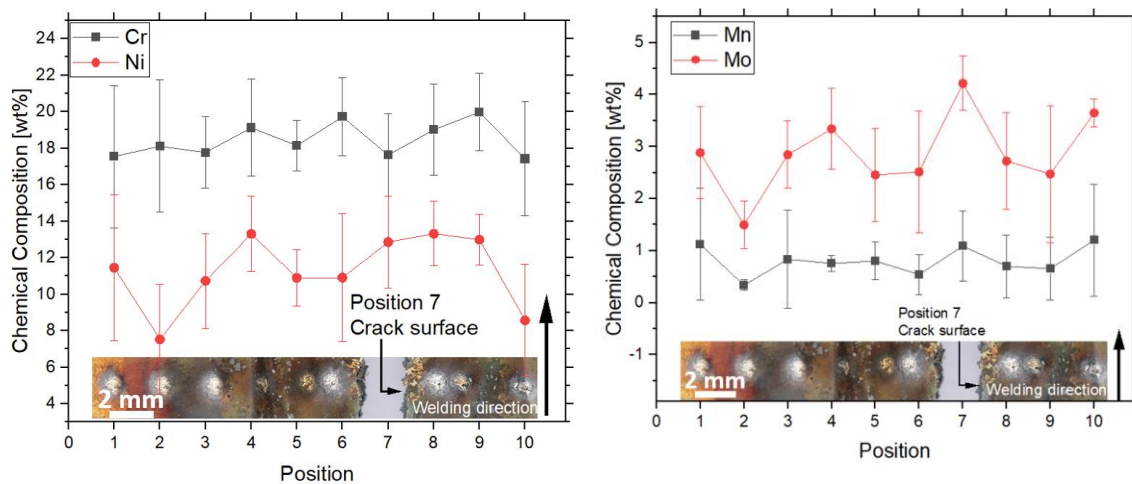
Figure 6-63: Sample 7 Crack surface SEM analysis on polished sample. Different phases are visible via image contrast. Main solidification driver can be seen as austenitic matrix with ferrite formation on grain boundaries and dendrite arm spacings. EDX Analysis spots are given below.

Table 18: EDX analysis of Figure 6-63

EDX Spot 1			EDX Spot 2		
Element Symbol	Element Name	Weight Conc.	Element Symbol	Element Name	Weight Conc.
Fe	Iron	66.18	Fe	Iron	66.69
Cr	Chromium	19.88	Cr	Chromium	15.59
O	Oxygen	5.21	O	Oxygen	4.58
Ni	Nickel	5.17	Ni	Nickel	10.43
S	Sulfur	1.92	S	Sulfur	0.98
C	Carbon	1.10	C	Carbon	1.01
Mn	Manganese	0.45	Mn	Manganese	0.17
P	Phosphorus	0.09	P	Phosphorus	0.08

Figure 6-63 demonstrates the SEM images from the cracked surfaces on a polished sample with requirement of the quantified EDX analysis. Different grain boundaries are immediately visible via image contrast. One can immediately see the main austenitic matrix with ferritic formation among the grain boundaries. This assumption can be supported with the EDX results, where the spot 2 (matrix) having about 5wt% more Ni content than spot 1 (grain boundary segregation). This is another indicator of a primary austenitic solidification modulus inducing a hot cracking situation. Online LIBS measurements are also in good agreement with the EDX analysis, which supports the in situ chemical composition change hypothesis from a different physical point of view.

Sample 9:



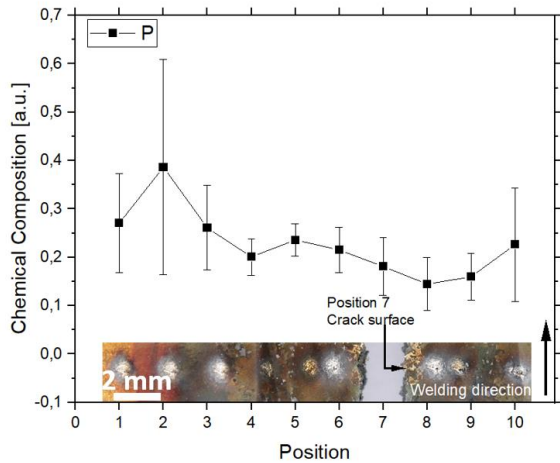


Figure 6-64: Sample 21 Post-weld line scan crack situation

Figure 6-64 is presenting data for ten positions from Sample 9, and for each position, it shows the Cr, Ni, Mn, Mo content in weight percent (wt%), P in arbitrary units (a.u.) and the standard deviation (St. Dev.) of the position. This is the representative measurement from cracked situation observed on the sample. The centerline crack can be seen in the middle of the 6th and 8th measurement spots. Measurement spot 7 was performed on the crack surface at the mid-range (approx. 1 mm below the surface) of the work piece from the sample surface level.

Figure 6-64 top left show data for the Cr and Ni content; it appears that the Cr and Ni content vary significantly between the different positions. The standard deviation for both elements is relatively high, indicating a large degree of variation in the content of these elements. In general, the Cr content tends to be higher in positions 1, 4, 5, 6, 8, and 9, while the Ni content tends to be higher in positions 4, 7, 8 and 9. However, it is important to note that the values for both elements are not consistently increasing or decreasing across the positions and there is a high degree of inhomogeneity in the distribution of these elements.

Figure 6-64 top right shows the chemical composition levels of Mn and Mo in various positions and standard deviation. From the data, the Mn content ranges from 0.33 wt% at position 2 to 1.20 wt% at position 10, with a standard deviation ranging from 0.09 at position 2 to 1.07 at position 10. Similarly, the Mo content ranges from 1.49 wt% at position 2 to 4.21 wt% at position 7, with a standard deviation ranging from 0.46 at position 2 to 0.26 at position 10. This suggests that there is some variation in the Mn and Mo content at different positions, with the standard deviation values indicating the degree of spread or dispersion of the data. One important takeaway is that the Mo content is the maximum at position 7, namely on the crack surface measurement.

Figure 6-64 bottom, the data presents each position having a corresponding value of P (in arbitrary units) and its standard deviation. In terms of main trends, it appears that the values of P are generally decreasing as the position number increases. The lowest value of P is at position 8, at a crack edge on surface, with a value of 0.14. The highest value of P is at position 1, with a value of 0.27. The standard deviations of the values of P are relatively small, with the

largest standard deviation being at position 2 with a value of 0.22.

Overall, it seems that the values of P are relatively stable, with only small fluctuations within each position. The standard deviations of the values of P are also relatively small, indicating that there is not a large amount of variation in the values of P at each position.

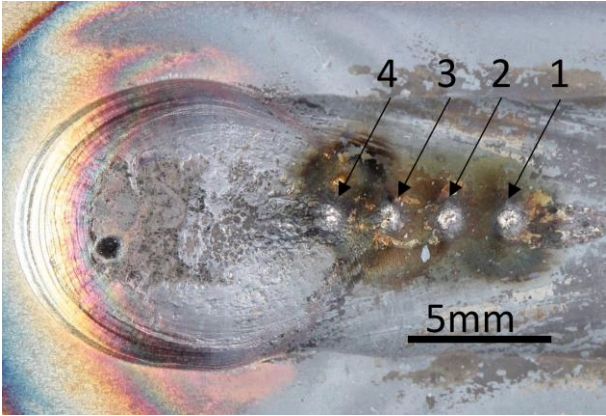
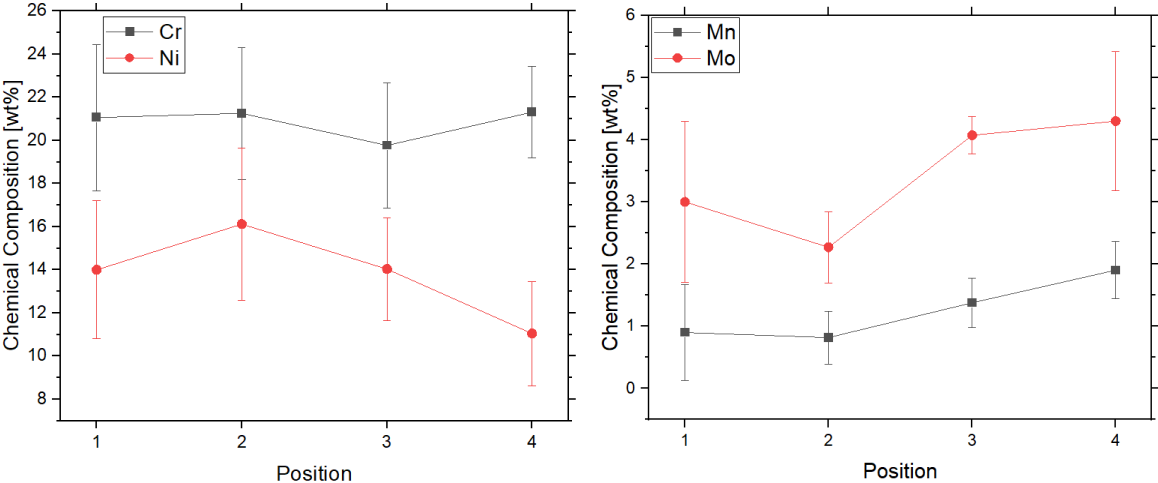


Figure 6-65: Sample 9 End crater LIBS measurement positions

Figure 6-65 shows the end crater of the Sample 9 and four positions of the post-weld LIBS measurement locations. The chemical composition measurements are given in Figure 6-66 below. This measurement was conducted to show alloying elements distribution especially in the mushy zone after solidification of the weld end crater was complete with 2 mm spatial difference between the measurement locations. Position 4 is exactly 2 mm behind where the weld electrode tip was pointed at the work piece.



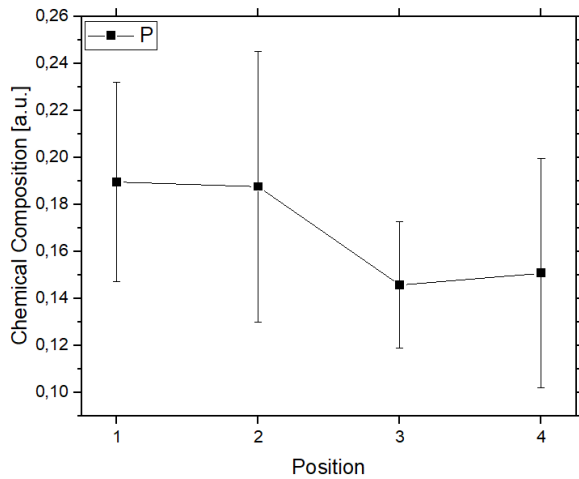


Figure 6-66: Sample 21 End crater LIBS analysis

Figure 6-66 top left shows data on the concentrations of the elements Cr and Ni in different positions. The concentration of Cr ranges from 19.7wt% to 21.3wt%, with a standard deviation ranging from 2.0wt% to 3.3wt%. The concentration of Ni ranges from 11.0wt% to 16.1wt%, with a standard deviation ranging from 2.42wt% to 3.53wt%. Overall, there is some variability in the concentrations of both elements, as indicated by the standard deviations. However, there is no clear trend in the concentrations of either element over the different positions.

Figure 6-66 top right shows the values of Mn and Mo in four different positions, along with the standard deviations of these values. The values of Mn range from 0.8wt% to 1.9wt%, with a standard deviation ranging from 0.42 to 0.45. The values of Mo range from 2.2wt% to 4.2wt% we, with a standard deviation ranging from 0.57 to 1.12. It appears that the values of both Mn and Mo increase from positions 1 to 4, with the largest value of Mn and Mo being observed in position 4. The standard deviations for both elements are generally lower in the first two positions compared to the last two positions. In general the Mn and Mo content increase towards the weld crater center, or their compositions tend to decrease towards the Mushy zone edge behind the weld pool. In this case, the decrease of the Mo towards the Mushy zone is in good agreement with a depleted ferrite promoting element from this region, thus supporting the conditions for the solidification cracking.

Figure 6-66 bottom shows the concentration of the element phosphorus (P) in four different positions, as well as the standard deviation of the concentration for each sample. The concentration is expressed in arbitrary units (a.u.).

In terms of main trends, it appears that the concentration of P decreases as the position increases, suggesting a higher P content at the edge of the mushy zone and close to the crack propagation point, with the highest concentration being in the first position and the lowest concentration being in the fourth position. P content shows approx. 0.14 a.u. close to origin point and about 19 a.u. at the crack edge suggesting higher P content at the crack propagation region at the edge of the mushy zone. The standard deviation also tends to decrease as the position increase, indicating that the concentration of P is more consistent in the position 3

and 4.

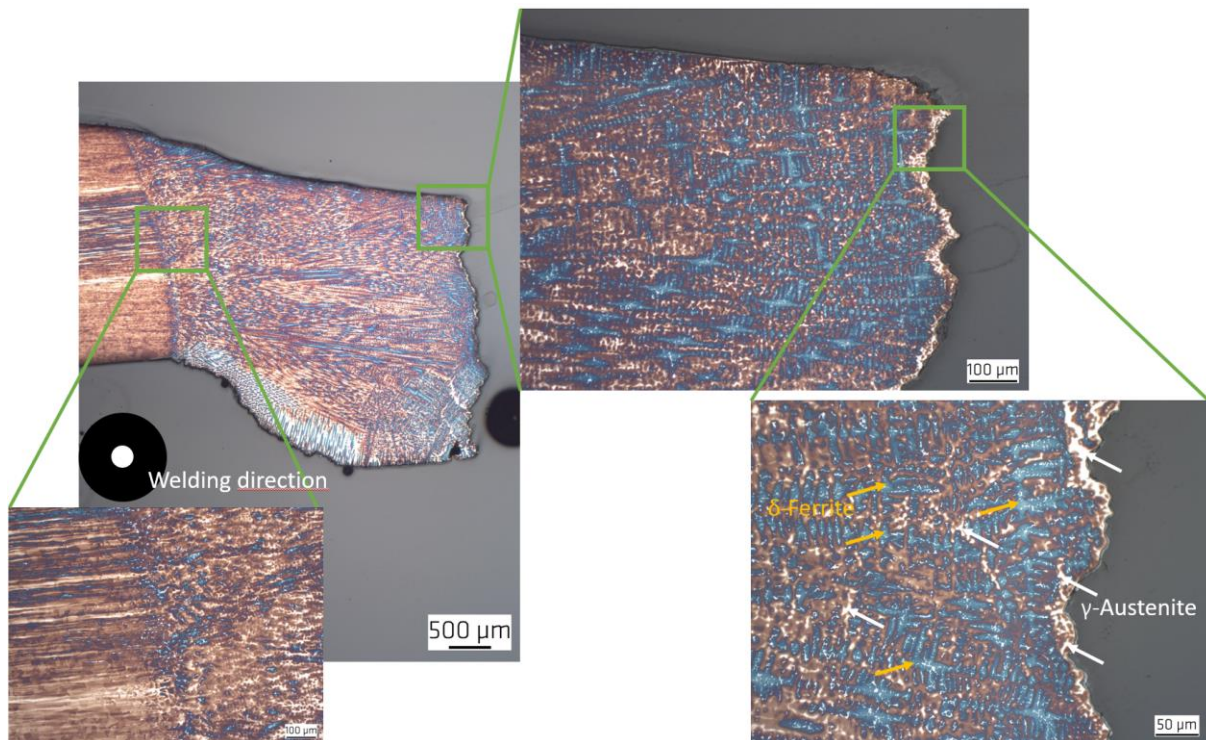


Figure 6-67: Sample 9 Crack situation metallography cross-section. Dendritic arm formation as primary ferrite in austenitic matrix towards weld center is visible in the fusion zone. Weld center consist of a thin austenitic film at the crack surface

Figure 6-67 demonstrate metallographic cross sections from the same sample, hence demonstrating the cracked sample in etched form, revealing the solidification structure and columnar dendritic formation. The austenitic matrix seems to be in mixture this section of the weld, a primary austenitic solidification mode for this weld is expected. The shining liquid film form at the crack surface is noteworthy, where the split of the sample took place at the terminal stage of the solidification sequence.

Furthermore, these sections were investigated with SEM and EDX analysis for further verification of the local changes of the chemical compositions on polished surfaces of the cracks.

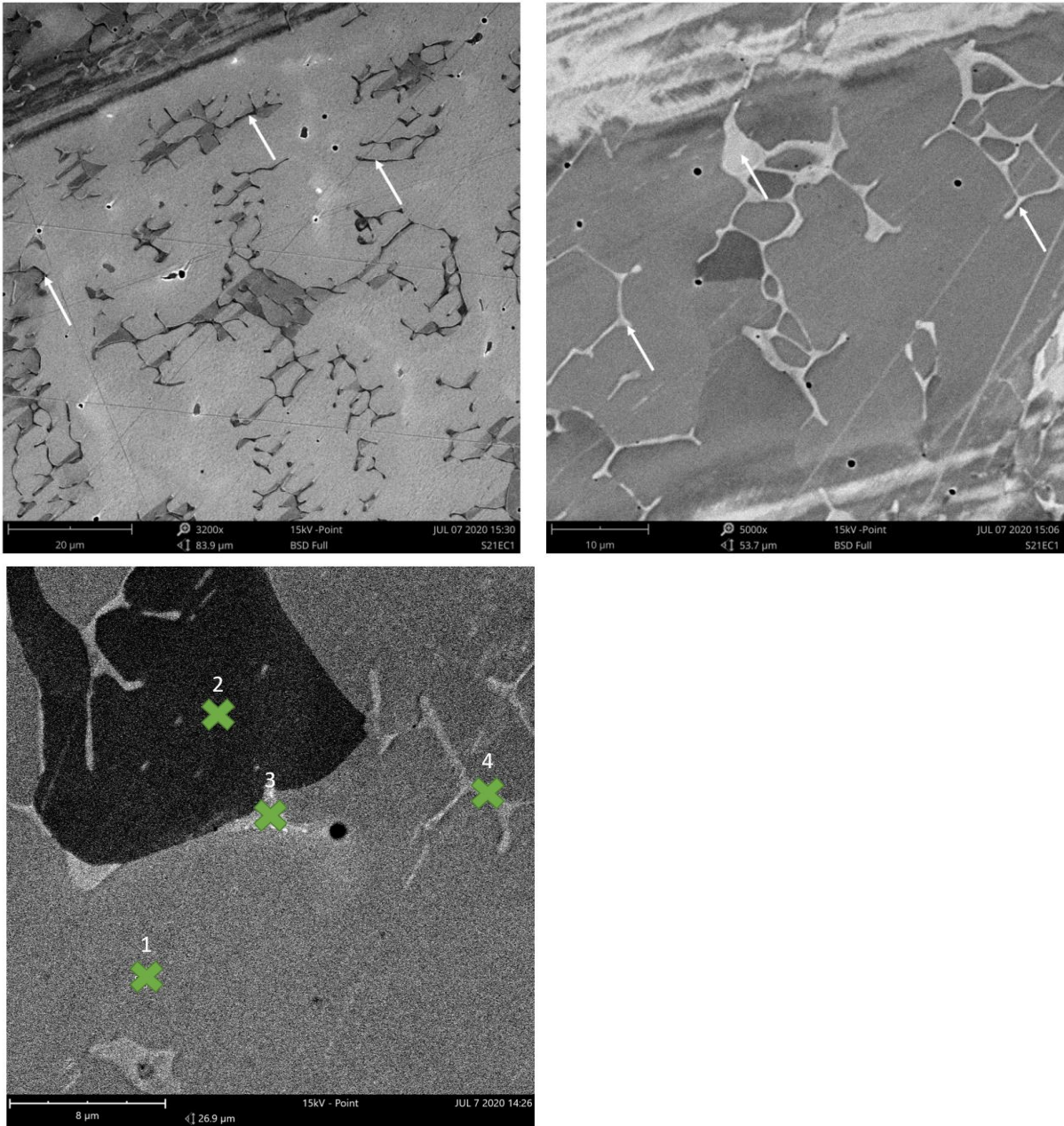


Figure 6-68: Sample 9 Crack surface SEM analysis on polished sample. Delta ferrite and gamma austenite phases are visible via image contrast. Main solidification driver can be seen as austenitic matrix with ferrite formation on grain boundaries and dendrite arm spacings. EDX Spot Analysis is given in Table 18.

Figure 6-68 demonstrates the SEM images from the cracked surfaces on a polished sample with requirement of the quantified EDX analysis. Different grains are immediately visible via image contrast. One can immediately see the main austenitic matrix with ferritic formation among the grain boundaries as well as voids where the liquid couldn't fill during rapid solidification. This assumption can be supported with the EDX results, where the spot 1 and 2 (matrix) having about 5wt% more Ni content than spot 3 and 4 (grain boundary segregation). This is another indicator of a primary austenitic solidification modus inducing a hot cracking. Online LIBS measurements hence the partition coefficient calculations are also in good

agreement with the EDX analysis, which supports the in situ chemical composition change hypothesis from a different physical point of view.

Table 19: EDX analysis of Figure 6-69

EDX Spot 1		
Element Symbol	Element Name	Weight Conc.
Fe	Iron	64.24
Cr	Chromium	16.85
Ni	Nickel	11.38
O	Oxygen	4.20
Mn	Manganese	1.28
S	Sulfur	0.95
Si	Silicon	0.58
C	Carbon	0.52
Mo	Molybdenum	0.00
P	Phosphorus	0.00

EDX Spot 2		
Element Symbol	Element Name	Weight Conc.
Fe	Iron	62.13
Cr	Chromium	16.70
Ni	Nickel	12.80
O	Oxygen	4.68
Mo	Molybdenum	1.17
Mn	Manganese	0.97
Si	Silicon	0.56
C	Carbon	0.52
S	Sulfur	0.47
P	Phosphorus	0.00

EDX Spot 3		
Element Symbol	Element Name	Weight Conc.
Fe	Iron	56.10
Cr	Chromium	21.44
Ni	Nickel	7.98
O	Oxygen	6.53
Mo	Molybdenum	5.49
Si	Silicon	0.78
Mn	Manganese	0.72
C	Carbon	0.62
P	Phosphorus	0.11
S	Sulfur	0.00

EDX Spot 4		
Element Symbol	Element Name	Weight Conc.
Fe	Iron	62.85
Cr	Chromium	21.41
Ni	Nickel	6.42
O	Oxygen	5.20
S	Sulfur	1.68
Mn	Manganese	1.09
Si	Silicon	0.72
C	Carbon	0.52
Mo	Molybdenum	0.11
P	Phosphorus	0.00

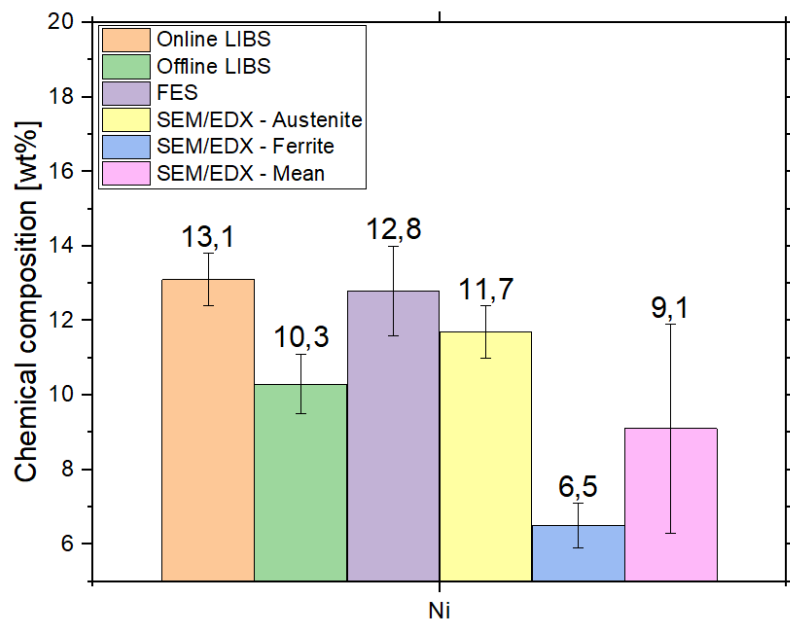
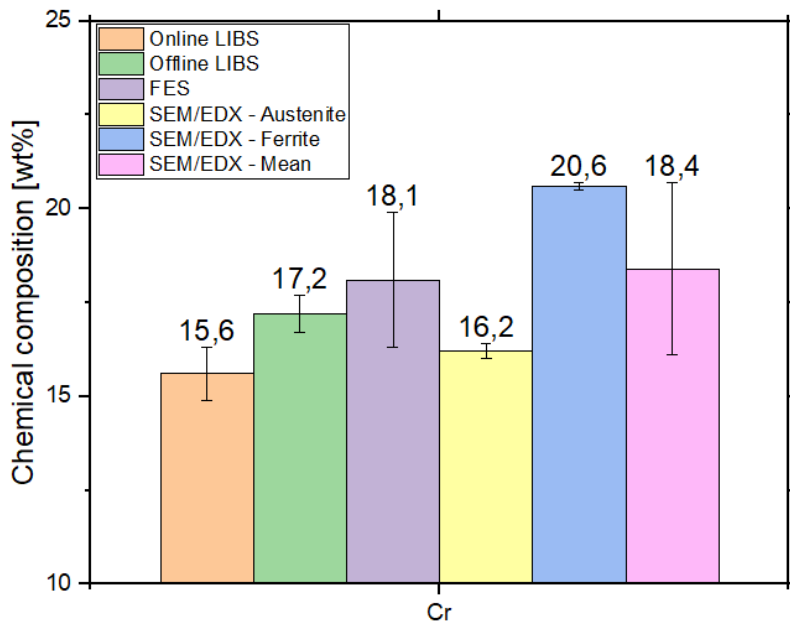


Figure 6-70: Sample 9 general Cr and Ni chemical composition comparison of four different methods including, online and offline LIBS (mean values), spark-optical emissions spectroscopy and SEM EDX .

Figure 6-70 is a general chemical composition comparison for Cr and Ni elements of the overall measurement methods used in this study, namely online and offline LIBS, conventional spark-optical emissions spectroscopy and SEM/EDX.

For the element Cr, the similarity between the spark-OES and the mean SEM method can be seen. However, the online LIBS method seems to be in good agreement with the austenitic

phase measurement from the SEM EDX, and offline LIBS remains in the tolerance limit of the spark-OES and mean SEM EDX measurements, thus having lower error margin compared to both methods. This can be also explained with a main austenitic solidification of the samples due to hot cracking inducing, hence the LIBS method being able to detect statistically the higher amount of the solidification phase in the region of interest.

Similarly, for Ni, the online LIBS method seems in good agreement with the spark-OES and SEM EDX method for austenitic phase, hence having lower error margin in comparison. Using the LIBS method, it shows lower correlation with the Ni content in the ferrite phase, hence making it difficult to correlate the online LIBS measurement with the primary ferrite phase, only relatable via the online partition coefficient calculation in a transient state.

Chapter 7

7. Conclusions and outlook

Main conclusions of this study can be listed as follows:

- Welding plasma was not sufficient to produce a detectable signal to produce sufficient data for welding process monitoring with the current set up of TIG welding. Strong emissions from Ar and W were observed during welding. Optical or computational filtering algorithms are required to generate useful data. Further research on topic is recommended in the future.
- Study suggests that it is feasible to use laser-induced breakdown spectroscopy (LIBS) to measure the main alloying elements of stainless steel e.g. Cr, Ni, Mn, in a molten weld pool from a distance without contact. LIBS is a spectroscopic technique that uses a laser pulse to ablate a small amount of material from the surface of the sample, which is then excited to emit light. The emitted light is analyzed to identify the elemental composition of the sample.
- Higher welding currents in TIG process, namely above 150A result in more distinguishable LIBS signal, hence the data analysis and processing had been more stable and less prone to external influencing factors due to arc jet stability.
- Local distribution and respective changes of chemical compositions were observed regarding the spatial location of the LIBS focus point on the weld pool. This is also validated via ex situ measurements and supported by local partition coefficient calculations via LIBS measurements.
- Higher welding currents generated higher amounts of local distributions of the elements, especially Ni showed a declining trend towards HAZ from the weld center. This finding is in good correlation with the literature.
- Spatial location of the LIBS measurement point can be implemented with at least 1mm spatial resolution within the liquid and solidified weld pool. LIBS method can be used minimum of 2mm from the welding arc center.
- The LIBS system can qualitatively detect the elemental composition differences between two different base materials with different chemical compositions during welding without calibration or reference materials.
- Weld shielding gas Ar flow rate has no distinguishable influence on the detected LIBS signal.
- Immediate in situ external element detection -Cu in this study- is possible using the LIBS monitoring system during the TIG welding process.
- As preliminary experiments, crack propagation was successfully initiated using external element Cu with different thermal and chemical properties in the solid solution. Higher welding arc currents resulted in higher dilution rates in the weld pool.

The wire experiment validates the capability of the LIBS system ability to detect the immediate changes of the chemical composition during welding, also non-ferrous material in this case.

- The utilized LIBS system in this study detects the information from mainly the surface area of the weld pool and an area of $200\mu\text{m}^2$. The future investigations on the topic can solve this problem implementing machine learning algorithms to calculate time and space resolved complex chemical compositions among the solid-liquid interface implementing complex mass transport and fluid flow models in the molten weld pool during the solidification process. Further research on the topic is required.
- From the investigated elemental lines of Fe, Cr, Ni and Mn -Fe I 373nm, 381nm, 430nm and 440nm; Cr I 359nm, 425nm and 428nm; Ni I 341nm and 349nm; Mn I 403.076nm, 403.298nm, 403.449nm and 406.353nm -, the underlined ones provided the highest resolution of spectra and therefore used in process implementation of the in situ weld monitoring. During the LIBS parameter investigation, 0,5 μs and 20 μs delay time and gate width respectively were found to be most optimized parameters to acquire a clean spectrum with the least background and suitable for data processing.
- Mn evaporates from the weld pool and accumulates back on the weld during welding process. Increasing the weld heat input increases the amount of the evaporation and consequent accumulation. This wasn't observed for the Cr element. Increasing the shielding gas flow rate increased the amount of accumulated Mn on the HAZ.
- The study suggests that the boundary welding heat input energy required to induce hot cracking for a specific sample geometry is dependent on the welding parameters used. Hot cracking is a common welding defect that occurs when the weld metal solidifies and contracts, leading to the formation of cracks.
- 1.4435 is more susceptible to hot cracking than 1.4404 due to higher austenite promoting alloying elements and primary austenitic solidification modus.
- The study suggests that the primary austenitic solidification mode is the main driver for hot cracking formation in high-alloyed stainless steel, hence dendritic formation in secondary ferrite phase detected on cross sections and via EDX analysis.
- This study suggests that online determination of the elemental partition coefficient during welding using the online measured chemical composition is possible. The partition coefficient is a measure of the distribution of an element between the liquid and solid phases during solidification. The partitioning properties were found to correlate with the primary solidification modus and microstructure properties, thus hot cracking behavior of the high alloyed stainless steel.
- This study suggests that there are differences in the local chemical composition of the alloying elements between the post-weld crack surface and solidified weld pool compared to the base material reference measurements. Specifically, there was a higher concentration of alloying elements in the weld pool due to non-equilibrium conditions during solidification . These differences in chemical composition can have

an impact on the properties of the welded material, hence causing weld defects mainly cracking issues.

- General comparison of the online LIBS method correlates good with the offline austenitic phase chemical compositions, especially for Cr element. To correlate the online chemical composition with the partitioning elements, a model was developed using the Scheil equation to calculate the online partition coefficient of the Cr and Ni in transition states of the material.

For the future work, the following points are recommended to be further researched:

- Producing and using customized reference materials for calibration model and enabling the detection of impurity elements e.g. P and S.
- Deploying the system with other material systems e.g. Duplex Stainless-Steels, Al-Alloy systems for deeper understanding of the driving solidification modulus and hot-cracking relation and online chemical compositions.
- Developing a fully automatic feedback loop between the welding system and the LIBS system to auto-correct welding parameters using the in situ chemical composition measurements.

List of Figures

Figure 1-1: Main causes of weld defects[1]	12
Figure 2-1: Worldwide crude steel production between 1950-2020 (Data source: World Steel Association) [7].....	14
Figure 2-2: Approximate cost of major alloying elements relative to iron	15
Figure 2-3: The alloy tree showing the interrelationships between the major alloy groups.....	17
Figure 2-4: Spatial- and time-dependent temperature distributions of a hypothetical steel sample [18] Left: Temperature distribution due to a line heat source at time t_0 when the peak temperature at the radius $r=1$ is equal to 1500°C . Right: Time variation of temperature at radius $r=1$ due to a line heat source as the peak temperature at r_0 is 1500	22
Figure 2-5: Schematic representation of tungsten-inert gas welding Modified and reprinted under Creative Commons License 2 [28]	34
Figure 2-6: Buoyancy or gravity force and consequent material flow and convection 27	27
Figure 2-7: Electromotive EMF or Lorentz, force and consequent material flow and convection[27].	27
Figure 2-8: Surface tension gradient driven convection or Marangoni convection, and consequent material flow in the weld pool 27	28
Figure 2-9: Shear stress induced by plasma jet and consequent material flow in the weld pool [27].	28
Figure 2-10: The allotropes of pure iron Triple point temperature and pressure values are 490°C and 110 kbars respectively [3]	31
Figure 2-11: Iron-cementite metastable phase diagram Modified and reprinted under Creative Commons License[38]	32
Figure 2-12: Weld microstructures and approximate temperatures in single fusion weld [49]. Data according to [50]	36
Figure 2-13: Portion of the partition coefficient displayed on a binary phase diagram 27	37
Figure 2-14: Schematic illustration of different forms of weld microstructure and corresponding supercooling conditions [52]	40
Figure 2-15: Effect of composition and solidification parameters on the resulting solidification mode [35] According to Borland [57]	42
Figure 2-16: Schaeffler Diagram from 1949, which is still in use[69]. Please note that the element Niobium Nb was formerly called as Columbium Cb.....	46
Figure 2-17: Classification of hot crack types in the FZ and HAZ [82, 83]	48
Figure 2-18: Interrelationships between the process parameters affecting the weld solidification cracking[34]	49
Figure 2-19: Solidification type on the pseudo-binary phase diagram for austenitic stain- less steels [12, 64] A-fully austenitic, AF-primary austenite with ferrite as second phase, FA-primary ferrite with austenite as second phase, F-fully ferrite	50
Figure 2-20: Weld solidification cracking susceptibility as a function of resulting weld microstructure [12].	51
Figure 2-21: Schematics of the possible solidification modes of Fe base Cr-Ni alloys and austenitic stainless steels in welding processes [85]	52
Figure 2-22: Solidification cracking behavior in austenitic stainless steel welds as a function of $\text{Cr}_{\text{eq}}/\text{Ni}_{\text{eq}}$ ratio and P+S composition[89]	53
Figure 2-23: Effect of the constitutional properties on cracking susceptibility for binary alloys Generalized Theory [57].....	54
Figure 2-24: Schematic of a typical LIBS system.....	60
Figure 2-25: Schematic representation of the different phases of the laser-induced plasma 115	61
Figure 2-26: Illustration of the laser material interaction (left) [116] and SEM image of an ablation crater on a crack surface of a steel sample (right-top), image of the ablation craters from a LIBS line-scan (right- bottom).....	62
Figure 2-27: Display of the characteristic values I_{max} , FWHM, b_0 and n_0 at the spectral line of iron Fe $440\ 475\ \text{nm}$	63
Figure 2-28: Characteristic univariate linear regression calibration model with 95% confidence band	

.....	64
Figure 5-1: Schematic experimental setup for the stationary weld monitoring situation.....	73
Figure 5-2: Schematic experimental setup for the moving weld monitoring situation. Veld pool is marked with dashed line for ease of.....	74
Figure 5-3: 3D CAD-drawing of the laser head with internal components and optical path representation.....	76
Figure 5-4: Optical setup Aryelle spectrometer [121].....	76
Figure 5-5: Schematic representation of the primary electron-sample interaction and the specific volumes of the emitted signals[123].....	80
Figure 5-6: Detection set up without the laser source. Optics focusing directly on the sample surface where the welding arc meets the work piece below the electrode. Signal is carried to the spectrometer via fiber optic cable.	82
Figure 5-7: Recorded elemental intensity counts (Fe, Cr, Ni, Mn, Ar, W) during welding of 1.4404 base material. Left: 80A; Right: 120A. Welding Speed = 10 cm/min constant, Shielding gas flow rate = 16 L/min.	84
Figure 5-8: Average intensity counts between time interval 10-35s. (IV, S6, a, b).....	85
Figure 5-9: Schematic of the top view of the weld pool and LIBS focus point.....	87
Figure 5-10: Relative intensities of the increasing welding currents vs. selected Cr I elemental lines. Average of the time interval 10-35s.....	88
Figure 5-11: Relative intensities of the increasing welding currents vs. selected Ni I elemental lines. Average of the time interval 10-35s.....	89
Figure 5-12: Relative intensities of the increasing welding currents vs. selected Mn I elemental lines. Average of the time interval 10-35s.	90
Figure 5-13: Spatially resolved (respective to the welding arc) relative -normalized- intensities of Cr I, Ni I and Mn I. a) recorded during welding: 0–14.4 s, b) After solidification: 73.8–91.8 s. Welding processes were performed at 160 A.[97].....	91
Figure 5-14: Post-weld spatially resolved normalized intensities of Cr I, Ni I and Mn I for different welding currents. LIBS measurements were conducted with 0.5 μ s delay time and 20 μ s gate width. The graphs are superimposed over photos of the respective spot weldments and the white spots are the respective LIBS measurement points.[97]	92
Figure 5-15: Bead-on-plate welding of (V-S12) 1.4435/b.2 base material with 4mm plate thickness. Left: 100A @10cm/min and 20cm/min; Right: 150A @10cm/min and 20cm/min. Constant shielding Ar gas flow rate 16 L/min. Values from the average of the time interval 10-35s.....	93
Figure 5-16: Bead-on-plate welding of 1.4565 base material with 6mm plate thickness. Left: 100A @10cm/min and 20cm/min; Right: 125A @10cm/min and 20cm/min; Bottom: 150A @10cm/min and 20cm/min. Constant shielding Ar gas flow rate 16 L/min. Values from the average of the time interval 10-35s.	95
Figure 5-17: Bead-on-plate welding of 1.4435 base material with 4mm plate thickness. Welding arc current=100A @10cm/min Shielding Ar gas flow rate dropped from 16 L/min to 8L/min. Values averaged from the welding process.....	96
Figure 5-18: Welding arc current=100A @10cm/min; shielding Ar gas flow rate = 16 L/min. Micrograph positions are indicated in the corresponding position on the diagrams within the circled number. Weld bead length = 90mm; Cu filler addition @ 45 mm (mid-weld) / Cu Filler Material consumption: 29 mm Cu wire in 45/90 mm.....	98
Figure 5-19: Top view of the completed weld bead (a) with Cu wire addition at 45mm.The radiograph of the completed weld is shown below the weld picture.	99
Figure 5-20: 100A, 10 cm/min. Micrograph positions are indicated in the corresponding position on the diagram within the circled number.....	100
Figure 5-21: SEM-EDX analysis locations in Micrograph 3 from Figure 6-15.	101
Figure 5-22: Welding arc current=100A @10cm/min; shielding Ar gas flow rate = 16 L/min. Micrograph positions are indicated in the corresponding position on the diagrams within the circled number. Weld bead length = 90mm; Cu filler addition @ 45 mm (mid-weld) / Cu Filler Material consumption: 55 mm Cu wire in 45/90 mm.....	103

Figure 5-23: Top view of the completed weld bead (b) with Cu wire addition at 45mm. The radiograph of the completed weld is shown below the weld picture.	103
Figure 5-24: 100A, 10 cm/min. Micrograph positions are indicated in the corresponding position on the diagram within the circled number. Repetition experiment.....	104
Figure 5-25: Welding arc current=150A @10cm/min; shielding Ar gas flow rate = 16 L/min. Micrograph positions are indicated in the corresponding position on the diagrams within the circled number. Weld bead length = 100mm; Cu filler addition @ 50 mm (mid-weld) / Cu Filler Material consumption: 43 mm Cu wire in 50/100 mm.	105
Figure 5-26: Top view of the completed weld bead (b) with Cu wire addition at 50mm. The radiograph of the completed weld is shown below the weld picture.	106
Figure 5-27: 150A, 10 cm/min. Micrograph positions are indicated in the corresponding position on the diagram within the circled number.	107
Figure 5-28: Welding arc current=150A @10cm/min; shielding Ar gas flow rate = 16 L/min. Micrograph positions are indicated in the corresponding position on the diagrams within the circled number. Weld bead length = 100mm; Cu filler addition @ 50 mm (mid-weld) / Cu Filler Material consumption: 50 mm Cu wire in 50/100 mm.	107
Figure 5-29: Top view of the completed weld bead (b) with Cu wire addition at 50mm. The radiograph of the completed weld is shown below the weld picture.	108
Figure 5-30: 150A, 10 cm/min. Micrograph positions are indicated in the corresponding position on the diagram within the circled number. Repetition experiment.	109
Figure 6-1: Signal-to-background for Fe lines. S/B as function of gate width at constant delay time = 0.5 μ s for the selected emission lines. Individual lines between data points were added as guide-to-the-eye.	111
Figure 6-2: Signal-to-background for Cr lines. S/B as function of gate width at constant delay time = 0.5 μ s for the selected emission lines. Individual lines between data points were added as guide-to-the-eye.	112
Figure 6-3: Signal-to-background for Ni lines. S/B as function of gate width at constant delay time = 0.5 μ s for the selected emission lines. Individual lines between data points were added as guide-to-the-eye.	112
Figure 6-4: Signal-to-background for In lines. S/B as function of gate width at constant delay time = 0.5 μ s for the selected emission lines. Individual lines between data points were added as guide-to-the-eye.	113
Figure 6-5: S/B as function of delay time at constant gate width = 20 μ s. Individual lines between data points were added as guide-to-the-eye.	113
Figure 6-6: S/B as function of delay time at constant gate width = 20 μ s. Individual lines between data points were added as guide-to-the-eye.	114
Figure 6-7: S/B as function of delay time at constant gate width = 20 μ s. Individual lines between data points were added as guide-to-the-eye.	114
Figure 6-8: S/B as function of delay time at constant gate width = 20 μ s. Individual lines between data points were added as guide-to-the-eye.	115
Figure 6-9: Signal-to-noise for Fe lines. S/N as function of gate width at constant delay time = 0.5 μ s for the selected emission lines. Individual lines between data points were added as guide-to-the-eye.	116
Figure 6-10: Signal-to-noise for Cr lines. S/N as function of gate width at constant delay time = 0.5 μ s for the selected emission lines. Individual lines between data points were added as guide-to-the-eye.	116
Figure 6-11: Signal-to-noise for Ni lines. S/N as function of gate width at constant delay time = 0.5 μ s for the selected emission lines. Individual lines between data points were added as guide-to-the-eye.	117
Figure 6-12: Signal-to-noise for In lines. S/N as function of gate width at constant delay time = 0.5 μ s for the selected emission lines. Individual lines between data points were added as guide-to-the-eye.	117
Figure 6-13: Signal-to-noise for Fe lines. S/N as function of gate width at constant delay time = 0.5 μ s for the selected emission lines. Individual lines between data points were added as guide-to-the-eye.	

.....	118
Figure 6-14: Signal-to-noise for Cr lines. S/N as function of gate width at constant delay time = 0.5 μ s for the selected emission lines. Individual lines between data points were added as guide-to-the-eye.	
.....	119
Figure 6-15: Signal-to-noise for Ni lines. S/N as function of gate width at constant delay time = 0.5 μ s for the selected emission lines. Individual lines between data points were added as guide-to-the-eye.	
.....	119
Figure 6-16: Signal-to-noise for In lines. S/N as function of gate width at constant delay time = 0.5 μ s for the selected emission lines. Individual lines between data points were added as guide-to-the-eye.	
.....	120
Figure 6-17: The surface of the welded sample was analyzed using laser-induced breakdown spectroscopy (LIBS) mapping to identify the distribution of manganese on the surface, with a particular focus on the accumulation of manganese in the heat-affected zone (HAZ). From paper- [96].....	122
Figure 6-18: The fitted Mn I triplet peaks around 403 nm. The curves for the "weld bead" and "base material" overlapped due to their similar chemical compositions. The welding parameters used were a welding current of 65 A, a welding speed of 10 cm/min (which resulted in a heat input of 491 J/mm), and a shielding gas flow rate of 18 l/min. The material used was EN 1.4404 / 327005. From paper [98].....	122
Figure 6-19: The distribution of chromium and manganese elements was studied using a line-scan with laser-induced breakdown spectroscopy (LIBS) perpendicular to the welding direction. The measurements were made at specific points along the line to determine the spatial distribution of the elements. From paper. [98].....	123
Figure 6-20: The chemical compositions of manganese (left) and chromium (right) at the base material, heat-affected zone (HAZ), and weld bead were plotted as a function of the welding heat input. Dashed lines were included as visual aids. Dashed lines are guide- to-the-eye. From paper. [98].....	124
Figure 6-21: The chemical compositions of manganese (left) and chromium (right) at the base material, heat-affected zone (HAZ), and weld bead were plotted as a function of the welding heat input.. Dashed lines are guide- to-the-eye. From paper [98].....	125
Figure 6-22: Different weld input energies and end condition of the finished product. Similar result for both 1.4404 and 1.4435. 1.4404 created wavy form and showed relatively less susceptibility to cracking. 1.4435 demonstrated higher susceptibility to center line cracking. 160A constant welding current, same sample geometry.....	127
Figure 6-23: Univariate calibration curve model for Cr with 95% confidence band marked in red. $R^2=0.97$. Used Certified Reference Materials (CRMs): BS 19, 271-1, BS 36B, BAS 475, 232-1 (AKP133), SS 468-1, SS 463-1, BAS 295-1, SS 464-1	129
Figure 6-24: Univariate calibration curve model for Ni with 95% confidence band marked in red. $R^2=0.99$. Used Certified Reference Materials (CRMs): BAS 296-1, 273-1, SS 461-1, SUS 1.4571, SS 462, SS 462-1, SS 464-1, SS 64, BAS 295-1	129
Figure 6-25: Univariate calibration curve model for Mn with 95% confidence band marked in red. $R^2=0.92$. Used Certified Reference Materials (CRMs): SUS 1.4034, SS 63, SS 64, SUS 1.4306, SUS 1.4541	130
Figure 6-26: Univariate calibration curve model for Mo with 95% confidence band marked in red. $R^2=0.98$. Used Certified Reference Materials (CRMs): SUS 1.4541, BAS 475, SS 66, SS 466-2.....	130
Figure 6-27: Finished weld seam of the Sample 1, LIBS measurement spot on the weld end crater is marked.	131
Figure 6-28: Sample 1 online weld monitoring of element Cr and Ni over time along with the temperature measurement on the same spot to the LIBS point respective to the welding arc position.	132
Figure 6-29: Finished weld seam of the Sample 1, LIBS measurement spot on the weld end crater is marked.	133
Figure 6-30: Sample 2 online weld monitoring of element Cr and Ni over time along with the temperature measurement on the same spot to the LIBS point respective to the welding arc position.	134

Figure 6-31: Finished weld seam of the Sample 3, LIBS measurement spot on the weld end crater is marked.	135
Figure 6-32: Sample 3, Online weld monitoring of element Cr and Ni over time along with the temperature measurement on the same spot to the LIBS point respective to the welding arc position.	136
Figure 6-33: Sample 3 In situ partitions coefficient calculation. Left: first 9 seconds of the welding process. Right: The terminal stage of the welding process between 42 nd and 50 th seconds.....	137
Figure 6-34: Finished weld seam of the Sample 4, LIBS measurement spot on the weld end crater is marked.	138
Figure 6-35: Sample 4, Online weld monitoring of element Cr and Ni over time along with the temperature measurement on the same spot to the LIBS point respective to the welding arc position.	139
Figure 6-36: Finished weld seam of the Sample 4, LIBS measurement spot on the weld end crater is marked.	140
Figure 6-37: Sample 5 Cr and Ni with highlighted area.....	141
Figure 6-38: Sample 5 Cr and Ni, first 15 s in higher magnification.	142
Figure 6-39: Sample 5 In situ partitions coefficient calculation. Left: first 10 seconds of the welding process. Right: The terminal stage of the welding process between 62 nd and 69 th seconds.....	142
Figure 6-40: Finished weld seam of the Sample 4, LIBS measurement spot on the weld end crater is marked.	143
Figure 6-41: Sample 6 Cr and Ni online weld monitoring of element Cr and Ni over time along with the temperature measurement on the same spot to the LIBS point respective to the welding arc position	144
Figure 6-42: Sample 6 Mo chemical composition at 386 nm, Mn in a.u.at 403nm, P in a.u. at 213 nm.	145
Figure 6-43: Sample 6 In situ partitions coefficient calculation. Left: first 10 seconds of the welding process. Right: The terminal stage of the welding process between 62 nd and 69 th seconds.....	146
Figure 6-44: Finished weld seam of the Sample 7, LIBS measurement spot on the weld end crater is marked.	147
Figure 6-45: Sample 7 Cr and Ni online weld monitoring of element Cr and Ni over time along with the temperature measurement on the same spot to the LIBS point respective to the welding arc position	148
Figure 6-46: chemical composition at 386 nm, Mn in a.u.at 403nm, P in a.u. at 213 nm	149
Figure 6-47: Sample 7 In situ partitions coefficient calculation. Left: first 6 seconds of the welding process. Right: The terminal stage of the welding process between 63 rd and 67 th seconds.	150
Figure 6-48: Finished weld seam of the Sample 8, LIBS measurement spot on the weld end crater is marked.	151
Figure 6-49: Sample 8 Cr and Ni online weld monitoring of element Cr and Ni over time along with the temperature measurement on the same spot to the LIBS point respective to the welding arc position	152
Figure 6-50: Finished weld seam of the Sample 8, LIBS measurement spot on the weld end crater is marked.	153
Figure 6-51 Sample 9 Cr and Ni online weld monitoring of element Cr and Ni over time along with the temperature measurement on the same spot to the LIBS point respective to the welding arc position	153
Figure 6-52: Sample 2 Post-weld LIBS line scan for Cr, Ni, Mn, Mo in wt%, and P in a.u. units across the weld bead and crack edges. Position 6 and 7 are the measurements taken at the crack edges.....	155
Figure 6-53: Sample 2 Post-weld Crack surface LIBS analysis	Fehler! Textmarke nicht definiert.
Figure 6-54: Sample 2 Crack surface SEM analysis. Dendritic formation is visible on the crack surface.	158
Figure 6-55: Sample 2 crack surface SEM analysis with the LIBS measurement spot. LIBS measurement spot can be seen along with the laser shockwave formation.	158
Figure 6-56: Sample 7 Post-weld line scan 1 no crack situation	159

Figure 6-57: Sample 7 No crack situation metallography cross-section. Dendritic formation is visible in the fusion zone. Voids form due to liquid phase not able to fill the dendrite spacings during solidification.	161
Figure 6-58: Sample 7 Post-weld line scan 2 crack situation	162
Figure 6-59: Sample 7 End crater LIBS measurement positions	163
Figure 6-60: Sample 7 End crater LIBS analysis	164
Figure 6-61: Sample 7 Crack situation metallography cross-section. Dendritic arm formation as primary ferrite in austenitic matrix towards weld center is visible in the fusion zone. Weld center consist of a thin austenitic film at the crack surface	165
Figure 6-62: Sample 7 Metallography cross-section of the fusion zone – base material transition zone. Dendritic formation is visible in the fusion zone where base metal shows equiaxed grains.	166
Figure 6-63: Sample 7 Crack surface SEM analysis on polished sample. Different phases are visible via image contrast. Main solidification driver can be seen as austenitic matrix with ferrite formation on grain boundaries and dendrite arm spacings. EDX Analysis is given below.....	166
Figure 6-64: Sample 21 Post-weld line scan crack situation	168
Figure 6-65: Sample 9 End crater LIBS measurement positions	169
Figure 6-66: Sample 21 End crater LIBS analysis	170
Figure 6-67: Sample 9 Crack situation metallography cross-section. Dendritic arm formation as primary ferrite in austenitic matrix towards weld center is visible in the fusion zone. Weld center consist of a thin austenitic film at the crack surface	171
Figure 6-68: Sample 9 Crack surface SEM analysis on polished sample. Delta ferrite and gamma austenite phases are visible via image contrast. Main solidification driver can be seen as austenitic matrix with ferrite formation on grain boundaries and dendrite arm spacings. EDX Spot Analysis is given in Table 18.	172
Figure 6-69: Sample 9 general Cr and Ni chemical composition comparison of four different methods including, online and offline LIBS (mean values), spark-optical emissions spectroscopy and SEM EDX	174

List of Tables

Table 1: Overview of material standards for stainless steels [13, 14]	18
Table 2: Physical properties of the selected metals [18]	22
Table 3: Austenite and ferrite promoting -or stabilizing- elements.....	45
Table 4: Constitutional diagrams in chronological order with the respective Cr_{eq} and Ni_{eq} formulas..	47
Table 5: Analytical techniques in comparison for elemental analysis [108]	58
Table 6: Advantages and disadvantages of the LIBS technique [115].....	60
Table 7: Work program of the experimental series.	71
Table 8: Chemical compositions of the base materials in weight % (Spark-optical emission spectrometry).....	72
Table 9: Chemical compositions of the Cu-based filler material in weight % according to DIN EN EN 10204-2.2 (manufacturer data sheet).....	73
Table 10: Chemical compositions of the CRMs (in wt.%) used to establish the calibration models. All CRMs have iron matrix, i.e. balance wt% is Fe.....	78
Table 11: LoD values for various alloying elements of the stainless steel using arc/spark OES method[124].....	81
Table 12: Chemical compositions of the marked positions from Figure 6.15 (SEM-EDX measurements).	102
Table 13:List of the selected emission lines and the spectroscopic parameters based on NIST database, observed wavelength (λ), lower (E_i) and upper energy (E_k) levels.	110
Table 14: Selected elemental lines for the calibration model and online process monitoring.	128
Table 15: Sample identification, input parameters and end condition.	131
Table 16: Cold LIBS measurements on the base material (no welding) 1.4435/b2 (Material thickness = 3mm)	131
Table 17: Cold LIBS measurements on the base material (no welding) 1.4404/b1 (Material thickness = 3mm)	143
Table 18: EDX analysis of Figure 6-63.....	167
Table 19: EDX analysis of Figure 6-63.....	173

References

1. Matthews, C. and A.S.o.M. Engineers, *ASME Engineer's Data Book*. 2005: ASME Press.
2. Hunt, R.W., *The manufacture of Bessemer Steels*. Journal of the Franklin Institute, 1889. **127**(5): p. 357-380.
3. Bhadeshia, H. and R. Honeycombe, *Chapter 12 - Stainless Steel*, in *Steels: Microstructure and Properties (Fourth edition)*. 2017, Butterworth-Heinemann. p. 343-376.
4. Zhang, L., *Microstructure-property relationship in microalloyed high-strength steel welds*. 2017, Otto-von-Guericke-Universität Magdeburg, Fakultät für Maschinenbau.
5. Shanthraj, P., et al., *Multi-component chemo-mechanics based on transport relations for the chemical potential*. Computer Methods in Applied Mechanics and Engineering, 2020. **365**: p. 113029.
6. Springer, H. and D. Raabe, *Rapid alloy prototyping: Compositional and thermo-mechanical high throughput bulk combinatorial design of structural materials based on the example of 30Mn–1.2C–xAl triplex steels*. Acta Materialia, 2012. **60**(12): p. 4950-4959.
7. World Steel Association, *World Steel in Figures*. 29.05.2020.
8. Farrar, C., *The Alloy Tree: A Guide to Low-Alloy Steels, Stainless Steels and Nickel-Base Alloys*. 2004: Elsevier Science.
9. Lo, K.H., C.H. Shek, and J.K.L. Lai, *Recent developments in stainless steels*. Materials Science & Engineering R-Reports, 2009. **65**(4-6): p. 39-104.
10. Papavinasam, S., *Chapter 3 - Materials*, in *Corrosion Control in the Oil and Gas Industry*, S. Papavinasam, Editor. 2014, Gulf Professional Publishing: Boston. p. 133-177.
11. DIN, *DIN EN 10020:2000 Begriffsbestimmung für die Einteilung der Stähle*. 2000.
12. Lippold, J.C. and D.J. Kotecki, *Welding metallurgy and weldability of stainless steels*. 2005: Wiley-Interscience.
13. DIN, *Nichtrostende Stähle – Teil 1: Verzeichnis der nichtrostenden Stähle; Deutsche Fassung EN 10088-1:2014*, in *DIN EN 10088-1_2014_de*. 2020.
14. DIN, *Nichtrostende Stähle – Teil 2: Technische Lieferbedingungen für Blech und Band aus korrosionsbeständigen Stählen für allgemeine Verwendung; Deutsche Fassung EN 10088-2:2014*. 2020.
15. McGuire, M.F., *Stainless steels for design engineers*. 2008.
16. Messler, R.W., *Principles of Welding: Processes, Physics, Chemistry, and Metallurgy*. 1999: Wiley.
17. Geiger, G.H. and D.R. Poirier, *Transport Phenomena in Metallurgy [by] G.H. Geiger [and] D.R. Poirier*. 1973: Addison-Wesley Publishing Company.
18. Lancaster, J.F., *Metallurgy of Welding*. 1999: Elsevier Science.
19. Seetharaman, S., *Fundamentals of metallurgy*. Woodhead Publishing in materials. 2005, Cambridge: Woodhead Pub. and Maney Pub. on behalf of the Institute of Materials. 1 Online-Ressource (xii, 574 S.).
20. Krishna, R., *Uphill diffusion in multicomponent mixtures*. Chem Soc Rev, 2015. **44**(10): p. 2812-36.
21. NIST, *Kelvin: Boltzmann Constant*. 11.06.2018.
22. Wikipedia, *Boltzmann constant*. 11.06.2020.
23. Bergman, T.L., et al., *Fundamentals of Heat and Mass Transfer*. 2011: Wiley.
24. Kučera, J. and K. Stránský, *Diffusion in iron, iron solid solutions and steels*. Materials Science and Engineering, 1982. **52**(1): p. 1-38.
25. Lauerer, A., et al., *Uphill diffusion and overshooting in the adsorption of binary mixtures in nanoporous solids*. Nature Communications, 2015. **6**(1): p. 7697.
26. Dong, W., et al., *GTAW liquid pool convections and the weld shape variations under helium gas shielding*. International Journal of Heat and Mass Transfer, 2011. **54**(7): p. 1420-1431.

27. Kou, S., *Welding metallurgy*. 2. ed. 2003, Hoboken, NJ: Wiley-Interscience.
28. Duk, *Gas-tungsten arc welding (GTAW)*, W. Commons, Editor. 17.06.2020.
29. Campbell, J., *Complete Casting Handbook: Metal Casting Processes, Techniques and Design*. 2011: Elsevier Science.
30. Aucott, L., et al., *Revealing internal flow behaviour in arc welding and additive manufacturing of metals*. Nature Communications, 2018. **9**(1): p. 5414.
31. Lu, S., H. Fujii, and K. Nogi, *Marangoni convection and weld shape variations in He–CO₂ shielded gas tungsten arc welding on SUS304 stainless steel*. Journal of Materials Science, 2008. **43**(13): p. 4583-4591.
32. Heiple, C.R. and J.R. Roper, *Mechanism for Minor Element Effect on GTA Fusion Zone Geometry*. Welding Journal, 1982: p. 97-102.
33. Block-Bolten, A. and T.W. Eagar, *Metal vaporization from weld pools*. Metallurgical Transactions B, 1984. **15**(3): p. 461-469.
34. Cross, C.E., *On the Origin of Weld Solidification Cracking*, in *Hot Cracking Phenomena in Welds*, T. Böllinghaus and H. Herold, Editors. 2005, Springer Berlin Heidelberg: Berlin, Heidelberg. p. 3-18.
35. Lippold, J.C., *Welding Metallurgy and Weldability*. 2015: John Wiley and Sons.
36. Yakel, H.L., *Crystal structures of stable and metastable iron-containing carbides*. International Metals Reviews, 1985. **30**(1): p. 17-44.
37. Föll, H., *Iron, Steel and Swords*. 24.06.2020.
38. Caesar, A., *Fe-C Phase diagram*, W. Commons, Editor. 23.06.2020.
39. Metals, A.S. and J.R. Davis, *ASM handbook. 1. Properties and selection: irons, steels, and high-performance alloys*. 2008: ASM International.
40. Britannica, E., *Curie point*. 25.06.2020.
41. Yurioka, N., *Physical metallurgy of steel weldability*. Isij International, 2001. **41**(6): p. 566-570.
42. Kujanpaa, V., et al., *Correlation between solidification cracking and microstructure in austenitic and austenitic-ferritic stainless steel welds*. Welding Research International, **1979**. **9**(2): p. 55-75.
43. Lundin, C.D., C.P.D. Chou, and C.J. Sullivan, *Hot Cracking Resistance of Austenitic Stainless-Steel Weld Metals*. Welding Journal, 1980. **59**(8): p. S226-S232.
44. Hunter, G.B. and T.W. Eagar, *Ductility of Stabilized Ferritic Stainless-Steel Welds*. Metallurgical Transactions a-Physical Metallurgy and Materials Science, 1980. **11**(2): p. 213-218.
45. Sharafi, S., *Microstructure of super-duplex stainless steels*, in *Department of Materials Science and Metallurgy*. 1993, University of Cambridge: Cambridge.
46. Knyazeva, M. and M. Pohl, *Duplex Steels. Part II: Carbides and Nitrides*. Metallography, Microstructure, and Analysis, 2013. **2**(5): p. 343-351.
47. Knyazeva, M. and M. Pohl, *Duplex Steels: Part I: Genesis, Formation, Structure*. Metallography Microstructure and Analysis, 2013. **2**(2): p. 113-121.
48. Sobol, O., *Hydrogen assisted cracking and transport studied by ToF-SIMS and data fusion with HR-SEM*. 2018, Otto-von-Guericke-Universität Magdeburg, Fakultät für Maschinenbau.
49. Rhode, M., *Hydrogen Diffusion and Effect on Degradation in Welded Microstructures of Creep-resistant Low-alloyed Steels*. 2016.
50. Mayr, P., et al., *Direct observation of phase transformations in the simulated heat-affected zone of a 9Cr martensitic steel*. International Journal of Materials Research, 2008. **99**(4): p. 381-386.
51. Liu, J. and S. Kou, *Effect of diffusion on susceptibility to cracking during solidification*. Acta Materialia, 2015. **100**: p. 359-368.
52. Katayama, S., *Solidification phenomena of weld metals (1st report). Characteristic solidification morphologies, microstructures and solidification theory*. Welding International, 2000. **14**(12): p. 939-951.
53. Katayama, S., *Solidification phenomena of weld metals (2nd report). Solidification theory*,

- solute redistribution and microsegregation behaviour*. *Welding International*, 2000. **14**(12): p. 952-963.
54. Davies, G.J. and J.G. Garland, *Solidification Structures and Properties of Fusion Welds*. *International Metallurgical Reviews*, 1975. **20**(1): p. 83-108.
 55. Rutter, J.W. and B. Chalmers, *A prismatic substructure formed during solidification of metals*. *Canadian Journal of Physics*, 1953. **31**(1): p. 15-39.
 56. Tiller, W.A., et al., *The redistribution of solute atoms during the solidification of metals*. *Acta Metallurgica*, 1953. **1**(4): p. 428-437.
 57. Borland, J.C., *Generalized Theory of Super-Solidus Cracking in Welds (and Castings)*. *British Welding Journal*, 1960: p. 508-512.
 58. Kurz, W., C. Bezencon, and M. Gaumann, *Columnar to equiaxed transition in solidification processing*. *Science and Technology of Advanced Materials*, 2001. **2**(1): p. 185-191.
 59. Folkhard, E. and G. Rabensteiner, *Welding metallurgy of stainless steels*. 1988: Springer-Verlag.
 60. Lin, D.-Y. and C.-C. Hsieh, *Precipitation examination of delta, sigma, and gamma phases using modified Cr/Ni equivalent ratios during the multipass welding of stainless steels*. *Metals and Materials International*, 2009. **15**(3): p. 507-514.
 61. Costa e Silva, A.L.V.d., *Non-metallic inclusions in steels – origin and control*. *Journal of Materials Research and Technology*, 2018. **7**(3): p. 283-299.
 62. Lundin, C.D., et al., *Weldability evaluations of modified 316 and 347 austenitic stainless steels: Part I - preliminary results*. *Welding Journal*, 1988. **67**: p. 35-46.
 63. Lundin, C.D., C.H. Lee, and R. Menon, *Hot Ductility and Weldability of Free Machining Austenitic Stainless Steel*. *Welding Journal*, 1988. **67**(6): p. 119-130.
 64. Shankar, V., et al., *Solidification cracking in austenitic stainless steel welds*. *Sadhana*, 2003. **28**(3-4): p. 359-382.
 65. Brooks, J.A. and F.J.L. Jr, *The Effects of Phosphorus, Sulfur and Ferrite Content on Weld Cracking of Type 309 Stainless Steel*. *Welding Journal*, 1978: p. 139-144.
 66. Olson, D.L., *Prediction of austenitic weld metal microstructure and properties*. *Welding Journal*, 1985: p. 281-295.
 67. Vitek, J.M., S.A. David, and C.R. Hinman, *Improved ferrite number prediction model that accounts for cooling rate effects - Part 2: Model results*. *Welding Journal*, 2003. **82**(2): p. 43s-50s.
 68. Vitek, J.M., S.A. David, and C.R. Hinman, *Improved ferrite number prediction model that accounts for cooling rate effects - Part 1: Model development - Details of a prediction model based on a neural network system of analysis are described*. *Welding Journal*, 2003. **82**(1): p. 10s-17s.
 69. Schaeffler, A.L., *Constitution diagram for stainless steel weld metal*. *Metal Progress*, 1949. **56**(11): p. 680-680B.
 70. DeLong, W.T., G.A. Ostrom, and E.R. Szumachowski, *Measurement and calculation of ferrite in stainless-steel weld metal*. *Welding Journal*, 1956. **35**: p. 521-528.
 71. DeLong, W.T., *Ferrite in Austenitic Stainless-Steel Weld Metal*. *Welding Journal*, 1974. **53**(7): p. S273-S286.
 72. DeLong, W.T., *Constitution Diagram for Stainless-Steel Weld Metal .1. DeLong Diagram*. *Metal Progress*, 1974. **106**(1): p. 226-226.
 73. Kotecki, D.J. and T.A. Siewert, *Wrc-1992 Constitution Diagram for Stainless-Steel Weld Metals - a Modification of the Wrc-1988 Diagram*. *Welding Journal*, 1992. **71**(5): p. S171-S178.
 74. Putz, A., et al., *Methods for the measurement of ferrite content in multipass duplex stainless steel welds*. *Welding in the World*, 2019. **63**(4): p. 1075-1086.
 75. Beck, F.H., et al., *New Cast HighStrength Alloy Grades by Structure Control*, in *Advances in the Technology of Stainless Steels and Related Alloys*. 1965, ASTM International.: West Conshohocken, PA. p. 174-183.
 76. Hull, F.C., *Delta ferrite and martensite formation in stainless steels*. *Welding Journal*, 1973.

- 52(5):** p. 193-203.
77. Carpenter, B., D.L. Olson, and D.K. Matlock, *A diagram to predict aluminum passivated stainless steel weld metal microstructure*, in *AWS 66th Annual Convention*. 1985: Las Vegas, Nevada.
 78. Kotecki, D.J., *A martensite boundary on the WRC-1992 diagram*. *Welding Journal*, 1999. **78(5)**: p. 180s-192s.
 79. Kotecki, D.J., *A martensite boundary on the WRC-1992 diagram - Part 2: The effect of manganese (vol 80, pg 353-s, 2000)*. *Welding Journal*, 2001. **80(2)**: p. 45s-45s.
 80. Wessman, S., *Evaluation of the WRC 1992 diagram using computational thermodynamics*. *Welding in the World*, 2013. **57(3)**: p. 305-313.
 81. Ramirez, A.J. and J.C. Lippold, *New Insight into the Mechanism of Ductility-Dip Cracking in Ni-base Weld Metals*, in *Hot Cracking Phenomena in Welds*, T. Böllinghaus and H. Herold, Editors. 2005, Springer Berlin Heidelberg: Berlin, Heidelberg. p. 19-41.
 82. Krafka, H. *Risse in Schweißverbindungen - Heißrissarten, Heißrissentstehung und Heißrissprüfung*. in *DVM-Bericht Festigkeits- und Bruchverhalten von Fügeverbindungen*. 2000. Berlin, Germany: DVM - Deutscher Verband für Materialforschung und -prüfung.
 83. Gollnow, C., *Beitrag zur Ermittlung vorrangig konstruktiver Einfl ussgrößen auf die Heißrissinitiierung an geschweißten Bauteilen*, in *Bundesanstalt für Materialforschung und -prüfung (BAM)*. 2015: Berlin. p. 183.
 84. Wilken, K., *Discussion and Evaluation of Some Extraordinary Cases of Hot Cracking*, in *Hot Cracking Phenomena in Welds*, T. Böllinghaus and H. Herold, Editors. 2005, Springer Berlin Heidelberg: Berlin, Heidelberg. p. 383-394.
 85. Koseki, T. and M.C. Flemings, *Solidification of undercooled Fe-Cr-Ni alloys: Part II. Microstructural evolution*. *Metallurgical and Materials Transactions A*, 1996. **27(10)**: p. 3226-3240.
 86. Koseki, T. and M.C. Flemings, *Solidification of undercooled Fe-Cr-Ni alloys: Part I. Thermal behavior*. *Metallurgical and Materials Transactions A*, 1995. **26(11)**: p. 2991-2999.
 87. Rajasekhar, K., et al., *Microstructural evolution during solidification of austenitic stainless steel weld metals: A color metallographic and electron microprobe analysis study*. *Materials Characterization*, 1997. **38(2)**: p. 53-65.
 88. Cieslak, M.J., A.M. Ritter, and W.F. Savage, *Solidification Cracking and Analytical Electron Microscopy of Austenitic Stainless Steel Weld Metals*. *Welding Journal*, 1982. **61**: p. 1-8.
 89. Kujanpaa, V.P., et al., *Correlation Between Solidification Cracking and Microstructure in Austenitic and Austenitic-Ferritic Stainless Steel*. *Welding Research International*, 1979. **9(2)**: p. 55-76.
 90. Bang, K.-s., S.-h. Pak, and S.-k. Ahn, *Evaluation of weld metal hot cracking susceptibility in superaustenitic stainless steel*. *Metals and Materials International*, 2013. **19(6)**: p. 1267-1273.
 91. Matsuda, F., *Hot crack susceptibility of weld metal*. *Advances in welding metallurgy*, 1990: p. 19-35.
 92. Mirapeix, J., et al., *Robust technique for spectroscopic plasma analysis with application in real-time arc welding quality monitoring*. *Optical Engineering*, 2006. **45(8)**: p. 083002-083002-5.
 93. Mirapeix, J., et al., *Welding Diagnostics by Means of Particle Swarm Optimization and Feature Selection*. *Journal of Sensors*, 2012. **2012**: p. 11.
 94. Huber, S., J. Glasschroeder, and M.F. Zaeh, *Analysis of the Metal Vapour during Laser Beam Welding*. *Lasers in Manufacturing 2011: Proceedings of the Sixth International Wlt Conference on Lasers in Manufacturing, Vol 12, Pt A*, 2011. **12**: p. 712-719.
 95. Zhang, Z.F., et al., *Real-time defect detection in pulsed GTAW of Al alloys through on-line spectroscopy*. *Journal of Materials Processing Technology*, 2013. **213(7)**: p. 1146-1156.
 96. Taparli, U.A., et al., *In situ laser-induced breakdown spectroscopy measurements of chemical compositions in stainless steels during tungsten inert gas welding*. *Spectrochimica Acta Part B: Atomic Spectroscopy*, 2018. **139**: p. 50-56.

97. Taparli, U.A., et al., *In situ chemical composition analysis of a tungsten-inert-gas austenitic stainless steel weld measured by laser-induced breakdown spectroscopy*. Spectrochimica Acta Part B: Atomic Spectroscopy, 2020. **167**: p. 105826.
98. Taparli, U.A., T. Kannengiesser, and A. Griesche, *Tungsten inert gas bead-on-plate weld chemical composition analysis by laser-induced breakdown spectroscopy*. IOP Conference Series: Materials Science and Engineering, 2020. **882**: p. 012023.
99. Gregor Gött, D.U., Ruslan Kozakov, *Spectral diagnostics of a pulsed gas metal arc welding process*. Weld World, 2013. **57**: p. 215-221.
100. Gott, G., et al., *Optical and Spectroscopic Study of a Submerged Arc Welding Cavern*. Welding Journal, 2016. **95**(12).
101. Il, R.D.S., et al., *The Determination of Hydrogen Distribution in High-Strength Steel Weldments Part 1: Laser Ablation Methods*. Welding Journal, 2001(May 2001).
102. Noll, R., et al., *LIBS analyses for industrial applications – an overview of developments from 2014 to 2018*. Journal of Analytical Atomic Spectrometry, 2018. **33**(6): p. 945-956.
103. Jolivet, L., et al., *Review of the recent advances and applications of LIBS-based imaging*. Spectrochimica Acta Part B: Atomic Spectroscopy, 2019. **151**: p. 41-53.
104. Ball, A.J., V. Hohreiter, and D.W. Hahn, *Hydrogen Leak Detection Using Laser-Induced Breakdown Spectroscopy*. Applied Spectroscopy, 2005. **59**(3): p. 348-353.
105. Eseller, K.E., F.Y. Yueh, and J.P. Singh, *Non-intrusive, on-line, simultaneous multi-species impurity monitoring in hydrogen using LIBS*. Applied Physics B, 2011. **102**(4): p. 963-969.
106. Schröder, S., et al., *Hydrogen detection with ChemCam at Gale crater*. Icarus, 2015. **249**: p. 43-61.
107. Karpate, T., et al., *LIBS: a potential tool for industrial/agricultural waste water analysis*. SPIE Photonics Europe. Vol. 9893. 2016: SPIE.
108. Kearton, B. and Y. Mattley, *Laser-induced breakdown spectroscopy: Sparking new applications*. Nat Photon, 2008. **2**(9): p. 537-540.
109. Cremers, D.A. and L.J. Radziemski, *Handbook of laser-induced breakdown spectroscopy*. 2. ed. 2006, Chichester: Wiley.
110. Noll, R., *Laser-induced breakdown spectroscopy fundamentals and applications*. 2012, Berlin: Springer.
111. F. Anabiarte, A.C., J.M. Lopez-Higuera, *Laser-Induced Breakdown Spectroscopy: Fundamentals, Applications, and Challenges*. ISRN Spectroscopy, 2012. **2012**.
112. Radziemski, L. and D. Cremers, *A brief history of laser-induced breakdown spectroscopy: From the concept of atoms to LIBS 2012*. Spectrochimica Acta Part B: Atomic Spectroscopy, 2013. **87**: p. 3-10.
113. NASA, *SuperCam for Scientists*. 2020.
114. Zhang, S., et al., *Chemometrics and theoretical approaches for evaluation of matrix effect in laser ablation and ionization of metal samples*. Spectrochimica Acta Part B: Atomic Spectroscopy, 2015. **107**: p. 17-24.
115. Müller, M., *Neue Wege zur Quantifizierung mit der laserinduzierten Plasmaspektroskopie (LIBS)*. 2010, Bundesanstalt für Materialforschung und -prüfung (BAM): Berlin. p. 1-159.
116. Vadillo, J.M. and J.J. Laserna, *Laser-induced plasma spectrometry: truly a surface analytical tool*. Spectrochimica Acta Part B: Atomic Spectroscopy, 2004. **59**(2): p. 147-161.
117. Gottlieb, C., *Einfluss der Korngröße auf die quantitative Elementanalyse heterogener, mineralischer Werkstoffe mittels der laserinduzierten Plasmaspektroskopie*. 2019, Technische Universität Clausthal.
118. Hahn, D.W. and N. Omenetto, *Laser-Induced Breakdown Spectroscopy (LIBS), Part I: Review of Basic Diagnostics and Plasma—Particle Interactions: Still-Challenging Issues within the Analytical Plasma Community*. Applied Spectroscopy, 2010. **64**(12): p. 335A-336A.
119. Hahn, D.W. and N. Omenetto, *Laser-Induced Breakdown Spectroscopy (LIBS), Part II: Review of Instrumental and Methodological Approaches to Material Analysis and Applications to*

- Different Fields*. Applied Spectroscopy, 2012. **66**(4): p. 347-419.
120. Sansonetti, J.E., *Wavelengths, Transition Probabilities, and Energy Levels for the Spectra of Potassium (KI through KXIX)*. Journal of Physical and Chemical Reference Data, 2008. **37**(1): p. 7-96.
 121. *ARYELLE Spectrograph Series Instruction Manual*. Lasertechnik Berlin GmbH, 2015.
 122. **Harris, D.C.**, *Quantitative Chemical Analysis*. 2007, New York: W. H. Freeman and Company.
 123. **Nanolmages**, *SEM Technology Overview – Scanning Electron Microscopy 2020*.
 124. Zhou, Z., et al., *Arc/Spark Optical Emission Spectrometry: Principles, Instrumentation, and Recent Applications*. Applied Spectroscopy Reviews, 2005. **40**(2): p. 165-185.
 125. Weglowski, M.S., *Monitoring of Arc Welding Process Based on Arc Light Emission*. Welding Processes, ed. R. Kovacevic. 2012.
 126. Huber, S., *In-situ-Legierungsbestimmung beim Laserstrahlschweißen*. 2014, Technische Universität München: Munic.
 127. Wu, C.S., M. Ushio, and M. Tanaka, *Analysis of the TIG welding arc behavior*. Computational Materials Science, 1997. **7**(3): p. 308-314.
 128. Mills, G.S., *Use of Emission-Spectroscopy for Welding Arc Analysis*. Welding Journal, 1977. **56**(3): p. S93-S96.
 129. Castro, J.P. and E.R. Pereira-Filho, *Twelve different types of data normalization for the proposition of classification, univariate and multivariate regression models for the direct analyses of alloys by laser-induced breakdown spectroscopy (LIBS)*. Journal of Analytical Atomic Spectrometry, 2016. **31**(10): p. 2005-2014.
 130. Syvilay, D., J. Guezenoc, and B. Bousquet, *Guideline for increasing the analysis quality in laser-induced breakdown spectroscopy*. Spectrochimica Acta Part B: Atomic Spectroscopy, 2019. **161**: p. 105696.
 131. Tognoni, E. and G. Cristoforetti, *[INVITED] Signal and noise in Laser Induced Breakdown Spectroscopy: An introductory review*. Optics & Laser Technology, 2016. **79**: p. 164-172.
 132. Blockbolten, A. and T.W. Eagar, *Metal Vaporization from Weld Pools*. Metallurgical Transactions B-Process Metallurgy, 1984. **15**(3): p. 461-469.
 133. Tashiro, S., et al., *Numerical analysis of fume formation mechanism in TIG welding*. Welding International, 2015. **29**(3): p. 165-172.
 134. Tanaka, M., Y. Tsujimura, and K. Yamazaki, *Dynamic Behaviour of Metal Vapour in ARC Plasma During TIG Welding*. Welding in the World, 2012. **56**(1): p. 30-36.
 135. Tanaka, K., et al., *Investigation of the bilayer region of metal vapor in a helium tungsten inert gas arc plasma on stainless steel by imaging spectroscopy*. Journal of Physics D: Applied Physics, 2019. **52**(35): p. 354003.
 136. Park, H., et al., *A computational model of gas tungsten arc welding of stainless steel: the importance of considering the different metal vapours simultaneously*. Journal of Physics D: Applied Physics, 2018. **51**(39): p. 395202.
 137. Shiri, S.G., et al., *Gas tungsten arc welding of CP-copper to 304 stainless steel using different filler materials*. Transactions of Nonferrous Metals Society of China, 2012. **22**(12): p. 2937-2942.
 138. Labutin, T.A., et al., *Comparison of the thermodynamic and correlation criteria for internal standard selection in laser-induced breakdown spectroscopy*. Spectrochimica Acta Part B: Atomic Spectroscopy, 2013. **87**: p. 57-64.
 139. Khan, P.A.A. and T. Debroy, *Alloying Element Vaporization and Weld Pool Temperature during Laser-Welding of Aisi 202 Stainless-Steel*. Metallurgical Transactions B-Process Metallurgy, 1984. **15**(4): p. 641-644.
 140. Zhang, Y.M., J.R.G. Evans, and S.F. Yang, *Corrected Values for Boiling Points and Enthalpies of Vaporization of Elements in Handbooks*. Journal of Chemical and Engineering Data, 2011. **56**(2): p. 328-337.
 141. Gui, L., et al., *Thermodynamic study on the solute partition coefficients on L/ δ and L/ δ + γ phase*

- interfaces for 1215 high-sulfur steel solidification by orthogonal design*. Journal of Materials Research and Technology, 2020. **9**(1): p. 89-103.
142. Wan, J., Y. Lou, and H. Ruan, *The partition coefficient of alloying elements and its influence on the pitting corrosion resistance of 15Cr-2Ni duplex stainless steel*. Corrosion Science, 2018. **139**: p. 13-20.
143. Ennis, B.L., et al., *The role of aluminium in chemical and phase segregation in a TRIP-assisted dual phase steel*. Acta Materialia, 2016. **115**: p. 132-142.
144. Kobayashi, Y., H. Todoroki, and K. Mizuno, *Problems in Solidification Model for Microsegregation Analysis of Fe–Cr–Ni–Mo–Cu Alloys*. ISIJ International, 2019. **59**(2): p. 277-282.